

**CHARMONIUM PRODUCTION AND SUPPRESSION IN  
Pb+Pb COLLISIONS AT  $\sqrt{s_{NN}} = 2.76$  TeV WITH CMS**

*By*

**ABDULLA ABDULSALAM**

**PHYS01200904016**

**Bhabha Atomic Research Centre, Mumbai**

*A thesis submitted to the  
Board of Studies in Physical Sciences  
In partial fulfillment of requirements  
for the Degree of*

**DOCTOR OF PHILOSOPHY**

*of*

**HOMI BHABHA NATIONAL INSTITUTE**



**July, 2014**

# Homi Bhabha National Institute

## Recommendations of the Viva Voce Board

As members of the Viva Voce Board, we certify that we have read the dissertation prepared by Abdulla Abdulsalam, entitled “Charmonium production and suppression in Pb+Pb Collisions at  $\sqrt{s_{NN}} = 2.76$  TeV with CMS” and recommend that it may be accepted as fulfilling the thesis requirement for the award of Degree of Doctor of Philosophy.

\_\_\_\_\_  
Chairman: Dr. V. M. Datar Date:

\_\_\_\_\_  
External Examiner: Prof. Kajari Mazumdar Date:

\_\_\_\_\_  
Guide: Dr. Prashant Shukla Date:

\_\_\_\_\_  
Member 1: Dr. A. K. Mohanty Date:

\_\_\_\_\_  
Member 2: Dr. Prof. R. Bhalerao Date:

Final approval and acceptance of this thesis is contingent upon the candidate's submission of the final copies of the thesis to HBNI.

I hereby certify that I/we have read this thesis prepared under my/our direction and recommend that it may be accepted as fulfilling the thesis requirement.

Guide:

Date:

## **STATEMENT BY AUTHOR**

This dissertation has been submitted in partial fulfillment of requirements for an advanced degree at Homi Bhabha National Institute (HBNI) and is deposited in the Library to be made available to borrowers under rules of the HBNI.

Brief quotations from this dissertation are allowable without special permission, provided that accurate acknowledgement of source is made. Requests for permission for extended quotation from or reproduction of this manuscript in whole or in part may be granted by the Competent Authority of HBNI when in his or her judgment the proposed use of the material is in the interests of scholarship. In all other instances, however, permission must be obtained from the author

ABDULLA ABDULSALAM

## **DECLARATION**

I, hereby declare that the investigation presented in the thesis has been carried out by me. The work is original and has not been submitted earlier as a whole or in part for a degree / diploma at this or any other Institution / University.

**ABDULLA ABDULSALAM**

## List of Publications

1. **“Measurement of prompt  $\psi(2S)$  to  $J/\psi$  yield ratios in Pb-Pb and p-p collisions at  $\sqrt{s_{NN}} = 2.76$  TeV”**, V. Khachatryan, A. Abdulsalam *et al.* [CMS Collaboration], Phys. Rev. Lett. **113**, 262301 (2014), (CMS HIN-12-007).
2. **“Suppression of bottomonia states in finite size quark gluon plasma in PbPb collisions at Large Hadron Collider”**, Abdulla Abdulsalam and Prashant Shukla, Int. J. Mod. Phys. A **28**, 1350105 (2013), arXiv:1210.7584.
3. **“Probing strongly interacting matter with heavy resonances in Pb+Pb collisions at LHC energies”**, Prashant Shukla and Abdulla Abdulsalam, J. Phys. Conf. Ser. **374** 012021 (2012).
4. **“Suppression of non-prompt  $J/\psi$  , prompt  $J/\psi$  and  $\Upsilon(1S)$  in PbPb collisions at  $\sqrt{s_{NN}} = 2.76$  TeV”**, S. Chatrchyan *et al.* [CMS Collaboration], J. High Energy Phys. **1205**, 63 (2012), CMS PAS HIN-10-006.
5. **“Prompt and non-prompt  $J/\psi$   $R_{AA}$  with  $150 \mu\text{b}^{-1}$  integrated PbPb luminosity at  $\sqrt{s_{NN}} = 2.76$  TeV”**, CMS PAS HIN-12-014 (2012).
6. **“Observation of Sequential  $\Upsilon$  Suppression in PbPb Collisions”**, S. Chatrchyan, A. Abdulsalam *et al.* [CMS Collaboration], Phys. Rev. Lett. **109**, 222301 (2012).
7. **“Bottomonium production in pp, pPb and PbPb collisions with CMS”**, Abdulla Abdulsalam [CMS collaboration], Nucl. Phys. A **931**, 649 (2014).

## Papers in DAE Symposium

1. **“Suppression of bottomonia states in finite size quark gluon plasma in PbPb collisions at LHC”**, Prashant Shukla, Abdulla Abdulsalam and Vineet Kumar, Proc. DAE Symp. Nucl. Phys. **57**, 830 (2012).
2. **“Charmonium Production in Pb+Pb Collisions  $\sqrt{s_{NN}} = 2.76$  TeV”**, Abdulla Abdulsalam, Vineet Kumar and Prashant Shukla, [CMS collaboration], Proc. DAE Symp. Nucl. Phys. **57**, 758 (2012).
3. **“Transverse momentum dependence of  $\Upsilon'/\Upsilon$  ratio in heavy ion collisions at LHC”**, P. Shukla, Abdulla Abdulsalam and Vineet Kumar, Proc. DAE Symp. Nucl. Phys. **56**, 1014 (2011).
4. **“ $J/\psi$  production in Pb+Pb collisions at  $\sqrt{s_{NN}} = 2.76$  TeV”**, Abdulla Abdulsalam, Vineet Kumar and P. Shukla, [CMS collaboration], Proc. DAE Symp. Nucl. Phys. **56**, 916 (2011).
5. **“ $J/\psi$  - $\mu$  correlation as probe for  $b$ - $\bar{b}$  production and interaction mechanism at LHC”**, A. Abdulsalam, P. Sett, P. Shukla and R. K. Choudhury, Proc. DAE Symp. Nucl. Phys. **55**, 600 (2010).

---

The thesis is based on first three publications in the list and partially on 4th and 5th publication.

ABDULLA ABDULSALAM

*To*

*my beloved parents and family*

## ACKNOWLEDGMENTS

First and foremost, I would like to praise Almighty God for endowing me with power, stability and patience to pursue the dream and to accomplish the task. His guidance in troublesome situation, his support in the time of hardship and his unconditional mercy towards me made this moments happen. Again I thank him.

I would like to express my sincere gratitude to my supervisor, Dr. Prashant Shukla, for his assistance, care and constant support throughout my research period. He always backed me when I needed and tried his best to resolve the problem I faced. His timely advice helped me achieve the goal faster. I am greatly indebted to him for any piece of work I did and reading my thesis.

I would like to thank all members of Doctoral committee for their valuable suggestions during my Ph.D. The present and past members are Dr. V. M. Datar (Chairman), Dr. Prashant Shukla (Guide & Convener), Dr. A. K. Mohanty, Prof. R. Bhalerao and Dr. R.K. Choudhury (former chairman,retired).

I utilise this opportunity to thank all my CMS dilepton colleagues; particularly Catherine, Raphael, Torsten, Camelia, Mihee, Dongho, Zhen hu and Hyunchul. I am happy to give a special thanks to Torsten with whom I have spent many day-nights in the search of Onia. The fruitful interaction with him, in-online and offline, benefited me in many ways.

Again, I am very happy to give a special and sincere thanks to Vineet who imparted to me the first lessons of research tools. His help and support always gave me a sense of relax when I was in the midst of work-pressure.

It was a wonderful time I spent with my colleagues; Priyanka, khandai, Ruchi, Prakhar, Kapil and the 'neighbours' Nithin, Eshita, Ankur, Sapna, Archana, Vishal, Sunil, Mahendra and Naveen; thanks to them for being good friends through out my

Ph.D, for their help and for having good chats during the tea-time or lunch/dinner. Thanks to Prakhar for providing useful suggestion and making fun in the dinner outings. The memory of those days with cheerful chats and healthy debate are still alive in my heart.

I want to thank all my batch mates, especially Yusuf Ali, Dileep, Suresh, Vivek, Jerina, Venkateswararao, Ahmed, Prashant, Raja Moorthy and Gangamallaiiah, who helped me without any condition in the world of real life (outside Lab).

Also I am very thankful to Dr. Pawan Kumar, Dr. Dipak Mishra, Dr. Dipanwita Dutta and Raman for their advice, encourage and fruitful discussion which resulted in improving my knowledge and understanding in High energy physics.

Finally, to my family. My words are not enough to express my deepest gratitude to my family members for their support, love and prayer; especially to my father Abdussalam. He always encouraged my education and endeavors at every turn and have never wavered in his love and support. To my wife Rafeeda, warm thanks for being with me in all my ups and downs of life, who endured all my shortcomings with smiling face. This is the great time to express my sincere thanks to my brother Anees, my sisters and brothers-in law.

# CONTENTS

	Page
LIST OF FIGURES . . . . .	viii
LIST OF TABLES . . . . .	xx
1      Introduction . . . . .	1
1.1. Particle physics: past to present . . . . .	2
1.2. Quantum Chromodynamics . . . . .	4
1.2.1. QCD phase transition . . . . .	7
1.3. Heavy ion collisions . . . . .	11
1.3.1. Stages of a heavy ion collision . . . . .	11
1.4. Soft probes/Bulk properties . . . . .	16
1.4.1. Multiplicity distributions . . . . .	16
1.4.2. Direct photons . . . . .	19
1.4.3. Azimuthal anisotropy . . . . .	20
1.5. Hard probes . . . . .	23
1.5.1. Nuclear modification factor, $R_{AA}$ . . . . .	23
1.5.2. Jet-quenching . . . . .	25
1.5.3. Dijet-imbalance . . . . .	26
1.5.4. Heavy quarks and heavy flavor mesons . . . . .	27
1.6. Quarkonium . . . . .	29
1.7. Outline of thesis . . . . .	30
2      Charmonium . . . . .	31
2.1. Introduction . . . . .	32
2.2. The charmonium hadroproduction models . . . . .	37
2.2.1. Color Evaporation Model (CEM) . . . . .	38
2.2.2. Color Singlet Model (CSM) . . . . .	38
2.2.3. Non-Relativistic QCD Model (NRQCDM) . . . . .	39
2.2.4. Experiment and model comparison . . . . .	42
2.3. Charmonium in p+A collisions . . . . .	44
2.3.1. Nuclear shadowing . . . . .	45
2.3.2. Cronin effect . . . . .	46
2.3.3. Nuclear absorption . . . . .	47

CHAPTER	Page
2.4. Charmonium in A+A collisions . . . . .	47
2.4.1. Suppression by comover collisions . . . . .	48
2.4.2. Suppression by color screening . . . . .	49
2.4.3. Enhancement through regeneration . . . . .	50
2.4.4. Transverse momentum behavior . . . . .	51
2.5. Experimental status . . . . .	51
<b>3 CMS experiment at LHC . . . . .</b>	<b>54</b>
3.1. LHC machine . . . . .	55
3.2. Luminosity . . . . .	57
3.3. Compact Muon Solenoid . . . . .	59
3.3.1. Magnet . . . . .	62
3.3.2. Tracker . . . . .	63
3.3.3. Calorimetry . . . . .	64
3.3.4. CMS muon system . . . . .	67
3.4. Centrality determination . . . . .	68
3.4.1. Trigger and Data acquisition . . . . .	70
3.4.2. CMS data flow . . . . .	72
<b>4 Data Selection . . . . .</b>	<b>74</b>
4.1. Introduction . . . . .	75
4.2. Definition of Minimum bias collisions . . . . .	76
4.2.1. The minimum bias trigger . . . . .	76
4.2.2. Offline event selection and cleaning . . . . .	77
4.3. The Double muon trigger . . . . .	80
4.4. Muon skim . . . . .	82
4.5. Data selection: 2011 PbPb run . . . . .	83
4.6. Muon quality selection . . . . .	84
4.6.1. Variables description . . . . .	85
4.6.2. Method . . . . .	86
4.6.3. Final cuts . . . . .	97
4.7. Muon selection study: 2011 PbPb data . . . . .	99
4.8. Kinematic threshold . . . . .	105
4.8.1. Statistical optimization . . . . .	105
4.8.2. Summary of offline selection . . . . .	105
4.9. Agreement MC/data . . . . .	106

5	Measurement of $J/\psi$ in PbPb collisions at $\sqrt{s_{\text{NN}}}=2.76$ TeV . . . . .	112
	5.1. Introduction . . . . .	113
	5.2. Data selection . . . . .	115
	5.3. Signal extraction . . . . .	116
	5.3.1. Yield extraction . . . . .	116
	5.3.2. Prompt and Non-prompt $J/\psi$ . . . . .	119
	5.4. Efficiency corrections . . . . .	123
	5.4.1. MC samples . . . . .	124
	5.5. Systematic uncertainties . . . . .	127
	5.6. Results . . . . .	128
	5.6.1. Prompt $J/\psi$ . . . . .	128
	5.6.2. Non-prompt $J/\psi$ . . . . .	128
6	Measurement of the $\psi(2\text{S})$ meson in PbPb collisions at $\sqrt{s_{\text{NN}}}=2.76$ TeV . . . . .	134
	6.1. Introduction . . . . .	135
	6.2. Signal extraction . . . . .	136
	6.3. Systematic checks and uncertainties . . . . .	146
	6.3.1. Signal extraction . . . . .	146
	6.4. Efficiency and Acceptance . . . . .	147
	6.4.1. Efficiency studies . . . . .	147
	6.4.2. Acceptance studies . . . . .	151
	6.4.3. b-Hadron contamination . . . . .	152
	6.4.4. Summary of systematic uncertainties . . . . .	153
	6.5. Confidence intervals and Limits . . . . .	153
	6.6. Results . . . . .	155
	6.6.1. Results with old data . . . . .	155
	6.6.2. Results with new data . . . . .	156
7	Suppression of quarkonia states in finite size quark gluon plasma in PbPb collisions at Large Hadron Collider . . . . .	162
	7.1. Introduction . . . . .	163
	7.2. Properties of the $\Upsilon$ states from potential models . . . . .	164
	7.3. Quarkonia suppression in finite size QGP . . . . .	165
	7.4. Results and discussions . . . . .	170

CHAPTER	Page
8 Conclusion . . . . .	180
REFERENCES . . . . .	186
APPENDIX A . . . . .	198
APPENDIX B . . . . .	201
APPENDIX C . . . . .	203

## SYNOPSIS

## Charmonium production and suppression in PbPb Collisions at $\sqrt{s_{NN}} = 2.76$ TeV with CMS

The theory of Quantum Chromodynamics (QCD), which describes the strong interaction between quarks and gluons in the Standard Model, predicts a phase transition from hadronic matter to a thermally equilibrated and strongly interacting matter called Quark Gluon Plasma (QGP) at very high temperature and high baryon density [1, 2]. In this new phase of matter partons (quarks and gluons) are deconfined (not bound into composite colourless hadrons). It is believed that the universe was created from a 'Big Bang' and was initially in a QGP state (just after the creation). Then the universe expanded and the energy density decreased which led to the transition to ordinary (confined) matter. The primary aim of the heavy ion experimental program is to produce the QGP and measure its properties. In 2005, RHIC experiments announced the discovery of the QGP.

The formation of QGP in high-energy nuclear collisions can be tested in a variety of ways. One of its most striking signatures is the suppression of quarkonium states, both of the charmonium ( $J/\psi, \psi(2S), \chi_c$  etc) and the bottomonium ( $\Upsilon(1S, 2S, 3S), \chi_b$  etc) families. This is thought to be a direct effect of deconfinement, when the binding potential between the constituents of a quarkonium state, a heavy quark and its anti-quark, is screened by the colour charges of the surrounding light quarks and gluons [3]. The suppression is predicted to occur above the critical temperature of the medium ( $T_c \sim 0.160$  GeV [4]) and depends on the  $Q\bar{Q}$  binding energy. Since the  $\Upsilon(1S)$  is the most tightly bound state among all quarkonia (Binding energy( $\Delta E$ ) = 1.10 GeV and radius( $r$ ) = 0.28 fm), it is expected to be the one with the highest dissociation temperature, while the  $\psi(2S)$  with the lowest binding energy( $\Delta E = 0.05$  GeV and  $r =$

0.90 fm), to be the one with the lowest dissociation temperature and hence the first to melt. Examples of dissociation temperatures are:  $T_{\text{diss}} \sim 1 T_c$ ,  $1.2 T_c$  and  $2 T_c$  for the  $\psi(2S)$ ,  $J/\psi$  and  $\Upsilon(1S)$  respectively [5]. The results from the PbPb collisions at LHC suggest that the temperature of the produced medium ( $T \sim 300$  MeV [6, 4]) goes well above the transition temperature predicted for the deconfinement phase transition by lattice QCD calculations. Therefore the study of quarkonium production in such a hot medium created at the LHC is very relevant. Also this sequential screening provides an effective thermometer for determining the temperature of the QGP by observing which quarkonium states survive and which were unable to form in the QGP [7, 132]. However, there are other possible changes to the quarkonium production in heavy-ion collisions over pp collisions. Cold-nuclear-matter effects, such as the modifications of the parton distribution functions inside the nucleus (shadowing), can reduce the production of quarkonia without the presence of a QGP [9, 10]. Such effects, unseen in the proton-proton collisions, can be understood with help of proton-nucleus (pA) collisions. The study of quarkonia production in pA collisions over a wide range of kinematic variables can provide constraints on the modification of parton distribution functions in the nuclei.

The currently running experimental facilities include Relativistic Heavy-Ion Collider (RHIC) at BNL and newly constructed Large Hadron Collider (LHC) at CERN. RHIC has produced collisions between pp, dAu, CuCu and AuAu at different energies ranging from centre-of-mass energy per nucleon ( $\sqrt{s_{NN}} = 7.7$  GeV to 200 GeV. At the end of 2010, the LHC started operation with heavy ion beams, colliding lead nuclei at  $\sqrt{s_{NN}} = 2.76$  TeV and opening a new era in ultra-relativistic heavy ion physics at energies exceeding previous accelerators by more than an order of magnitude. The measurements were performed with the data recorded by the Compact Muon Solenoid (CMS) experiment during the PbPb runs, at the end of 2010 ( $\mathcal{L} \sim$

7.3  $\mu\text{b}^{-1}$ ) and 2011 ( $\mathcal{L} \sim 150 \mu\text{b}^{-1}$ ), and during the pp runs, in March 2011 ( $\mathcal{L} \sim 231 \text{nb}^{-1}$ ) and at the beginning of 2013 ( $\mathcal{L} \sim 5.4 \text{pb}^{-1}$ ), all at  $\sqrt{s_{\text{NN}}} = 2.76 \text{TeV}$ . At this significantly higher energy and integrated luminosity the role of LHC after the RHIC is 1) to quantify the difference in the properties of matter produced in the heavy ion collisions such as the energy density, initial temperature and lifetime etc. 2) to do quantitative and systematic study of the QGP with higher precision (eg: viscosity and Debye screening mass). On quarkonium side, we can do precision measurement in production and suppression of different quarkonia states relative to their ground states. In the beginning of 2013, CMS collected  $\mathcal{L} \sim 31 \text{nb}^{-1}$  of pPb collisions at  $\sqrt{s_{\text{NN}}} = 5.02 \text{TeV}$ , important reference data for the PbPb studies. In this thesis we mainly focus on charmonium production in PbPb collisions at  $\sqrt{s_{\text{NN}}} = 2.76 \text{TeV}$  with CMS at LHC. We describe the production and suppression of prompt and non-prompt  $J/\psi$  with 2010 and 2011 PbPb data and the study on the relative suppression of  $J/\psi$  and  $\psi(2\text{S})$  using ratio of their yields in PbPb and pp data. Also we did a phenomenological study on quarkonium suppression due to color screening in an expanding QGP based on a dynamical model which takes into account lifetime and size of QGP.

The CMS detector is best suited for quarkonia analysis. The excellent momentum resolution of CMS results in well-resolved  $J/\psi$  or  $\Upsilon$  peaks in the dimuon mass spectrum. The central feature of CMS detector is a superconducting solenoid of 6m internal diameter, providing a magnetic field of 3.8 T. Within the field volume are the silicon pixel and strip tracker, the crystal electromagnetic calorimeter, and the brass/scintillator hadron calorimeter. The coordinate system adopted by CMS has the origin centered at the nominal collision point inside the experiment, the y-axis pointing vertically upward, and the x-axis pointing radially inward toward the center of the LHC. Thus, the z-axis points along the beam direction. The azimuthal angle  $\phi$  is measured from the x-axis in the x-y plane. The polar angle  $\theta$  is measured from

the z-axis. Pseudorapidity is defined as  $\eta = -\ln \tan(\theta/2)$ . Thus, the momentum and energy measured transverse to the beam direction, denoted by  $p_T$  and  $E_T$ , respectively. Muons are detected in the range  $|\eta| \leq 2.4$ , with detection planes based on three technologies: drift tubes, cathode strip chambers, and resistive plate chambers. Because of the strong magnetic field and the fine granularity of the tracker, the muon  $p_T$  measurement based on information from the tracker alone has a resolution between 1 to 2 % for a typical muon in this analysis.

### 0.1. Prompt and non-prompt $J/\psi$ measurement

In this analysis we measure the inclusive  $J/\psi$  production produced in PbPb collisions at  $\sqrt{s_{NN}} = 2.76$  TeV. *Non-prompt*  $J/\psi$  from B hadron decays have been separated from *prompt*  $J/\psi$  (directly produced or decayed from higher excited states) utilising the reconstructed decay vertex of the  $\mu^+\mu^-$  pair. Muons are reconstructed by matching tracks in the muon detectors and silicon tracker. The same offline reconstruction algorithm and selection criteria are applied to the PbPb and pp data samples. An explicit study was carried out to tune and optimise the cut variables (number of valid tracker hits,  $\chi^2/ndof$  of both the inner track and the global fit, etc) which are applied in physics analysis to obtain good quality muons. Experimentally, the suppression is quantified by the ratio of the yield measured in heavy-ion collisions over the yield measured in pp collisions where no QGP is formed. Such a ratio is called nuclear modification factor,  $R_{AA}$ .

$$R_{AA} = \frac{N_{\text{PbPb}}}{N_{\text{coll}} \cdot N_{\text{pp}}} \cdot \frac{\varepsilon_{\text{pp}}}{\varepsilon_{\text{PbPb}}} \quad (0.1)$$

where  $N_{\text{coll}}$  is the number of binary nucleon-nucleon collisions and  $\varepsilon_{\text{pp}}$  and  $\varepsilon_{\text{PbPb}}$  are the combined trigger and reconstruction efficiency in pp and PbPb respectively. In

the absence of medium effects, one would expect  $R_{AA} = 1$  for hard processes. The  $R_{AA}$  of prompt and non-prompt  $J/\psi$  has been measured separately by CMS in bins of transverse momentum ( $p_T$ ), rapidity ( $y$ ) and collision centrality. In CMS experiment the centrality is estimated using the sum of transverse energy deposited in towers from both forward calorimeter (HF) at positive and negative  $z$  positions. The distribution of the total transverse energy was used to divide the event sample into bins, each representing particular % of the total nucleus-nucleus interaction cross section, where 0% denotes the most central collisions. A strong, centrality-dependent suppression has been observed for  $J/\psi$  with  $p_T > 6.5$  GeV/c [11]. The ALICE experiment has acceptance down to  $p_T = 0$  and has shown a moderate ( $R_{AA} \simeq 0.6$ ) suppression of inclusive  $J/\psi$  for all centralities, at forward rapidity.

## 0.2. Charmonia double ratio measurement

As the  $\psi(2S)$  meson is less bound than the  $J/\psi$  it is expected to melt already at lower temperatures. This sequential melting should manifest itself in nuclear modification factors ( $R_{AA}$ ) for the  $\psi(2S)$  that are smaller, or at most equal, to those measured for the  $J/\psi$ . It has been predicted that, due to the large number of charm quarks and anti-quarks produced in PbPb collisions ( $O(100)$ ) at  $\sqrt{s_{NN}} = 2.76$  TeV, charmonia may be produced at the hadronization stage of the PbPb collisions from initially uncorrelated charm and anti-charm quarks, produced in the initial inelastic collisions [12]. Such recombination effects would be contributing mostly at low charmonium  $p_T$ , for which CMS has only acceptance in the forward rapidity region. The analysis is performed in two (dimuon  $p_T$ ,  $y$ ) kinematical ranges:

- 1)  $1.6 \leq |y| \leq 2.4$ ,  $3.0 \leq p_T \leq 30$  GeV/c
- 2)  $|y| \leq 1.6$ ,  $6.5 \leq p_T \leq 30$  GeV/c.

Dimuons are restricted to  $p_T \leq 30\text{GeV}/c$  in order to have a well defined kinematic interval. The centrality classes are 40-100%, 20-40% and 0-20% (most central), ordered from the lowest to the highest HF calorimeters energy deposit. In the  $\psi(2S)$  analysis, prompt and non-prompt  $J/\psi$  or  $\psi(2S)$  are not separated because of the limited significance of the  $\psi(2S)$  yield. The main result is presented in the form of a double ratio, which compares the ratio of  $\psi(2S)$  over  $J/\psi$  yields ( $R = N_{\psi(2S)}/N_{J/\psi}$ ) in PbPb and pp collisions. The double ratio can also be written as the ratio of  $\psi(2S)$  and  $J/\psi$  nuclear modification factors.

$$(N_{\psi(2S)}/N_{J/\psi})_{\text{PbPb}}/(N_{\psi(2S)}/N_{J/\psi})_{\text{pp}} = R(\text{PbPb})/R(\text{pp}) = R_{\text{AA}}(\psi(2S))/R_{\text{AA}}(J/\psi). \quad (0.2)$$

Such a double ratio has the advantage that efficiency and acceptance corrections cancel, leading to reduced uncertainty. For  $6.5 \leq p_T \leq 30 \text{ GeV}/c$  and  $|y| \leq 1.6$  the double ratio is always less than unity, meaning that high- $p_T$   $\psi(2S)$  are more suppressed than  $J/\psi$ . However, in lower  $p_T$  ( $3 < p_T < 30 \text{ GeV}/c$ ) and forward rapidity region, the double ratio is  $5.32 \pm 1.03$  (stat.)  $\pm 0.79$  (syst.)  $\pm 2.58$  (pp) in the most central collisions. It means that more  $\psi(2S)$  are produced compared to  $J/\psi$  in PbPb than in pp collisions. Currently the data does not allow for a strong conclusion due to large statistical uncertainty related to the small pp data sample.

An iterative track reconstruction (RegIt-Regional Iterative Tracking) is employed in PbPb to find tracks in the silicon tracker that can be matched to the standalone muons. The pp reconstruction algorithm includes an iterative tracking step in the full silicon tracker. This analysis is updated with RegIt PbPb data and 2013 pp data ( $\mathcal{L} \sim 5.4 \text{ pb}^{-1}$ ), with which the large statistical uncertainty of the double ratio is reduced significantly. Also an extensive study was done to obtain best shapes for signal and background. The new result shows that in the most central collisions the double ratio

is  $2.31 \pm 0.53$  (stat.)  $\pm 0.37$  (syst.)  $\pm 0.15$  (pp) in lower  $p_T$  and at forward rapidity. Also we did a preliminary study on ratio of  $\psi(2S)$  to  $J/\psi$  with pPb data at  $\sqrt{s_{NN}} = 5.02$  TeV. It shows an interesting variation of the ratios in different  $p_T$  bins.

### 0.3. Phenomenology study on quarkonium suppression

We estimated the bottomonia survival probability,  $S$  due to color screening in an expanding QGP using a dynamical model which takes into account the finite lifetime and spatial extent of the system [136]. The competition between the resonance formation time and the plasma characteristics such as temperature, lifetime and spatial extent decides the dependence of the survival probabilities of  $\Upsilon$  states on  $p_T$  and centralities. The properties of  $\Upsilon$  states from potential models and their dissociation temperatures have been used as ingredients in the study.

The model assumes that quark gluon plasma is formed at some initial entropy density in PbPb collisions at  $\sqrt{s_{NN}} = 2.76$  TeV, which undergoes an isentropic expansion by Bjorken's hydrodynamics [14]. Taking account of the position at which the bottom-quark pair is created, we calculated the survival probability as a function of  $p_T$ .

$$S(p_T, R) = \frac{\int_0^R dr r \rho(r) \phi(\mathbf{r}, \mathbf{p}_T)}{\int_0^R dr r \rho(r)}. \quad (0.3)$$

where  $\rho(r)$  is the probability of a quark pair to be created at  $r$  and  $\phi(\mathbf{r}, \mathbf{p}_T)$  is the angle between  $\mathbf{r}$  and  $\mathbf{p}_T$ . Then the model is extended to get the survival probability  $S$  as a function of centrality of the collision. Also we obtained the  $R_{AA}$  and the double ratio by applying the feed-down corrections. We compared our model calculations with the bottomonia yields measured with CMS in PbPb collisions at  $\sqrt{s_{NN}} = 2.76$  TeV. The model calculations explain the data very well [146]. Similarly, using the same model, we calculate the  $S$ ,  $R_{AA}$  and the double ratio for Charmonium states.

## REFERENCES

- [1] E. V Shuryak, Phys. Rept. **61**, 71-158 (1980).
- [2] F. Karsch, Nucl. Phys. A **698**, 199 (2002).
- [3] T. Matsui and H. Satz, Phys. Lett. B **178**, 416 (1986).
- [4] B. Muller *et al.*, CERN-OPEN-2012-005, arXiv:1202.3233.
- [5] A. Mocsy and P. Petreczky, Phys. Rev. Lett. **99**, 211602 (2007).
- [6] M. Wilde for the ALICE collaboration, arXiv:1210.5958.
- [7] H. Satz, Int. J. Mod. Phys. E **21**, 1230006 (2012).
- [8] A. Mocsy, P. Petreczky and M. Strickland, Int. J. Mod. Phys. A **28**, 1340012 (2013).
- [9] R. Vogt, Phys. Rev. C **81**, 044903 (2010), arXiv:1003.3497.
- [10] X. Zhao and R. Rapp, Nucl. Phys. A **859**, 114 (2011), arXiv:1102.2194.
- [11] S. Chatrchyan *et al.* [CMS Collaboration], J. High Energy Phys. **1205**, 63 (2012).
- [12] A. Andronic, P. Braun-Munzinger, K. Redlich and J. Stachel, Nucl. Phys. A **789**, 334 (2007).
- [13] M. C. Chu and T. Matsui, Phys. Rev. D **37**, 1851 (1988).
- [14] J. D. Bjorken, Phys. Rev. D **27**, 140 (1983).
- [15] Abdulla Abdulsalam and Prashant Shukla, Int. J. Mod. Phys. A **28**, 1350105 (2013), arXiv:1210.7584v2.

## LIST OF FIGURES

FIGURE	Page
1	Elementary particles in the standard model. . . . . 3
2	Feynman diagrams for the vertices of QED and QCD. . . . . 5
3	The strong coupling $\alpha_s(Q)$ (full line) and its total uncertainty (band) determined using a two-loop solution to the RGE as a function of the momentum transfer $Q = p_T$ [4]. The values of $\alpha_s$ at lower scales determined by the H1, ZEUS, and D0 collaborations are shown for comparison. Recent CMS measurements, which are in agreement with the $\alpha_s(M_Z)$ determination are displayed as well. The results on $\alpha_s$ reported here are consistent with the energy dependence predicted by the RGE. . . . . 6
4	Schematic view of QCD phase diagram in terms of the baryon chemical potential $\mu_B$ and temperature T [9]. . . . . 8
5	Lattice calculation of Energy density (Left) and Pressure (Right) as a function of temperature, Figures are taken from Ref. [14]. . . . . 10
6	The schematic space-time diagram of ultra-relativistic nuclear collisions [16]. . . . . 14
7	Schematic representation of a non-central heavy-ion collision, characterized by an almond-shaped initial overlap zone, and a subsequent pressure-driven build-up of elliptic flow. Picture taken from Ref. [17]. . . . . 15

8	(Left) $dN_{\text{ch}}/d\eta _{\eta=0}$ as a function of centrality class in 2.76 TeV PbPb collisions from CMS experiment (solid circles) [23] and from ALICE (open squares) [24]. The statistical uncertainties are negligible, while the systematic uncertainties are shown as two bands. Systematic uncertainties affecting the scale of the measurements from the analysis [23] are shown as inner green error bands and the total systematic uncertainties as an outer grey band, while the error bars indicate statistical uncertainties. The black stars are shifted slightly to the right for better visibility. (Right) Charged-particle multiplicity normalized to $N_{\text{part}}/2$ in pp and central A+A (Au+Au and Pb+Pb) collisions as a function of $\sqrt{s_{\text{NN}}}$ [25]. . . . .	17
9	Direct-photon yield in PbPb collisions at $\sqrt{s_{\text{NN}}} = 2.76$ TeV for 0-40% centrality with NLO pQCD predictions. . . . .	19
10	(a) Elliptic flow $v_2$ measured by LHC as a function of $p_T$ for different particle species grouped by centrality class 10-20% of PbPb collisions at $\sqrt{s_{\text{NN}}} = 2.76$ TeV. (b) The $p_T$ -differential $v_2$ of pions for different centralities of Pb-Pb collisions at $\sqrt{s_{\text{NN}}} = 2.76$ TeV grouped by particle species [28]. . . . .	21
11	(Left) Measurements of the nuclear modification factor $R_{\text{AA}}(p_T)$ in central heavy-ion collisions at three different center-of-mass energies, as a function of $p_T$ , for neutral pions and charged particles [34, 18], compared to several theoretical predictions [33]. (Right) $R_{\text{AA}}$ measurements for photon, $Z$ , $W$ and non-prompt $J/\psi$ measurements. For the $Z$ and $W$ results, the data point is plotted at the rest mass of the particle, while for photons, the data points are plotted at their $m_T = p_T$ (transverse mass, or transverse momentum) value [32]. . . . .	24
12	Charged hadron $R_{\text{AA}}$ in $\sqrt{s_{\text{NN}}} = 2.76$ TeV central (0-5%) Pb+Pb collisions at LHC [34] compared to $R_{\text{AA}}$ of $\pi^0$ in $\sqrt{s_{\text{NN}}} = 200$ GeV central (0-5%) Au+Au collisions [36] at RHIC. . . . .	26

13	Subleading jet transverse momentum fraction ( $p_{T2}/p_{T1}$ ), in bins of leading jet transverse momentum from $120 < p_{T1} < 150$ GeV/ $c$ to $p_{T1} > 300$ GeV/ $c$ for subleading jets of $p_{T2} > 30$ GeV/ $c$ and $\Delta\phi_{1,2} > 2\pi/3$ between leading and subleading jets. Results for 0-20% central PbPb events are shown as points, while the histogram shows the results for pythia dijets embedded into hydjet PbPb simulated events. The arrows show the mean values of the distributions and the error bars represent the statistical uncertainties [41]. . . . .	27
14	(a) Average $R_{AA}$ of D mesons in the 0-20% centrality class [43], compared to that of charged particles [46], $\pi^\pm$ [42] and non-prompt $J/\psi$ from B decays [45]. (b) Nuclear modification factor ( $R_{AA}$ ) of electrons (circles and stars, depending on the pp reference) and muons (triangles) [48, 49] from heavy-flavour hadron decays in PbPb collisions at $\sqrt{s} = 2.76$ TeV for the centrality class 0-10%. (c) Average $R_{AA}$ of D mesons as a function of centrality [43] compared to that of non-prompt $J/\psi$ from B decays [45]. . . . .	28
15	Charmonium spectrum . . . . .	34
16	Schematic representation of color-Debye screening in a deconfined medium. . . . .	35
17	Charmonium binding energies as a function of Debye mass . . . . .	36
18	Generic Feynman diagrams for $J/\psi$ production in hadron collisions via color-singlet and color-octet model. . . . .	41
19	Prompt $J/\psi$ production cross-section from ATLAS experiment [73] are compared to the predictions of the CEM for prompt $J/\psi$ production and a calculation of the direct $J/\psi$ production cross-section in the CSM at next-to-leading order (NLO) and a partial next-to-next-leading order calculation (NNLO). . . . .	42

20	Measured differential cross section for prompt $J/\psi$ and $\psi(2S)$ production (left and right, respectively) as a function of $p_T$ for different rapidity bins. The error bars on the data points include all the statistical and systematic contributions except luminosity and polarization. The coloured (dark) bands indicate the theoretical predictions from NRQCD calculations. The lines are added only for illustrative purposes [75]. . . . .	43
21	Comparison of the differential cross-section for the production of prompt $J/\psi$ meson (under the assumption of zero polarisation) as a function of $p_T$ with direct production in an NLO NRQCDM (orange diagonal shading), an NNLO* CSM (solid yellow) and an NLO CSM (blue vertical shading). The points show the measurements reported in the analysis [76]. . . . .	44
22	Modification of gluon distribution function at $Q^2 = 1.69 \text{ GeV}/c^2$ for Pb nucleus ( $R_G^{Pb}$ ). Figure is taken from Ref. [77]. . . . .	45
23	$J/\psi$ $R_{AA}$ (normalized to Drell-Yan pairs) vs. $L$ for various p+p, p+A and S+U (Sulphur + Uranium) systems. “ $L$ ” is the effective average length travelled by (pre-) charmonium states. The figure is taken from Ref. [78]. . . . .	47
24	$J/\psi$ suppression by comover collisions (Left) and sequential $J/\psi$ suppression by color screening (Right) [78]. . . . .	49
25	$J/\psi$ enhancement by statistical regeneration [85]. . . . .	50
26	Compilation of results on the $J/\psi$ $R_{AA}$ from the SPS, RHIC and the LHC. . . . .	52
27	CERN accelerator complex . . . . .	56
28	LHC ring . . . . .	56
29	CMS Detector figure . . . . .	61
30	CMS Detector Slice figure . . . . .	61
31	CMS Magnet artistic view . . . . .	63

32	CMS Tracker 3D drawing . . . . .	64
33	CMS ECAL . . . . .	65
34	CMS HCAL . . . . .	66
35	CMS Muon system . . . . .	67
36	Distribution of the total transverse energy in the HF used to determine the centrality of the PbPb interactions. The centrality boundaries for each 5% centrality interval are shown by the dashed lines.	69
37	Correlation between the number of pixel hits and the total energy deposited by the HF. Good collisions have a tight correlation, while events firing the BSC halo bits and events which have PKAM features are off-diagonal. . . . .	78
38	The so called “monster” (or PKAM) cut. Events with large number of pixel hits (horizontal axis) but a small degree of compatibility between the vertex position and the cluster lengths (vertical axis) are eliminated from the analysis (i.e. those events that fall below the cut shown by the red line). The right panel is a zoomed version of the left panel. . . . .	79
39	Event centrality distribution of the minimum bias events is compared to events selected by the double-muon trigger. Only events selected by HLT_L1DoubleMuOpen with 2010 Run (Left) and by HLT_HIL1DoubleMu0_HighQ_v1 with 2011 Run (Right). . . . .	82
40	CMS Integrated Luminosity, PbPb 2010 and 2011 Run, $\sqrt{s_{NN}}=2.76$ TeV. . . . .	84
41	Illustration of the signal and the background side band fits to extract the number of signal and background in the cut study. These are the mass distributions with MC(left) and with real data(right). . . . .	87
42	Number of inner track valid cut study while applying all other cuts: left, significance on the data and right, efficiency and background rejection on MC. Final cut $>10$ . . . . .	90

43	Number of pixel layers reached by a single muon studied while applying all other cuts: left, significance on the data and right, efficiency and background rejection on MC. Final cut $>0$ . . . . .	91
44	Single muon inner track $\chi^2/ndf$ studied while applying all other cuts: left, significance on the data and right, efficiency and background rejection on MC. Final cut $<4$ . . . . .	92
45	Single muon global track $\chi^2/ndf$ studied while applying all other cuts: left, significance on the data and right, efficiency and background rejection on MC. Final cut $<20$ . . . . .	93
46	$D_{xy}$ study while applying all other cuts: left, significance on the data and right, efficiency and background rejection on MC. . . . .	94
47	$D_z$ study while applying all other cuts: left, significance on the data and right, efficiency and background rejection on MC. . . . .	95
48	Vertex probability cut studied while applying all other cuts: left, significance on the data and right, efficiency and background rejection on MC. . . . .	96
49	Number of muon inner track valid cut study (default: $> 10$ ). . . . .	102
50	Number of muon pixel layers cut study (default: $> 0$ ). . . . .	102
51	Number of muon inner track $\chi^2/ndf$ cut study (default: $< 4$ ). . . . .	102
52	Number of muon global track $\chi^2/ndf$ cut study (default: $< 20$ ). . . . .	103
53	Number of valid muon hits cut study (default: $\geq 0$ ). . . . .	103
54	$D_{xy}$ cut study (default: $< 3$ ). . . . .	103
55	$D_z$ cut study (default: $< 15$ ). . . . .	104
56	Dimuon vertex probability cut study (default: $> 5\%$ ). . . . .	104
57	Significance of $\Upsilon(1S)$ peak as a function of the single muon $p_T$ cut . . . . .	106
58	Kinematics and quality variables distributions for MC in red and data in green. . . . .	109

59	Kinematics and quality variables distributions for MC in red and data in green. . . . .	110
60	Kinematics and quality variables distributions for MC in red and data in green. . . . .	111
61	Reconstruction single muon efficiency illustrating the limits of what is considered a detectable single muon (Single muon acceptance).	117
62	Invariant mass spectrum of $\mu^+\mu^-$ -pairs (black circles) with $ y  < 2.4$ , $0 < p_T < 30$ GeV/ $c$ and 0-100% from events. . . . .	118
63	$\mu^+\mu^-$ -pairs raw counts versus $p_T$ , for $ y  < 2.4$ in 0-100% centrality bin. All pairs passed all analysis cuts, but there is no separation of the signal J/ $\psi$ dimuons from the background. . . . .	120
64	Invariant-mass spectra (left) and pseudo-proper decay length distribution (right) of $\mu^+\mu^-$ -pairs integrated over centrality (top) and 0–10% most central collisions (bottom). The spectra are integrated over the rapidity range $0 <  y  < 2.4$ and the $p_T$ range $6.5 < p_T < 30$ GeV/ $c$ . The projections of the two-dimensional fit onto the respective axes are overlaid as solid black lines. The dashed red lines show the fitted contribution of non-prompt J/ $\psi$ . The fitted background contributions are shown as dotted blue lines. . . . .	121
65	Single muons $\eta$ vs $\Phi$ distributions in MC (left) and data (right) illustrating the presence of dead tracker areas in both MC and data ( $\eta > 2$ and $\Phi \in [0, 1]$ , $\eta < -2$ and $\Phi \in [-3, -2]$ ). . . . .	123
66	Illustration of the reconstructed mass for the prompt J/ $\psi$ in a centrality-integrated bin used for the efficiency calculation with the peak counting method. . . . .	125
67	Efficiency corrections as a function of event centrality (left), $p_T$ (right) and rapidity (bottom) for prompt and non-prompt J/ $\psi$ . . . . .	126

68	The nuclear modification factor as function of centrality ( <i>left</i> ), $p_T$ ( <i>right</i> ) and rapidity ( <i>bottom</i> ) for the prompt $J/\psi$ . The gray boxes plotted at $R_{AA} = 1$ indicate the scale of the global uncertainties: (left) the uncertainty of 6% on the measured integrated luminosity of the pp data sample, together with the statistical and systematic uncertainty on the pp data set; (right and bottom) the pp luminosity and the $T_{AA}$ uncertainties. The bin boundaries are indicated by small horizontal lines where meaningful. . . . .	129
69	The nuclear modification factor as function of centrality ( <i>left</i> ), $p_T$ ( <i>right</i> ) and rapidity ( <i>bottom</i> ) for the non-prompt $J/\psi$ . The gray boxes plotted at $R_{AA}=1$ indicate the scale of the global uncertainties: (left) the uncertainty of 6% on the measured integrated luminosity of the pp data sample, together with the statistical and systematic uncertainty on the pp data set; (right and bottom) the pp luminosity and the $T_{AA}$ uncertainties. The bin boundaries are indicated by small horizontal lines where meaningful. . . . .	131
70	(Left) The nuclear modification factor ( $R_{AA}$ ) of $J/\psi$ in PbPb collisions at $\sqrt{s_{NN}} = 2.76$ TeV as a function of number of participants measured by CMS experiment [97, 107]. RHIC measurements are shown for comparison [108]. (Right) Nuclear modification factor ( $R_{AA}$ ) of $J/\psi$ as a function of $p_T$ measured by CMS [97, 107], ALICE [109] and PHENIX [86] experiments. . . . .	132
71	Pseudo-proper decay length distributions of prompt and non-prompt $J/\psi$ (left sub-panels) in pp MC simulations. The right sub-panels shows the prompt efficiencies and non-prompt rejection efficiencies as a function of $\ell_{J/\psi}$ . Each row is for different kinematic region, which is indicated in the figure. . . . .	138
72	Prompt and non-prompt pseudo-proper decay length distributions of $J/\psi$ (left sub-panels) in PbPb MC simulations. The right sub-panels show the prompt efficiency and non-prompt rejection efficiency as a function of $\ell_{J/\psi}$ . Each panel is for different kinematic region, which is indicated in the figure. . . . .	139

73	Invariant-mass spectrum of $\mu^+\mu^-$ pairs in pp and PbPb data (0-20%, 20-40% and 40-100%). The $p_T$ and rapidity bins are $6.5 < p_T < 30 \text{ GeV}/c$ and $ y  < 1.6$ . The fit to the data with the functions discussed in the text is shown as the black line. The black dashed line represents the background. The orange and green dashed lines are the CB and Gaussian contributions on top of the background, respectively. The shaded bands represent $\pm 1 \sigma$ uncertainty bands due to the statistical uncertainty of the data. The pp data are also overlaid with a shape (red dashed line), in which $R_\psi$ has been set to the value found in each centrality bin. The bottom sub-panels show the pull distributions between data and fit. The small inserts in the upper sub-panel show the pull projections. . . . .	144
74	Invariant-mass spectrum of $\mu^+\mu^-$ pairs in pp and PbPb data (0-20%, 20-40% and 40-100%). The $p_T$ and rapidity bins are $3 < p_T < 30 \text{ GeV}/c$ and $1.6 <  y  < 2.4$ . The fit to the data with the functions discussed in the text is shown as the black line. The black dashed line represents the background. The orange and green dashed lines are the CB and Gaussian contributions on top of the background, respectively. The shaded bands represent $\pm 1 \sigma$ uncertainty bands due to the statistical uncertainty of the data. The pp data are also overlaid with a shape (red dashed line), in which $R_\psi$ has been set to the value found in each centrality bin. The bottom sub-panels show the pull distributions between data and fit. The small inserts in the upper sub-panel show the pull projections. . . . .	145
75	Reconstruction efficiency as a function of centrality for simulated $J/\psi$ and $\psi(2S)$ from RegIt PbPb and pp. The blue square denotes the efficiency of $\psi(2S)$ and the magenta circle that of $J/\psi$ . . . . .	149
76	Scan with Feldman-Cousins method for 95% confidence intervals using 100 Toy MC experiments at each scanned point for centrality bin 40–100% at $ y  < 1.6$ and $6.5 < p_T < 30 \text{ GeV}/c$ . The left column shows the result of the FC scan: the red and dashed blue line indicate confidence levels of 95% and 68% ( $1\sigma$ ). The right panel displays the Toy MC distributions for the signal+background and background only hypothesis. . . . .	155

- 77 Measured yield double ratio  $(N_{\psi(2S)}/N_{J/\psi})_{PbPb}/(N_{\psi(2S)}/N_{J/\psi})_{pp}$  as a function of centrality with PbPb data ( $150 \mu\text{b}^{-1}$ ) and pp data ( $231 \text{nb}^{-1}$ ). The  $p_T$  and rapidity bins are  $6.5 < p_T < 30 \text{GeV}/c$  and  $|y| < 1.6$  (left), and  $3.0 < p_T < 30 \text{GeV}/c$  and  $1.6 < |y| < 2.4$  (right). The error bars and boxes stand for the PbPb statistical and systematic uncertainties, respectively. The shaded band is the uncertainty on the pp measurement, common to all double-ratio points. 157
- 78 Double ratio as a function of centrality (left panel): Blue squares show the result integrated over the range  $6.5 < p_T < 30 \text{GeV}/c$  and  $|y| < 1.6$ . This is compared to the result in  $3 < p_T < 30 \text{GeV}/c$  and  $1.6 < |y| < 2.4$  (red circles). The latter points are shifted by  $\Delta N_{\text{part}} = 2$  for better visibility. The right panel displays the centrality integrated results. Statistical (systematic) uncertainties are shown as bars (boxes). In the left panel, boxes at one indicate the global uncertainties from the pp data. . . . . 158
- 79 a) Measured  $(dN/d\eta)/(N_{\text{part}}/2)$  [140] as a function of  $N_{\text{part}}$  along with the function  $(dN/d\eta)/(\pi R^2)$ . (b) The initial temperature obtained from measured multiplicity using Eq. (7.11) . . . . . 170
- 80 The screening radius  $r_D$  (in fm) as a function of  $p_T$  for  $R = 6.8$  fm (corresponding to head-on collisions) and  $R = 3.7$  fm (corresponding to minimum bias collisions) for (a)  $\Upsilon(1S)$  and (b)  $\Upsilon(2S)$ . The straight lines  $|\mathbf{r} + \frac{\tau_F \mathbf{p}_T}{M}|$  mark the distance a bottom quark pair (created at  $r = 0$ ) will travel before forming a bound state. The mesh region in both the figures marks the escape region for bottom quark pair in case of head-on collisions and total shaded (mesh+lines) region marks the escape region in case of minimum bias collisions. . . . . 171
- 81 (a) The survival probability as a function of  $p_T$  for  $\Upsilon(1S)$ ,  $\Upsilon(2S)$ ,  $\Upsilon(3S)$  and  $\chi_b(1P)$  for  $R = 3.7$  fm (corresponding to average  $N_{\text{part}} = 114$  for minimum bias collisions). (b) The nuclear modification factor for  $\Upsilon(1S)$ ,  $\Upsilon(2S)$  and  $\Upsilon(3S)$  which is obtained from survival probabilities including feed down corrections. The solid squares are  $\Upsilon(1S)$   $R_{AA}$  measured in the minimum bias PbPb collisions at  $\sqrt{s_{NN}} = 2.76$  TeV by CMS experiment [97]. . . . . 172

82	The nuclear modification factor, $R_{AA}$ as a function of $N_{\text{part}}$ for $\Upsilon(1S)$ , $\Upsilon(2S)$ and $\Upsilon(3S)$ . The solid squares and circles are measured $R_{AA}$ by CMS experiment in PbPb collisions at $\sqrt{s_{NN}} = 2.76$ TeV [99] for $\Upsilon(1S)$ and $\Upsilon(2S)$ respectively and solid triangles are the minimum bias data points. The boxes at unity are the common systematic uncertainties in pp luminosity measurement and the pp yield. The lines(solid for $\Upsilon(1S)$ , dashed for $\Upsilon(2S)$ and dotted for $\Upsilon(3S)$ ) represent the present model calculations. . . . .	173
83	Double ratio, $[\Upsilon(2S)/\Upsilon(1S)]_{PbPb}/[\Upsilon(2S)/\Upsilon(1S)]_{pp}$ as a function of $N_{\text{part}}$ measured by CMS experiment [99] along with the present calculation (solid line). The box at unity is the common systematic uncertainty in the pp yield. . . . .	174
84	The survival probability as a function of $p_T$ for $J/\psi$ , $\psi(2S)$ , and $\chi_c(1P)$ for $R = 3.7$ fm (corresponding to average $N_{\text{part}} = 114$ for minimum bias collisions). . . . .	176
85	(Left) The nuclear modification factor, $R_{AA}$ as a function of $N_{\text{part}}$ for $J/\psi$ . The solid circles are measured $R_{AA}$ by CMS experiment in PbPb collisions at $\sqrt{s_{NN}} = 2.76$ TeV with $p_T > 6.5$ and $ y  < 2.4$ [45] for $J/\psi$ . (b) $R_{AA}$ measured by ALICE with $p_T > 0$ and $2.5 <  y  < 4.0$ [109]. . . . .	177
86	Double ratio, $(\psi(2S)/J/\psi)_{PbPb}/(\psi(2S)/J/\psi)_{pp}$ as a function of $N_{\text{part}}$ measured by CMS experiment along with the present calculations for double ratio, $J/\psi$ $R_{AA}$ and $\psi(2S)$ $R_{AA}$ (solid line, dashed line and dotted line respectively). The $p_T$ and rapidity bins are (Left) $3 < p_T < 30$ , $1.6 <  y  < 2.4$ and (Right) $6.5 < p_T < 30$ , $ y  < 1.6$ . Also the double ratio measured with ALICE is given for comparison [127]. . . . .	178
87	Nuclear modification factor ( $R_{AA}$ ) of $J/\psi$ as a function of $p_T$ measured by CMS [97, 107], ALICE [109] and PHENIX [86] experiments.	182

- 88 Double ratio as a function of centrality (left panel): Blue squares show the result integrated over the range  $6.5 < p_T < 30 \text{ GeV}/c$  and  $|y| < 1.6$ . This is compared to the result in  $3 < p_T < 30 \text{ GeV}/c$  and  $1.6 < |y| < 2.4$  (red circles). The right panel displays the centrality integrated results. Statistical (systematic) uncertainties are shown as bars (boxes). In the left panel, boxes at one are the global uncertainties from the pp data. . . . . 184
- 89 The nuclear modification factor,  $R_{AA}$  as a function of  $N_{\text{part}}$  for  $\Upsilon(1S)$ ,  $\Upsilon(2S)$  and  $\Upsilon(3S)$ . The solid squares and circles are measured  $R_{AA}$  by CMS experiment in PbPb collisions at  $\sqrt{s_{NN}} = 2.76 \text{ TeV}$  [99] for  $\Upsilon(1S)$  and  $\Upsilon(2S)$  respectively and solid triangles are the minimum bias data points. The lines (solid for  $\Upsilon(1S)$ , dashed for  $\Upsilon(2S)$  and dotted for  $\Upsilon(3S)$ ) represent the present model calculations. . . . . 185
- 90 Schematic representation of the geometry of Glauber model. Left panel: transverse view. Right panel: longitudinal view. . . . . 198

## LIST OF TABLES

TABLE	Page
I	Past, present and future accelerator experiments for heavy-ion collisions. 12
II	Charmonium states and their properties. . . . . 33
III	LHC beam parameters. . . . . 58
IV	Average $N_{\text{part}}$ values and their uncertainties for each PbPb centrality range defined in 5 percentile segments of the total inelastic cross section. The values were obtained using a Glauber MC simulation with the same parameters as in Ref. [40]. . . . . 71
V	Minimum bias event counts, and reduction due to various good event quality cuts. % values are always with respect to the first line (the cuts are applied in sequence). . . . . 80
VI	Signal efficiency and background rejection efficiency in % on MC when applying each cut, in 3 rapidity bins. . . . . 97
VII	Signal efficiency and background rejection efficiency in % on MC after applying all other cuts but the one listed, in 3 rapidity bins. . . 98
VIII	Signal efficiency and background rejection efficiency in % on real data after applying all other cuts but the one listed, in 3 rapidity bins. 99
IX	Estimated $\Upsilon(1S)$ yield significance, signal efficiency (MC) and background rejection in % after applying all other cuts but the one listed. . . . . 107
X	Systematic uncertainties on the prompt and non-prompt $J/\psi$ $R_{AA}$ measured in PbPb collisions. . . . . 127
XI	Cuts on the pseudo-proper decay length $\ell_{J/\psi}$ to reject non-prompt $J/\psi$ and $\psi(2S)$ . . . . . 137
XII	Order of Chebychev polynomials used as background shapes in the fitting of pp and PbPb data as determined by a LLR test. . . . 141

XIII	Negative loglikelihoods for fits with Chebychev polynomials of orders 0–5 of pp and PbPb data (0-100%) in $ y  < 1.6$ and $6.5 < p_T < 30\text{GeV}/c$ . In addition the p-values of the LLR-test for the null-hypothesis are listed. If the p-value is less than 5%, the null-hypothesis is rejected and the higher order polynomial is preferred. Tests of which the null-hypothesis cannot be rejected for two consecutive orders are highlighted in bold, together with the corresponding order. . . . .	142
XIV	Exponential background shapes used as alternatives in the fitting of pp and PbPb data as determined by a LLR test. . . . .	147
XV	Absolute and relative systematic uncertainty on the data fits. Absolute uncertainties are multiplied by $10^{-3}$ . The pp column is only to illustrate the size of the variations on $R_\psi(\text{pp})$ . These variations are already included in the variations of the double ratios shown in the other columns and do not enter as additional term in the systematic uncertainties. . . . .	148
XVI	Reconstruction efficiency for $J/\psi$ and $\psi(2S)$ using bin counting method with RegIt PbPb and pp MC. . . . .	150
XVII	Acceptance of $\psi(2S)$ and $J/\psi$ . . . . .	152
XVIII	Summary of relative systematic uncertainties. For comparison, the statistical uncertainty on the double ratio is shown as well. . . . .	154
XIX	95% confidence intervals using the Feldman-Cousins method . . . . .	156
XX	Raw ratios of $\psi(2S)$ over $J/\psi$ yields ( $R_\psi$ ) for pp and PbPb collisions and their double ratio ( $R_\psi(\text{PbPb})/R_\psi(\text{pp})$ ). Listed uncertainties are statistical first, systematic second, and global scale third. . . . .	159
XXI	Quarkonia properties from non-relativistic potential theory [62, 139].	166
XXII	$N_{\text{coll}}$ , $N_{\text{part}}$ , impact parameter $b$ , and $T_{\text{AA}}$ values in bins of centrality.	201
XXIII	Active L1 Trigger Summary . . . . .	204
XXIV	HLT path names with their accepted fraction and rate at 200 Hz . . . . .	205

# CHAPTER 1

## Introduction

### 1.1. Particle physics: past to present

The modern era of particle physics begins with Eightfold model introduced by Murray Gell-Mann in 1961. The model which consists of an abstract ordering of particles onto geometric shapes introduced a way to theoretically predict the existence of new particles. After the very success of this model, Gell-Mann and Zweig independently proposed quark model in 1964 which states that all the hadrons are composed of more elementary constituents called quarks by Gell-Mann and partons by Feynman [1]. This quark model postulated that baryons carried three quarks while mesons carried a quark and an anti-quark. For every quark flavor, there is a corresponding type of antiparticle known as anti-quark, with properties of equal magnitude but opposite sign. Studies of deep-inelastic scattering of electrons on hadrons showed that the virtual photon emitted by an electron suddenly seemed to be hitting a point particle with no structure rather than a finite size of hadron.

In the view of modern Standard Model the matter of the universe is made up of three kinds of elementary particles: leptons, quarks and mediators of interaction. These are six flavors of quarks: up ( $u$ ), down ( $d$ ); charm ( $c$ ), strange ( $s$ ); top ( $t$ ), bottom ( $b$ ) and six types of leptons: electron ( $e$ ), electron neutrino ( $\nu_e$ ); muon ( $\mu$ ), muon neutrino ( $\nu_\mu$ ); tau ( $\tau$ ), tau neutrino ( $\nu_\tau$ ) along with antiparticles for each of these states. They fall into three generations which are summarized in Fig. 1.

These fundamental particles interact via four forces: gravitational, electromagnetic, weak and strong nuclear interactions. The latter three are known to be mediated by photons,  $W^\pm$  and  $Z^0$  bosons, and gluons respectively. The Standard Model (SM) of particle physics has been tested by many experiments over the last four decades and has been shown to successfully describe high energy particle interactions. However, the mechanism that breaks electroweak symmetry in the SM has not

	mass → charge → spin →	$\approx 2.3 \text{ MeV}/c^2$ 2/3 1/2 <b>u</b> up	$\approx 1.275 \text{ GeV}/c^2$ 2/3 1/2 <b>c</b> charm	$\approx 173.07 \text{ GeV}/c^2$ 2/3 1/2 <b>t</b> top	0 0 1 <b>g</b> gluon	$\approx 126 \text{ GeV}/c^2$ 0 0 <b>H</b> Higgs boson
<b>QUARKS</b>		$\approx 4.8 \text{ MeV}/c^2$ -1/3 1/2 <b>d</b> down	$\approx 95 \text{ MeV}/c^2$ -1/3 1/2 <b>s</b> strange	$\approx 4.18 \text{ GeV}/c^2$ -1/3 1/2 <b>b</b> bottom	0 0 1 <b><math>\gamma</math></b> photon	
		$0.511 \text{ MeV}/c^2$ -1 1/2 <b>e</b> electron	$105.7 \text{ MeV}/c^2$ -1 1/2 <b><math>\mu</math></b> muon	$1.777 \text{ GeV}/c^2$ -1 1/2 <b><math>\tau</math></b> tau	0 0 1 <b>Z</b> Z boson	<b>GAUGE BOSONS</b>
<b>LEPTONS</b>		$< 2.2 \text{ eV}/c^2$ 0 1/2 <b><math>\nu_e</math></b> electron neutrino	$< 0.17 \text{ MeV}/c^2$ 0 1/2 <b><math>\nu_\mu</math></b> muon neutrino	$< 15.5 \text{ MeV}/c^2$ 0 1/2 <b><math>\nu_\tau</math></b> tau neutrino	$\approx 80.4 \text{ GeV}/c^2$ $\pm 1$ 1 <b>W</b> W boson	

Fig. 1. Elementary particles in the standard model.

been verified experimentally. This mechanism which gives mass to massive elementary particles through the Yukawa interaction, implies the existence of a scalar field, the Higgs boson. The mass  $m_H$  of the SM Higgs boson is not predicted by theory. However, general considerations suggest that  $m_H$  should be smaller than 1 TeV. The discovery or exclusion of the SM Higgs boson has been one of the primary scientific goals of the Large Hadron Collider (LHC). On 4-July-2012 both the ATLAS and CMS Collaborations at the LHC jointly announced the observation of a new boson which later confirmed that the boson behave, interact and decay in many of the ways like the SM Higgs boson and also confirmed the boson is a CP-even, spin-0 particle [2, 3].

Quantum field theory calculations using the Standard Model have been astoundingly accurate in describing electromagnetic (EM) and weak interactions, typically with perturbative calculations that expand in powers of  $\alpha_{EM} = 1/137$  and can be graphically described by Feynman diagrams. To describe the strong interaction, we turn to Quantum Chromodynamics (QCD).

## 1.2. Quantum Chromodynamics

The strong interaction between quarks and gluons is explained by the QCD theory. It was so named because quarks have an additional quantum number that can take three values, analogous to red-green-blue light in optics. Therefore, this quantum number is known as color charge, and the theory was given the name Chromodynamics. The quarks can be red, green or blue, while the gluons have eight color states known as the color octet. The color-neutral singlet state is not allowed for gluons. The fundamental degrees of freedom in QCD are quarks and gluons. Their interaction is described by the following Lagrangian,

$$\mathcal{L}_{QCD} = \sum_f^{N_f} \bar{\psi}_f (i\gamma^\mu D_\mu - m_f) \psi_f - \frac{1}{4} F_a^{\mu\nu} F_{\mu\nu}^a . \quad (1.1)$$

Here the gluon field strength tensor  $F_{\mu\nu}^a$  reads

$$F_{\mu\nu}^a = \partial_\mu A_\nu^a - \partial_\nu A_\mu^a + ig f_{abc} A_\mu^b A_\nu^c , \quad (1.2)$$

in terms of the gluon gauge fields  $A_a^\mu$  ( $a=1\cdots 8$ ). The colored quark fields  $\psi_f$  ( $f = u, d, s, c, b, t$ ) are coupled to the gluons through the gauge co-variant derivative

$$D_\mu = \partial_\mu - ig \frac{\lambda_a}{2} A_\mu^a , \quad (1.3)$$

where  $\lambda_a$  are the Gell-Mann matrices, which are generators of the  $SU(3)_c$  group satisfying

$$[\lambda_a, \lambda_b] = f_{abc} \lambda_c , \quad (1.4)$$

$f_{abc}$  being the structure constants of  $SU(3)_c$ .

The important properties of QCD include **asymptotic freedom** and **confinement**. The quark-quark and quark-anti-quark interactions induce a color charge-screening effect analogous to that found between electromagnetic charges. In the EM

case, at large distance vacuum polarization effects screen the electric charge, and at large enough distances the effective charge is the typical value  $e$ . However, as the distance scale of the interaction goes to zero, the effects of vacuum polarization diminish and the bare charge is seen by the interaction. However, in the QCD case,

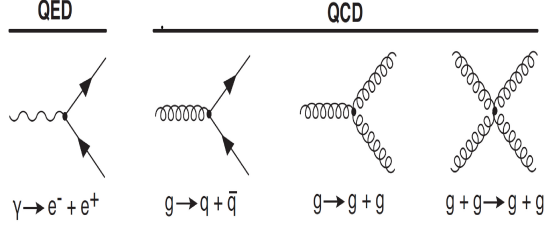


Fig. 2. Feynman diagrams for the vertices of QED and QCD.

gluons are allowed to interact with other gluons, as shown in the basic Feynman diagram vertices of Fig. 2. This feature adds an additional term to the QCD field tensor  $F_{\mu\nu}$  in Eq. 1.2 compared to the EM field tensor, which leads to important physical consequences. Contrary to the EM case described above, the introduction of gluon-gluon interactions creates an overall anti-screening effect for color charges in QCD interactions, whereby the interaction becomes stronger at larger distance scales. As the distance between a pair of quarks grows and the potential energy increases, it eventually becomes energetically favorable for a new quark-antiquark pair to tunnel out of the vacuum, and the original pair splits into new pairs. This is known as **confinement**, and this is the reason that free quarks are not observed in nature. The coupling constant  $\alpha_s$  varies depending on the  $Q$  (momentum-transfer between particles) and distance of the interaction.

$$\alpha_s(Q^2) = \frac{g^2(Q^2)}{4\pi} = \frac{4\pi N_c}{(11N_c - 2N_f) \ln(Q^2/\Lambda_{QCD}^2)}, \quad (1.5)$$

where  $\Lambda_{QCD} \simeq 200$  MeV is introduced as a “non-perturbative” scale at which  $\alpha_s(Q)$

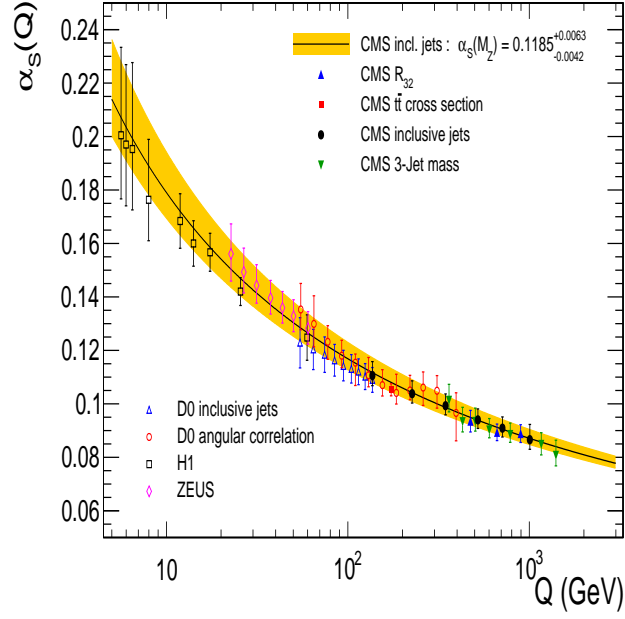


Fig. 3. The strong coupling  $\alpha_s(Q)$  (full line) and its total uncertainty (band) determined using a two-loop solution to the RGE as a function of the momentum transfer  $Q = p_T$  [4]. The values of  $\alpha_s$  at lower scales determined by the H1, ZEUS, and D0 collaborations are shown for comparison. Recent CMS measurements, which are in agreement with the  $\alpha_s(M_Z)$  determination are displayed as well. The results on  $\alpha_s$  reported here are consistent with the energy dependence predicted by the RGE.

formally diverges. Measurement of this running of  $\alpha_s(Q)$  are shown in Fig. 3. The strong coupling constant determined with CMS at the Z boson mass  $M_Z$  is  $\alpha_s(M_Z) = 0.1185 \pm 0.0019$  (exp), which is in agreement with the world average  $\alpha_s(M_Z)$  value of  $0.1184 \pm 0.0007$  [4]. The observed scale dependence of the strong coupling constant is in good agreement with the D0, ZEUS and H1  $\alpha_s$  values. The recent results from ATLAS are consistent with the RGE predictions up to an energy scale of 800 GeV [5]. The logarithmic behavior in Eq. (1.5) is based on perturbative

calculations, which break down at momentum transfer well above  $\Lambda_{QCD}$ . As a result, expansions in terms of  $1/\alpha_s$  may not converge quickly or at all for interactions at low energies. At short distance scales or large  $Q^2$ , however, the effective coupling constant becomes small enough that partons are essentially moving freely and their interactions may be calculated with perturbation theory [6, 7]. This effect is known as **asymptotic freedom**. Asymptotic freedom was discovered and described in 1973 by Frank Wilczek, David Gross, and independently by David Politzer the same year. All three shared the Nobel Prize in physics in 2004.

Another remarkable features of the QCD theory are (a) chiral symmetry breaking which expresses the fact that quarks confined in hadrons do not appear as nearly massless constituents but are endowed with a dynamically generated mass of several hundred MeV, and (b) at low energies, the QCD vacuum is characterized by non-vanishing expectation values of certain operators, called vacuum condensates which characterize the nonperturbative physical properties of the QCD vacuum. The quark condensate describes the density of quark-antiquark pairs found in the QCD vacuum and is the expression of chiral symmetry breaking. The gluon condensate measures the density of gluon pairs in the QCD vacuum.

### 1.2.1. QCD phase transition

It has been established, since Hubble's first discovery in the 1920's, that the universe has been expanding for about  $\sim 13.8$  billion years [8]. The universe began as a "big bang" where it was much smaller and hotter, and then evolved by expansion and cooling. The present understanding of the laws of physics allows to discuss the earliest moment the so-called Planck time  $t_P \sim 10^{-43}$  when the temperature of the

universe is at the Planck scale  $T \sim M_{pl}$ .

$$M_{pl} = \left( \sqrt{\frac{\hbar c}{G_N}} \right) = 1.22 \times 10^{19} \text{GeV} \quad (1.6)$$

where  $G_N$  is Newtons gravitational constant. When the temperature drops below the electroweak scale ( $T < 100 \text{ GeV}$ ) the early universe would be a hot gas of the standard model particles: quarks, leptons, gluons and photons and the system would be dominated by the strongly interacting degrees of freedom, quarks and gluons. Study of matter at this extreme conditions of temperature and/or density provides interesting possibilities for insight into the fundamental properties of QCD.

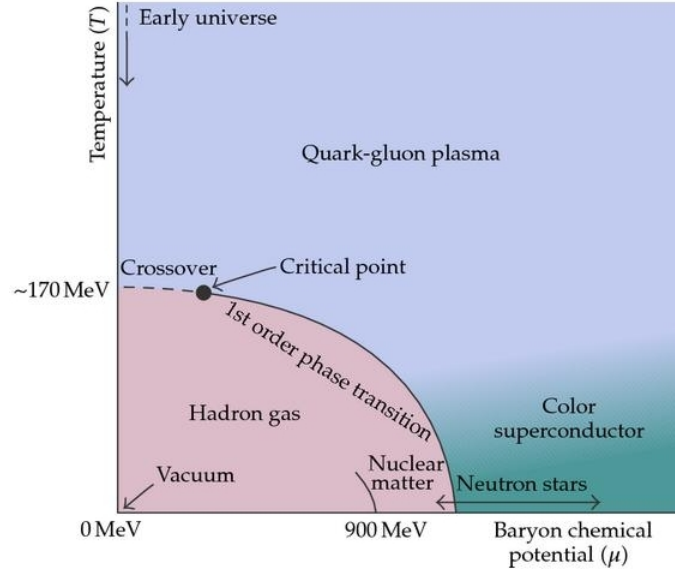


Fig. 4. Schematic view of QCD phase diagram in terms of the baryon chemical potential  $\mu_B$  and temperature  $T$  [9].

It is an important aspect to figure out the symmetries of a physical system to understand the observed pattern; especially the phase structure of QCD is dictated by its symmetries. It is not uncommon in nature that spontaneously broken symmetries are restored at high temperature through phase transitions, e.g ferromagnetism and superconductivity. As the temperature increases in QCD, the interactions among

quanta occur at ever shorter distances as shown in Fig 3. As a consequence, nuclear matter at very high temperature exhibits neither confinement nor chiral symmetry breaking. This new phase of QCD is called the quark-gluon plasma (QGP). Following the definition proposed by the STAR collaboration at RHIC: Quark-Gluon Plasma is defined as a (locally) thermally equilibrated state of matter in which quarks and gluons are deconfined from hadrons, so that they propagate over nuclear, rather than merely nucleonic, volumes [10]. Two essential ingredients of this definition are (1) the constituents of the matter should be quarks and gluons, and (2) the matter should have attained (local) thermal equilibrium, i.e. unlike a system in global equilibrium, here temperature and chemical potential may depend on space-time coordinates. Any claim of discovery of QGP can follow only after these two requirements are shown to be fulfilled unambiguously [11].

Since there exist order parameters, such as the quark condensate, which vanish at high temperature, there is good chance that the transition between the low-temperature and high-temperature manifestations of QCD is not smooth but exhibits a discontinuity leading to a phase transition. A schematic representation of QCD phase diagram in terms of the baryon chemical potential  $\mu_B$  and temperature  $T$  is shown in Fig. 4 [9]. Lattice results indicate that the transition at vanishing  $\mu_B$  is a crossover; while a number of models [12, 13] indicate a first order phase transition as a function of temperature at finite  $\mu_B$ . From this, one can expect that as the chemical potential is decreased and the temperature is increased, the first order transition line ends at a critical point and turns into a crossover. But the existence of the critical point is not established experimentally [11]. In the regime with low temperature and high baryon density (characterized by large baryon chemical potential,  $\mu_B$ ), theoretical studies [12, 13] reveal the existence of another deconfined phase, see Fig. 4, where the high density quarks form Cooper pairs which condense ( $\langle qq \rangle \neq 0$ ) and result in

superconducting of color charge.

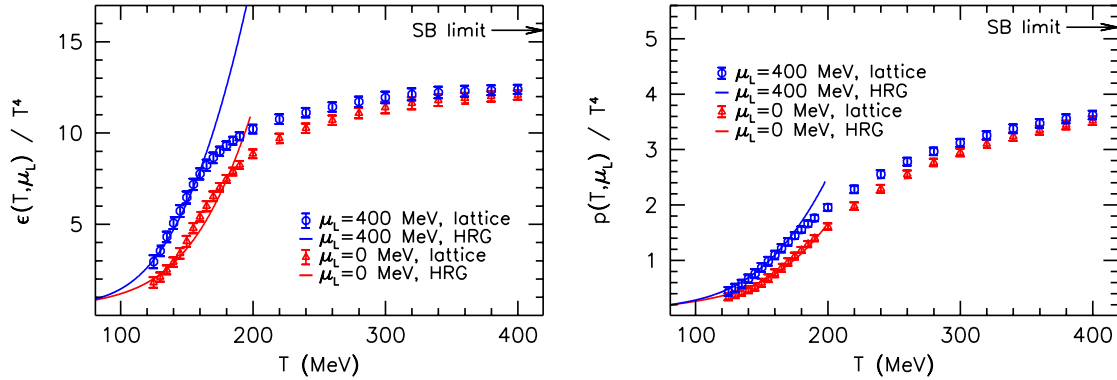


Fig. 5. Lattice calculation of Energy density (Left) and Pressure (Right) as a function of temperature, Figures are taken from Ref. [14].

The pQCD calculations work for very small distances between the quarks, but fail as the interaction strength grows at larger distances. For distance scales over 1 fm, lattice QCD (lQCD) calculations can provide quantitative results. The Figures 5 show the lattice results for the QCD equation of state (EoS) at vanishing chemical potential in the temperature range  $100 \text{ MeV} \leq T \leq 1000 \text{ MeV}$  for physical light and strange quark masses  $m_{u,d,s}$ . The energy density ( $\epsilon$ ) and pressure ( $P$ ) shows a rapid rise in the temperature region around 170-190 MeV, as shown in the figures which implies the relevant degrees of freedom have indeed transitioned into quarks and gluons, forming QGP. Note also that in the limit of high  $T$  the EoS approaches the form  $\epsilon = 3P$  expected of massless particles. However,  $\epsilon$  is significantly less than  $\epsilon_{SB}$  (Stefan-Boltzmann limit) showing that the system is far from being in an ideal gaseous state.

### 1.3. Heavy ion collisions

Relativistic heavy-ion collisions make it possible to study the properties of strongly interacting matter at energy density far above those of nuclear matter. In collider experiment two beams of nuclei (Pb ion at LHC) are accelerated to ultra-relativistic velocity ( $0.999c$ ) and directed to collide with each other. In the collisions, a large amount of energy is deposited into a small spatial region and converted to thermal energy resulting in extremely high temperature. The currently running experimental facilities include Relativistic Heavy-Ion Collider (RHIC) at BNL and Large Hadron Collider (LHC) at CERN. The new Facility for Anti-proton and Ion Research (FAIR) at GSI (Germany) will be completed within a few years. The RHIC and LHC fall into category of collider experiment where the advantage is that higher collision energy can be reached and the FAIR is a fixed target experiment (only one beam of ions is accelerated). The latter category have higher luminosity (leading to a larger number of collision events per unit time) so that more rare reactions can be studied, but a large amount of the energy of the projectile is wasted on the kinetic energy of colliding nuclei. The Table I is the summary of different experiments, species used and their colliding energy. In this work we mainly focus on charmonium production in Pb+Pb collisions at  $\sqrt{s_{NN}} = 2.76$  TeV with CMS experiment at LHC.

#### 1.3.1. Stages of a heavy ion collision

The time evolution of a typical heavy-ion collision is sketched in Fig. 6. Two Lorentz-contracted nuclei approach each other at close to the speed of light until primordial nucleon-nucleon collisions occur. Prior to the collision, these lorentz-contracted nuclei with lorentz boost factor  $\gamma \sim 100$  are mostly composed with gluons. The lorentz factor

Accelerator	Collision energy, $\sqrt{s_{NN}}$ (GeV)	Colliding Nuclei	Starting Year
AGS (BNL)	5	p+A, O+A, Si+A, Au+Au	1986
SPS (CERN)	17.3 19.4	Pb+Pb p+A, S+U	1986
RHIC (BNL)	510, 500, 200, 62.4 200 200, 62.4, 22.4 7.7, 9.2, 15, 19, 19.6, 27 39, 62.4, 130, 200	p+p d+Au Cu+Cu Au+Au	2001-13 2002/2008 2005 2000-14
CBM (GSI)	2-29 2-11	p+p Au+Au	2018 2018
LHC (CERN)	900, 2.76, 7, 8, 13, 14 TeV 5.02 TeV 2.76, 5.5 TeV	p+p, p+Pb Pb+Pb	2009-2013 2013 2010/2015

Table I. Past, present and future accelerator experiments for heavy-ion collisions.

is defined as

$$\gamma = \left( \frac{1}{\sqrt{1 - \beta^2}} \right) \quad \text{where} \quad \beta = \frac{\mathbf{P}}{\mathbf{E}}, \quad E^2 = p^2 + m^2$$

$$\gamma = \frac{E}{m}$$

For RHIC at  $\sqrt{s} = 100 A$  GeV and  $m = A$  GeV ( $A$  is mass number = 196 for Au ion)

$$\gamma = \frac{100 \times 196}{196} \sim 100$$

for LHC at  $\sqrt{s} = 1.38 A$  TeV and  $A = 208$  for Pb ion,

$$\gamma = \frac{1380 \times 208}{208} \sim 1000.$$

These gluons carry only tiny fractions  $x \ll 1$  of the longitudinal momenta of their parent nucleons, but whose density is rapidly increasing with  $1/x$ . Let the two outgoing partons be characterized by the respective transverse momenta,  $p_{a\perp}$  and  $p_{b\perp}$ , and rapidities  $y_a$  and  $y_b$  so that

$$x_1 = \frac{p_{a\perp}}{\sqrt{s}} e^{y_a} + \frac{p_{b\perp}}{\sqrt{s}} e^{y_b}, \quad x_2 = \frac{p_{a\perp}}{\sqrt{s}} e^{-y_a} + \frac{p_{b\perp}}{\sqrt{s}} e^{-y_b}.$$

For particle production at RHIC or the LHC, the average transverse momentum of a hadron in the final state is below 1 GeV; moreover, 99% of the multiplicity (i.e. of the total number of produced hadrons) has  $p_{\perp} \leq 2$  GeV. For  $p_{a,b\perp} = 1$  GeV and central rapidities  $y_{a,b} \simeq 0$ , the above relation implies

$$x_i \simeq 10^{-2} \text{ at RHIC } (\sqrt{s} = 200 \text{ GeV})$$

$$\text{and } x_i \simeq 10^{-4} \text{ at the LHC } (\sqrt{s} = 2.76 \text{ TeV})$$

The gluonic form of matter, which is dense and weakly coupled, and dominates the wave function of any hadron (nucleon or nucleus) at sufficiently high energy, is known as the colour glass condensate (CGC). At time  $\tau = 0$ , the two nuclei hit with each other and the hard processes (those involving relatively large transferred momenta  $Q \geq 10$  GeV) occur faster within a time  $\tau \sim 1/Q$ , by the uncertainty principle. These processes are responsible for the production of hard particles, i.e. particles carrying transverse energies and momenta of the order of  $Q$ . At a time  $\tau \sim 0.2$  fm/c, corresponding to a semi-hard transverse momentum scale  $Q \sim 1$  GeV, the bulk of

the partonic constituents of the colliding nuclei are liberated by the collision. This is when most of the multiplicity in the final state is generated.

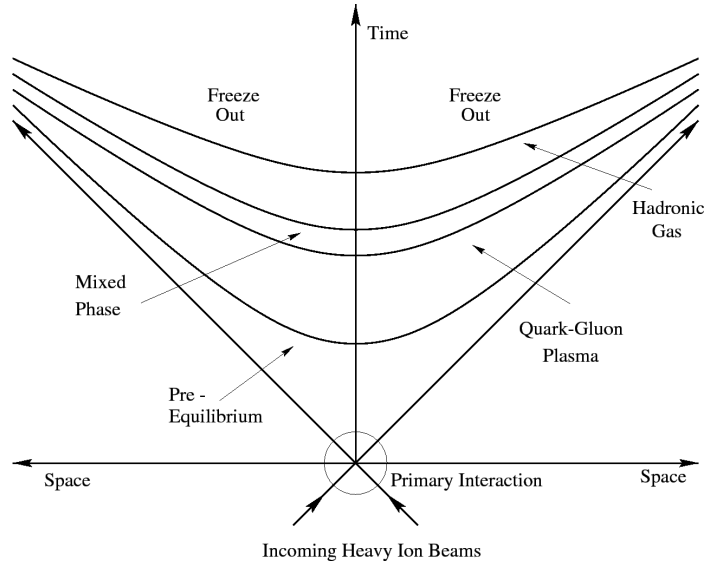


Fig. 6. The schematic space-time diagram of ultra-relativistic nuclear collisions [16].

If the produced partons did not interact with each other, then they would rapidly separate from each other and independently evolve (via fragmentation and hadronization) towards the final-state hadrons. This is the situation in proton-proton collisions. But the data for heavy ion collisions at both RHIC and LHC exhibit collective phenomena like the elliptic flow which clearly show that the partons liberated by the collision do actually interact with each other and quite strongly. This partonic matter rapidly approaches towards thermal equilibrium in short thermalisation time, of order  $\tau \sim 1 \text{ fm}/c$  [15]. Such a rapid thermalization indicates that the dense partonic matter produced in the intermediate stages of a heavy ion collisions may be a strongly coupled fluid.

The outcome of this thermalisation process is QGP. Driven by the pressure gradient, the QGP expands and cools down (for a duration of  $\tau \sim 3\text{-}5 \text{ fm}/c$ ) and it

eventually hadronises. This implies that the temperature is space and time dependent, i.e. thermal equilibrium is reached only locally. Hadronization occurs when the temperature becomes of the order of the critical temperature  $T_c$  for deconfinement, known from lattice QCD studies as  $T_c \sim 154\text{-}175$  MeV. In PbPb collisions at the LHC, this is estimated to happen around a time  $\tau \sim 10$  fm/c [15]. The hadronization then follows with further expansion in the hadronic phase until the “chemical freeze-out” point when inelastic interactions cease with particle abundances fixed; after further expansion/cooling until “kinetic freeze-out” point when elastic interactions stop with particle transverse momentum spectra fixed. The total fireball lifetime is approximately 10-20 fm/c depending on the beam energy.

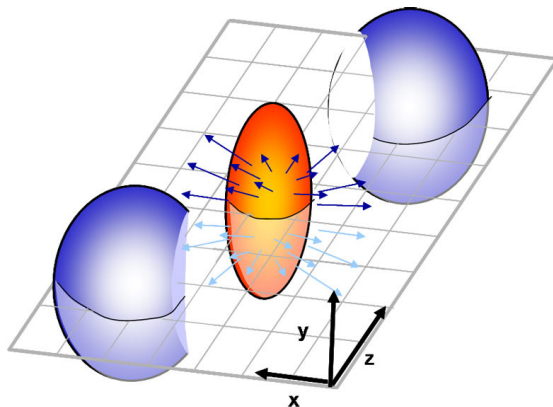


Fig. 7. Schematic representation of a non-central heavy-ion collision, characterized by an almond-shaped initial overlap zone, and a subsequent pressure-driven build-up of elliptic flow. Picture taken from Ref. [17].

It is convenient to introduce the standard coordinate system for heavy-ion collisions: The  $z$  axis is parallel to the beam line. Since most nucleus-nucleus (A-A) collisions are not head-on collisions, there exists a two-dimensional vector connecting centers of the colliding nuclei in the plane transverse to  $z$  axis, which is called the impact vector,  $\vec{b}$ , its length is the impact parameter,  $b$ . The  $x$ -axis is chosen to be parallel to the impact vector,  $\vec{b}$ , see Fig. 7. The  $x$ - and  $z$ -axes span the “reaction

plane” of a given collision. The  $x$ - and  $y$ -axes span the “transverse plane”. The component of the 3-momentum of produced particles parallel to  $z$ -axis is denoted by  $p_z$ , and the transverse component is  $\vec{p}_T$ . For relativistic particles it is convenient to use the (longitudinal) rapidity instead of the (longitudinal) velocity. The former is defined as

$$y = \tanh^{-1} \left( \frac{p_z}{E} \right) = \tanh^{-1} v_z . \quad (1.7)$$

Here  $E = \sqrt{m^2 + \vec{p}^2}$  is the energy of a particle. Due to the short lifetime of the medium, special probes are needed to access the properties of the medium. The only probes turn out to be the produced particles themselves. According to their energies the probes are divided into two categories: soft probes and hard probes.

#### 1.4. Soft probes/Bulk properties

The soft probes are associated with the particles with relatively low energy (e.g.,  $\lesssim 2$  GeV), which constitute the bulk medium ( $> 95\%$  [18]) created in heavy-ion collisions. The soft probes include multiplicity distributions, which can be related to the initial energy density reached during the collision, yields and momentum spectra of identified particles, which are determined by the conditions at and shortly after hadronization, and correlations between particles. The correlations measure both size and lifetime of the dense matter state as well as some of its transport properties via collective flow phenomena.

##### 1.4.1. Multiplicity distributions

The most basic quantity is the number of charged particles produced per unit of (pseudo)rapidity,  $dN_{\text{ch}}/dy$  ( $dN_{\text{ch}}/d\eta$ ), in a central, “head-on” collision. From the measured multiplicity one can derive a rough estimate of the energy density with the

help of a formula proposed first by Bjorken [19] relating the energy density to the transverse energy:

$$\varepsilon \geq \frac{dE_T/d\eta}{\tau_0 \pi R^2} = \frac{3}{2} \langle E_T/N \rangle \frac{dN_{\text{ch}}/d\eta}{\tau_0 \pi R^2} \quad (1.8)$$

where  $\tau_0$  denotes the thermalisation time,  $R$  is the nuclear radius, and  $E_T/N \approx 1$  GeV is the transverse energy per emitted particle. The value measured at the LHC implies that the initial energy density (at  $\tau_0 = 1$  fm/c) is about 15 GeV/fm<sup>3</sup> [18, 20], approximately a factor three higher than in Au+Au collisions at the maximum energy of RHIC [21, 22]. The high multiplicity at LHC, together with the large experimental

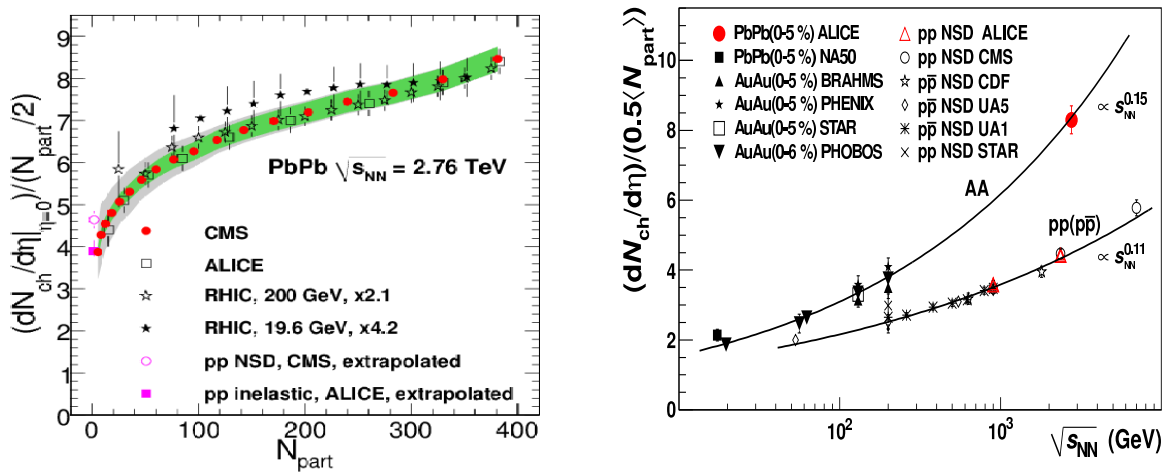


Fig. 8. (Left)  $dN_{\text{ch}}/d\eta|_{\eta=0}$  as a function of centrality class in 2.76 TeV PbPb collisions from CMS experiment (solid circles) [23] and from ALICE (open squares) [24]. The statistical uncertainties are negligible, while the systematic uncertainties are shown as two bands. Systematic uncertainties affecting the scale of the measurements from the analysis [23] are shown as inner green error bands and the total systematic uncertainties as an outer grey band, while the error bars indicate statistical uncertainties. The black stars are shifted slightly to the right for better visibility. (Right) Charged-particle multiplicity normalized to  $N_{\text{part}}/2$  in pp and central A+A (Au+Au and Pb+Pb) collisions as a function of  $\sqrt{s_{NN}}$  [25].

acceptance of the detectors, allow for a very precise determination of the collision geometry (impact parameter and reaction plane orientation) in each event.

The Fig. 8 (Left) presents the measured charged particle multiplicity  $dN_{\text{ch}}/d\eta|_{\eta=0}$  values as a function of centrality. The statistical uncertainties are negligible, while the systematic uncertainties are shown as two bands. Events are classified according to “centrality”, where e.g. the 0-5% (90-100%) centrality bin contains the 5% (10%) of all hadronic interaction events with the largest (smallest) final-state multiplicity and therefore the smallest (largest) impact parameters. The details of centrality estimation in CMS experiment is given in chapter 3. The charged hadron density for the most-central events (0-5%) is measured with CMS to be  $dN_{\text{ch}}/d\eta|_{\eta=0} = 1612 \pm 55$ . These results are consistent with those of ALICE [24] within the uncertainties. Also we observe that the charged particle production increases by a factor two as the energy increases from RHIC to LHC. In spite of difference in operating conditions and measurement techniques at LHC, the  $dN_{\text{ch}}/d\eta$  versus  $N_{\text{part}}$  results for Pb+Pb collisions at  $\sqrt{s_{\text{NN}}} = 2.76$  TeV shows a remarkable consistency across the experiments CMS, ATLAS and ALICE [26]. The charged particle multiplicity per participant pair  $dN_{\text{ch}}/d\eta|_{\eta=0}/(0.5\langle N_{\text{part}} \rangle)$ , is shown in Fig 8 (Right) together with lower energy data for A+A collisions and pp collisions. Particle production is not compatible with a logarithmic dependence with  $\sqrt{s}$ , contrary to what was seen for the data up to top RHIC energy, but follows a power law type of dependence. A power law ( $a + s_{\text{NN}}^n$ ) fit to the pp collision charged particle multiplicity density leads to a dependence  $\approx s^{0.11}$  while those for A+A collisions goes as  $\approx s^{0.15}$ . Since there is no scaling behaviour observed between elementary collisions like pp and heavy-ion collisions it can be concluded that A+A collisions at RHIC and LHC are not a simple superposition of several pp collisions [25].

### 1.4.2. Direct photons

Prompt photons with high transverse energy/momentum in hadronic collisions are produced directly from the hard scattering of two partons. At lowest order in perturbative QCD calculations, three partonic mechanisms produce prompt photons in hadronic collisions: (i) quark-gluon Compton scattering  $q + g \rightarrow \gamma + q$ , (ii) quark-antiquark annihilation  $q + \bar{q} \rightarrow l^+ + l^-$  and (iii) collinear fragmentation of a final-state parton into a photon. Prompt photons from (i) and (ii) are called “direct”; those from (iii) are called “fragmentation”. Measured photon production cross sections provide a direct test of pQCD and constrain the proton and nuclear PDFs.

In the QGP phase, photons should be produced by the scattering of hard partons traversing the medium with thermalized partons, as well as by the scattering of thermalized partons. The thermalized nature of the production medium should be reflected in the  $p_T$  distribution of the produced thermal photons. In heavy-ion collisions, an average temperature of the medium can be extracted from thermal photon signals [27]. Fig. 9 shows direct-photon yield in PbPb collisions at  $\sqrt{s_{NN}} = 2.76$  TeV

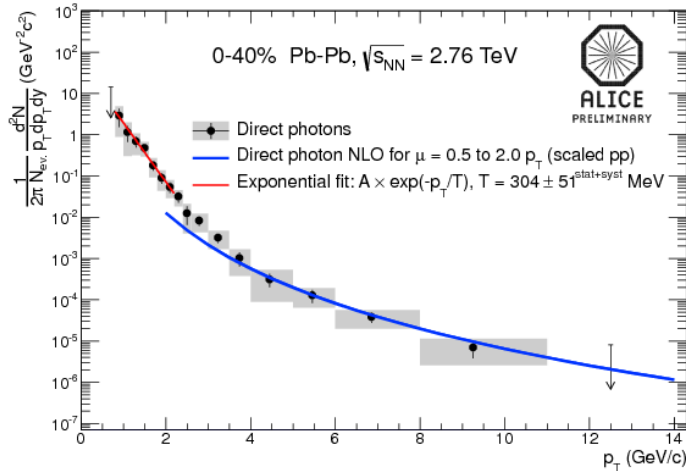


Fig. 9. Direct-photon yield in PbPb collisions at  $\sqrt{s_{NN}} = 2.76$  TeV for 0-40% centrality with NLO pQCD predictions.

for 0-40% centrality with a direct-photon NLO calculation for pp at  $\sqrt{s} = 2.76$  TeV scaled by  $N_{\text{coll}}$  and an exponential fit to the low momentum part of the spectrum. The low momentum photons (below 4 GeV/ $c$ ) contain a significant part of photons produced from a thermalized medium. The temperature is extracted as the inverse slope parameter of the exponential for  $0.8 \text{ GeV}/c < p_T < 2.2 \text{ GeV}/c$  and is given as  $T_{\text{LHC}} = 304 \pm 51^{\text{sys}+\text{stat}}$  MeV and in similar way, PHENIX measures an inverse slope parameter for 0-20% Au-Au collisions at  $\sqrt{s_{\text{NN}}} = 200$  GeV with  $T_{\text{RHIC}} = 221 \pm 19^{\text{stat}} \pm 19^{\text{sys}}$  MeV. The ALICE result shows that the system at LHC is hotter than the one at RHIC [27].

### 1.4.3. Azimuthal anisotropy

The azimuthal anisotropy parameter  $v_2$  (elliptic flow) measured at RHIC and LHC provides a unique opportunity to study the transport properties of the fundamental constituents of any visible matter. The elliptic flow,  $v_2$ , characterizes the azimuthal asymmetry of particles like  $\pi$ ,  $K$ ,  $p$  in the transverse plane in terms of the second harmonic coefficient of an azimuthal Fourier decomposition of the momentum spectra,

$$\left. \frac{dN}{d^2p_T dy} \right|_{y=0} = \frac{dN}{\pi dp_T^2 dy} [1 + 2v_2(p_T) \cos(2\phi) + \dots]. \quad (1.9)$$

Here  $\phi$  is the azimuthal angle in the transverse plane with  $\phi=0$  for  $x$ -axis. At mid-rapidity the system is symmetric about  $y-z$  plane, so there is no  $\cos \phi$  term. For soft particles ( $p_T < 2 \text{ GeV}/c$ ) the elliptic flow arises because, in semi-central collisions, the geometry of the initial interaction region has the shape of an ellipse, see Fig. 7. Once the system thermalises this initial geometrical anisotropy translates into stronger pressure gradients in the direction of the smaller axis of the ellipse. This induces momentum correlations among particles which *flow* preferentially along the small axis

of the ellipse, leading to a positive  $v_2$ . Since the spatial anisotropy is largest at the beginning of the evolution, a measurement of  $v_2$  provides access to the thermalisation time scale of the system. Applications of ideal relativistic hydrodynamics have shown that the experimentally (RHIC) measured  $v_2(p_T)$  for various hadrons ( $\pi$ ,  $K$ ,  $p$ ,  $\Lambda$ ) is described well when implementing a thermalisation time of  $\tau_0=0.5-1$  fm/ $c$  [28]. Fig. 10 (a) presents  $v_2$  for all different particles measured in PbPb collisions at  $\sqrt{s_{NN}}$

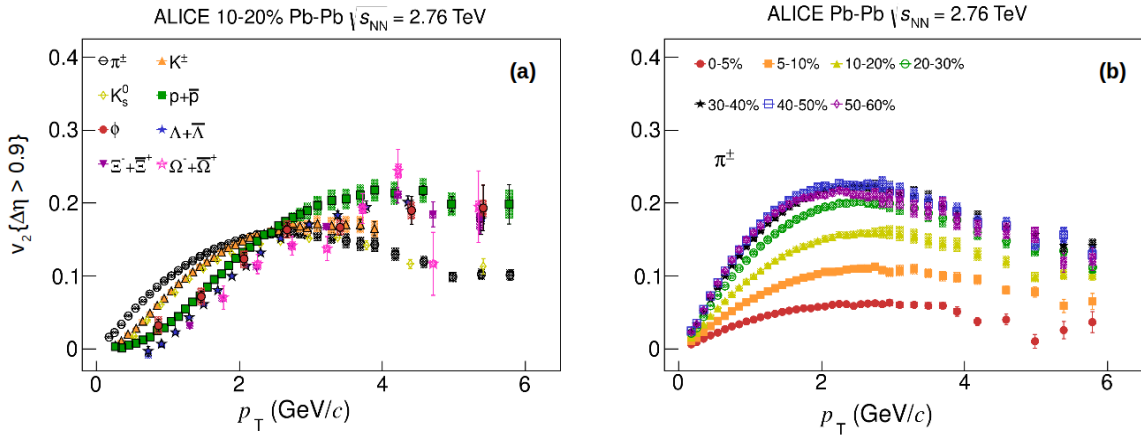


Fig. 10. (a) Elliptic flow  $v_2$  measured by LHC as a function of  $p_T$  for different particle species grouped by centrality class 10-20% of PbPb collisions at  $\sqrt{s_{NN}} = 2.76$  TeV. (b) The  $p_T$ -differential  $v_2$  of pions for different centralities of Pb-Pb collisions at  $\sqrt{s_{NN}} = 2.76$  TeV grouped by particle species [28].

= 2.76 TeV with ALICE as function of  $p_T$ . The results are in given centrality bin (10-20%), to illustrate how  $v_2$  develops for different particle species within the same centrality, for  $\pi^\pm$ ,  $K^\pm$ ,  $K_S^0$ ,  $p+\bar{p}$ ,  $\phi$ ,  $\Lambda+\bar{\Lambda}$ ,  $\Xi+\bar{\Xi}$  and  $\Omega+\bar{\Omega}$ . A clear mass ordering is seen for all centralities in the low  $p_T$  region (i.e.  $p_T < 3$  GeV/ $c$ ), attributed to the interplay between elliptic and radial flow. Radial flow tends to create a depletion in the particle  $p_T$  spectrum at low values, which increases with increasing particle mass and transverse velocity. The net result is that at a fixed value of  $p_T$ , heavier particles

have smaller  $v_2$  value compared to lighter ones [28]. The characteristic mass splitting is originated due to the fact that collective radial flow tends to equalise the velocities of particles, not their momenta, and therefore shifts heavy particles out to higher  $p_T$  than light ones [29].

Fig. 10 (b) presents the  $p_T$ -differential  $v_2$  of pion particles measured in Pb-Pb collisions at  $\sqrt{s_{NN}} = 2.76$  TeV. The error bars correspond to statistical uncertainties, while the shaded colour boxes around each point indicate the systematic uncertainties. The value of  $v_2$  progressively increases from central to peripheral collisions up to the 40-50% centrality interval for all particle species. This is consistent with the picture of the final state anisotropy driven by the geometry of the collision, as represented by the initial state eccentricity which increases for peripheral collisions. For more peripheral events, the magnitude of  $v_2$  does not change significantly within the systematic uncertainties compared to the previous centrality interval. This might originate from a convolution of different effects such as the smaller lifetime of the fireball in peripheral compared to more central collisions that does not allow  $v_2$  to further develop, the less significant (compared to more central events) contribution of eccentricity fluctuations and to final state hadronic effects [28].

A study of identified particle  $v_2$  and its constituent quark-number scaling ( $n_q$ ) behavior is performed with 2.76 TeV PbPb data at LHC. The basis of such a scaling is the splitting of  $v_2(p_T)$  between baryons and mesons at intermediate  $p_T$  (2-6 GeV/c). It was also reported that if both  $v_2$  and  $p_T$  are scaled by  $n_q$ , the various identified hadron species approximately follow a common behaviour [28]. The  $n_q$ -scaled  $v_2$  data from CMS experiment suggest a stronger violation of quark-number scaling in peripheral range of centrality (60-100%) than what is expected [30]. Similar behavior is observed in peripheral AuAu collisions at RHIC, while the scaling holds better for central AuAu and PbPb collisions [28, 31].

## 1.5. Hard probes

The hard probes are associated with the particles with relatively high energy ( $> 2$  GeV) including either light particles with large momentum or heavy particles irrespective of their momenta. Usually a hard probe can only be generated in initial hard collisions (their energy scale is usually much larger than the typical temperature of the medium) and their initial production can be estimated from pp collisions. By measuring the modification of hard probes after traversing the QGP medium, one can obtain information on the microscopic interaction between strongly interacting medium and the probe particle.

### 1.5.1. Nuclear modification factor, $R_{AA}$

The single particle production rates at previous experiments have shown a large suppression of hadrons in nuclear collisions relative to pp collisions, whereas particles that do not interact strongly, e. g. photons and  $Z$  bosons, are not modified by the medium produced in the collisions [32]. Thus, these electroweak particles ( $W^\pm$ ,  $Z^0$  and photons) constitute particularly “clean” probes of the initial state of the collision. A direct comparison of production cross sections of such probes in pp and nuclear collisions allows one to estimate possible modifications of the nuclear parton densities by the medium. Comparing to the previous experiments, the LHC can significantly extend the accessible  $p_T$  range and allow the measurement of heavy particles which are most likely formed in the very early stages of the collisions. The suppression effects of a given particle are typically expressed in terms of the nuclear modification factor:

$$R_{AA}(p_T) = \frac{d^2 N_{AA}/dp_T d\eta}{\langle T_{AA} \rangle d^2 \sigma_{NN}/dp_T d\eta}, \quad (1.10)$$

$\sqrt{s_{NN}} = 2.76$  TeV). In the absence of nuclear effects the factor  $R_{AA}$  is unity (see Chapter 5 for more details of  $R_{AA}$ ). Instead of  $R_{AA}$  one can also approximate the

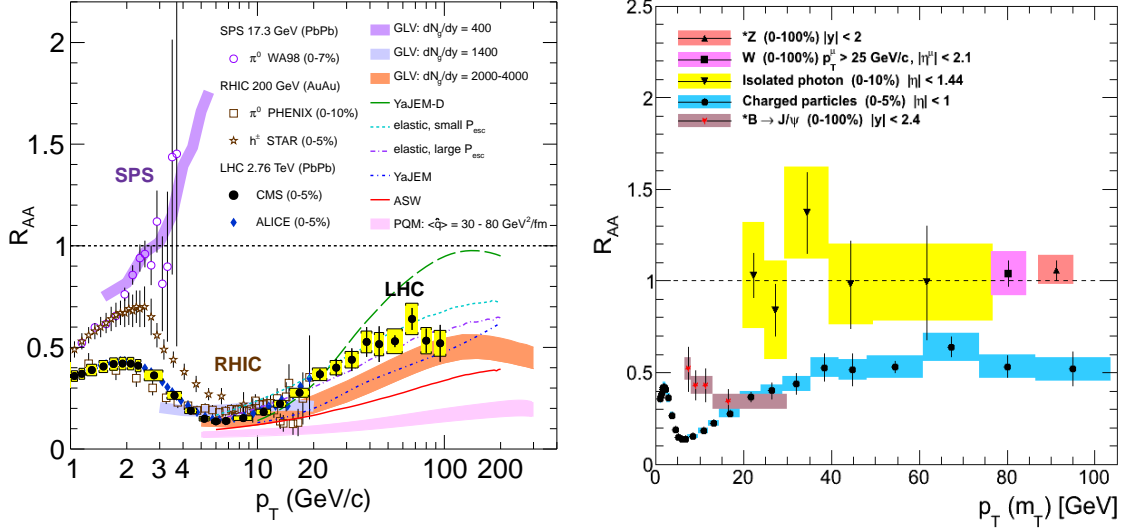


Fig. 11. (Left) Measurements of the nuclear modification factor  $R_{AA}(p_T)$  in central heavy-ion collisions at three different center-of-mass energies, as a function of  $p_T$ , for neutral pions and charged particles [34, 18], compared to several theoretical predictions [33]. (Right)  $R_{AA}$  measurements for photon,  $Z$ ,  $W$  and non-prompt  $J/\psi$  measurements. For the  $Z$  and  $W$  results, the data point is plotted at the rest mass of the particle, while for photons, the data points are plotted at their  $m_T = p_T$  (transverse mass, or transverse momentum) value [32].

centrality dependence by measuring  $R_{CP}$ , the ratio of central over peripheral events. It is also interesting to measure the nuclear suppression factor for individual particle species to distinguish the exact mechanisms of energy loss. A summary of  $R_{AA}$  measurements with center-of-mass energy, from the SPS to RHIC and then to the LHC for different particle species is shown in Fig. 11. RHIC results with neutral pions and charged hadrons shows that the latter is less suppressed below  $p_T \approx 8$  GeV/c possibly due to parton recombination processes that enhance proton(hadron)

production. Below  $p_T \approx 10 \text{ GeV}/c$ , charged hadron production at the LHC is found to be about 50% more suppressed than at RHIC [33]. Fig. 11 (Right) displays  $R_{AA}$  of isolated photon as a function of  $m_T = p_T$  (transverse mass, or transverse momentum) for the 0-10% most central PbPb collisions, along with  $Z$  and  $W$ . The ratio is compatible with unity within the experimental uncertainties for all  $p_T$  values, consistent with the expectation that nuclear parton densities are not significantly modified compared to the proton PDF in the kinematic range, dominated by high- $p_T$  photons. The result establishes photons and electroweak bosons production as a valuable perturbative probe of the initial state in heavy-ion collisions and provides a baseline for the study of in-medium parton energy loss [32].

### 1.5.2. Jet-quenching

One of the key measurements of hard probes at RHIC and LHC is the observation of jet-quenching [35] for high  $p_T$  particles. A jet is a narrow cone of hadrons produced by the hadronization of a high momentum parton. If these partons traverse the QGP they are expected to undergo collisional and medium-induced radiational energy loss. The energy loss will be reflected in the suppression of high  $p_T$  hadron multiplicities. The first measurement from the LHC of suppression of particles from hard-scattering in central Pb+Pb collisions at  $\sqrt{s_{NN}} = 2.76 \text{ GeV}$  is shown in Fig. 12 [34, 36]. Despite more than a factor of 20 higher  $\sqrt{s_{NN}}$ , the  $R_{AA}$  measurements for charged hadrons by ALICE at LHC appear to be nearly identical to that for neutral pions from PHENIX at RHIC for  $5 < p_T < 20 \text{ GeV}/c$ . It is interesting to note that due to the flatter  $p_T$  spectrum at the LHC ( $p_T^n$  with  $n \sim 6$  compared to  $n \sim 8$  at RHIC), a  $\sim 25\%$  larger shift in the  $p_T$  spectrum from p-p to A+A is required at LHC to get the same  $R_{AA}$ , likely indicating  $\sim 25\%$  larger fractional energy loss at LHC than at RHIC in this  $p_T$  range [37]. This suppression of hadrons, the signal of jet quenching discovered

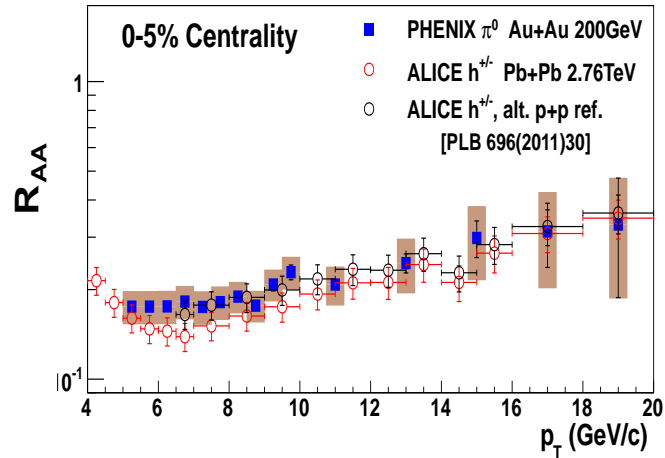


Fig. 12. Charged hadron  $R_{AA}$  in  $\sqrt{s_{NN}} = 2.76$  TeV central (0-5%) Pb+Pb collisions at LHC [34] compared to  $R_{AA}$  of  $\pi^0$  in  $\sqrt{s_{NN}} = 200$  GeV central (0-5%) Au+Au collisions [36] at RHIC.

at RHIC [38], is still a very useful and sensitive observable even in the era of fully reconstructed jets, and severely constrains the various models of jet quenching at LHC.

### 1.5.3. Dijet-imbalance

Measuring the energy of fully reconstructed jets allows one to distinguish between energy redistribution among the leading parton and the remainder of the jet. Regarding the energy dissipation out of the jet into the thermal medium, one of the promising channels are dijets, in particular their transverse energy balance and azimuthal angle correlation. The measurement of the dijet asymmetry  $A_J = (p_{T1} - p_{T2}) / (p_{T1} + p_{T2})$ , where 1 and 2 refer to the leading and subleading jet, respectively, was performed by both ATLAS [39] and CMS [40] at LHC. The striking observation by both experiments is the large centrality-dependent increase of the imbalance in the energy of the two jets, as measured in the calorimeters [40, 41]. The shape of the dijet mo-

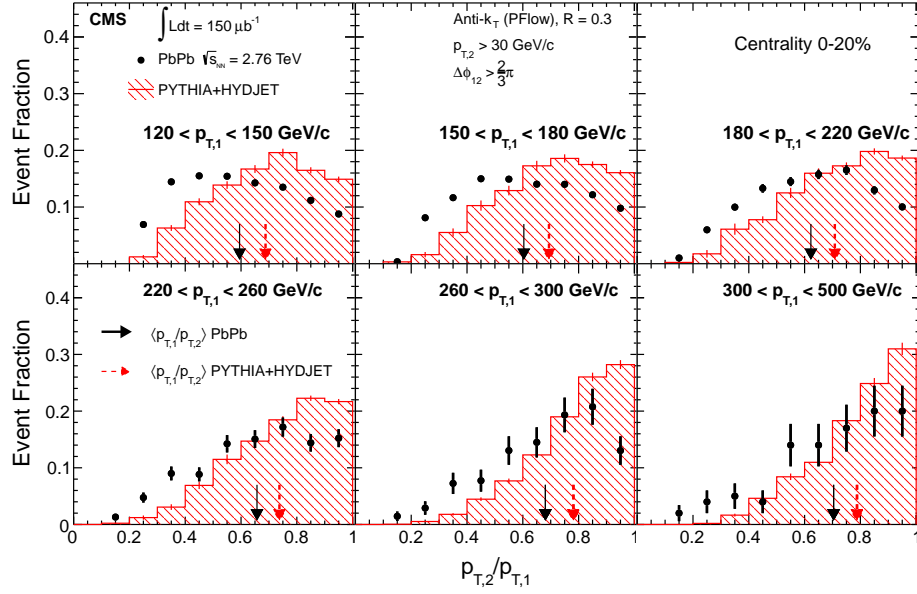


Fig. 13. Subleading jet transverse momentum fraction ( $p_{T2}/p_{T1}$ ), in bins of leading jet transverse momentum from  $120 < p_{T1} < 150$  GeV/ $c$  to  $p_{T1} > 300$  GeV/ $c$  for subleading jets of  $p_{T2} > 30$  GeV/ $c$  and  $\Delta\phi_{1,2} > 2\pi/3$  between leading and subleading jets. Results for 0-20% central PbPb events are shown as points, while the histogram shows the results for pythia dijets embedded into hydjet PbPb simulated events. The arrows show the mean values of the distributions and the error bars represent the statistical uncertainties [41].

momentum imbalance distribution experiences a gradual change with collision centrality, towards more imbalance. Also, the dependence of the energy loss on the leading jet momentum can be studied using the jet transverse momentum ratio,  $p_{T2}/p_{T1}$ . The distribution of the ratio, shown Fig. 13, provide a intuitive way of quantifying the energy loss [41].

#### 1.5.4. Heavy quarks and heavy flavor mesons

Another important hard probe is the heavy quark, which is expected to be only partially thermalised in the medium considering its large mass and the limited fireball

lifetime. They are tracers created essentially only in hard scattering processes and their energy loss should be smaller than the one of gluons (different colour charge) or of light quarks (mass dependent reduction of energy loss). The production of heavy quarks and its properties has been studied both at RHIC and LHC. The suppression observed at LHC for open heavy flavour  $D^0$ ,  $D^+$  and  $D^{*+}$  mesons from  $c$  quarks reaches factor about 4 for  $p_T > 5$  GeV/ $c$  as shown in Fig. 14 (a) , almost as large as that observed for light hadrons (dominated by pions from gluon fragmentation) providing an indication of no strong colour charge or mass dependence of the in-medium energy loss, although there seems to be a tendency for  $R_{AA}^\pi < R_{AA}^D$  at low  $p_T$  [42, 43, 44]. But the  $R_{AA}$  of non-prompt  $J/\psi$  from B decays, measured by the CMS Collaboration, shows lesser suppression with respect to D-mesons [45]. Fig. 14

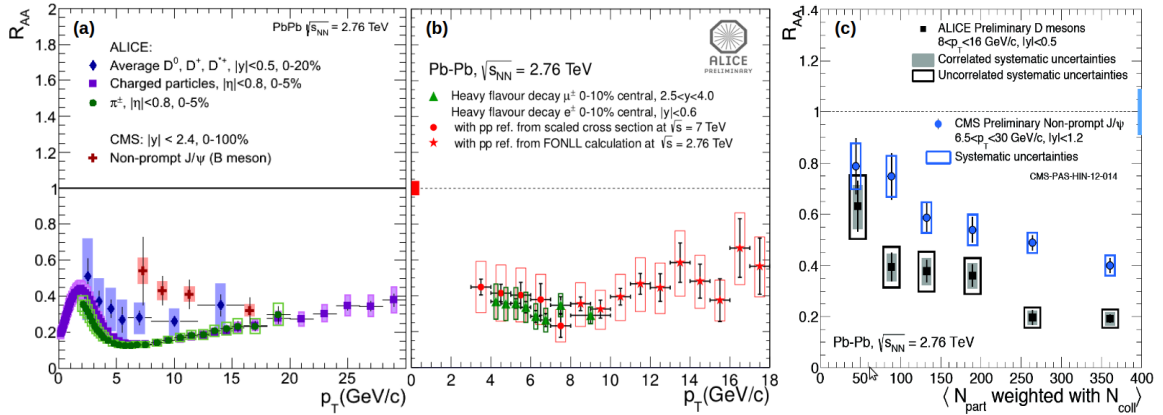


Fig. 14. (a) Average  $R_{AA}$  of D mesons in the 0-20% centrality class [43], compared to that of charged particles [46],  $\pi^\pm$  [42] and non-prompt  $J/\psi$  from B decays [45]. (b) Nuclear modification factor ( $R_{AA}$ ) of electrons (circles and stars, depending on the pp reference) and muons (triangles) [48, 49] from heavy-flavour hadron decays in PbPb collisions at  $\sqrt{s_{NN}} = 2.76$  TeV for the centrality class 0-10%. (c) Average  $R_{AA}$  of D mesons as a function of centrality [43] compared to that of non-prompt  $J/\psi$  from B decays [45].

(b) shows  $R_{AA}$  for heavy-flavour decay muons and electrons, at forward and central rapidity, respectively, for the centrality class 0-10%. Both lepton species exhibit a suppression of factor of about 3 up to  $p_T = 10 \text{ GeV}/c$ , and about 2 for electrons up to  $p_T = 18 \text{ GeV}/c$  in a momentum range where fixed order next-to-leading log (FONLL) calculations [47] predict that the leptons from B-meson decays start to dominate, thus hinting at a significant in-medium energy loss for beauty quarks [48, 49]. Similar suppression of single  $e^\pm$  from heavy quark ( $c$ ,  $b$ ) decay observed at RHIC was a surprise, a major discovery and a problem since it strongly disfavors the radiative energy loss explanation of jet-quenching because heavy quarks should radiate much less than light quarks or gluons [37].  $R_{AA}$  versus  $N_{\text{part}}$  for D meson and non-prompt  $J/\psi$  (from B meson), shown in Fig. 14 (c), indicates a different suppression for charm and beauty hadrons in central collisions. pQCD model including mass-dependent radiative and collisional energy loss predicts a difference between the D-meson and non-prompt  $J/\psi$  similar to that observed at LHC [50]. Overall indications from these results are consistent with the expected hierarchy of suppression,  $R_{AA}^\pi < R_{AA}^D < R_{AA}^B$ .

## 1.6. Quarkonium

Typical hard probe particles have only one “hard” scale characterized by their high energy, therefore they are not particularly sensitive to physics at the energy scale of medium temperature,  $T$ . However there exists one special hard probe particle which has an additional (softer) energy scale (on the order of  $T$ ) making it very sensitive to physics at the medium temperature. This probe is the measurement of quarkonium. Heavy quarkonia are important probes of the quark gluon plasma since they are produced early in the collision and their survival is affected by the surrounding medium [51]. The bound states of charm and bottom quarks are predicted to be

suppressed in heavy ion collisions in comparison with pp, primarily as a consequence of deconfinement (melting) in the QGP.

## 1.7. Outline of thesis

The thesis is organized as follows. In Chapter 2 we discuss quarkonium production mechanism and its modification in the hot medium with brief experimental status on charmonium measurement. Chapter 3 gives an overview of the CMS detector and its main components. Then we give a description of the data selection after which the muon reconstruction and identification are discussed in detail in Chapter 4. Chapter 5 describes the measurement of  $J/\psi$  in PbPb collisions at  $\sqrt{s_{\text{NN}}} = 2.76$  TeV, explaining the yield extraction and calculation of efficiency and systematic uncertainties. In Chapter 6, we describe the methods to measure the single ratios of  $\psi(2S)$  to  $J/\psi$  in PbPb and pp collisions, used for the double ratio measurement of charmonia. Then a phenomenology study on suppression of quarkonia states in finite size quark-gluon plasma is presented in Chapter 7, followed by conclusion in Chapter 8.

# CHAPTER 2

## Charmonium

## 2.1. Introduction

A quarkonium is a bound state of a quark and its own antiquark. A quarkonium made of a pair of heavy quarks ( $c, b$ ) is called heavy quarkonium. Heavy quarkonium includes charmonium ( $c\bar{c}$ ) and bottomonium ( $b\bar{b}$ ). The heaviest toponium does not exist because the top quark decays through the electroweak interaction ( $\tau_t=1/\Gamma_t \simeq 0.1\text{fm}/c$ ) before a bound state can form. In this thesis we focus on charmonium which can be rather abundantly produced at LHC energies.

The  $J/\psi$ , with mass  $\approx 3.1 \text{ GeV}/c^2$  and spin of 1, was discovered concurrently and independently by groups at Brookhaven National Laboratory (BNL) [52] and the Stanford Linear Accelerator Center (SLAC) [53], and the discoveries were announced together on November 11, 1974. It was the first discovered hadron containing charm quarks (D mesons, though much lighter, were not discovered until 1976), as well as the first discovered charm-anticharm meson (charmonium). The BNL group (fixed target) used the reaction

$$p + Be \rightarrow J/\psi + X \rightarrow e^+ + e^- + X \quad (2.1)$$

while the SLAC group ( $e^+ e^-$  colliding beam) used

$$e^+ + e^- \rightarrow J/\psi \rightarrow \text{hadrons}, e^+e^-, \mu^+\mu^- \quad (2.2)$$

Since that discovery, many more charmonium states have been observed, such as the  $\psi'$ ,  $\eta_c$ , and  $\chi_c$ , as well as hadrons containing a mixture of charm and other quarks (e.g. D mesons and the  $\Lambda_c$ ). Several of the most common charmonia states are listed in Table II, where  $\epsilon_B$  is binding energy of the states (see Eq. 2.5). One advantage to a bound state of heavy quarks is that it is relatively well-described by the non-relativistic Schrodinger equation. We can write the QCD potential energy of the

Table II. Charmonium states and their properties.

state	$\eta_c$	$J/\psi$	$\chi_{c0}$	$\chi_{c1}$	$\chi_{c2}$	$\eta_c(2S)$	$\psi'$
mass [GeV]	2.98	3.10	3.42	3.51	3.56	3.64	3.69
$\epsilon_B$ [GeV]	0.75	0.64	0.32	0.22	0.18	0.10	0.05

bound state as having two components, one similar to a typical Coulomb potential and a second linear term for confinement that increases as the quarks are pulled apart. This is known as a Cornell potential [54, 55], and is written:

$$V(r; T = 0) = -\frac{4\alpha_s}{3r} + \sigma r, \quad (2.3)$$

with  $\alpha_s(m_Q) \simeq 0.35$  for  $m_c = 1.5$  and  $\sigma \simeq 1$  GeV/fm [56]. The first term corresponds to a Coulombic part which originates from one-gluon exchange and is dominant at small distance ( $r$ ), the second term linear in  $r$  reflects the confining interaction.

Following the procedure of [57] and plugging this potential into the non relativistic Schrodinger equation:

$$\left\{ 2m_c - \frac{\nabla^2}{m_c} + V(r) \right\} \Phi_i(r) = M_i \Phi_i(r) \quad (2.4)$$

one can reproduce the experimental masses of the  $J/\psi$ ,  $\chi_{c0}$  and  $\psi'$  to within 1%. The Particle Data Group (PDG) value of  $J/\psi$  and  $\psi'$  mass is 3.0969 GeV/ $c^2$  and 3.68609 GeV/ $c^2$  respectively [58]. Charmonia which have mass below the energy threshold for producing two D mesons (3.73 GeV) are shown in Fig. 15 with their major decay modes.

In this thesis we mainly focus on the measurement of vector charmonium, such as,  $J/\psi$  and  $\psi'$  which can couple to virtual photons and have dilepton as the decay

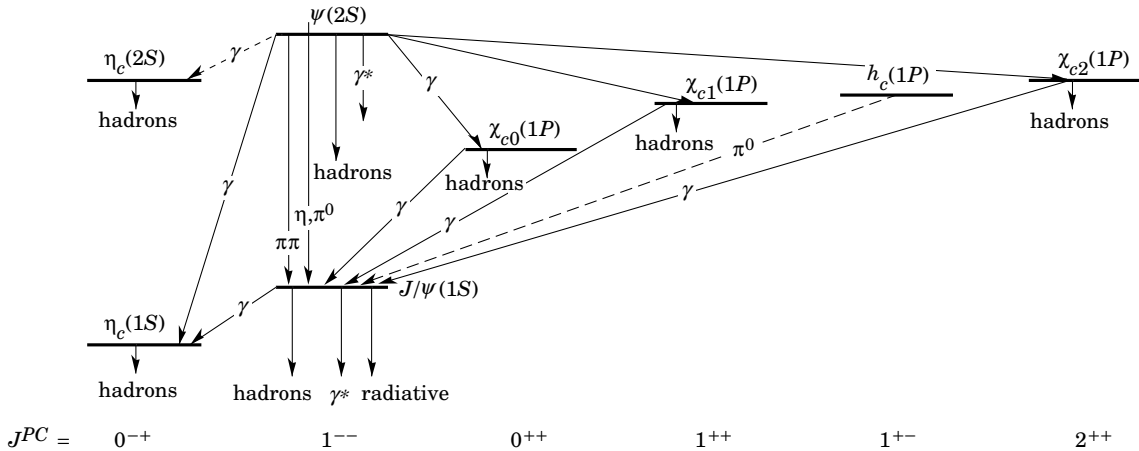


Fig. 15. Charmonium spectrum with decay modes [58].

product. It will allow for quite accurate measurements, keeping in mind that 32% (8%) of observed  $J/\psi$  are from feed-down of  $\chi_c(\psi')$  [59, 60], which happens at around  $1000\text{fm}/c$ , much later than typical thermal medium lifetime ( $\sim 10\text{fm}/c$ ).

Unlike light quarkonium states the heavy quarks move inside the heavy quarkonium with a speed significantly smaller than the speed of light, with, *e.g.*,  $\langle v^2/c^2 \rangle \sim 0.25$  for  $J/\psi$  [61]. The charmonium states typically have binding energies of the order of several hundred MeV, *e.g.*,  $\epsilon_B^{J/\psi} = 640$  MeV, which is on the same order of typical medium temperatures at Ultra relativistic Heavy-Ion Collisions (URHIC). The charmonium binding energy is usually counted as the difference between the charmonium mass and the open-charm threshold,

$$\epsilon_B = 2m_D - m_\Psi, \quad (2.5)$$

with  $m_D \simeq 1.87$  GeV. In vacuum the  $D\bar{D}$  pair is usually considered as the open charm threshold for charmonium states.

If a charmonium is put inside the deconfined QGP medium the color force be-

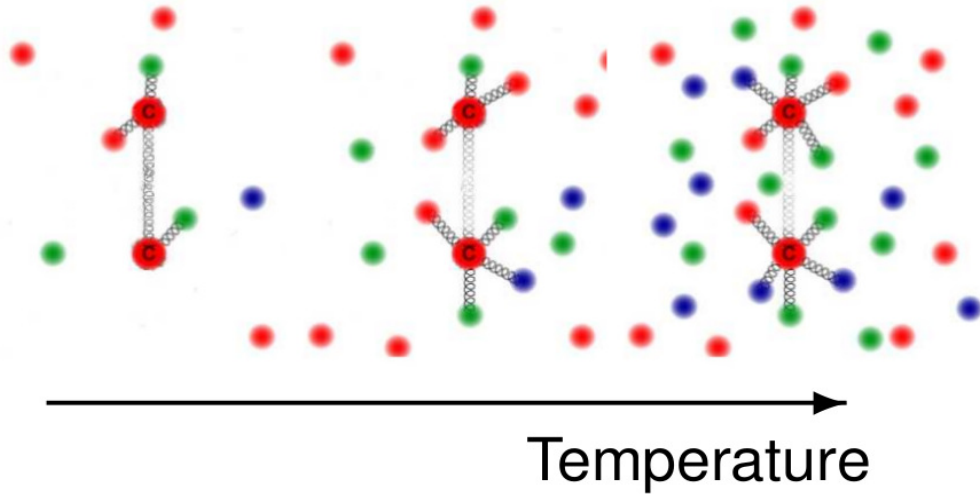


Fig. 16. Schematic representation of color-Debye screening in a deconfined medium.

tween  $c$  and  $\bar{c}$  is subject to screening by the surrounding colored partons, see Fig. 16, in a way similar to screening of the electric field in dielectric materials: The  $c(\bar{c})$  quark attracts partons in the medium with opposite color charge and forms the “Debye cloud” which screens the color field of the  $c(\bar{c})$  quark. The screening effect in the Coulombic part of the Cornell potential can be evaluated with thermal pQCD. In the confining parts it is usually described by a phenomenological ansatz in early calculations, leading to the following form of the screened Cornell potential at finite temperature [62],

$$V_{\bar{Q}Q}(r; T) = \frac{\sigma}{\mu_D(T)} (1 - e^{-\mu_D(T)r}) - \frac{4\alpha_s}{3r} e^{-\mu_D(T)r} . \quad (2.6)$$

Where  $\mu_D(T)$  is Debye-screening mass. A direct consequence of the color Debye-screening is the lowering of charmonium binding energies, see Fig. 17. According to thermal pQCD calculations the Debye mass is related to the temperature of the medium,  $T$ , via

$$\mu_D(T) \sim gT. \quad (2.7)$$

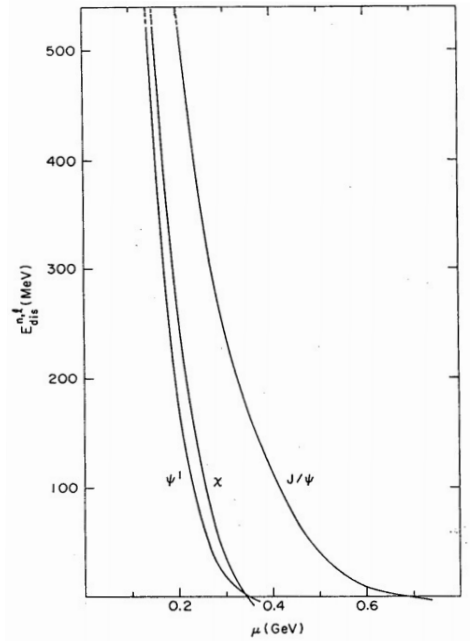


Fig. 17. Charmonium binding energies as a function of Debye mass. They are estimated from Eq. (2.6). Figure is taken from [62].

Here  $g$  is the strong coupling constant. Inserting  $g \sim 2$  (corresponding to  $\alpha_s \sim 0.35$ ), we see that above a temperature of  $T \sim 350\text{MeV}$  the  $J/\psi$  is not bound any more and is expected to dissolve into separate  $c$  and  $\bar{c}$  quarks. Based on this mechanism  $J/\psi$  suppression was first suggested in 1986 as a signature of QGP [63]. Similar phenomena are expected for the excited charmonium states, such as  $\psi'$  and  $\chi_c$ . Their smaller binding energies imply lower dissociation temperatures. Therefore the entire charmonium spectra could provide a “thermometer” for the matter created in heavy-ion collisions.

Although associated with large uncertainties, these lattice QCD (lQCD) data suggest that the  $J/\psi$  bound states might still survive above the critical temperature. As a consequence the  $c$  and  $\bar{c}$  pairs produced in initial hard collisions may coalesce and regenerate  $J/\psi$  in QGP [64, 65], rendering the original picture with  $J/\psi$  suppression as the signal of QGP more complicated. Quantitative calculations disentangling

primordial  $J/\psi$  production and regeneration are thus necessary for utilizing  $J/\psi$  to assess the basic properties of the hot and dense medium created in URHICs.

## 2.2. The charmonium hadroproduction models

At p+p machines charmonium can be produced in the following ways:

**Prompt direct:** the charmonium states are produced directly from the pp interaction.

**Prompt feed-down:** the charmonium states are a decay product of a directly produced quarkonium. For example: if a directly produced  $\chi_c$  decays in  $\chi_c \rightarrow J/\psi + \gamma$  final state, the  $J/\psi$  is considered feed-down.

**Non-Prompt:** the charmonium states are the decay product of a b-hadron. The above categories are experimentally often difficult to distinguish. The separation between prompt and non-prompt can be performed by exploiting the large b-hadron lifetime with a fit of the charmonium proper time distribution. In order to separate direct from feed-down, the production cross-section of each mother resonance is required.

The prompt direct production of charmonium states at hadron machines (also called hadroproduction) is a QCD process which takes place at both perturbative and non-perturbative scales. This interplay between perturbative and non-perturbative regimes made quarkonia an excellent test of QCD predictions. Despite over thirty years of studies in this sector there is still no agreement on what should be the hadroproduction mechanism. The most commonly used models for predicting production-related quantities in the quarkonium sector are: the Color Evaporation Model (CEM), the Color Singlet Model (CSM) and the Non-Relativistic QCD model (NRQCDM). These three models perform a clear separation between the production of the heavy

quark and antiquark pair  $Q\bar{Q}$  and the hadronization of the  $Q\bar{Q}$  into a quarkonium state. This separation, called factorization, reflects the different energy scales of the two processes. The  $Q\bar{Q}$  production is a perturbative (also called short distance) process so it can be calculated with an expansion in powers of  $\alpha_s$  (the QCD coupling constant). The  $Q\bar{Q}$  hadronization involves non-perturbative (long distance) processes which have to be parametrised.

### 2.2.1. Color Evaporation Model (CEM)

The Color Evaporation Model (CEM) was introduced in 1977 [66, 67], and was later revived in 1996 by Halzen et al. [68]. It is able to reproduce a number of experimental results very well, such as the  $J/\psi$  cross section from  $p + p$  or  $p + \bar{p}$  collisions as a function of  $\sqrt{s}$ , as well as the polarized production cross sections. The model assumes that the color state of the produced  $c\bar{c}$  is completely random, and consequently there is a 1/9 chance of ending up with a colorless (singlet state) meson (the other cases are assumed to result in open charm mesons). This can be written as:

$$\sigma(J/\psi) = \frac{\rho}{9} \int_{2m_c}^{2m_D} dm \frac{d\sigma_{c\bar{c}}}{dm} \quad (2.8)$$

where  $\frac{d\sigma_{c\bar{c}}}{dm}$  is the differential production cross section with respect to mass, and the natural value of  $\rho$  is the inverse of the number of quarkonia states between  $2m_c$  and  $2m_D$ . However, in practice the determination of  $\rho$  is usually done from the data, leaving the CEM rather phenomenological.

### 2.2.2. Color Singlet Model (CSM)

The Color Singlet Model (CSM) is based on the postulate that the creation of the two heavy quarks and the formation of the meson state can be factorized. The first process is considered to be perturbative due to the heavy mass of the quarks, allowing

the cross section to be calculated using the usual Feynman diagram techniques. The second step is assumed to happen with the quarks at rest in the meson frame, and this is known as the static approximation. Finally, it is assumed that the color and spin of the  $q\bar{q}$  do not change during binding, and therefore the  $q\bar{q}$  pair is required to be produced in the color singlet state. Only the color singlet states are colorless, hence the name of the model. For charmonium states in P-wave or above (for example the  $\chi_c$ ) the color singlet matrix element term leads to infrared divergences, hence the CSM is not a self-consistent theory for these quarkonium states. In order to cancel these divergences the color octet contributions have to be included. The Color Octet Model (COM) was proposed in 1995 [69], and offers an alternative to the CSM-CDF puzzle that CSM underestimates the observed cross-section for single  $J/\psi$  production at high transverse momentum ( $p_T$ ) at the Tevatron(CDF) [70].

### 2.2.3. Non-Relativistic QCD Model (NRQCDM)

The Non-Relativistic QCD Model(factorization) is an Effective Field Theory (EFT) based on the factorization of short distance and long distance contributions. It assumes that the heavy quark velocity  $v$  in the centre-of-mass of the charmonium state is small and the charmonium system can be treated non-relativistically. This effective field theory provides the foundation for much of the current theoretical work. According to NRQCD, the production of heavy quarkonium factorises into two steps: a heavy quark-antiquark pair is first created at short distances and subsequently evolves non-perturbatively into quarkonium at long distances. The NRQCD calculations depend on the color-singlet (CS) and color-octet (CO) matrix elements, which account for the probability of a heavy quark-antiquark pair in a particular color state to evolve into a heavy quarkonium state. The inclusive cross-section of the quarkonium state,  $\sigma_{J/\psi}$ , is expressed in powers of  $v$ ; this is equivalent to expressing it in terms of the

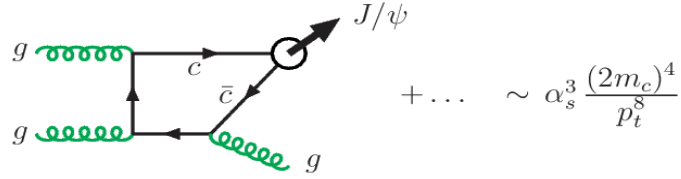
momentum scale  $m_c v$ . The formula is:

$$\sigma(J/\psi) = \sum_n \sigma_n(\Lambda) \langle \mathcal{O}_n^{J/\psi}(\Lambda) \rangle. \quad (2.9)$$

Here,  $\Lambda$  is the cut off scale of the effective theory. The coefficients  $\sigma_n(\Lambda)$  represent the partonic cross sections to create a  $q\bar{q}$  pair and they are calculated in pQCD. They are process dependent, calculated as an expansion in  $\alpha_s$ . The matrix elements  $\langle \mathcal{O}_n^{J/\psi}(\Lambda) \rangle$  represent the probability of a  $q\bar{q}$  pair to evolve into quarkonium. The matrix elements can be color singlet and color octet operators representing the  $q\bar{q}$  pair created or annihilated in a color singlet and a color octet state. The sum in Equation 2.9 is an expansion in  $\alpha_s$  and velocity  $v$ . To describe previous experimental data, it was found that next-to leading order (NLO) corrections in  $\alpha_s$  have to be included in calculations of hadroproduction cross sections of  $S$  [71] and  $P$  [72] charmonium.

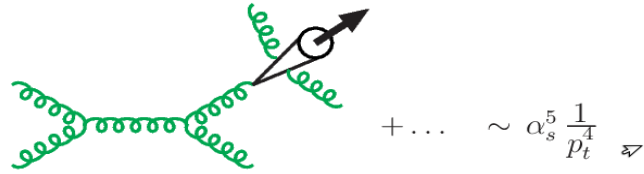
(a) leading-order colour-singlet:

$$g + g \rightarrow c\bar{c}[{}^3S_1^{(1)}] + g$$



(b) colour-singlet fragmentation:

$$g + g \rightarrow [c\bar{c}[{}^3S_1^{(1)}] + gg] + g$$



(c) colour-octet fragmentation:

$$g + g \rightarrow c\bar{c}[{}^3S_1^{(8)}] + g$$



(d) colour-octet fusion:

$$g + g \rightarrow c\bar{c}[{}^1S_0^{(8)}, {}^3P_J^{(8)}] + g$$



Fig. 18. Generic Feynman diagrams for  $J/\psi$  production in hadron collisions via colour-singlet and color-octet model.

### 2.2.4. Experiment and model comparison

Prompt production data from ATLAS experiment [73] are compared, in Fig. 19, to the predictions of the CEM for prompt  $J/\psi$  production and a calculation of the direct  $J/\psi$  production cross-section in the CSM at next-to-leading order (NLO) and a partial next-to-next-leading order calculation (NNLO). The CEM predictions include contributions from  $\chi_c$  and  $\psi(2S)$  feed-down and can be directly compared with the prompt  $J/\psi$  data. But the CSM (including higher-order corrections) or the LO NRQCDM (which includes singlet and octet components) are only available for the direct  $J/\psi$  production component. The NLO and NNLO predictions are overlaid with

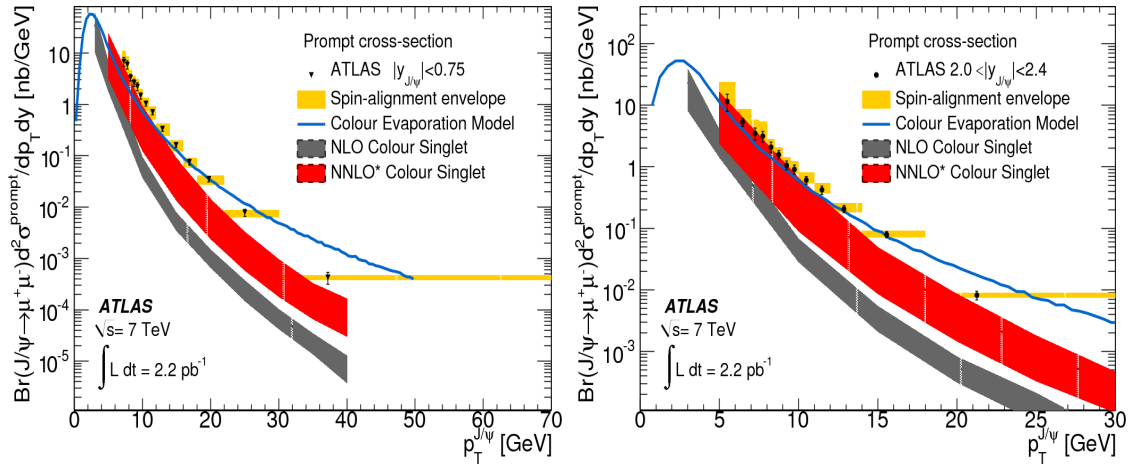


Fig. 19. Prompt  $J/\psi$  production cross-section from ATLAS experiment [73] are compared to the predictions of the CEM for prompt  $J/\psi$  production and a calculation of the direct  $J/\psi$  production cross-section in the CSM at next-to-leading order (NLO) and a partial next-to-next-leading order calculation (NNLO).

the ATLAS measurements in the Fig. 19 for two rapidity region. The dashed lines represent the central NLO and NNLO predictions while the shaded areas show the range of the prediction due to factorisation and renormalisation scale variation. The CSM predictions at NNLO show significant improvement in describing the  $p_T$  dependence and normalisation of prompt  $J/\psi$  production over NLO, and vast improvement

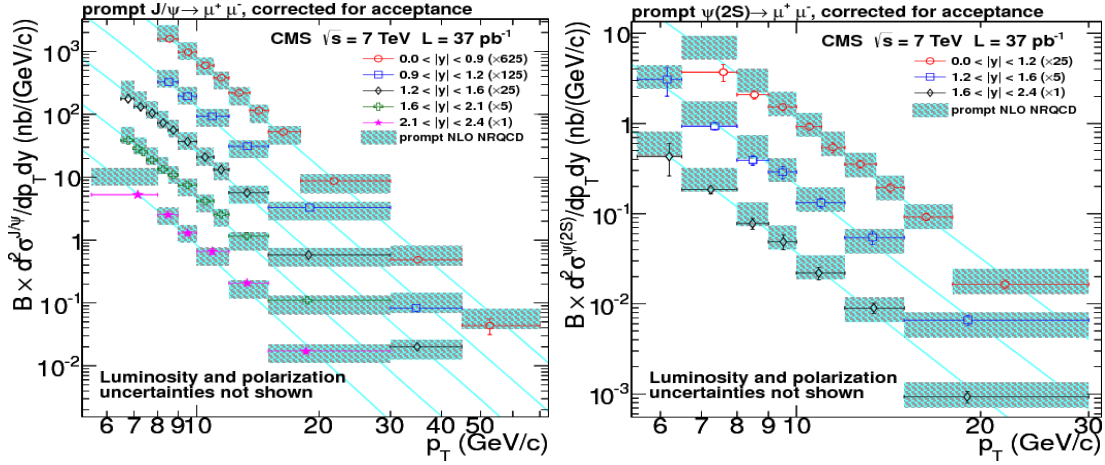


Fig. 20. Measured differential cross section for prompt  $J/\psi$  and  $\psi(2S)$  production (left and right, respectively) as a function of  $p_T$  for different rapidity bins. The error bars on the data points include all the statistical and systematic contributions except luminosity and polarization. The coloured (dark) bands indicate the theoretical predictions from NRQCD calculations. The lines are added only for illustrative purposes [75].

over earlier LO predictions that are compared to Tevatron data, although these predictions still fall short of fully describing the production mechanisms of prompt  $J/\psi$ , particularly at the highest transverse momenta [73].

Fig. 20 show the measured prompt cross sections for the  $J/\psi$  and the  $\psi(2S)$  as a function of  $p_T$ , for the various rapidity bins and corrected for detector acceptance in pp collisions at  $\sqrt{s} = 7$  TeV with the CMS experiment. They are compared with theoretical predictions from NRQCD model [74, 75].

Similarly the measured differential cross-sections with LHCb at  $\sqrt{s} = 8$  TeV for the production of prompt  $J/\psi$  mesons as a function of  $p_T$  are compared in Fig. 21 to three theoretical models that assume no polarisation [76]. Here both the NNLO\* CSM and the NLO NRQCDM provide reasonable descriptions of the experimental data. In contrast, the CSM at NLO underestimates the cross-section by an order of magnitude.

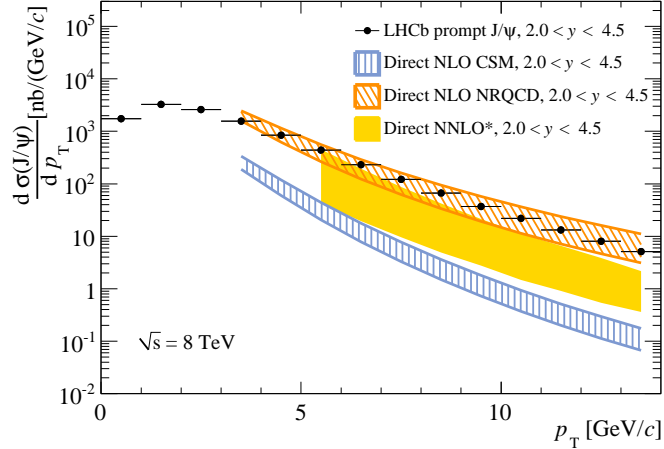


Fig. 21. Comparison of the differential cross-section for the production of prompt  $J/\psi$  meson (under the assumption of zero polarisation) as a function of  $p_T$  with direct production in an NLO NRQCD (orange diagonal shading), an NNLO\* CSM (solid yellow) and an NLO CSM (blue vertical shading). The points show the measurements reported in the analysis [76].

### 2.3. Charmonium in p+A collisions

In p+A collisions, the presence of normal nuclear matter can affect charmonium production. Here it is presumed that there is no formation of hot medium, so that such collisions provide a tool to probe charmonium production, evolution and absorption in confined matter.

#### Cold Nuclear Matter Effects

The notion that  $J/\psi$  production in A+A collisions can be viewed as superposition of independent nucleon-nucleon collisions is not true. The deviation of primordial  $J/\psi$  production in A+A from  $N_{\text{coll}}$ -scaled p+p collisions is usually attributed to the so-called cold nuclear matter (CNM) effects. In this section we appraise following three aspects of CNM effects: 1) Nuclear shadowing, 2) Cronin effect 3) Nuclear

absorption. These CNM effects can be estimated from p+A collisions where no hot medium is expected to form.

### 2.3.1. Nuclear shadowing

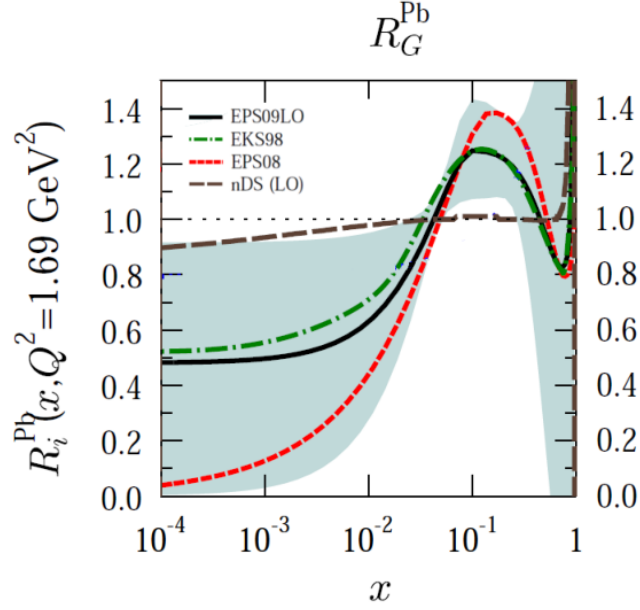


Fig. 22. Modification of gluon distribution function at  $Q^2 = 1.69 \text{ GeV}/c^2$  for Pb nucleus ( $R_G^{Pb}$ ). Figure is taken from Ref. [77].

It is a well-established fact that the partonic structure of high-energy nuclei is different from the incoherent superposition of the constituent nucleons. This modification is usually parametrised by

$$R_i^A(x, Q^2) = \frac{f_i^A(x, Q^2)}{A f_i(x, Q^2)}, \quad i = q, \bar{q}, g, \quad (2.10)$$

defined as the ratio of the parton distribution function for a nucleon inside the nucleus (nPDF),  $f_i^A(x, Q^2)$ , to the corresponding one for a free proton (PDF),  $f_i(x, Q^2)$ , where  $x$  is the longitudinal momentum fraction of the parton within the nucleon. The European Muon Collaboration (EMC) conducted experiments (deep inelastic

scattering of muons on deuteron and on iron) at CERN in 1983. The analysis showed that the self-volume of nucleon quarks is larger for nucleons of the heavier nucleus; it means quarks in nuclei move throughout a larger confinement volume and, as the uncertainty principle implies, they carry less momentum than quarks in free nucleons. As illustrated in Fig. 22, different names have been assigned to these modifications depending on the relevant range of  $x$  under consideration: 1) *Shadowing* for the suppression observed at small ( $x \lesssim 0.05$ ). 2) *Antishadowing* for the enhancement at moderate values of  $0.05 \lesssim x \lesssim 0.3$ . 3) *EMC effect* for the suppression observed in the region  $0.3 \lesssim x \lesssim 0.7$ ; and 4) *Fermi motion* for the enhancement when  $x \rightarrow 1$ . Assuming that the initially produced charm quark pair has the same rapidity as the charmonium into which they evolve, the momentum fraction of the incoming partons  $x$  is

$$x_{1,2} = \frac{m_t}{\sqrt{s_{NN}}} \exp(\pm y) , \quad (2.11)$$

with the transverse mass  $m_T = \sqrt{m_\psi^2 + p_T^2}$  of  $J/\psi$  , and  $y$  being its momentum rapidity.

### 2.3.2. Cronin effect

The Cronin effect refers to an enhancement of hadron production at intermediate and high  $p_T$  in p+A relative to p+p collisions (scaled by  $N_{\text{coll}}$ ). This effect is generally attributed to multiple soft scatterings of the projectile partons propagating through the target nucleus before the hard scattering. From the transverse kicks in the soft scatterings the partons acquire additional  $\langle p_t^2 \rangle$  and therefore the  $\langle p_t^2 \rangle$  of the finally produced charmonia increases correspondingly.

### 2.3.3. Nuclear absorption

In p+A or A+A collisions the “pre-resonance”  $c\bar{c}$  states (those  $c\bar{c}$  pairs close to each other in phase space which would form charmonium if there were no rescattering off surrounding particles, *i.e.*, in p+p collisions) are subject to dissociation through inelastic collisions with passing-by nucleons before they are fully developed into charmonia. Nuclear absorption is observed in p+A collisions at SPS, where the energy deposited is too small to create a hot medium: charmonium production is substantially suppressed relative to p+p collisions, see Fig. 23.

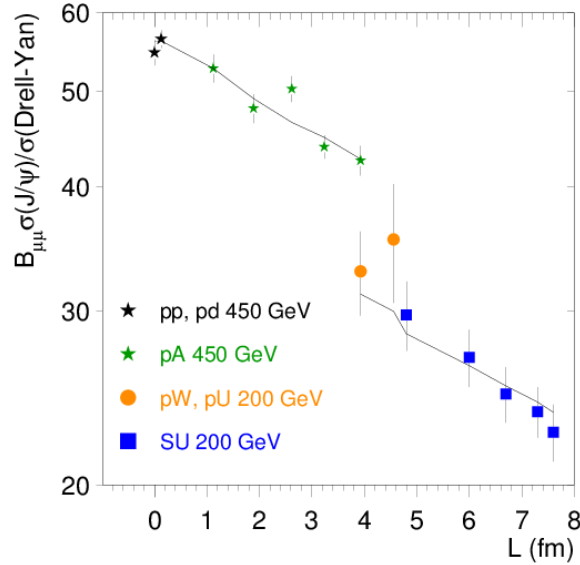


Fig. 23.  $J/\psi$   $R_{AA}$  (normalized to Drell-Yan pairs) vs.  $L$  for various p+p, p+A and S+U (Sulphur + Uranium) systems. “ $L$ ” is the effective average length travelled by (pre-) charmonium states. The figure is taken from Ref. [78].

### 2.4. Charmonium in A+A collisions

After having fixed charmonium production in p+p collisions the next step is to scale it by the number of binary nucleon-nucleon (NN) collisions,  $N_{\text{coll}}$ , to estimate char-

monium primordial production in A+A collisions, which is a standard procedure for a hard probe.  $N_{\text{coll}}$  is usually calculated with the Glauber model, which plays an important role in connecting p+p and A+A collisions. Brief review of the main results from the (optical) Glauber model are given in Appendix- A [79]. A charmonium state produced in such a collision will in its early stages always be subject to the possible effects of the nuclear medium, just as it is in p+A collisions. Knowing the p+A behaviour at the corresponding energy is thus a necessary baseline for probing the additional effects of the produced medium.

#### 2.4.1. Suppression by comover collisions

A charmonium state produced in a primary NN collision can be dissociated through interactions with the constituents of any medium subsequently formed in the collision. Such dissociation could occur in a confined [80] as well as in a deconfined medium [81]. If the charmonium state moves in a random scattering pattern through the produced medium, its survival rate is approximately given by [78]

$$S_i = \exp\{-\sigma_i n \tau_0 \ln[n/n_f]\} \quad (2.12)$$

with  $\sigma_i$  denoting the dissociation cross section,  $n$  the initial density of the medium after a formation time  $\tau_0$ , and  $n_f$  the ‘freeze-out’ density, at which the interactions stop. Since the cross section for  $J/\psi$  break-up through gluon collisions is large and the gluon density high at LHC energy, there will be significant charmonium suppression in a deconfined medium, even if this is not thermalized [81]. The traditional gluon-dissociation process ( $\Psi + g \rightarrow c + \bar{c}$ ) was proposed by Bhanot and Peskin in the 1970s [82]. This mechanism is valid only if the energy of the incoming gluon,  $E_g$  is much less the charmonium binding  $E_g \ll \epsilon_B$ . In Fig 24 (Left) we illustrate

schematically the overall behaviour expected for  $J/\psi$  dissociation through comover collisions [78].

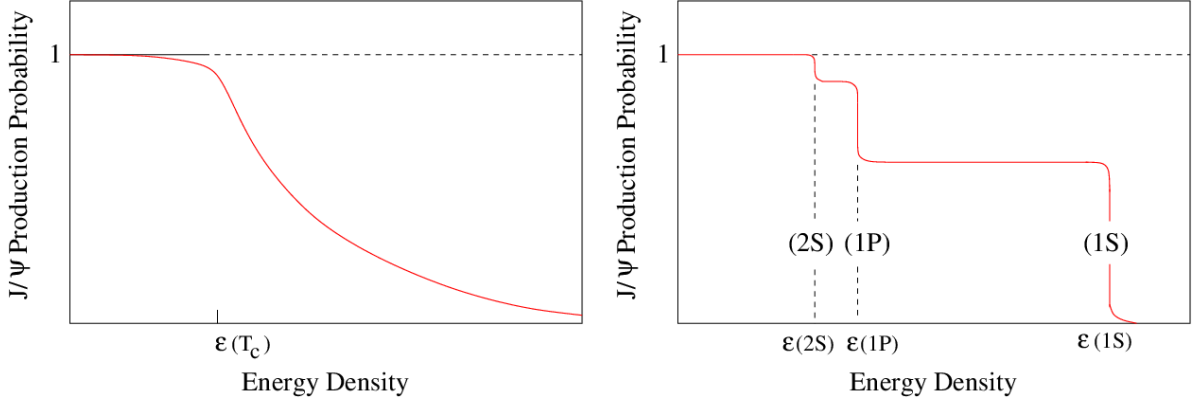


Fig. 24.  $J/\psi$  suppression by comover collisions (Left) and sequential  $J/\psi$  suppression by color screening (Right) [78].

#### 2.4.2. Suppression by color screening

As discussed in section 2.1, the colour field between the heavy quarks are modified due to the presence of a medium of unbound colour charges. A crucial consequence of  $J/\psi$  suppression by deconfinement is its sequential nature [83, 84]. In the feed-down production of  $J/\psi$ , the produced medium affects the intermediate excited states, so that with increasing temperature, first the  $J/\psi$ 's originating from  $\psi(2S)$  decay and then those from  $\chi_c$  decay should be dissociated. Only considerably higher temperatures would be able to remove the directly produced  $J/\psi$ 's. The result is a step-wise suppression pattern as function of the energy density or temperature as illustrated in Fig. 24 (Right)

### 2.4.3. Enhancement through regeneration

In a collective medium formed through superposition of many NN collisions, such as a quark-gluon plasma, a  $c$  from one NN collision can in principle also bind with a  $\bar{c}$  from another NN collision, known as recombination or coalescence. If the medium would contain sufficiently many remaining unbound pairs, and if these would become part of the thermalized plasma, then at the hadronization point, a  $c$  from one collision could statistically combine with a  $\bar{c}$  from another collision to make a  $J/\psi$  [85]. These  $c\bar{c}$  pairs are not necessarily created during the same hard scattering nor do they require any initial correlation. For such secondary  $J/\psi$  production (which scales  $N_{J/\psi} \sim N_{c\bar{c}}/N_h$  where  $N_h$  represents the number of light hadrons and  $N_{c\bar{c}}$  is the total number of produced  $c\bar{c}$  pairs), the necessary prerequisite is that there is a sufficiently large number of available charm/anticharm quarks or the nuclear collision energy has to be high enough. The prediction of such statistical combination is just the opposite of sequential suppression [85], see the Fig 25.

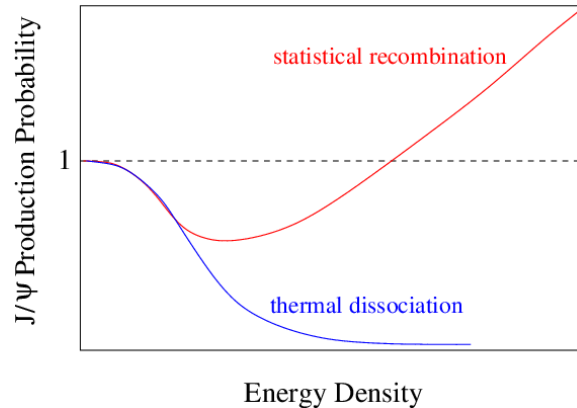


Fig. 25.  $J/\psi$  enhancement by statistical regeneration [85].

#### 2.4.4. Transverse momentum behavior

The production pattern of charmonia as function of their transverse momentum can provide information about the production process, the evolution of the resonance formation and of that of the produced medium. As discussed in subsection 2.3.2 the transverse momentum distribution of charmonia measured in p+A as well as in A+A collisions is generally broadened in comparison to that in p+p interactions. For the squared transverse momentum of the produced  $J/\psi$

$$\langle p_T^2 \rangle_{pA} = \langle p_T^2 \rangle_{pp} + N_c^A \delta_0 \quad (2.13)$$

in p+A and to

$$\langle p_T^2 \rangle_{AA} = \langle p_T^2 \rangle_{pp} + N_c^{AA} \delta_0 \quad (2.14)$$

in A+A collisions. Here  $N_c^A$  denotes the average number of collisions of a projectile parton in the target nucleus A, and  $N_c^{AA}$  the sum of the average number of collisions of a projectile parton in the target and vice versa, at the given centrality. The parameter  $\delta_0$  specifies the average “kick” which the incident parton receives in each subsequent collision.

#### 2.5. Experimental status

$J/\psi$  production has been measured at the CERN SPS in fixed target S+U (Sulphur + Uranium), Pb+Pb and In+In collisions at  $\sqrt{s_{NN}} = 20, 17.3$  and at RHIC PHENIX experiment in Au+Au collisions at  $\sqrt{s_{NN}} = 39, 62, \text{ and } 200$  GeV and in Cu+Cu collisions at  $\sqrt{s_{NN}} = 200$  GeV. Regarding the medium modification on  $J/\psi$  production, the first “anomalous”  $J/\psi$  suppression was discovered in PbPb collisions at  $\sqrt{s_{NN}} = 17.3$  GeV at the SPS, which was considered as a hint of QGP formation. The RHIC measurements in Au+Au at  $\sqrt{s_{NN}} = 200$  GeV [86] showed almost the same suppres-

sion at a much higher energy contrary to the expectation [87]. Such an observation was consistent with the scenario that at higher collision energy the expected greater suppression is compensated by regeneration of  $J/\psi$  by recombination of two independently produced charm quarks [88]. A compilation of the measured  $J/\psi$  suppression

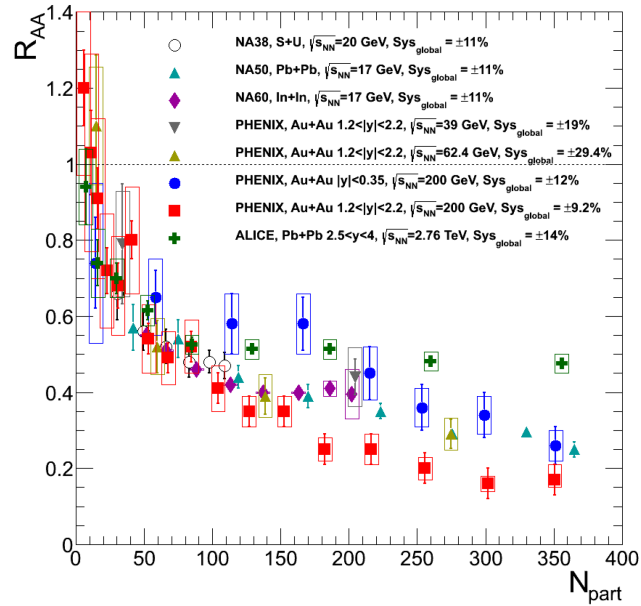


Fig. 26. Compilation of results on the  $J/\psi$   $R_{AA}$  from the SPS, RHIC and the LHC.

in A+A collisions spanning an energy range  $\sqrt{s_{NN}} = 17$  GeV–2.76 TeV is shown in Fig. 26. The evolution of the suppression with  $N_{part}$  appears to be similar at all energies out to  $N_{part} \approx 100$ , at which point the ALICE data flattens while the other energies continue to show a decreasing  $R_{AA}$  [89].

In contrast to the PHENIX result at forward rapidity at  $\sqrt{s_{NN}} = 200$  GeV ( $R_{AA} \approx 0.2$  for  $N_{part} > 250$ ), the ALICE result at forward rapidity shows a clear suppression independent of centrality (flat at  $R_{AA} \approx 0.5$ ) for  $N_{part} > 70$ . The factor of  $\sim 2$  higher  $R_{AA}$  at the higher LHC energies could be an indication of  $J/\psi$  coalescence. The measurement of the  $J/\psi$  production in LHC p+Pb collisions which should quantify the role of cold nuclear matter effects (shadowing/saturation and final state interactions),

heavy quark diffusion and recombination will allow one to sharpen the interpretation of these results.

# CHAPTER 3

## CMS experiment at LHC

### 3.1. LHC machine

The Large Hadron Collider (LHC) is the world's largest and most powerful particle accelerator. **Large** due to its size, **Hadron** because it accelerates protons or ions, which are hadrons, and **Collider** because these particles form two beams travelling in opposite directions, which collide at four interaction points where the two rings of the machine intersect. It is designed to collide proton beams at center of mass energy of 14 TeV. It has circumference of 27 *kms* and is placed in a tunnel, 175 meters under the ground near Geneva. The LHC is the final stage of a system of accelerators shown in Fig. 27- 28. Protons in the beams are taken from a bottle of hydrogen gas and first accelerated in Linac and Proton Synchrotron to 26 GeV. Then the particles are injected into Super Proton Synchrotron and accelerated to 450 GeV. The final acceleration to 7 TeV per proton beam is done in the two rings of the LHC. There are dipole magnets along the rings which bend the beams. Then the two beams are focused and brought into collision at the interaction points along the rings. The proton beams are accelerated with a radio frequency of 400 MHz. This gives rise to synchrotron oscillations which group the protons in the beams into packets. The LHC is designed for 2808 packets in a single beam with 25 *ns* separation and  $1.15 \times 10^{11}$  proton per bunch. It is expected to address some of the most fundamental questions of physics, advancing the understanding of the deepest laws of nature. The LHC project was approved by the CERN Council in December 1994. It is originally designed to provide proton-proton collisions with unprecedented luminosity  $\mathcal{L} = 10^{34} \text{ cm}^{-2}\text{s}^{-1}$  and a centre-of-mass energy of 14 TeV. In hadron machine the energy loss due to brehmsstrahlung is less. The heavy particles such as protons (protons are around 2000 times more massive than electrons) have a much lower energy loss per turn through synchrotron radiation than light particles such as electrons, which

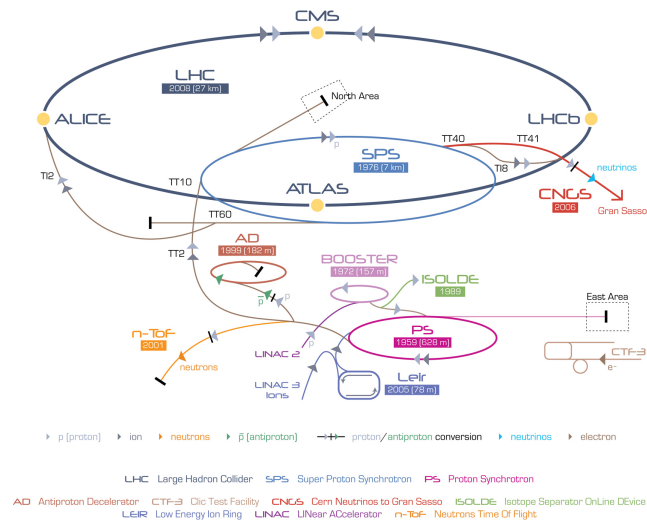


Fig. 27. LHC accelerator complex

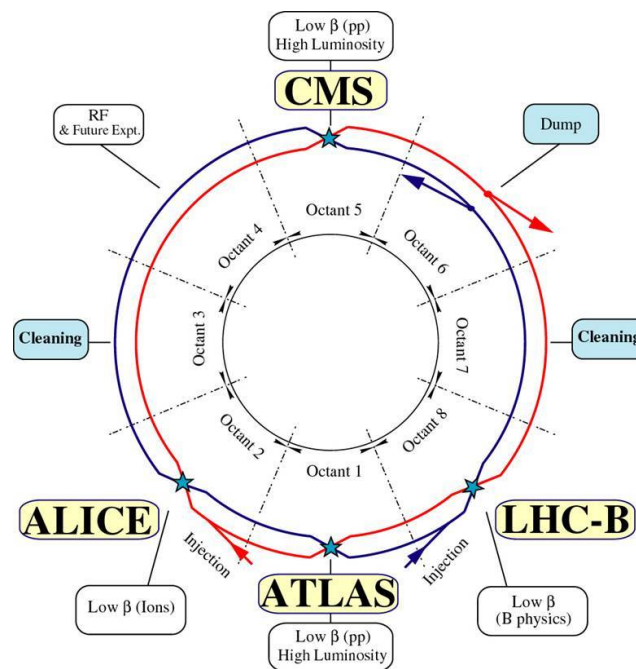


Fig. 28. LHC ring

is proportional to the fourth power of  $\mathbf{E}/\mathbf{m}$ . Compared to electrons, the energy loss is reduced by a factor of  $\langle \mathcal{O}^{12} \rangle$ . In addition to p+p operation, the LHC had heavy nuclei (Pb+Pb) collisions in 2009 and 2011 with an energy of 2.76 TeV per nucleon. The availability of high energy heavy-ion beams (14 times higher than at the present other accelerators) will allow us to further extend the range of the heavy-ion physics program to include studies of hot nuclear matter. The two LHC symmetrical rings are divided into eight octants and arcs and eight straight sections approximately 528  $m$  (Fig 28). The two high luminosity experimental insertions are located at diametrically opposite straight sections: the A Toroidal LHC Apparatus (ATLAS) experiment is located at Point 1 and the Compact Muon Solenoid (CMS) experiment at Point 5. The other two large experiments, A Large Ion Collider Experiment (ALICE) and Large Hadron Collider beauty (LHCb 3.8), are located at Point 2 and at Point 8, respectively. The remaining four straight sections do not have beam crossings. The two beams are injected into the LHC in two different octants, octant 2 and octant 8 respectively for clockwise and anticlockwise beam. The octants 3 and 7, instead, contain two collimation systems for the beam cleaning. The main parameters of the beams at collision energies are given in Table III.

### 3.2. Luminosity

The quantity that measures the ability of a particle accelerator to produce the required number of interactions is called the luminosity. The machine luminosity depends only on the beam parameters and can be written as:

$$\mathcal{L} = \frac{n \cdot f_{rev} \cdot N_1 \cdot N_2}{A_T^{eff}} \quad (3.1)$$

Table III. LHC beam parameters.

		pp	PbPb	units
Energy per nucleon	E	7000	2759	GeV
Relativistic gamma		7461	2963.5	
Number of particles per bunch	$N_p$	$1.15 \times 10^{11}$	$7 \times 10^7$	
Number of bunches	$k_B$	2808	592	
Bunch separation		25	100	ns
Pileup		16.15	0.00113	
RMS beam size		70.9	15.9	$\mu\text{m}$
Revolution frequency		11.245		kHz
Design luminosity	$\mathcal{L}$	$1 \times 10^{34}$	$1 \times 10^{27}$	$\text{cm}^{-2}\text{s}^{-1}$
Instantaneous luminosity (2011 Run)	$\mathcal{L}$	$353.5 \times 10^{31}$	$3 \times 10^{25}$	$\text{cm}^{-2}\text{s}^{-1}$

where  $A_T^{eff}$  is the effective transverse area of the proton beam,  $n$  is the number of bunches the beam is splitted to and  $f_{rev}$  is the frequency of revolution around the ring.  $N_1$  and  $N_2$  are the number of protons in each bunch. As an example, the number of particles per bunch is  $1.15 \times 10^{11}$ , the beam sizes in the two planes  $\sim 16.7 \mu\text{m}$ . With the revolution frequency of 11.245 kHz and 2808 bunches, we get for the head-on luminosity  $1.2 \times 10^{34} \text{ cm}^{-2}\text{s}^{-1}$ .

The integrated luminosity is defined as

$$\mathcal{L}_{int} = \int_0^T \mathcal{L}(t) dt \quad (3.2)$$

The integral is taken over the time period over which the data is collected. It directly relates to the number of observed events:

$$N = \mathcal{L}_{int} \times \sigma$$

where  $\sigma$  is the cross section for the collisions process under study. With respect to other high energy colliders, the design luminosity of LHC is several magnitudes larger. This is needed because LHC is designed to discover new particles at TeV scale. At these scales the interaction rates with momentum transfers more than 1 TeV are very low. Therefore more data needs to be collected which can only be achieved by having large luminosity. The LHC luminosity is not constant over physics a run, but decays due to the degradation of intensities and emittance of circulating beams. The main cause of the luminosity decay during normal LHC operation is the beam loss from collisions.

### 3.3. Compact Muon Solenoid

The Compact Muon Solenoid (CMS) (see Fig 29) is a high granularity detector built around and inside a superconducting solenoid that provides a strong magnetic field of 3.8 T. Inside it, the inner tracking comprises a Pixel detector surrounded by the Silicon Strip detector. Its high granularity (70 millions pixels, 10 millions strip) and precision ensures good track reconstruction efficiency. It is surrounded by Electromagnetic calorimeter (ECAL) made of 76000 lead tungstate crystals grouped in 36 barrel and 4 endcap super-modules. The brass-scintillator sampling hadron calorimeter (HCAL) completes the in-coil detectors. To ensure hermeticity the in-coil calorimetric system is extended, away from the central detector, by the hadron outer detector (HO) and a quartz fiber very forward calorimeter (HF) to cover  $|\eta| < 5$ . Outside the solenoid a muon system is built in the magnet steel return yoke. It is formed by 4 stations of muon chambers: Drift Tube (DT) in the barrel region, Cathode Strip Chambers (CSC) in the endcap, Resistive Plate Chamber (RPC) in both parts, providing muon detection redundancy.

Two trigger levels are employed in CMS. The Level-1 Trigger (L1) is implemented using custom hardware processors and is designed to reduce the event rate to 100 kHz during LHC operation using information from the calorimeters and the muon detectors. It operates nearly dead time-free and synchronously with the LHC bunch crossing frequency of 40 MHz. The High Level Trigger (HLT) is implemented across a large cluster of commodity computers referred to as the event filter farm, and provides further rate reduction to  $\mathcal{O}(100)$  Hz using filtering software applied to data from all detectors at full granularity. The overall dimension of CMS are a length of 21.6 *m*, a diameter of 14.6 *m* and a total weight of 12500 tons.

A slice of the transverse view of the CMS detector is shown in Figure 30. The principle of detection of charged and neutral particles in the various sub-detectors is shown. All charged particles leave signals in the inner tracking system. Electrons and photons deposit their energy in the electromagnetic calorimeter. Charged Hadrons ( $K^\pm$ ,  $\pi^\pm$  ...) and neutrons deposit their energy in the hadronic calorimeter. Muon is a particle which passes through calorimeters losing only small energy, but which leaves a track of its passage in the muon chambers. Neutrinos, barely interacting, will escape from all direct detections. While adding the transverse momenta of all the particles detected by the detector, one can determine the imbalance of energy in the transverse plane, so called the missing transverse energy. The coordinate system of CMS has its origin inside the detector at the primary interaction point. The x-axis points radially towards the center of the LHC, whereas the y-axis points vertically upward. Thus, the z-axis shares the same direction with the beam line. The azimuthal angle  $\phi$  is measured from the x-axis in the xy plane whereas the polar angle  $\theta$  is measured from the z-axis. Particle physicists often use a Lorentz invariant

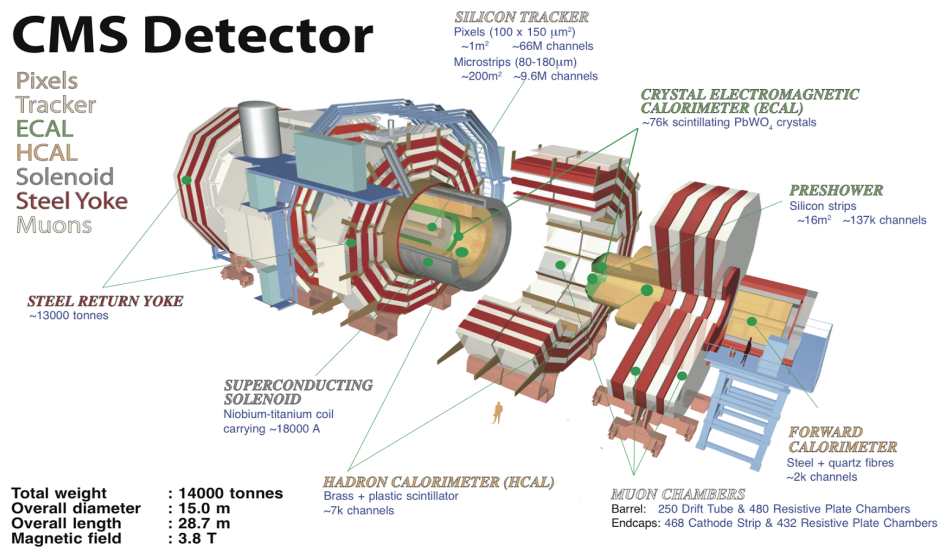


Fig. 29. CMS detector figure

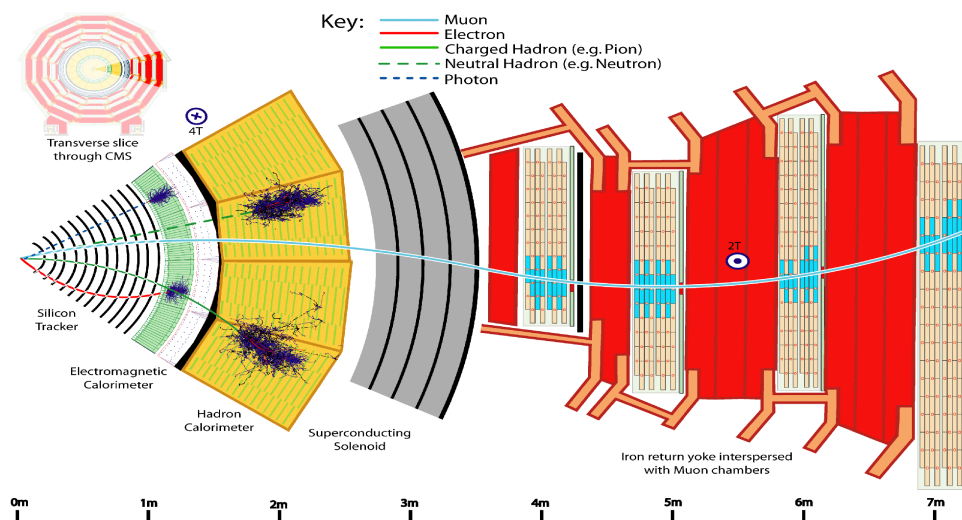


Fig. 30. CMS detector figure slice

quantity called rapidity  $y$  instead of  $\theta$ . It is defined as:

$$y = \frac{1}{2} \ln \frac{E + p_z}{E - p_z} = \tanh^{-1} \frac{p_z}{E} \quad (3.3)$$

and equals, in case of mass-less particles, the pseudo-rapidity  $\eta$  given by

$$\eta = -\ln[\tan(\theta/2)] \quad (3.4)$$

The angular distance between two particles observed from the origin of the coordinate system is

$$\Delta R = \sqrt{\Delta\phi^2 + \Delta\eta^2} \quad (3.5)$$

Measurable quantities like momentum and energy transverse to the beam line are denoted by  $p_T$  and  $E_T$ , respectively, and can be derived from its x and y components.

### 3.3.1. Magnet

The superconducting solenoid magnet reaches a maximum magnetic field of 3.8  $T$  in the positive  $z$  direction in the inner detectors. A high magnetic field provides a large bending power in the transverse plane for charged particles, which makes possible to reach precise measurement of muon momenta. The magnet is 12.5  $m$  long and with an inner radius of 6  $m$  and is made of four-layers of NbTi. It is the largest superconducting magnet ever built, with the capacity to store an energy of 2.6 GJ at full current. The magnetic flux is returned via a 1.5  $m$  thick iron yoke instrumented with four stations of muon chambers. In this part of the detector the magnetic field is saturated at 2  $T$ . Figure 31 shows artistic view of CMS magnet, a humanoid is also present on figure to highlight the huge size of magnet.

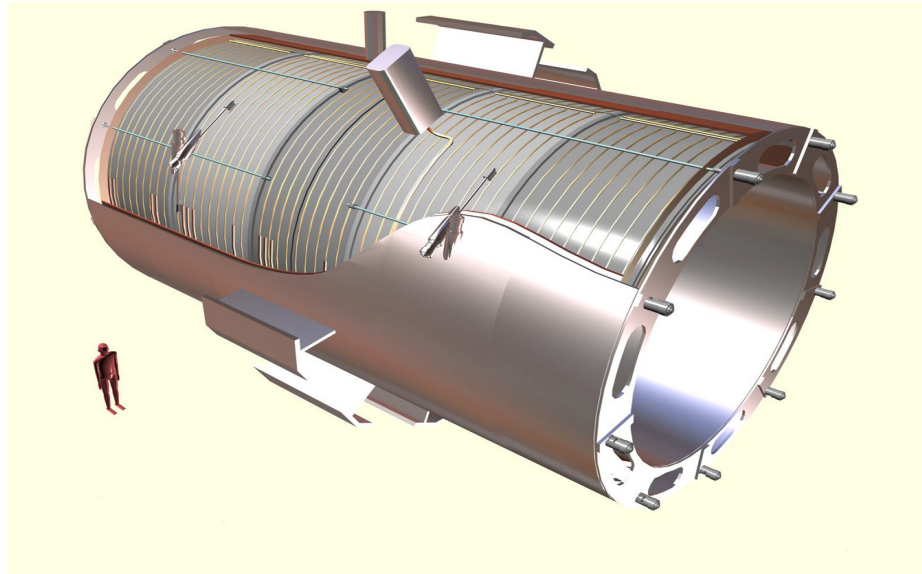


Fig. 31. CMS Magnet

### 3.3.2. Tracker

The Tracker is the sub-detector system which is closest to the interaction point, a general layout is presented in Figure 32. It is designed to provide an efficient measurement of the trajectories of charged particles emerging from the LHC collisions, as well as a precise reconstruction of secondary vertices. The CMS Tracking System is composed of silicon pixel detector close to the interaction region and a strip detector covering radii from  $0.2\text{ m}$  to  $1.1\text{ m}$ . The Pixel Detector consists of 1440 pixel modules arranged in three barrel layers and two disks in each end-cap. The barrel layers are located at radii of  $4.4$ ,  $7.3$  and  $10.2\text{ cm}$  around the interaction point with a length of  $53\text{ cm}$ . On each side of the barrel, two discs are placed at  $|z| = 32.5\text{ cm}$  and  $46.5\text{ cm}$ .

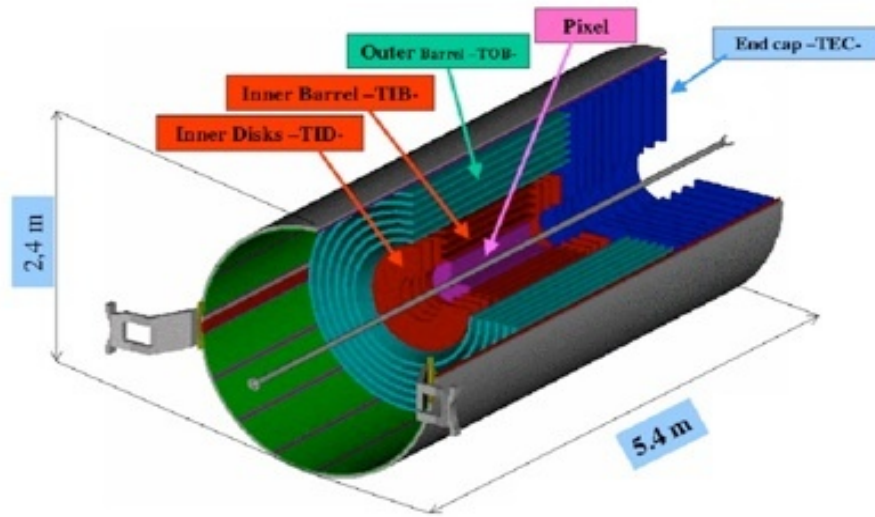


Fig. 32. CMS Tracker

### 3.3.3. Calorimetry

#### ECAL

The electromagnetic calorimeter (ECAL) is used to measure the energy of photons and electrons. The ECAL is a high precision scintillating crystal calorimeter. The structure of the ECAL can be seen in Figure 33. It is composed of 61,200 lead tungstate ( $\text{PbWO}_4$ ) crystals in the barrel region and 7,324 crystals in the endcaps. The choice of that material is motivated by its fast response and high radiation resistance and its very good resolution. In front of each ECAL Endcap is a preshower detector (ES), from  $1.65 \leq |\eta| \leq 2.6$  made from silicon strip detectors in order to identify neutral pions ( $\pi^0$ ). The nominal energy resolution, measured with electron beams having momenta between 20 and 250 GeV, is:

$$\frac{\sigma_E}{E} = \left(\frac{S}{\sqrt{E}}\right)^2 + \left(\frac{N}{E}\right)^2 + C^2. \quad (3.6)$$

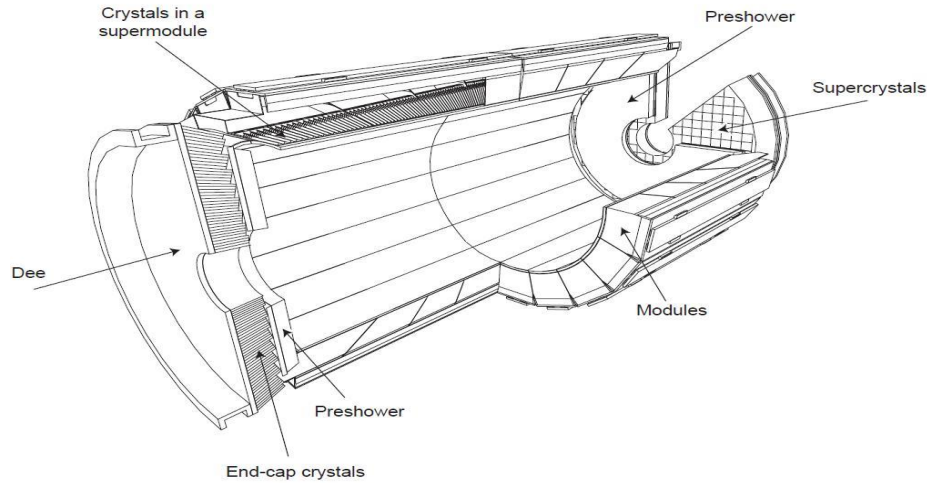


Fig. 33. CMS ECAL detector

where  $S$  is the stochastic term, which includes fluctuations in the shower containment as well as a contribution from photo-statistics,  $N$  is the noise term, which accounts for the electronic, digitization, and pileup noise, and  $C$  is the constant term, which comes from the light collection non-uniformity, errors on the inter-calibration among the modules, and the energy leakage from the back of the crystal.

## HCAL

The hadronic calorimeter (HCAL) is designed to measure the energy of hadrons. The HCAL is comprised of four subsystems: the HCAL Barrel (HB), the outer calorimeter (HO), the HCAL Endcap (HE), and the forward calorimeter (HF). Figure 34 gives a schematic overview on the HCAL sub-detector. The HB is a sampling calorimeter that covers the range  $|\eta| < 1.3$ . It consists of 36 identical azimuthal wedges aligned parallel to the beam-line. It is located between the ECAL and the solenoid coil and is supplemented by the HO located between the solenoid and the muon chambers. The HO is designed to absorb the remnant of the hadronic shower which has not

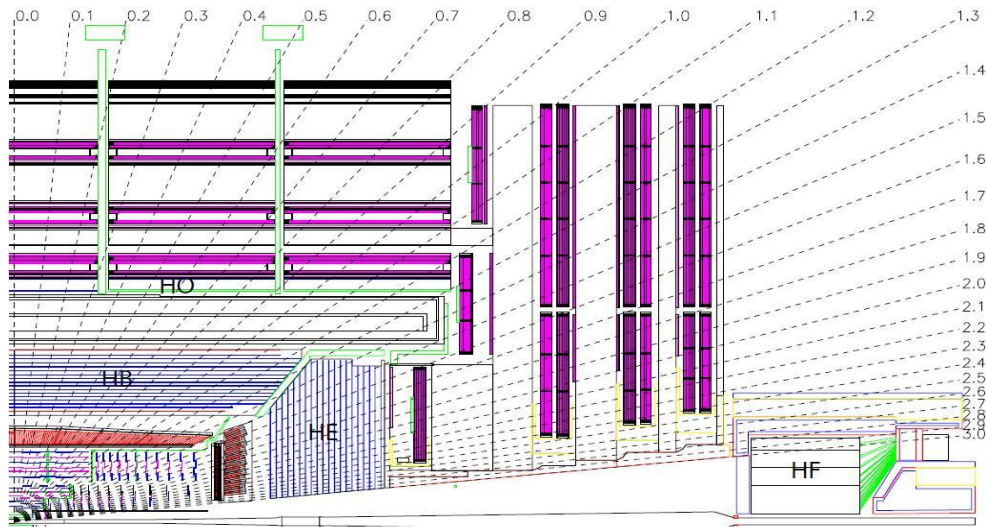


Fig. 34. CMS HCAL detector

been fully absorbed in the HB. The HE covers a large portion of the solid angle,  $1.3 < |\eta| < 3$ . Beyond that region, the HF placed at  $11.2 \text{ m}$  from the interaction point extends the pseudo-rapidity coverage up to  $|\eta| < 5.2$ . The HE must have high radiation tolerance, with  $10 \text{ Mrad}$  expected after 10 years of operation. The reason for the absorber material to be non-magnetic is that it must not affect the magnetic field. The HF experiences the harshest radiation environment and therefore requires an extremely radiation tolerant material. The active material chosen is quartz fibers. The fibers are mounted in grooves in the steel absorber plates. The inner part of the HF will be exposed to close to  $100 \text{ Mrad/year}$ . As the absorber will become radioactive the entire HF can be moved into a garage to limit exposure of personnel during maintenance periods.

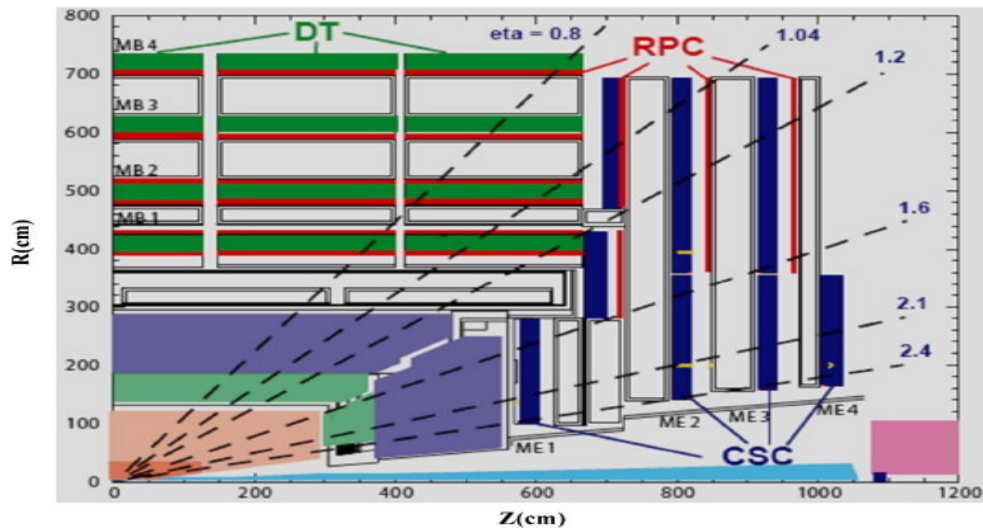


Fig. 35. CMS Muon system

### 3.3.4. CMS muon system

One of the main design objectives of the CMS detector was to obtain a high precision muon momentum measurement, for its key role both in new physics searches and in Standard Model measurements. The CMS muon system uses three different types of gaseous detectors to detect muons. In the barrel region, Drift Tubes (DTs) and Resistive Plate Chambers (RPCs) are used, while in the endcap there are Cathode Strip Chambers (CSCs) and also RPCs. The layout of the CMS muon system is shown in Figure 35.

#### Drift Tubes

In the central region of CMS,  $|\eta| < 1.2$ , the muon system consists of four concentric cylinders containing 250 gas drift chambers. Each Drift Tube is filled with a mix of 85% Argon and 15%  $\text{CO}_2$  with active wires for charge collection. As muons pass through the gas they leave an ionization trail. The charge drifts to the wires, which

detect the charge. The size of the drift cell was chosen so the maximum drift time is 380 *ns*. There are 172000 active wires in the entire system. The use of DTs is only possible in this region due its low magnetic field.

### **Cathode Strip Chambers**

In the endcap, the muon system is comprised of Cathode Strip Chambers (CSC). The CSC's cover the  $0.9 < |\eta| < 2.4$  pseudo-rapidity range. Each CSC is trapezoidal in shape and consists of 6 gas gaps, each gap having a plane of radial cathode strips and a plane of anode wires running almost perpendicularly to the strips. The CSC is a fast detector (response time of 4.5 *ns*), but with rather coarse position resolution; a precise position measurement is made by determining the centre-of-gravity of the charge distribution induced on the cathode strips (spatial resolution 200  $\mu\text{m}$ , angular resolution 10 mrad).

### **Resistive Plate Chambers**

In order to improve muon trigger system and for a good measurement of the bunch crossing time, resistive plate chambers (RPC) are mounted in the barrel and endcap region ( $|\eta| < 1.6$ ). The RPCs are able to provide independent and fast trigger with high segmentation and sharp  $p_T$  threshold over a large portion of the pseudo-rapidity range. However, the RPCs have coarser position resolution making them more useful for the trigger

## **3.4. Centrality determination**

In studies with heavy ions, it is important to determine the degree of overlap of the two colliding nuclei, the so-called centrality of the interaction. In Compact Muon Solenoid experiment the centrality is estimated using the sum of transverse energy deposited in towers from both forward calorimeter (HF) at positive and negative  $z$

positions. The distribution of the total transverse energy, after the trigger efficiency and the Ultra Peripheral Collision (UPC) corrections, was used to divide the event sample into bins, each representing 5% of the total nucleus-nucleus interaction cross section. The bin corresponding to the most central events (i.e. smallest impact parameter) is the 0-5% bin, the next one is 5-10% and so on. The distribution of the HF signal, along with the cuts used to define the various event classes, is shown in Fig. 36. The UPC are concentrated in the two most-peripheral bins. To avoid them completely, only the 0-90% bins are used for the measurements as reported in [23]. The centrality binning using equal fractions of the total interaction cross section can

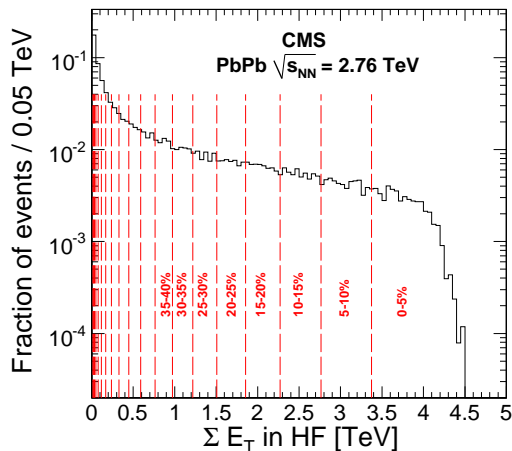


Fig. 36. Distribution of the total transverse energy in the HF used to determine the centrality of the PbPb interactions. The centrality boundaries for each 5% centrality interval are shown by the dashed lines.

be correlated with more detailed properties of the collision. The quantity of interest for the measurement is the total number of nucleons in the two Pb nuclei that experienced at least one inelastic collision,  $N_{\text{part}}$ . The average values of  $N_{\text{part}}$  for the various centrality bins (from most-central to most-peripheral), together with their un-

certainties, are given in Table IV. The  $N_{\text{part}}$  values were obtained using a Glauber MC simulation [90, 91] with the same parameters as in Ref. [40]. These calculations were translated into reconstructed centrality bins using correlation functions between  $N_{\text{part}}$  and the measured total transverse energy, obtained from AMPT simulated events [92]. Different Glauber MC samples were produced varying the Glauber parameters within the uncertainties from Refs. [93]. The variation in the final results is quoted as the uncertainty in  $N_{\text{part}}$ . The AMPT model is a hybrid model that includes four main stages of high-energy heavy-ion collisions: the initial condition, parton cascade, hadronization, and hadronic rescatterings. The initial condition, which includes the spatial and momentum distributions of minijet partons and soft string excitations, is obtained from HIJING model. Then the strings are melted into quarks, and thus a quark and antiquark plasma are formed and start to evolve. The parton cascade process is simulated by Zhang’s parton cascade (ZPC) model, where the partonic cross section is an elastic cross section controlled by the value of strong-coupling constant and the Debye screening mass. The AMPT model recombines partons via a simple coalescence model to produce hadrons when the partons freeze out. The dynamics of the subsequent hadronic rescatterings is then described by a relativistic transport (ART) model.

### 3.4.1. Trigger and Data acquisition

The CMS trigger system is designed to cope with an unprecedented high luminosity and interactions rates. The LHC will collide proton bunches at a rate of 40 MHz which leads to  $10^9$  interactions per second at design luminosity. Since it is not possible to record events at this rate, a two-part trigger system, consisting of a hardware-based trigger (Level 1) and a software-based trigger (High Level Trigger) is used. The rate is then reduced by a factor of  $10^6$ .

Table IV. Average  $N_{\text{part}}$  values and their uncertainties for each PbPb centrality range defined in 5 percentile segments of the total inelastic cross section. The values were obtained using a Glauber MC simulation with the same parameters as in Ref. [40].

Cent	0–5%	5–10%	10–15%	15–20%	20–25%	25–30%
$N_{\text{part}}$	$381 \pm 2$	$329 \pm 3$	$283 \pm 3$	$240 \pm 3$	$203 \pm 3$	$171 \pm 3$
Cent	30–35%	35–40%	40–45%	45–50%	50–55%	55–60%
$N_{\text{part}}$	$142 \pm 3$	$117 \pm 3$	$95.8 \pm 3.0$	$76.8 \pm 2.7$	$60.4 \pm 2.7$	$46.7 \pm 2.3$
Cent	60–65%	65–70%	70–75%	75–80%	80–85%	85–90%
$N_{\text{part}}$	$35.3 \pm 2.0$	$25.8 \pm 1.6$	$18.5 \pm 1.2$	$12.8 \pm 0.9$	$8.64 \pm 0.56$	$5.71 \pm 0.24$

### Level 1 Trigger

The Level 1 (L1) trigger is designed to achieve a maximum output rate of 100 kHz and consists of custom-designed, programmable electronics. The front-end (FE) electronics can store information from up to 128 consecutive events, which equates to 3  $\mu\text{s}$ . To cope with the time limitation, the L1 trigger system uses only coarsely segmented data from the muon system and the calorimeters while the full granularity data are stored in the FE electronics waiting for the L1 decision. The L1 muon trigger is organized into subsystems representing the three different muon detectors: the DT trigger in the barrel, the CSC trigger in the endcap and the RPC trigger covering both barrel and endcap. The Level-1 muon trigger also has the Global Muon Trigger (GMT) that combines the trigger information from the DT, CSC, and RPC muon subsystems, as well as from the calorimeter subsystem, and sends it to the Level-1 Global Trigger.

### High Level Trigger

The High Level Trigger (HLT) exploits the full amount of collected data for each

bunch crossing accepted by Level 1 Trigger and is capable of complex calculations such as the offline ones. It is structured in two levels, Level 2 (L2) and Level 3 (L3) implemented in software. The L2 uses information from the muon spectrometer (parameters from the L1 muon candidates converted into seeds) to perform a standalone reconstruction, providing a muon  $p_T$  measurement with a precision of about 15%. The L2 reconstruction follows closely the offline standalone reconstruction using Kalman-filter techniques. The L3 takes L2 candidates as seeds and adds information from the inner tracker by performing track reconstruction in the silicon tracker. This reconstruction is regional, it performs pattern recognition and track fitting only in a small  $\eta - \phi$  slice of the tracker, to keep execution time low. Trajectories are then reconstructed using Kalman-filter techniques. Level 3 provides a much more precise  $p_T$  measurement (1% - 2% in the barrel region) than Level 2, as well as the ability to select on the basis of the track impact parameter with respect to the beam spot. After the HLT decisions, the event rate decreases down to  $\sim 150$ Hz for mass storage which corresponds to a data rate of 150 Mbyte/s. A summary of trigger rate for 2011 PbPb run is given in Appendix-C.

### 3.4.2. CMS data flow

Raw data that passed HLT and CMS Online Data Acquisition system (system which collects data from different detectors and builds events) is stored at a storage facility at CERN, known as Tier-0. The raw data contains information for every single proton-proton collision which passed HLT and it is called an event. There are about  $10^9$  events ( $10^7$  seconds  $\times$  150 Hz) per year stored at Tier-0 [94]. Standard CMS algorithms perform calibration and alignment of the detector using raw data and do prompt (first) reconstruction of physics objects like muons, electrons, jets etc. Later, their momenta, energies and trajectories are measured and this is done by using all

detectors of CMS experiment. The output data from prompt reconstruction is saved in different primary datasets based on trigger information. The data from Tier-0 is transferred to Tier-1 storage facilities worldwide where further calibration and re-reconstruction is performed centrally to be used by all CMS analyzes. The Tier-2 centers are more numerous and they are based at different universities in the world. They have limited disk space and are used for running individual analysis and Monte Carlo simulations. Data is stored in three types of root files which contain information about raw, reconstructed and analysis object data, respectively RAW, RECO and AOD root files. The RAW root files contain information about the recorded event in raw format as hits, energy deposits in the detector etc. The RECO root files contain detailed information of reconstructed physics objects and the AOD root files are simplified version of the RECO files which are mostly used in the analyses. Tier-0, Tier-1 and Tier-2 centers form a GRID based computer infrastructure in 35 countries.

# CHAPTER 4

## Data Selection

#### 4.1. Introduction

The CMS apparatus has various ways to trigger on PbPb collisions. The expected cross section for hadronic inelastic collisions is 7.65 barns, while ultra-peripheral collisions (UPC) with large impact parameters lead to the breakup of one, or both, Pb nuclei with a much larger probability (more than 200 barns for one or more neutrons in one ZDC (Zero Degree Calorimeter) and the cross section for ZDC coincidences is almost twice the hadronic interaction rate). Collisions in which the Pb nuclei interact hadronically can produce anywhere from just a few up to about 1600 particles per unit pseudo-rapidity, depending on the impact parameter. As a result, more than 97% of these collisions produce double-sided (coincidence) trigger signals in the BSC (Beam Scintillator Counters), and in the HF calorimeters. In addition, most of them are also detected by coincidences in the ZDC and in the BRAN scintillators (with scintillators placed behind the ZDC electromagnetic section), a plastic scintillator added in front of the BRAN detectors. The BRAN (Beam RATE of Neutrals) detector is a fast ionization chamber designed to measure the relative luminosity of the LHC at the interaction points. About 75% of the hadronic collisions also fire the BSC High Multiplicity trigger. In order to suppress non-collision related noise, cosmics, radioactivity, trigger afterglow and beam background, all of these triggers were protected by the BPTX coincidence, i.e. two colliding ion bunches were required to be present in coincidence with each of these triggers. The collision rate was 1-1.85 Hz per colliding bunch pair during the PbPb data taking period. Therefore (taking into account the 11245 Hz orbit frequency) the average number of collisions per bunch crossing was  $0.9-1.6 \times 10^4$ . In contrast to nuclear interactions, UPC collisions were found to be unable to activate the HF and BSC coincidence triggers. However, they contribute significantly to coincidence and singles triggers in the ZDC and in the BRAN scintil-

lators. The additional trigger rate for these coincidence triggers from UPC collisions is comparable to that from hadronic collisions, while the single sided rates (which have very low or no noise) are more than an order of magnitude higher than the hadronic collision rate. For these reasons, the BSC and HF coincidence triggers are used to select hadronic PbPb collisions. These triggers have low noise (fake) rate (less than 1 Hz with two non-colliding beams at full intensity with 121 bunches), but very high efficiency (about 97% [95] even after an additional reconstructed vertex requirement).

## 4.2. Definition of Minimum bias collisions

### 4.2.1. The minimum bias trigger

Two heavy ion (Pb+Pb) runs were held at LHC after its functioning in 2009; first one in 2010 and second in 2011. The PbPb data used for physics analysis were collected during these Runs. Hadronic PbPb collisions were selected using information from the two Beam Scintillator Counters (BSC) and Forward Hadronic calorimeters (HF), in coincidence with a bunch crossing identified by the BPTX. Two trigger combinations were used, which gave a low noise (fake) rate and very high efficiency ( $97 \pm 3\%$ ):

- The BSC coincidence “threshold 1”, which requires at least one segment firing on each side of the interaction point, associated with a coincidence with the BPTX. This trigger is the bit “L1 Algorithm 4”, named “L1\_BscMinBiasThreshold1\_BptxAND”.
- “L1 Algorithm 12”, named “L1\_HcalHfCoincPmORBscMinBiasThresh1\_BptxAND”, which is the Level-1 OR combination of the above L1\_BscMinBiasThreshold1\_BptxAND and of the “L1 Algorithm 94” named “L1\_HcalHfCoincidencePm\_BptxAND”. The

latter trigger bit is based on the HF, and requires at least two HF towers to have energies deposited that exceed the threshold set by the firmware, and a coincidence with the BPTX.

The minimum bias trigger was unrescaled at the Level-1 (L1) before reaching about 60 Hz collision rate. Then it was prescaled by 2 or 3, depending on the collision rate, to fit into the 150 Hz total High Level Trigger (HLT) physics trigger limitation. The HLT passed those minimum-bias events to the *AllPhysics* data stream, while to the *CorePhysics* data stream has those events further prescaled by a factor of 10, together with hard probe triggers like dimuons or jets.

#### 4.2.2. Offline event selection and cleaning

In order to clean the minimum bias events from background, beam gas, PKAM (Previously Known As Monsters) and UPC events, a few more cuts have been applied to select events off-line. These cleaning cuts have only a small effect on the number of selected events.

1. BSC halo-filter: events in which any of the BSC halo bits fired (L1 Technical Trigger bits 36, 37, 38 or 39) were excluded from the analysis. This happened only at the 0.01 % level, thus any possible biases are negligible. Fig. 37 shows a correlation between the number of hits in the first pixel layer, and the total HF energy. Collisions (black) have a very tight correlation between the two quantities. However, events that fire the BSC beam halo bits have very small HF energy and quite a large number of pixel hits. These are excluded from the analysis.
2. The requirement of a reconstructed primary vertex with two or more tracks was imposed. In peripheral events, all tracks above 75 MeV/ $c$  transverse

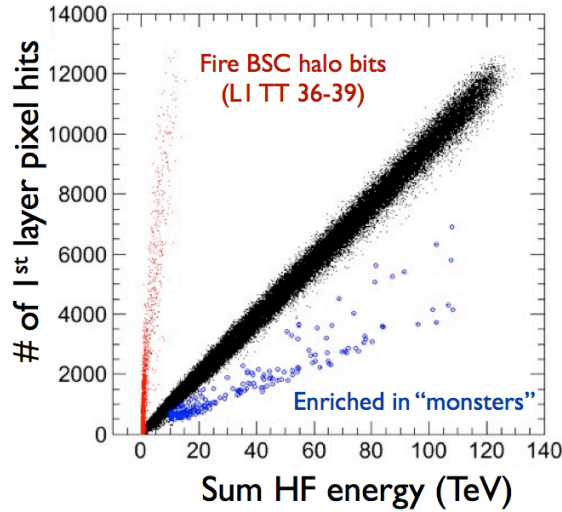


Fig. 37. Correlation between the number of pixel hits and the total energy deposited by the HF. Good collisions have a tight correlation, while events firing the BSC halo bits and events which have PKAM features are off-diagonal.

momentum were used to reconstruct the vertex. In central events, the minimum  $p_T$  cut was increased to  $700 \text{ MeV}/c$ , and the tracking region was narrowed down, to keep the maximum number of fitted tracks stable around 40–60, ensuring time-efficient reconstruction.

3. To remove PKAM events, we required that the pixel cluster-length is compatible (see below) with the vertex. Fig. 37 illustrates background events (blue) where the HF energy deposits are much smaller (at any given number of pixel hits value) than for normal PbPb collisions. Those events are mostly eliminated by the compatibility cut; some, but not most of them, could be removed by the BSC beam halo filter alone; but they are all eliminated by the combination of these two cuts. Fig. 38 shows the cluster-vertex compatibility as a function of pixel hit multiplicity. The compatibility variable is the number of clusters that

have a length (in global  $z$  direction) that is compatible with the reconstructed vertex, divided by the number of hits that are compatible with an artificially displaced vertex position (that is offset by  $\pm 10$  cm). If this ratio is high, that indicates a well defined vertex and good collision. If the ratio is about unity, that indicates that the vertex is ill-defined; a characteristic feature of PKAM events. The right panel is the same as the left panel, but zoomed in to the low pixel multiplicity region.

4. An additional off-line HF coincidence, requiring at least 3 towers on each side of the interaction point in the HF with at least 3 GeV energy deposited per tower in order to remove UPC events.

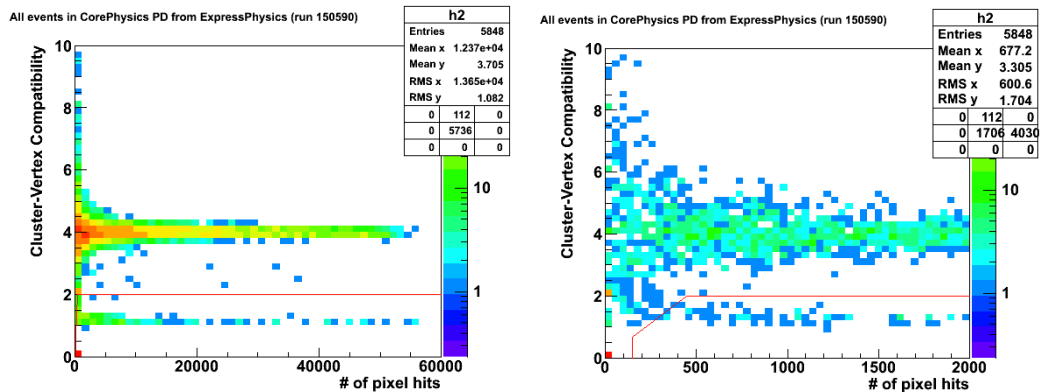


Fig. 38. The so called “monster” (or PKAM) cut. Events with large number of pixel hits (horizontal axis) but a small degree of compatibility between the vertex position and the cluster lengths (vertical axis) are eliminated from the analysis (i.e. those events that fall below the cut shown by the red line). The right panel is a zoomed version of the left panel.

To compute the number of good events, we counted the number of events in the *All-Physics* stream that passed the quality cuts defined above, triggered by the active

minimum bias trigger and multiplied the numbers by the corresponding prescale factors. The effect of each cut is summarized in Table V. Thus the data sample used

Table V. Minimum bias event counts, and reduction due to various good event quality cuts. % values are always with respect to the first line (the cuts are applied in sequence).

Cut	events remaining	% of events
All Physics	68 447 547	100.00
MB Triggers	32 017 452	46.78
Monsters	31 663 573	46.26
HF offline coincidence	30 613 653	44.73
Vertex	29 951 836	43.76
× prescales	1.8	
Final number of events	54 024 821	

(*e.g.* with 2010 Run) corresponds to a sampled number of minimum bias events of:

$$N_{MB} = 54\,024\,821 / \varepsilon_{MB} = 55\,695\,692 \quad (4.1)$$

where  $\varepsilon_{MB} = 97 \pm 3\%$  is the minimum bias trigger efficiency [95]. Assuming an inelastic PbPb cross-section of  $\sigma_{PbPb} = 7.65$  b, this sample corresponds to an integrated luminosity of  $\mathcal{L} = 7.28 \mu\text{b}^{-1}$ .

### 4.3. The Double muon trigger

As not all minimum bias collisions could be recorded (only about half of them), Level-1 and HLT double muon trigger have been employed to select interesting events for

the dilepton analyses. In addition a series of single muon trigger have been used in order to measure the double muon trigger efficiency.

With 2010 Run data the analysis was performed on the *AllPhysics* dataset, which includes an unrescaled, very loose double muon trigger, named HLT\_HIL1DoubleMuOpen. It is based solely on L1 decisions and requires the presence of two L1 muon objects without any constrain on their momenta and the coincidence of the BPTX trigger. This double muon trigger is adapted to quarkonia as it is loose in  $p_T$  and selects dimuons. Events for the analysis were selected from the set of HLT\_HIL1DoubleMuOpen triggered events. To select events which fulfill the definition of a minimum bias collision the OR of the following two L1 triggers has been required in addition

- coincidence of two BSC triggers: L1\_BscMinBiasThreshold1 (L1a36)
- coincidence of two HF triggers: L1\_HcalHfCoincidencePm (L1a44)

Similarly HLT double and single muon triggers have been employed during the 2011 PbPb Run to select events for the dimuon analyses.

Figure 39 summarizes the minimum bias centrality distribution in black and how the double muon triggered events are more peaked in central events, in red. The details on the centrality definition and calculation are described in CMS Analysis Note 2010-412 [95]. The minimum bias trigger efficiency is very high, and the 3% loss arises in the peripheral bin. The fraction of double muon triggered events from the minimum bias events in the most central bin is only 1.6%. Events triggered by double muon triggers are biased towards central collisions.

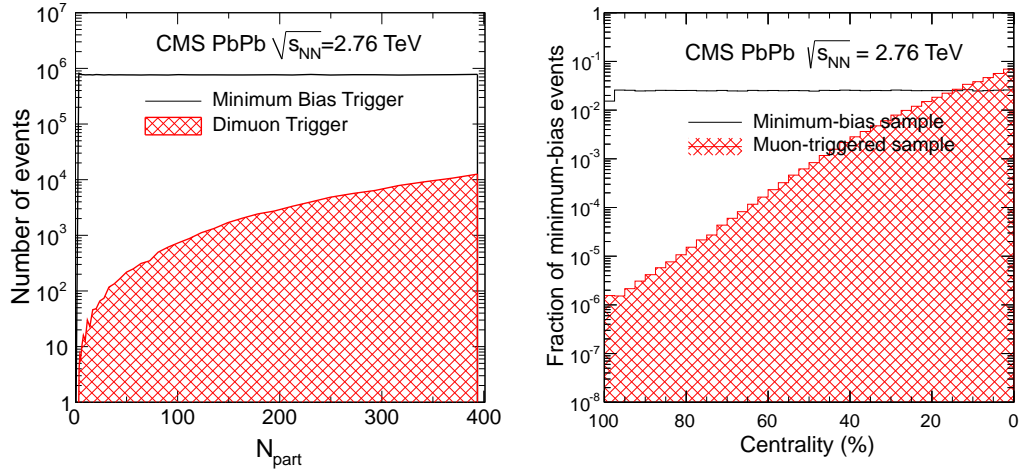


Fig. 39. Event centrality distribution of the minimum bias events is compared to events selected by the double-muon trigger. Only events selected by HLT\_L1DoubleMuOpen with 2010 Run (Left) and by HLT\_HIL1DoubleMu0\_HighQ\_v1 with 2011 Run (Right).

#### 4.4. Muon skim

To allow faster processing of the data, a secondary dataset, the “OniaSkim”, has been produced from the prompt-reconstructed HIDiMuon dataset, based on the good collision event selection and requiring with an invariant mass of at least  $2 \text{ GeV}/c^2$  and quality criteria on both single and pair muon. The secondary dataset contains 11 548 009 events in certified lumi sections. Lumi section is sub-section of a run during which time the instantaneous luminosity is unchanging. Production data files will contain one or many whole lumi sections. Data are certified as good for physics analysis if all subdetectors, trigger and physics object (tracking, electron, muon, gamma, jet and MET) show an expected performance. The output was an “edm” file which contained all information necessary for the further analysis, i.e. collections of single muons, muon pairs, L1 and HLT information, primary vertices, and centrality, tracks

and event plane. It is referred as the Onia2MuMu\_skim.

#### 4.5. Data selection: 2011 PbPb run

The PbPb analysis starts from the dataset /HIDiMuon/HIRun2011-PromptReco-v1/RECO. This primary dataset was skimmed for the presence of two global muons. Only officially certified luminosity sections in the run number range 181530-183126 were considered. Furthermore the standard good event selection has been applied that requires a reconstructed primary vertex formed by at least two tracks and a coincidence with the minimum bias trigger. Default beam halo and PKAM event filters have been applied and a detailed description can be found in CMS Analysis Note AN-11-496 [96]. The muon triggered PbPb sample is equivalent to 1126 653 312 minimum bias events. Assuming an inelastic PbPb cross section of  $= 7.65 \text{ b}$  and correcting for the 97% minimum bias trigger efficiency, this corresponds to an integrated luminosity of  $\mathcal{L} = 152 \mu\text{b}^{-1}$ . The lumi-Calc tool reports an integrated luminosity of  $\mathcal{L} = 150 \mu\text{b}^{-1}$  based on a Van-der-Meer scan. The Fig. 40, gives a graphical representation of luminosity delivered/recorded during the beam run in the year 2010 and 2011 shows that delivered luminosity is  $166.7 \mu\text{b}^{-1}$  and corresponding recorded luminosity is  $157.6 \mu\text{b}^{-1}$ . For the analysis (to be discussed in following chapters), only events triggered by HLT\_HIL1DoubleMu0\_HighQ were selected. This trigger was unpre-scaled during the whole run. It is based solely on L1 decisions and requires the presence of two L1 muon objects with quality  $> 4$ , without any constraint on their momenta, but with the requirement of coincidence with the BPTX trigger.

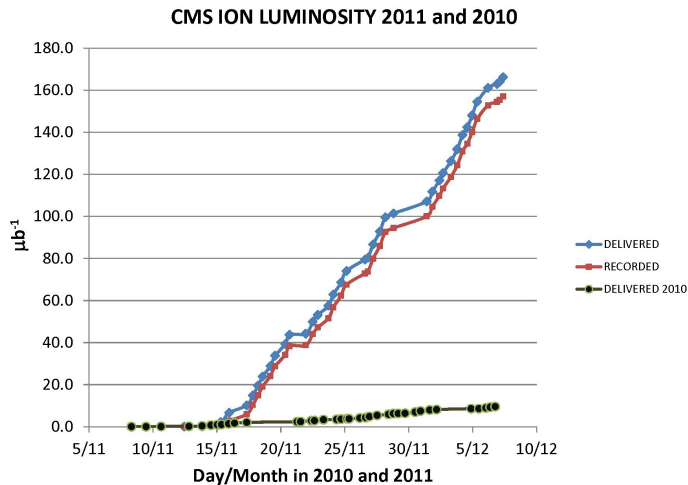


Fig. 40. CMS Integrated Luminosity, PbPb 2010 and 2011 Run,  $\sqrt{s_{NN}} = 2.76$  TeV.

#### 4.6. Muon quality selection

The data analysis starts with the Onia2MuMu skim which contains all pairs of global muons with an invariant mass larger than  $2 \text{ GeV}/c^2$ . All charge combinations are considered and all possible combinations within an event are kept. Starting from this skim a TTree is filled with single muons and muon pairs that pass quality criteria to reject the background of fake muons while keeping the efficiency of selecting real muons high. The quality cuts have been tuned on Monte Carlo and is described in this chapter.

The TTree furthermore contains event information regarding the trigger, centrality and primary vertex position. For the muon pairs properties like the common vertex probability and the pseudo-proper decay length were computed and stored as well. In order to select good quality muons, different variables were studied. This section describes how the cuts are defined and what is the final set of quality criteria that would be used in the analysis. Muon candidates are selected if reconstructed as

*global muons*. Muon arbitration requirements are applied, specifically muons must be both global and tracker muons (accessed via the standard methods `isGlobal()` and `isTracker()`). The muon quality cuts are studied by tuning with 2010 PbPb data for  $J/\psi$  and  $\Upsilon$  measurement [97, 98] and similar cuts study was done with 2011 PbPb data for  $\Upsilon$  analysis [99].

#### 4.6.1. Variables description

The following variables are being studied :

- `InnerTrack_Hits`: The number of valid hits within the pixels and the strips (inner tracker) a single muon track has, indicating how good the inner track part of the track is;
- `PixelLayers`: The number of pixel layers, with valid hits, crossed by a single muon. There are 2-3% of muons with tracks with 0 pixel hit;
- `InnerTrack $\chi^2/ndf$` : The  $\chi^2/ndf$  of the single muon inner track, which indicates the quality of the inner track fit;
- `GlobalTrack $\chi^2/ndf$` : The  $\chi^2/ndf$  of the single muon global track, which indicates the quality of the global fit;
- `$D_{xy}$`  and  `$D_z$` : The distance between the event vertex and the muon track in the transverse plane and the longitudinal plane respectively which indicates if the muon comes from a decay in flight or is a prompt muon, and removes cosmics;
- `TrackerMuonArbitrated`: The arbitration cut on the muons is applied. It helps resolving ambiguities when two muons share the same segment in the muon stations. Detail are given in CMS AN-2008/097 (chapter 6.2);

- `isGlobal()` and `isTracker()`: The muons must be both global and tracker muons.
- `vProb`: The probability of two tracks to belong to the same decay vertex;

The number of valid muon hits of the single muon outer track is a cut that was removed as there is an inconsistent bug in MC and data.

#### 4.6.2. Method

In order to estimate what would be the best set of cuts to reject background but keep as much signal as possible, the following samples were used :

- Realistic  $J/\psi$  embedded in HYDJET PbPb background: One signal is embedded per minimum bias event; where the signal efficiency can be studied.
- Prompt reconstruction of the data : where the background rejection efficiency can be studied

The quantities that will help deciding on the best set of cuts are :

- The leading figure of merit employed in the cut optimisation study is the Significance  $\mathcal{S}$ , defined as

$$\mathcal{S} \equiv \frac{N_{\text{signal}}}{\sqrt{N_{\text{signal}} + N_{\text{background}}}}, \quad (4.2)$$

where  $N_{\text{signal}}$  and  $N_{\text{background}}$  are the signal and background yields. The significance of the signal using the data sample as it has the right background proportion.

- the efficiency of the signal using the MC sample is defined as the number of signal measured after applying the cut over the number of signal measured without the cut.

- the background rejection using the MC sample is defined as  $1 - \frac{\text{background estimated after applying the cut}}{\text{background estimated without the cut}}$ .

Each variable is studied for muons falling in the  $J/\psi$  mass range in  $[2.6, 3.5]$   $\text{GeV}/c^2$ , using a Gaussian fit. For significance calculations, the signal events are obtained by the integration of the fit result in  $[-2\sigma, 2\sigma]$  around the mean of  $J/\psi$  ( $m_0 = 3.0969 \text{ GeV}$ ) and with  $\sigma$  (mass resolution) about  $25 \text{ MeV}$  extracted from the fitting. For comparison, the decay width of  $J/\psi$  is given as  $92.9 \pm 2.8 \text{ keV}$ . For estimating the background, we fit it in the same window  $[-2\sigma, 2\sigma]$  and extract its level from the integral of the fit. Such a fit is illustrated in Fig. 41. For efficiency studies, the signal events are obtained by total fit peak area. The background is estimated by integrating the background function fit in the windows  $[2.6, m_0 - 4\sigma]$  and  $[m_0 + 4\sigma, 3.5]$ . Cuts will be chosen very loose and within reasonable selections to stay away from data/MC disagreements. It is important to note that using the significance on data to check

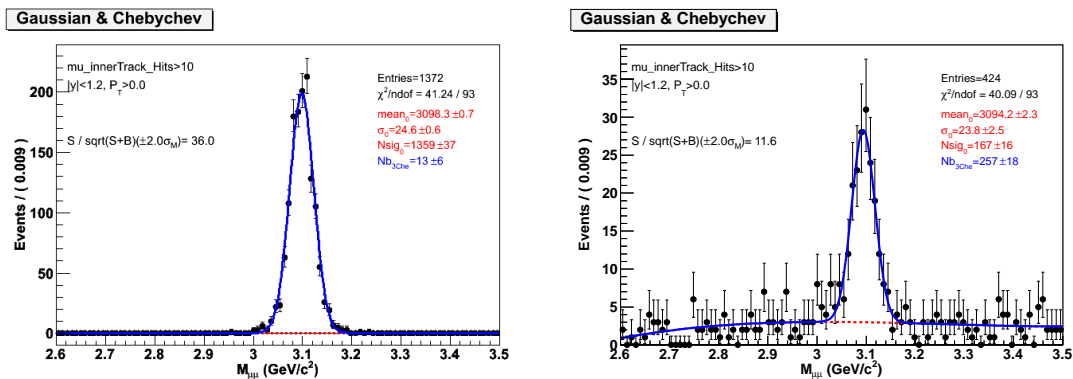


Fig. 41. Illustration of the signal and the background side band fits to extract the number of signal and background in the cut study. These are the mass distributions with MC (left) and with real data (right).

the effect of a cut on the signal and background could lead to a bias in the results if

one would try to optimize the signal only looking at the data. This is why a careful attention was made to only use the significance as an indicator of the impact of the background rejection. We always associated the significance value with the efficiency estimation based on the MC sample.

These quantities will be estimated for each variable, applying all other set of cuts, for each cut value. This process is an iterative process and all the other set of cuts were only suggested after having a first look at the results. The figures below are only illustrating the last iteration, looking at each variable applying all the other cuts. The effect of individual cuts without applying the others will be reported once cuts are defined in Table VI.

The following results are presented in 3 rapidity region :  $|y| < 1.2$ ,  $|y| \in [1.2, 1.6]$  and  $|y| \in [1.6, 2.4]$  to check that the background and efficiency does not behave differently in each part of the detector. Figures from 42 to 45 show for each variable applying all cuts but the one on the variable studied, on the left the significance on the data and on the right the efficiency and background rejection on MC, this for different value of the cut, for each rapidity bin. In general, the cut chosen is the one that keeps as much signal as possible on the MC with a relatively good significance. For all plots the background rejection behaves similarly (but symmetrically) to the efficiency. This suggests that the background is mostly made of real tracks and/or muons, and thus difficult to reduce.

Figure 42 shows that, for the inner track number of valid hit, the significance starts dropping when more than 13 valid hits for the muon inner track is required on the data and the efficiency at 12 (or 10 for the bin  $|y| \in [1.2, 1.6]$ ) .

The cut chosen is *InnerTrack\_Hits* > 10.

Figure 43 shows that for the number of pixel layers, with valid hits, crossed, the significance and the efficiency are flat for 1 or 2 but there is a slight efficiency drop

with the requirement of 3 pixel layers to be fulfilled, as does the significance slightly. The cut chosen is  $PixelLayers > 0$ .

Figure 44 shows that for the inner track  $\chi^2/ndf$ , the significance is mostly flat while the efficiency increases until about 2 and then stay maximal.

The conservative cut picked is :  $InnerTrack\_chi2NDOF < 4$

Figure 45 shows that for the global track  $\chi^2/ndf$ , the significance increases in the barrel up to above 4 and then is constant . For the other rapidity bins, the trend fluctuates more below 4 but stabilizes after. The conservative cut picked is:  $GlobalTrack\_chi2NDOF < 20$

The study of  $D_{xy}$  and  $D_z$  were done similarly but as the significance and efficiency as a function of the cut value are constant (above 0.02 for  $D_{xy}$ ). Figures 46 and 47 shows the significance on data and the efficiency and background rejection on MC for different values of  $D_{xy}$  and  $D_z$  while applying all other cuts.

The final cut are chosen conservatively in order not to remove secondary  $J/\psi$  :  $D_{xy} < 3.0$  cm and  $D_z < 15.0$  cm.

Figures 48 show for for the vertex probability study, the significance and efficiency are constant as all other cuts are applied.

As the values are constant for the significance and efficiency, a reasonable 1% for the vertex probability is chosen. It is to be noted that the arbitration cut (the requirement of the muon to be both global and tracker muon) has already a very good efficiency, and thus is applied in the final set of quality criteria.

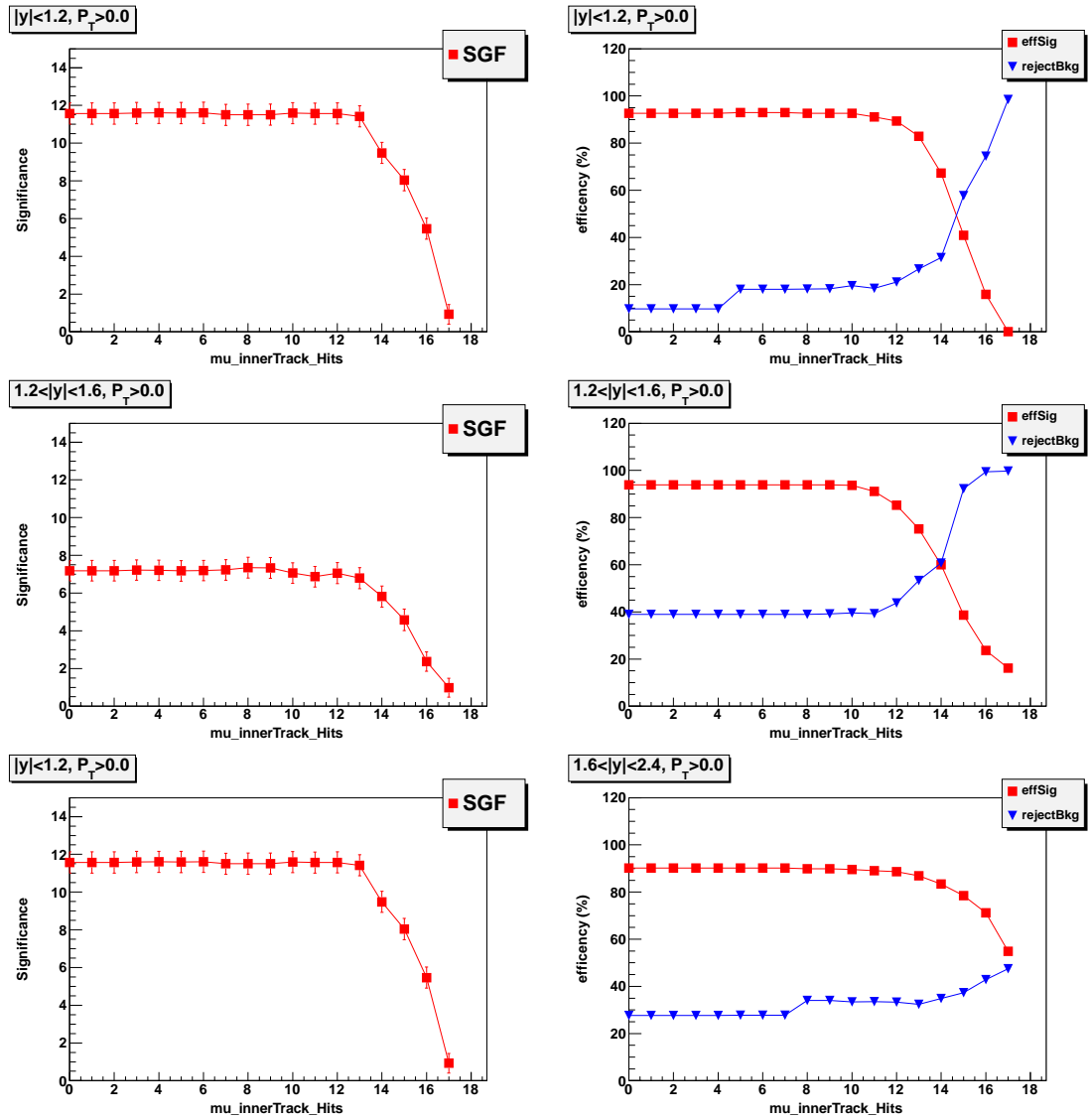


Fig. 42. Number of inner track valid cut study while applying all other cuts: left, significance on the data and right, efficiency and background rejection on MC. Final cut  $> 10$ .

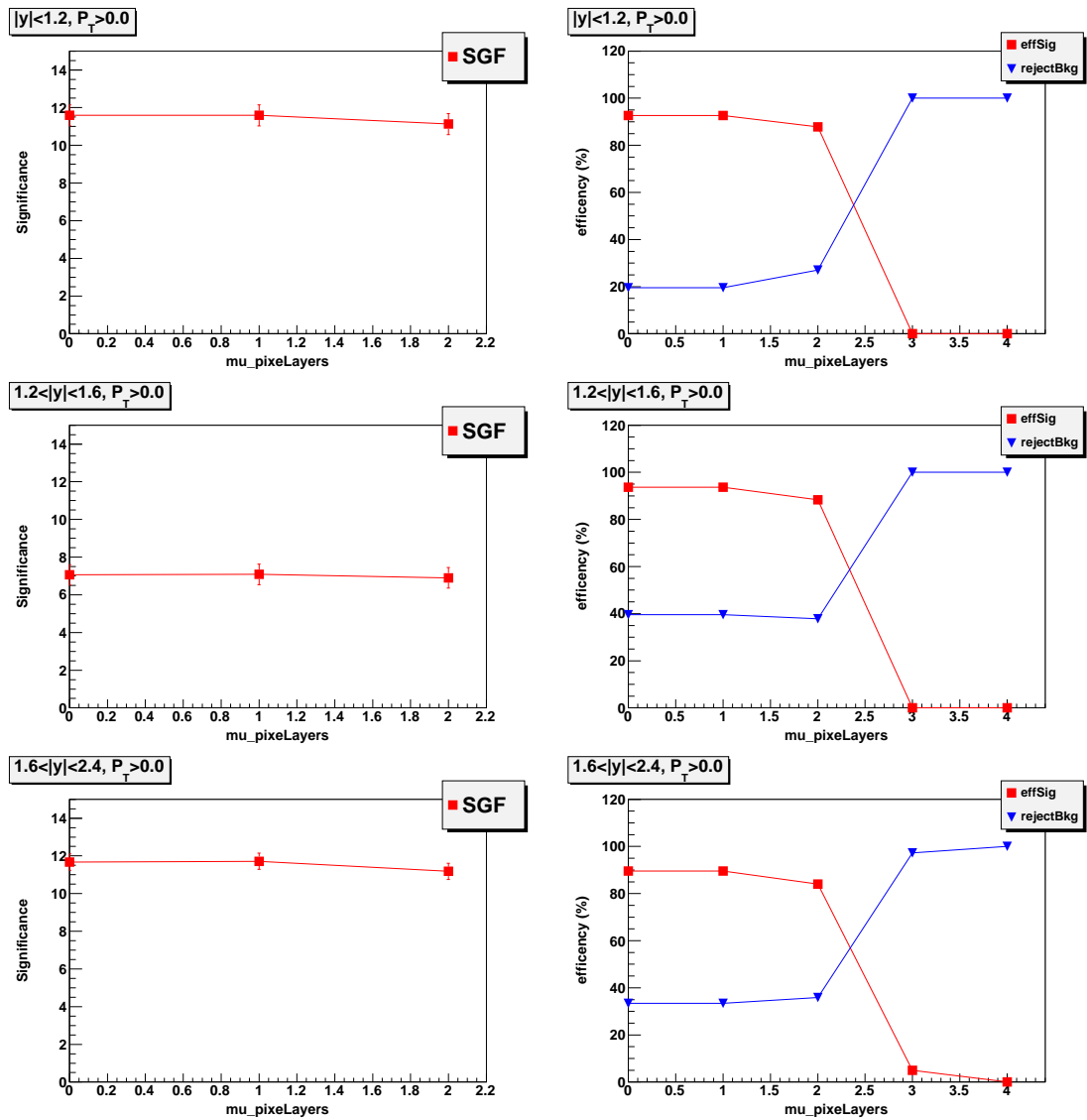


Fig. 43. Number of pixel layers reached by a single muon studied while applying all other cuts: left, significance on the data and right, efficiency and background rejection on MC. Final cut  $> 0$ .

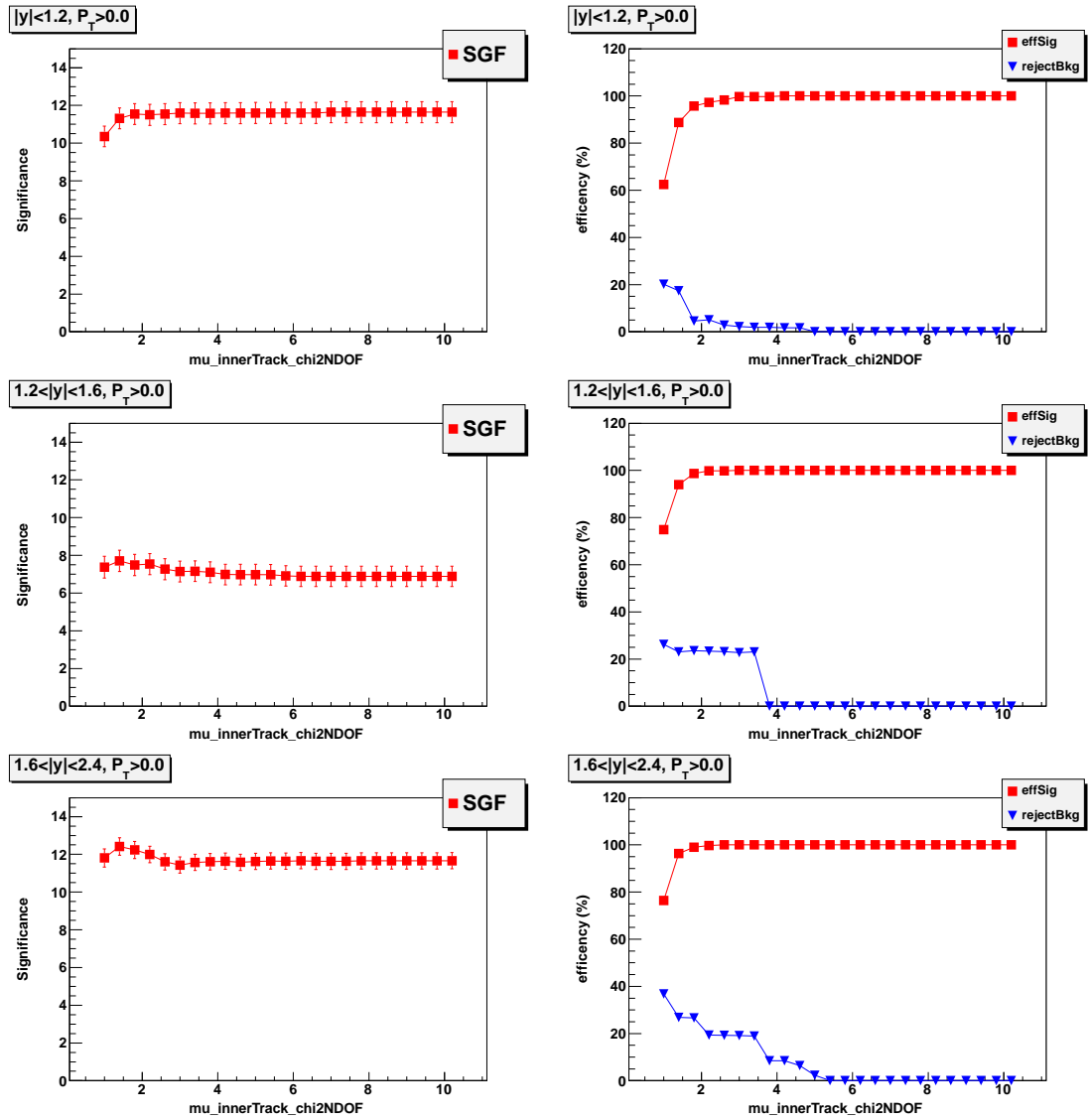


Fig. 44. Single muon inner track  $\chi^2/ndf$  studied while applying all other cuts: left, significance on the data and right, efficiency and background rejection on MC. Final cut  $< 4$ .

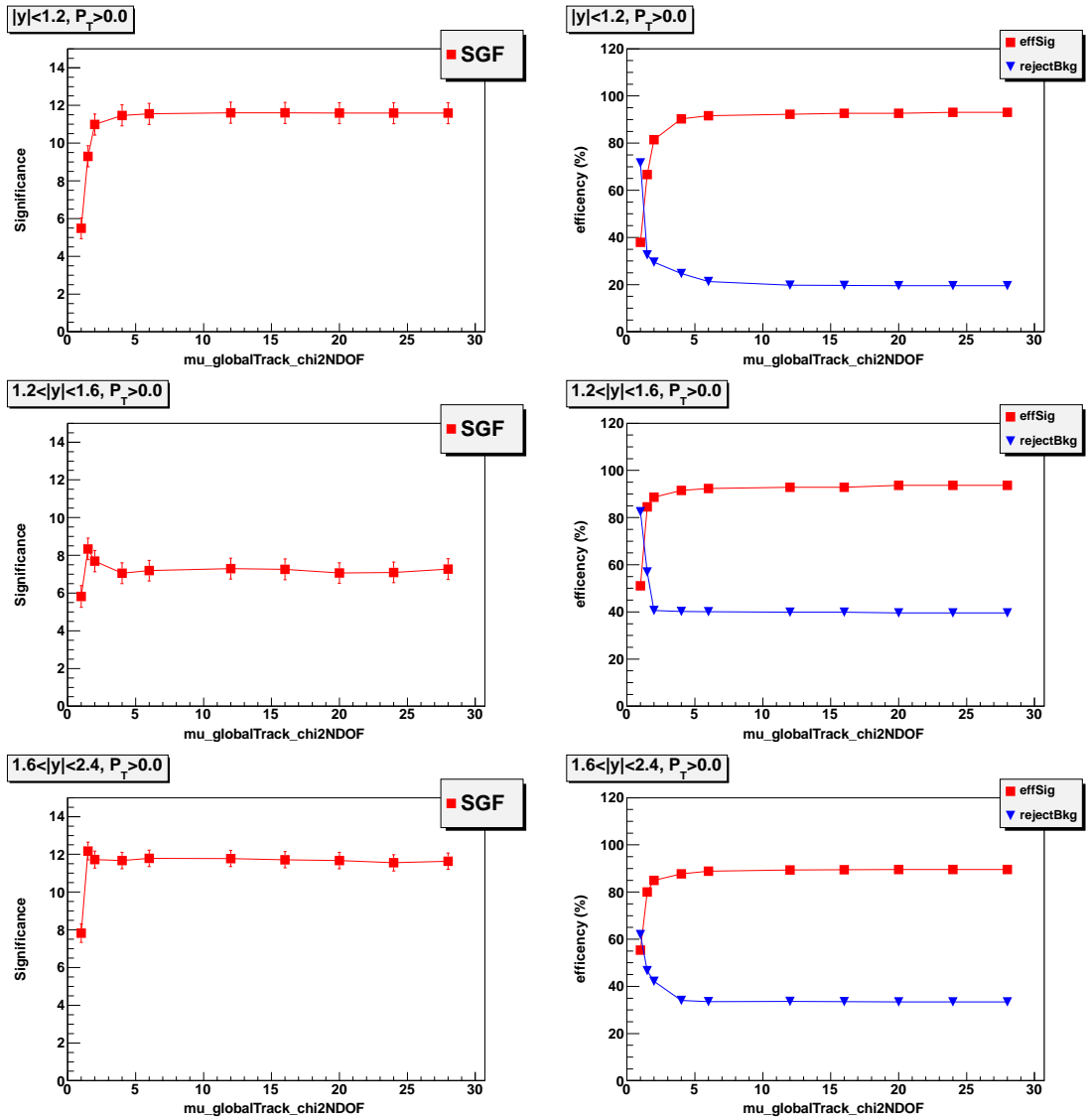


Fig. 45. Single muon global track  $\chi^2/ndf$  studied while applying all other cuts: left, significance on the data and right, efficiency and background rejection on MC. Final cut  $< 20$ .

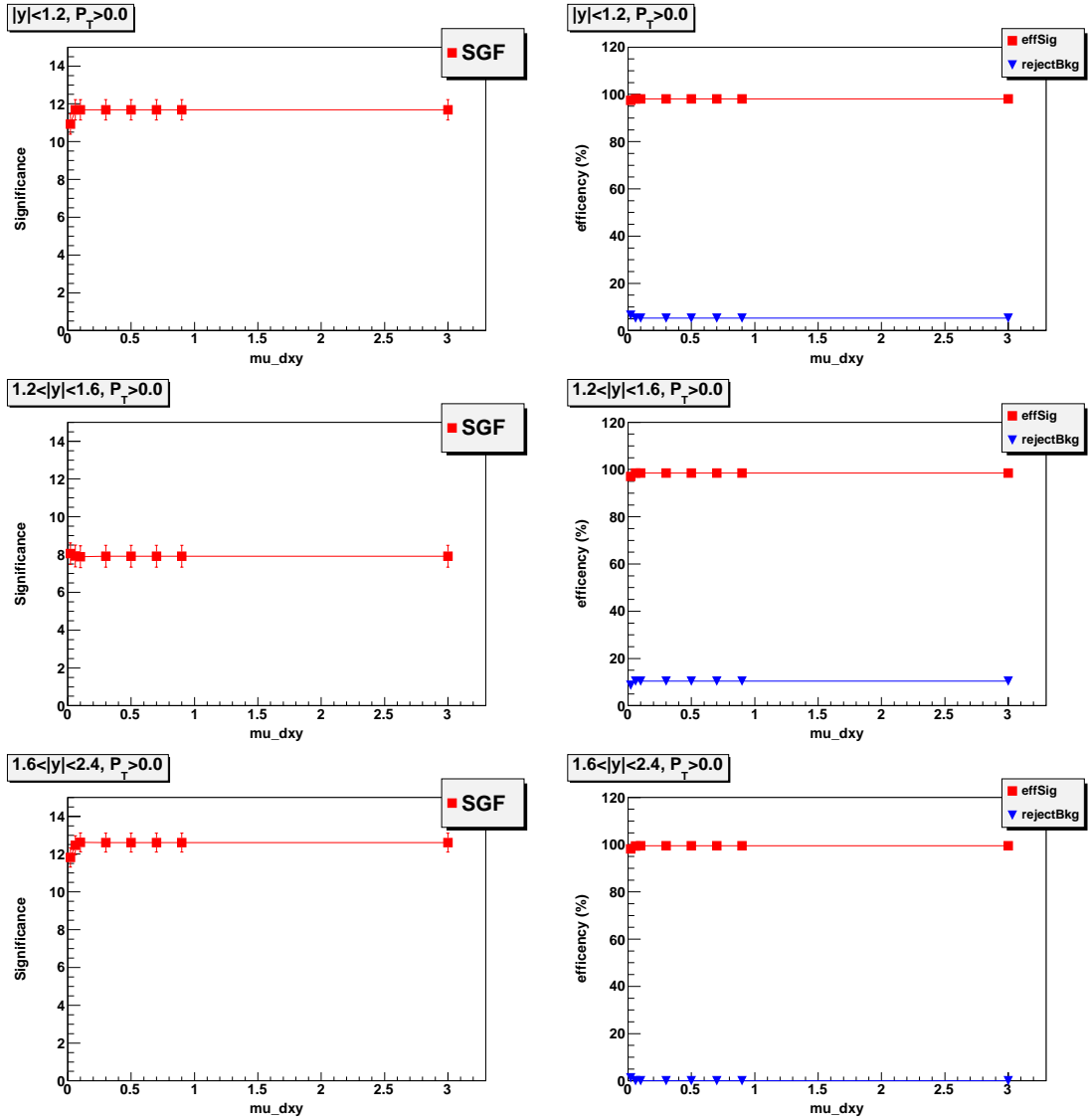


Fig. 46.  $D_{xy}$  study while applying all other cuts: left, significance on the data and right, efficiency and background rejection on MC.

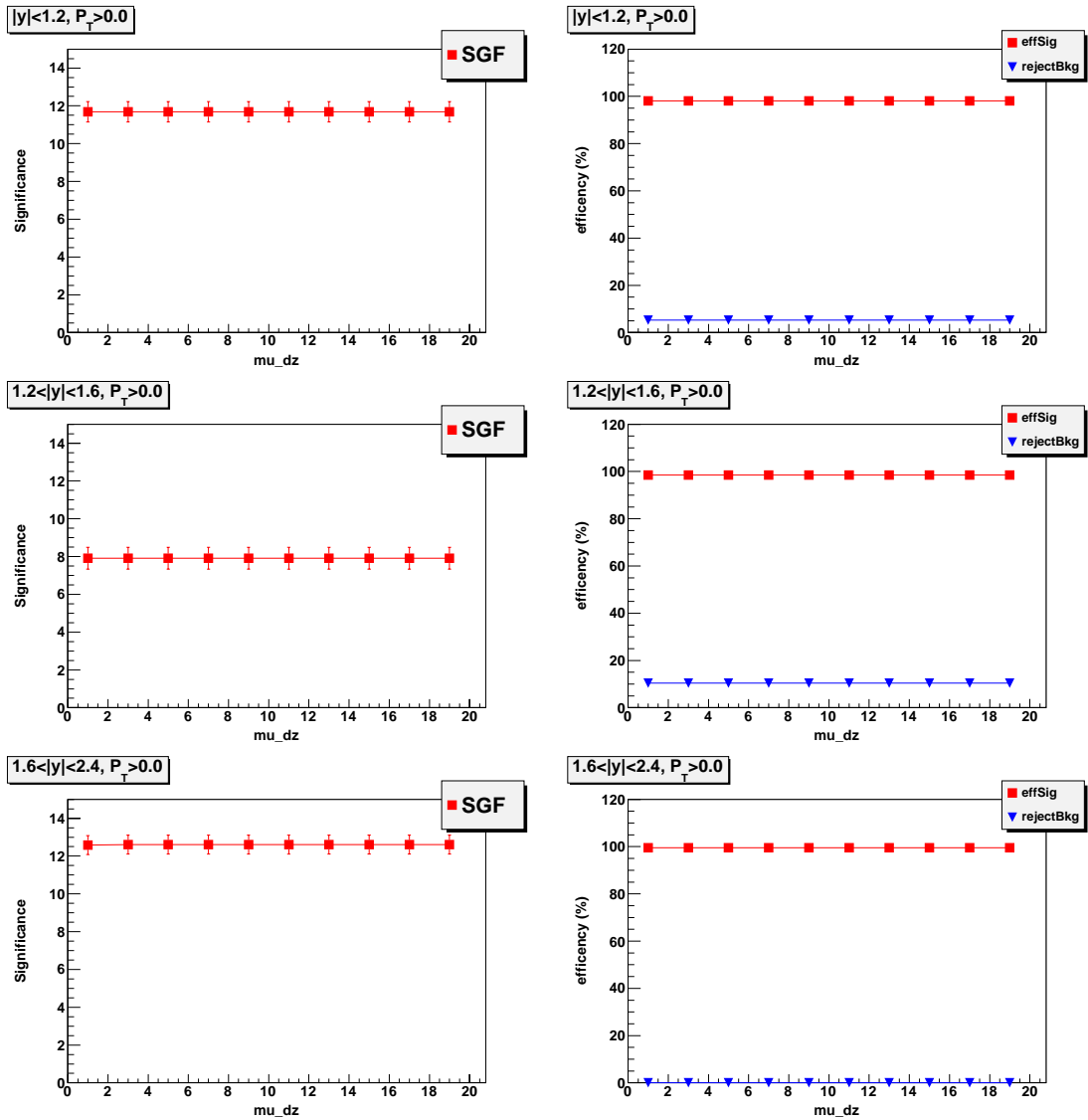


Fig. 47.  $D_z$  study while applying all other cuts: left, significance on the data and right, efficiency and background rejection on MC.

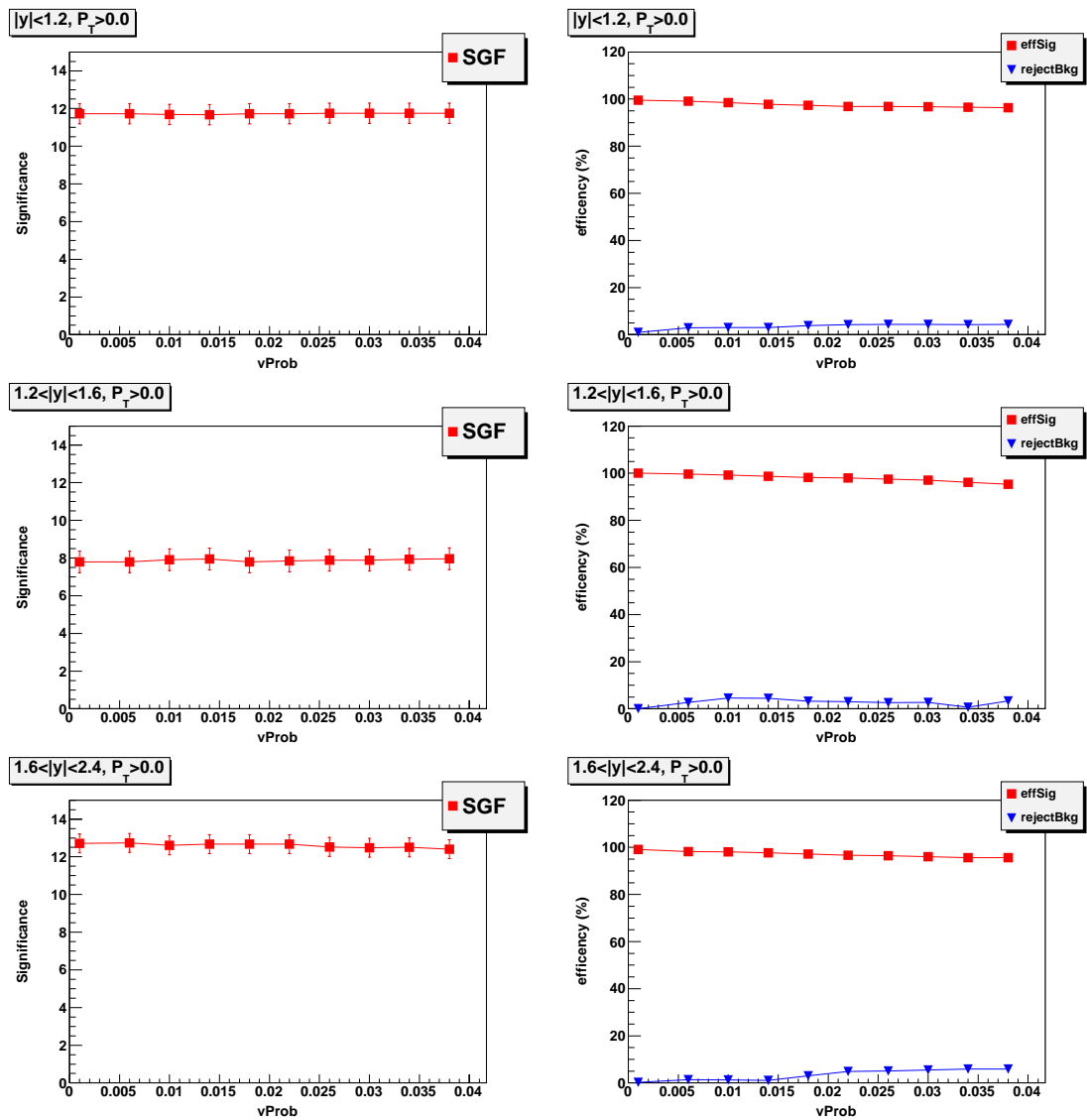


Fig. 48. Vertex probability cut studied while applying all other cuts: left, significance on the data and right, efficiency and background rejection on MC.

Table VI. Signal efficiency and background rejection efficiency in % on MC when applying each cut, in 3 rapidity bins.

Cut Variable	$ y  < 1.2$		$1.2 <  y  < 1.6$		$1.6 <  y  < 2.4$	
	$\varepsilon_{Sig}$	$\varepsilon_{Bkg}$	$\varepsilon_{Sig}$	$\varepsilon_{Bkg}$	$\varepsilon_{Sig}$	$\varepsilon_{Bkg}$
InnerTrackHits > 10	97.7	17.2	98.7	24.0	99.1	19.1
PixelLayers > 0	98.1	0.0	98.8	0.4	99.8	5.0
InnerTrack $\chi^2/ndf < 4$ .	99.7	1.8	99.9	0.07	100	8.4
Dxy < 3. cm	98.1	0.0	98.8	0.4	99.8	5.0
Dz < 15. cm	98.1	0.0	98.8	0.4	99.8	5.0
GlobalTrack $\chi^2/ndf < 20$	96.3	1.2	99.7	0.4	98.7	0.8
vProb > 0.01	98.5	10.3	98.3	5.5	97.3	15.4
TrackerMuonArbitrated =1	96.9	0	95.8	32.3	93.5	26.1
All cut	92.6	19.5	93.6	39.6	89.5	33.4

### 4.6.3. Final cuts

The following tables would summarise the effect of the cuts chosen. Table VI indicates the impact of applying only a particular cut on the efficiency and background rejection using the MC sample. Applying all the cuts keeps between 89% and 94% of the signal depending on the rapidity region, with is an intermediate value at 92%, for the outer  $J/\psi$ . Slightly more signal is lost at forward than a mid-rapidity. The background rejection is estimated to be between 19% to 40%, the bigger rejection being in the intermediate region. Requiring the number of inner tracker hit to be higher than 10 together with the muon arbitration cut have the biggest impact on the background

Table VII. Signal efficiency and background rejection efficiency in % on MC after applying all other cuts but the one listed, in 3 rapidity bins.

Cut Variable	$ y  < 1.2$		$1.2 <  y  < 1.6$		$1.6 <  y  < 2.4$	
	$\varepsilon_{Sig}$	$\varepsilon_{Bkg}$	$\varepsilon_{Sig}$	$\varepsilon_{Bkg}$	$\varepsilon_{Sig}$	$\varepsilon_{Bkg}$
InnerTrackHits	92.6	9.7	93.9	38.9	90.1	27.7
PixelLayers	92.6	19.5	93.6	39.6	89.5	33.4
InnerTrack $\chi^2/ndf$	92.6	19.3	93.6	39.6	89.5	33.4
Dxy	92.6	19.5	93.6	39.6	89.5	33.4
Dz	92.6	19.5	93.6	39.6	89.5	33.4
GlobalTrack $\chi^2/ndf$	95.9	19.2	93.9	39.2	90.4	33.1
vProb	93.4	19.6	95.3	33.5	91.8	34.6
TrackerMuonArbitrated	93.7	20.3	96.7	30.2	95.5	26.9
All cut	92.6	19.5	93.6	39.6	89.5	33.4

rejection.

Table VII and VIII shows the effect on the signal efficiency and background rejection when applying all other cuts but the one studied, on MC and data respectively. It gives an indication of the correlation between the cuts. The cuts have very little impact on the signal loss. The arbitration cut is the one that removes the most background in the data. The final cuts are based on the efficiency on MC from Tab. VI and the background rejection from VIII. They are listed in the first column of table VI.

Table VIII. Signal efficiency and background rejection efficiency in % on real data after applying all other cuts but the one listed, in 3 rapidity bins.

Cut Variable	$ y  < 1.2$		$1.2 <  y  < 1.6$		$1.6 <  y  < 2.4$	
	$\varepsilon_{Sig}$	$\varepsilon_{Bkg}$	$\varepsilon_{Sig}$	$\varepsilon_{Bkg}$	$\varepsilon_{Sig}$	$\varepsilon_{Bkg}$
InnerTrackHits	83.6	61.6	78.4	58.8	100	59.6
PixelLayers	82.8	65.4	72.9	62.1	100	64
InnerTrack $\chi^2/ndf$	83.6	65.3	70.7	61.0	100	64.3
Dxy	82.8	65.4	72.9	62.1	100	64
Dz	82.8	65.4	72.9	62.1	100	64
GlobalTrack $\chi^2/ndf$	85.9	63.2	80.5	59.5	100	63.5
vProb	84.7	58.7	80.1	57.9	100	59.9
TrackerMuonArbitrated	85.8	39.5	78.4	33.2	83.2	21.3
All cut	82.8	65.4	72.9	62.1	100	64

#### 4.7. Muon selection study: 2011 PbPb data

Similar Muon quality cuts study was done with 2011 PbPb data for the  $\Upsilon$  analysis. The method of selection and cut values finally optimised are same as with 2010 PbPb data except for the variable Vertex Probability. The figure of merit employed in this study is the Significance,  $\mathcal{S}$  for  $\Upsilon(1S)$ . The  $N_{\text{signal}}$  and  $N_{\text{background}}$  of  $\Upsilon(1S)$  signal and background yields are estimated in a  $\pm 100$  MeV/ $c^2$  signal window around the  $\Upsilon(1S)$  peak. The signal yields are obtained from the Monte Carlo sample. The background yields are estimated from the data in the signal window. The starting signal/background level is set from a fit to the data obtained with default cuts. Possible dependencies of the determined significance on the starting default cuts or

signal-window size are inspected. In addition to the significance  $\mathcal{S}$ , the following factors are also estimated: (i) The efficiency of the signal using the MC sample, (ii) The background rejection efficiency using data.

These estimators are evaluated for each variable, applying all other cuts, as a function of the cut threshold value. This is an iterative process, where the standard thresholds of Ref. [100] are used as a first iteration step. The procedure is applied to several track quality criteria. The aim is to confirm the goodness of the standard thresholds applied, and identify potential gains in significance that could be attained by adjusting the threshold of some of the inspected variables. Figures 49–56 show, for each variable, the variation of the significance  $\mathcal{S}$ , on the left. On the right hand side, the signal efficiency and background rejection, as a functions of the probed cut value, are also displayed. For all variables but the one being studied, the default values are applied. Figure 49 shows that, for the inner track number of valid hits, the significance starts dropping when more than 13 valid hits for the muon inner track is required on the data and the efficiency at 12. The cut chosen is `InnerTrack_Hits>10`. Figure 50 shows that for the number of pixel layers, with valid hits, crossed, the significance and the efficiency are flat for 1 or 2 but there is a slight efficiency drop with the requirement of 3 pixel layers to be fulfilled, as does the significance slightly. The cut chosen is `PixelLayers> 0`. Figure 51 shows that for the inner track  $\chi^2/ndf$ , the significance is mostly flat while the efficiency increases until about 2 and then stay maximal. The conservative cut picked is: `InnerTrack_chi2NDOF<4`. Figure 52 shows that for the global track  $\chi^2/ndf$ , the significance increases up to above 4 and then is constant. The conservative cut picked is: `GlobalTrack_chi2NDOF<20`. Figures 54 and 55 shows the significance on data and the efficiency and background rejection on MC for different values of  $D_{xy}$  and  $D_z$  while applying all other cuts. The final cuts are chosen: `mu_dxy < 3.0 cm` and `mu_dz < 15.0 cm`.

Figures 56 show for for the vertex probability study, the significance is constant as all other cuts are applied. A reasonable 5% cut for the vertex probability is chosen.

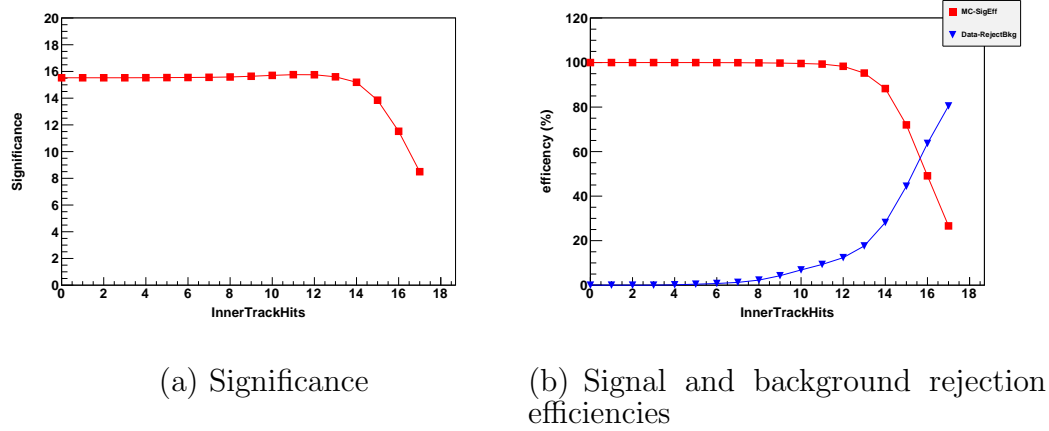


Fig. 49. Number of muon inner track valid cut study (default:  $> 10$ ).

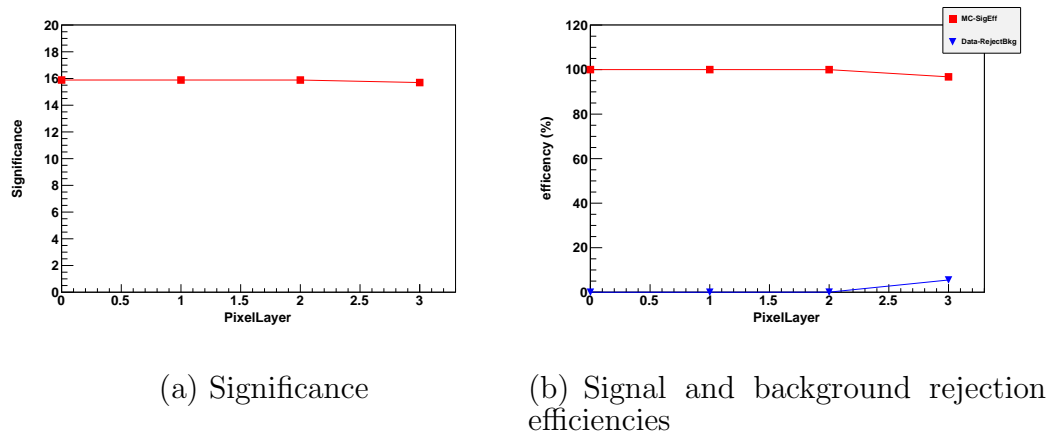


Fig. 50. Number of muon pixel layers cut study (default:  $> 0$ ).

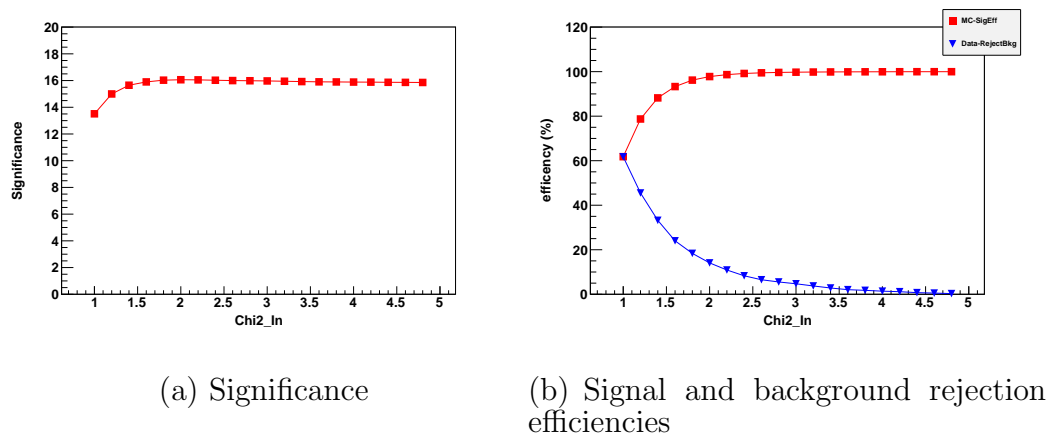


Fig. 51. Number of muon inner track  $\chi^2/\text{ndf}$  cut study (default:  $< 4$ ).

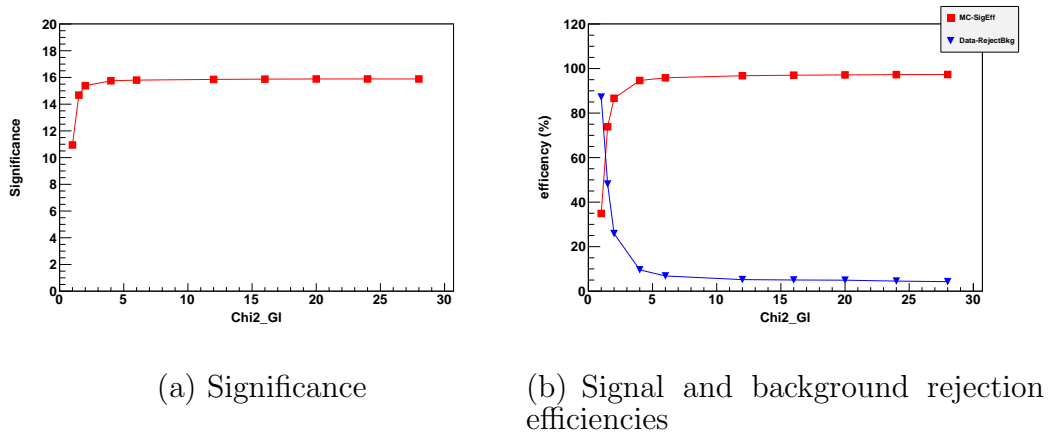


Fig. 52. Number of muon global track  $\chi^2/\text{ndf}$  cut study (default:  $< 20$ ).

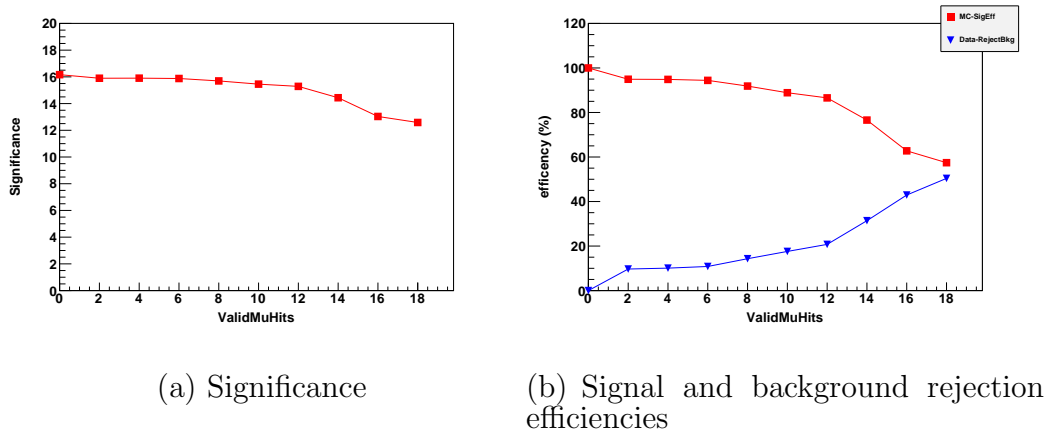


Fig. 53. Number of valid muon hits cut study (default:  $\geq 0$ ).

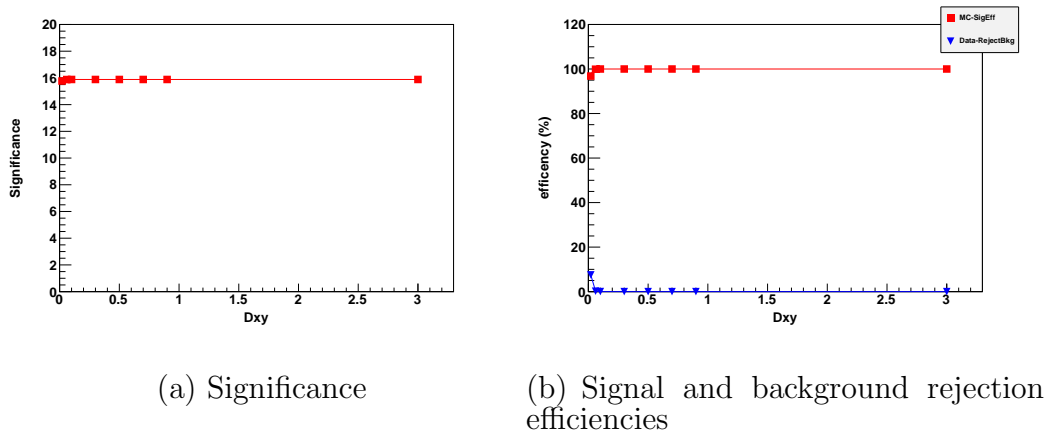
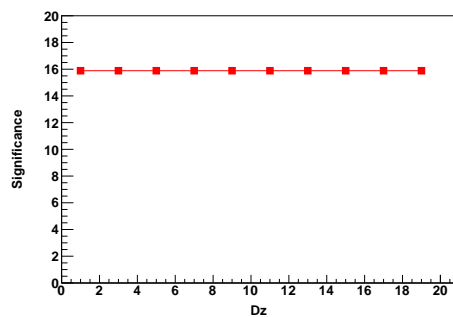
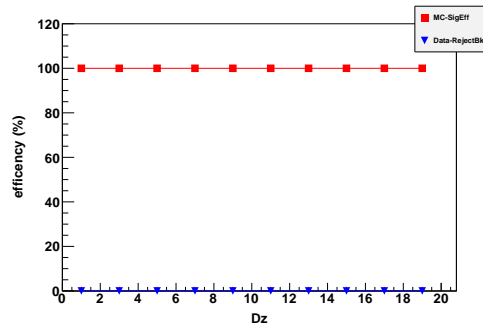


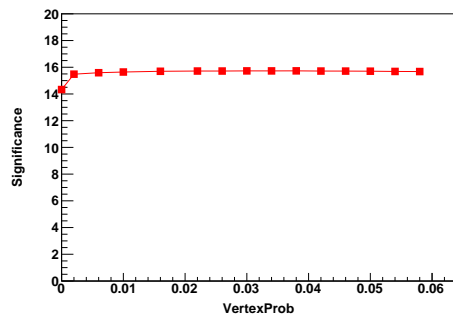
Fig. 54.  $D_{xy}$  cut study (default:  $< 3$ ).



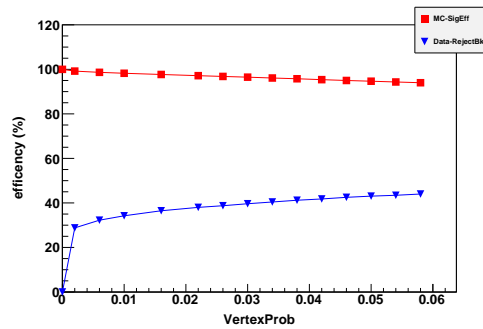
(a) Significance



(b) Signal and background rejection efficiencies

Fig. 55.  $D_z$  cut study (default:  $< 15$ ).

(a) Significance



(b) Signal and background rejection efficiencies

Fig. 56. Dimuon vertex probability cut study (default:  $> 5\%$ ).

## 4.8. Kinematic threshold

The single muon  $p_T$  cut was chosen according to the described optimization procedure considering the effect of the  $p_T$  cut on the shape of the background.

### 4.8.1. Statistical optimization

The optimization of the single muon  $p_T$  cut is here based on the  $1S$  peak significance, as in Eq. 4.2. Similarly to what was already described above, the signal is determined from MC counting the dimuons falling into the  $\pm 100 \text{ MeV}/c^2$  mass window around the  $\Upsilon(1S)$  peak normalized to the signal in data. The signal level in data is determined from the simultaneous fit of the  $\Upsilon(nS)$  mass peaks and the background, where we take the integral of the  $1S$  peak fit in the same mass window. The background is derived from the mass sidebands, counting the dimuons falling into two  $1 \text{ GeV}/c^2$  wide intervals placed symmetrically around the  $\Upsilon(1S)$  peak. The number of counts then is normalized to the size of the signal window to estimate the background below the peak. The results of the calculation are shown in Fig. 57, for three different values of the signal mass window size. The points show a maximum at the single muon  $p_T > 4.0 \text{ GeV}/c$ , independent of the size of the signal window chosen. This optimization method indicates the best choice of the cut value to be  $4.0 \text{ GeV}/c$ .

### 4.8.2. Summary of offline selection

Here we give a summary of selection of good quality muons with 2011 PbPb data for the  $\Upsilon$  analysis. In order to select such muons the effect of different cut thresholds on a variable set was studied. Table IX shows the effect on the significance, as well as signal efficiency and background rejection, when applying all other cuts but the one studied. It further gives an indication of the correlation between the cuts. Once the

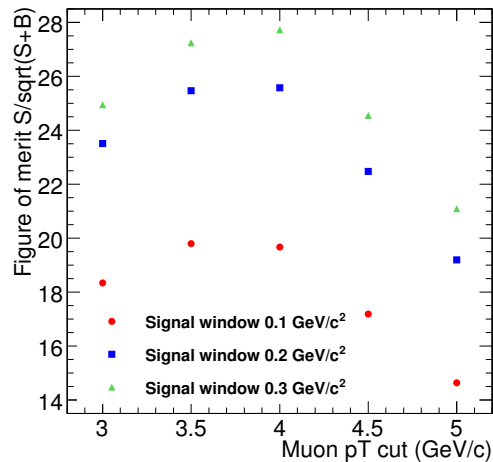


Fig. 57. Significance of  $\Upsilon(1S)$  peak as a function of the single muon  $p_T$  cut

nominal cut thresholds are applied, variations of a single cut have little impact on the significance.

#### 4.9. Agreement MC/data

While studying variables as detailed in the previous paragraph in order to improve the analysis quality and background rejection, one must be careful that data and Monte-Carlo distributions match closely enough. Indeed, cutting on a variable based on a MC sample that does not reproduce the real data distributions can lead to unaccounted loss of signal and biased results. Figures 58 and 59 show the kinematic and quality variables for the MC in red and data in green. Plots were scaled by their integral. As the background in data is very high, the MC/data comparison is done after applying all the cuts except the one of the variable that is plotted, so that we select good quality muons. The muons also come from selecting a region in mass for the dimuons of opposite charge in  $[2.95\text{--}3.25]$  GeV/ $c^2$ , thus reducing a lot the

Table IX. Estimated  $\Upsilon(1S)$  yield significance, signal efficiency (MC) and background rejection in % after applying all other cuts but the one listed.

Cut Variable	real data	MC	Significance
	$1 - \varepsilon_{\text{Bkg}}$ [%]	$\varepsilon_{\text{Sig}}$ [%]	
InnerTrackHits > 10	51.0	85.0	14.5
PixelLayers > 0	54.1	84.6	14.6
InnerTrack $\chi^2/ndf$ <4.	53.2	84.7	14.5
Dxy < 3. cm	54.1	84.6	14.6
Dz < 15. cm	54.1	84.6	14.6
GlobalTrack $\chi^2/ndf$ <20	51.8	87.2	15.1
vProb > 0.05	20.2	89.5	13.7
TrackerMuonArbitrated =1	52.7	84.9	14.5
All cuts	54.1	84.6	14.6

background contamination.

The cuts applied for the analysis remain very conservative with respect to those distributions. They are reminded with a blue dashed line on the figures (when the axis allow it to be drawn). Shape wise, the two data samples are consistent within statistical uncertainty. We make the ratio of the integrals of MC and real data distributions above the analysis cut value, and chose this ratio to quantify the level of agreement between the two samples. The results are printed on each individual plot, and shows a match better than 1% accounted for in the MC/data agreement systematics obtained from tag and probe.

The  $p_T$  and  $\eta$  distribution discrepancies are related to physics processes that generates single muons in heavy-ion collisions and are not accurately modeled by the

HI event generator. The reason is that not many muon measurements exist to help a global effort of tuning the Heavy Ion (HI) event generators at present. Energy loss effects and nuclear modification of Parton Distribution Functions are only two of the most important effects that can influence the production of muons differently in HI than in pp. However, we mention here that the overall multiplicity of our background sample is tuned to match the real data multiplicity, hence all the cuts and efficiency studies that are influenced by the environment track density, are not influenced by the single muon multiplicity (the efficiency reconstruction in the muon chambers being similar to the one in pp).

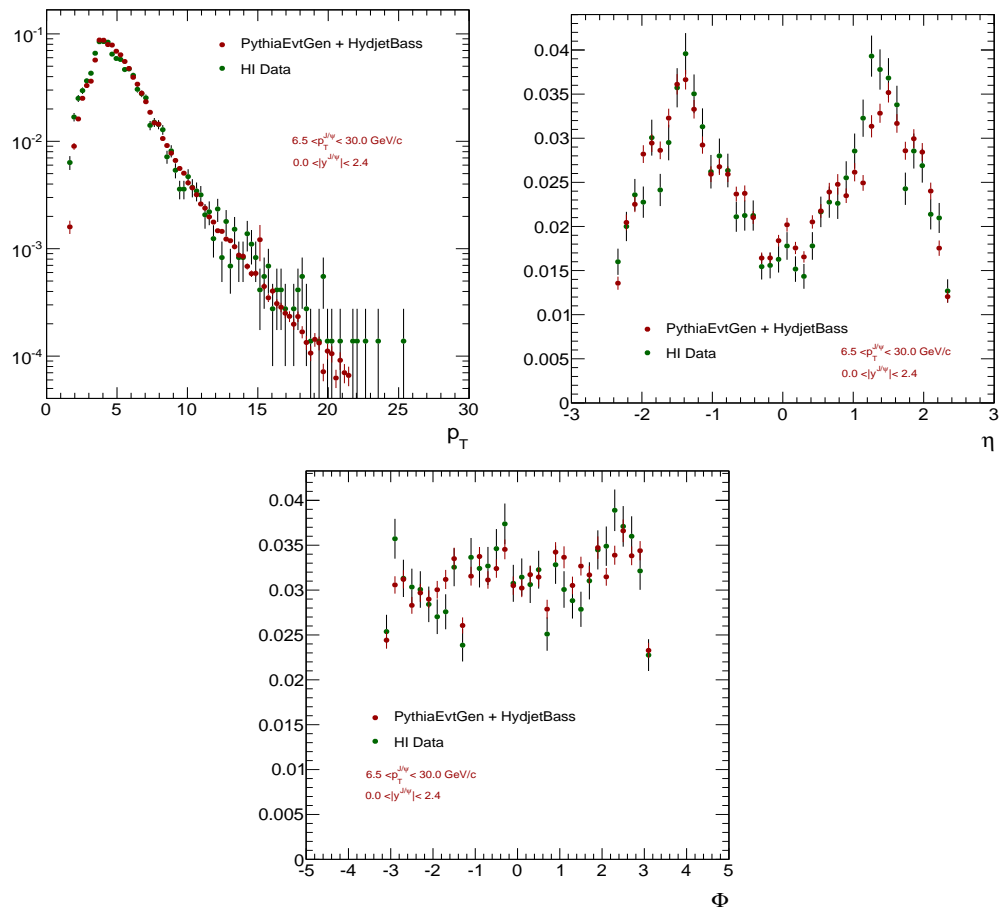


Fig. 58. Kinematics and quality variables distributions for MC in red and data in green.

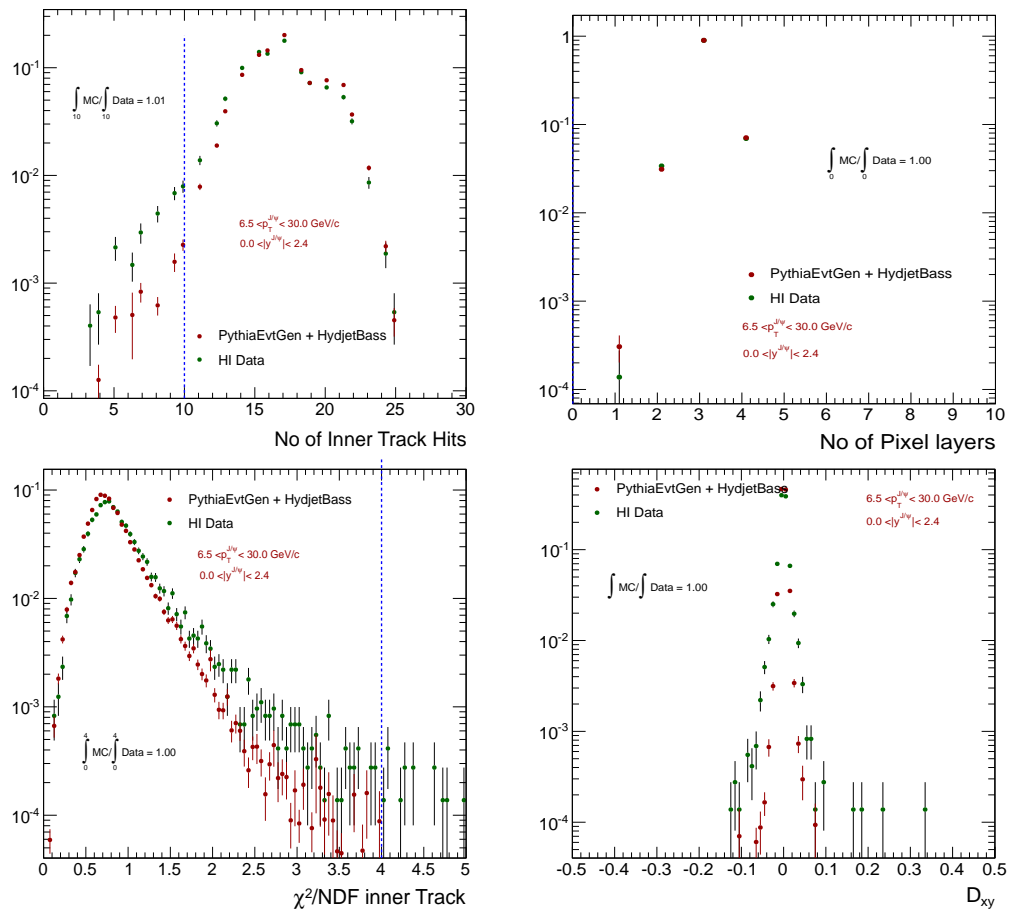


Fig. 59. Kinematics and quality variables distributions for MC in red and data in green.

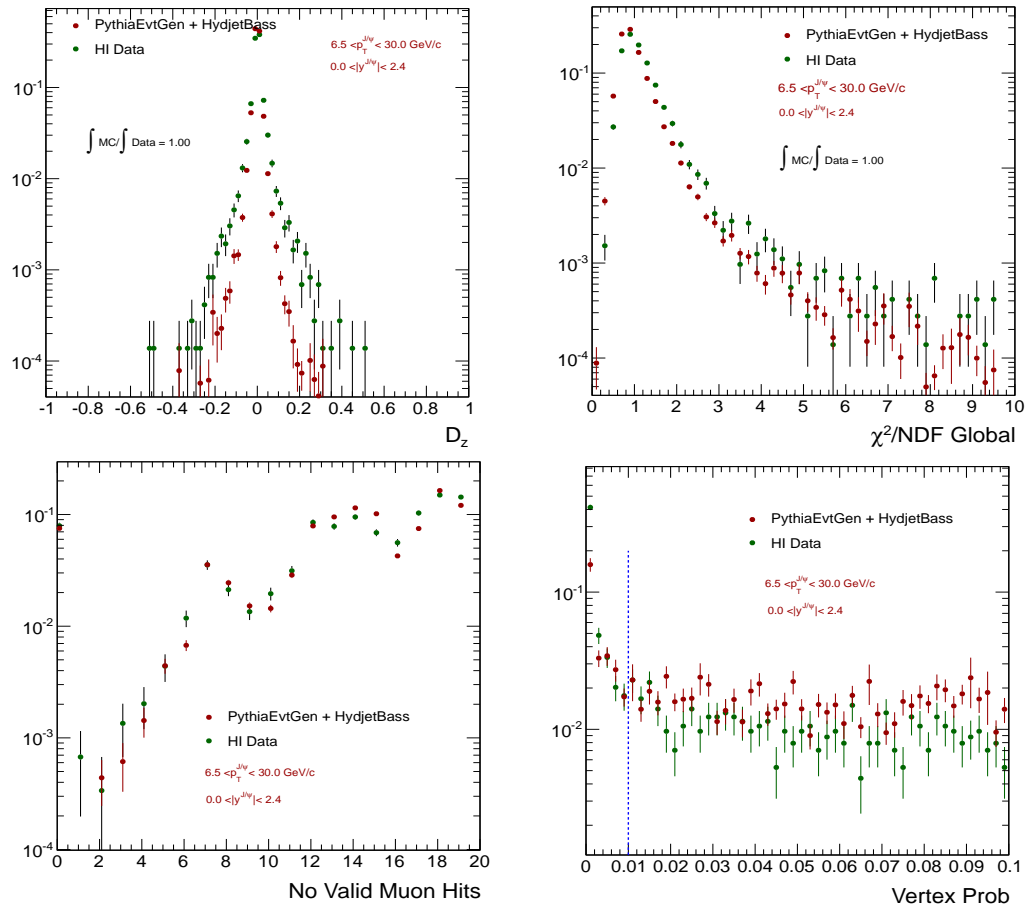


Fig. 60. Kinematics and quality variables distributions for MC in red and data in green.

# CHAPTER 5

Measurement of  $J/\psi$  in PbPb collisions at  
 $\sqrt{s_{\text{NN}}} = 2.76 \text{ TeV}$

## 5.1. Introduction

The formation of a QGP in high-energy nuclear collisions can be evidenced in a variety of ways. Quarkonium states ( $J/\psi$ ,  $\Upsilon$  and etc.) have been one of the most popular tools since their suppression was proposed as a signal of QGP [63]. This suppression is thought to be a direct effect of deconfinement, when the binding potential between the constituents of a quarkonium state, a heavy quark ( $Q$ ) and its antiquark ( $\bar{Q}$ ), is screened by the colour charges of the surrounding light quarks and gluons. The suppression is predicted to occur above a certain dissociation temperature of the medium ( $T_d$ ) depending on the  $Q\bar{Q}$  binding energy. Since the  $\Upsilon(1S)$  is the most tightly bound state among all quarkonia, it is expected to be the one with the highest dissociation temperature, while the  $\psi(2S)$  with the lowest binding energy, to be the one with the lowest dissociation temperature and hence the first to melt. However, there are further possible changes to the quarkonium production in heavy-ion collisions. On the one hand, cold-nuclear-matter effects, such as the modifications of the parton distribution functions inside the nucleus (shadowing), can reduce the production of quarkonia without the presence of a QGP. On the other hand, the large number of heavy quarks produced in heavy-ion collisions, in particular at the energies accessible by the Large Hadron Collider (LHC), could lead to an increased production of quarkonia via statistical recombination [64].

At LHC energies, the inclusive  $J/\psi$  yield contains a significant non-prompt contribution from b-hadron decays. Owing to the long lifetime of the b hadrons ( $\mathcal{O}(500)\mu m/c$ ), compared to the QGP lifetime ( $\mathcal{O}(10)\text{ fm}/c$ ), this contribution should not suffer from colour screening, but instead reflects the b-quark energy loss in the medium. Such energy loss would lead to a suppression of the b-hadron yield at high  $p_T$ . The importance of an unambiguous, detailed, measurement of open bottom

flavour is driven by the lack of knowledge regarding key features of the dynamics of parton energy loss in the QGP, such as its colour-charge and parton-mass dependencies and the relative role of radiative and collisional energy loss.

Experimentally, the suppression is quantified by the ratio of the yield measured in heavy-ion collisions and a reference, which usually is the yield measured in pp collisions, the ‘vacuum-like’ system where no QGP is formed. Such a ratio is called the nuclear modification factor,  $R_{AA}$ . In the absence of medium effects, one would expect  $R_{AA} = 1$  for hard processes, which scale with the number of inelastic nucleon-nucleon collisions. The  $R_{AA}$  of prompt and non-prompt  $J/\psi$  has been measured separately by CMS, with 2010 PbPb data, in bins of transverse momentum ( $p_T$ ), rapidity ( $y$ ) and collision centrality [97]. A strong, centrality-dependent suppression has been observed for  $J/\psi$  with  $p_T > 6.5$  GeV/ $c$ .

This chapter describes the updated  $R_{AA}$  measurements of prompt and non-prompt  $J/\psi$  mesons produced in PbPb collisions at  $\sqrt{s_{NN}} = 2.76$  TeV (2011 Run), using an integrated luminosity of  $\mathcal{L}_{int} = 150 \mu\text{b}^{-1}$ . This corresponds to an increase of the PbPb data sample by a factor 20 compared to the 2010 PbPb Run data. The measurement with 2010 PbPb data is published previously by CMS [97]. The *non-prompt*  $J/\psi$  from b-hadron decays have been separated from *prompt*  $J/\psi$  utilizing the reconstructed decay vertex of the  $\mu^+\mu^-$  pair. Directly-produced  $J/\psi$  as well as those from decays of higher charmonium states (e.g.  $\psi(2S)$  and  $\chi_c$ ) are considered *prompt* as their decay length is unmeasurably small compared to those from B decays and are not distinguished in this analysis. Using data from the pp run at  $\sqrt{s} = 2.76$  TeV, the new PbPb results are reported in the form of nuclear modification factor,  $R_{AA}$  :

$$R_{AA} = \frac{\mathcal{L}_{pp}}{T_{AA}N_{MB}} \frac{N_{PbPb}}{N_{pp}} \cdot \frac{\varepsilon_{pp}}{\varepsilon_{PbPb}}, \quad (5.1)$$

where

- $N_{PbPb}$  is the raw number of prompt  $J/\psi$  or non-prompt  $J/\psi$  decayed in the  $\mu^+\mu^-$  channel measured in PbPb;
- $N_{pp}$  is the raw number of prompt  $J/\psi$  or non-prompt  $J/\psi$  decayed in the  $\mu^+\mu^-$  channel measured in pp;
- $N_{MB}$  is the number of minimum bias events sampled by the event selection in PbPb;
- $\varepsilon_{pp}$  and  $\varepsilon_{PbPb}$  are the combined trigger and reconstruction efficiency in pp and PbPb respectively;
- $T_{AA}$  is the nuclear overlap function which varies with the centrality of the collision and has units of  $\mu b^{-1}$ , measuring the equivalent number of pp collisions corresponding to a specific centrality PbPb collision;
- $\mathcal{L}_{pp} = (231 \pm 6) \text{ nb}^{-1}$  is the integrated luminosity of the pp data set.

## 5.2. Data selection

Inelastic hadronic PbPb collisions are selected using information from the HF calorimeters and the BSC, in coincidence with a bunch crossing identified by the beam pick ups, BPTX, (one on each side of the detector). The details are discussed in Chapter 4. The muon offline reconstruction algorithm starts by reconstructing tracks in the muon detectors. These tracks are then matched to tracks reconstructed in the silicon tracker by means of an algorithm optimized for the heavy-ion environment [101, 102]. The final muon-track parameters result from a global fit of the muon and a tracker track. Due to better momentum resolution, up to  $p_T \sim 100 \text{ GeV}/c$ , the kinematics of the global fit are assigned to be those of the inner track. These are the muons used in this analysis. In order to have a clear separation between acceptance and

efficiency corrections a single muon acceptance is defined in  $p_T^\mu$ - $\eta^\mu$  space along the contour which roughly matches a global muon reconstruction efficiency of 10%. A muon is declared to be *detectable* if its reconstruction efficiency<sup>1</sup> is higher than 10%. Fig. 61 presents the result of this efficiency in single muon coordinates  $p_T^\mu$  as a function of  $\eta^\mu$ . The superimposed white lines highlight the contour of the kinematical limits that will be used for the prompt and non-prompt  $J/\psi$ , also given by Eq. 5.2 : The same single muon acceptance criteria as in Ref. [97] have been applied to ensure reasonable ( $> 10\%$ ) reconstruction efficiencies:

$$\begin{aligned}
 |\eta^\mu| < 1.0 &\rightarrow p_T^\mu > 3.4 \text{ GeV}/c, \\
 1.0 \leq |\eta^\mu| < 1.6 &\rightarrow p_T^\mu > 5.8 - 2.4 \times |\eta^\mu| \text{ GeV}/c, \\
 1.6 \leq |\eta^\mu| < 2.4 &\rightarrow p_T^\mu > 3.4 - 0.78 \times |\eta^\mu| \text{ GeV}/c.
 \end{aligned}
 \tag{5.2}$$

Additional muon selection criteria (number of valid tracker hits,  $\chi^2/ndof$  of both the inner track and the global fit, etc) are applied as reported in the same reference.

### 5.3. Signal extraction

#### 5.3.1. Yield extraction

The invariant mass spectrum of  $\mu^+\mu^-$  pairs is shown in Fig 62 in the region  $2.6 < m_{\mu\mu} < 3.5 \text{ GeV}/c^2$  for pairs with  $p_T < 30 \text{ GeV}/c$  and  $|y| < 2.4$ , after applying the single muon quality requirements. No minimum pair- $p_T$  requirement has been applied explicitly in this plot. However, the CMS acceptance for  $\mu^+\mu^-$  pairs in this mass range requires a minimum  $p_T$ , which is strongly  $y$ -dependent and as large as  $6.5 \text{ GeV}/c$  at  $y = 0$ . The black curve is an extended (the number of signal and background are

---

<sup>1</sup>The reconstruction efficiency here is defined as all reconstructed single muons over all generated muons.

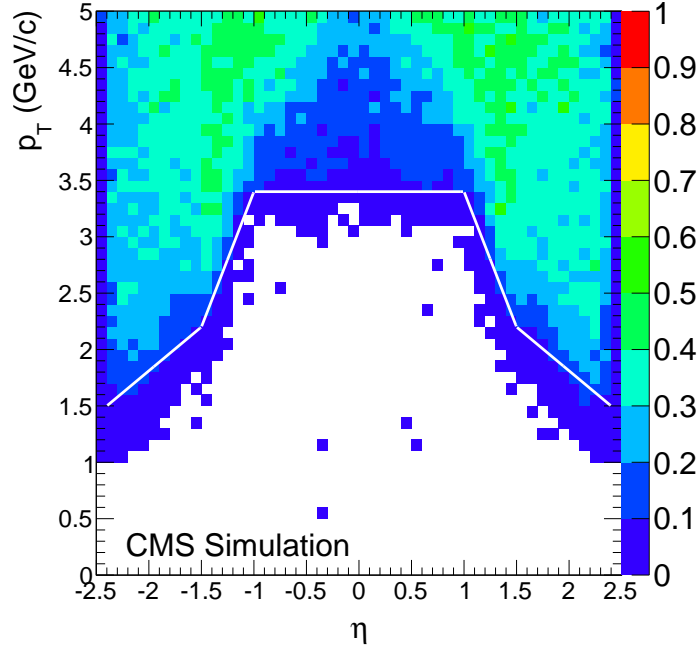


Fig. 61. Reconstruction single muon efficiency illustrating the limits of what is considered a detectable single muon (Single muon acceptance).

directly calculated) unbinned maximum likelihood fit to the  $\mu^+\mu^-$  pair spectrum with the sum of a Crystal Ball and a Gaussian functions for the signal, with common mean,  $m_0$ , and independent widths,  $\sigma_{CB}$  and  $\sigma_{Gaus}$ , and an exponential for the background. The Crystal Ball function combines a Gaussian core with a power-law tail, described by exponent the  $n$ , to account for energy loss due to final-state photon radiation:

$$f_{CB}(m) = \begin{cases} \frac{N}{\sqrt{2\pi}\sigma_{CB}} \exp\left(-\frac{(m-m_0)^2}{2\sigma_{CB}^2}\right), & \text{for } \frac{m-m_0}{\sigma_{CB}} > -\alpha; \\ \frac{N}{\sqrt{2\pi}\sigma_{CB}} \left(\frac{n}{|\alpha|}\right)^n \exp\left(-\frac{|\alpha|^2}{2}\right) \left(\frac{n}{|\alpha|} - |\alpha| - \frac{m-m_0}{\sigma_{CB}}\right)^{-n}, & \text{for } \frac{m-m_0}{\sigma_{CB}} \leq -\alpha. \end{cases} \quad (5.3)$$

The parameter  $\alpha$  defines the threshold, in units of  $\sigma_{CB}$ , between the Gaussian and the power-law functions. In the present analysis, only the events that fire double muon trigger without  $p_T$  cut was used. This condition selects  $13869 \pm 326$   $J/\psi$ . In order to study the  $p_T$ ,  $y$  and centrality dependence of  $R_{AA}$ , the results were split in several bins of the  $J/\psi$  meson  $p_T$  and rapidity: low vs high- $p_T$ , mid-rapidity vs forward rapidity.

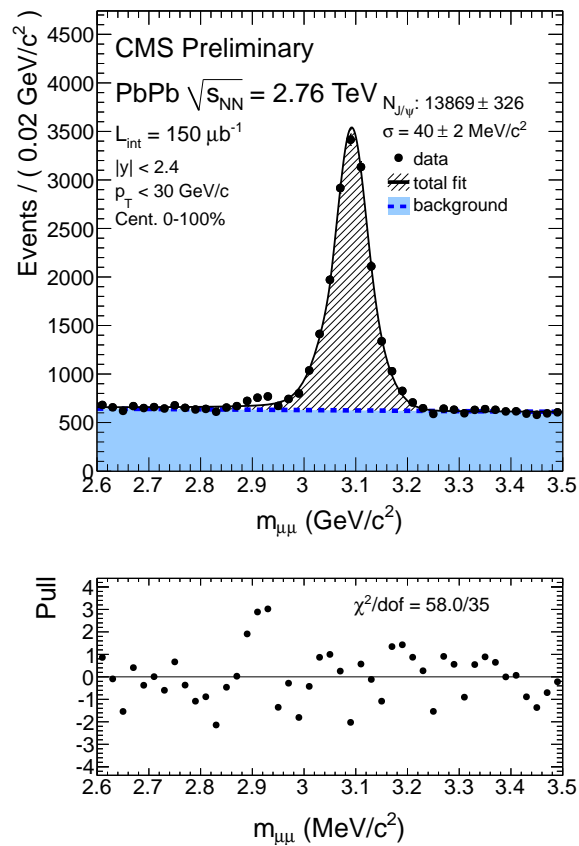


Fig. 62. Invariant mass spectrum of  $\mu^+\mu^-$  pairs (black circles) with  $|y| < 2.4$ ,  $0 < p_T < 30 \text{ GeV}/c$  and 0-100% from events.

Integrating over all centrality (0–100%) and  $p_T$  ( $6.5 < p_T < 30 \text{ GeV}/c$ ) the rapidity bins are

$$|y| < 1.2, \quad 1.2 < |y| < 1.6, \quad \text{and} \quad 1.6 < |y| < 2.4.$$

For the most forward bin, the CMS acceptance extends to lower  $p_T$ , so results are also presented for the bin

$$1.6 < |y| < 2.4 \quad \text{and} \quad 3 < p_T < 30 \text{ GeV}/c.$$

These values allow a better comparison with the low- $p_T$  measurements of the ALICE experiment, which has acceptance for  $J/\psi$  with  $p_T > 0$  GeV/ $c$  for the rapidity intervals  $|y| < 0.9$  and  $2.4 < y < 4.0$ , in the electron and muon decay channels, respectively [103]. Integrating over all centrality (0–100%) and rapidity ( $|y| < 2.4$ ) the  $p_T$  bins are

$$6.5 < p_T < 8 \text{ GeV}/c, \quad 8. < p_T < 10 \text{ GeV}/c, \quad 10 < p_T < 13 \text{ GeV}/c \text{ and } 13 < p_T < 30 \text{ GeV}/c.$$

When integrating over the  $p_T$  range  $6.5 < p_T < 30$  GeV/ $c$  and rapidity  $|y| < 2.4$ , or over  $3 < p_T < 30$  GeV/ $c$  and rapidity  $1.6 < |y| < 2.4$ , the centrality bins are: 0–10%, 10–20%, 20–30%, 30–40%, 40–50%, and 50–100%. We give two reason for the choice of the upper bound of the  $p_T$  value of 30 GeV/ $c$  chosen. First, it will allow to use the exact cuts as with 2010 data measurement for a direct and unambiguous comparison. Second, the number of dimuons lost by this cut is not big, as it is illustrated in Fig. 63, where the raw counts of all dimuons, integrated over centrality, 0-100%, versus their  $p_T$  are plotted. The extended unbinned maximum likelihood fit with the sum of Crystal Ball and Gaussian functions is performed in each of these bins. Because of the regular kinematical bins (centrality, rapidity, transverse momentum) that limits the amount of data, the parameters of the signal shape are fitted in integrated bins of  $p_T$ , centrality and rapidity intervals. As the dominant effect on the mass shape is the rapidity-dependent mass resolution, for the  $p_T$  and  $y$  binning, all parameters of the fit are left free. In the case of centrality binning, the sigma of the Crystal-Ball function is left free while the rest of the parameters are fixed to the minimum bias bin with given  $p_T$  and  $y$  bin.

### 5.3.2. Prompt and Non-prompt $J/\psi$

#### Yield extraction

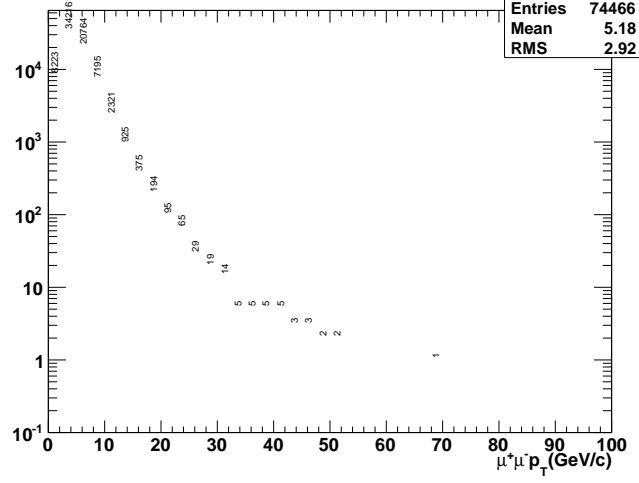


Fig. 63.  $\mu^+\mu^-$  pairs raw counts versus  $p_T$ , for  $|y| < 2.4$  in 0-100% centrality bin. All pairs passed all analysis cuts, but there is no separation of the signal  $J/\psi$  dimuons from the background.

The identification of  $J/\psi$  mesons coming from b-hadron decays relies on the measurement of a secondary  $\mu^+\mu^-$  vertex displaced from the primary collision vertex. The displacement between the  $\mu^+\mu^-$  vertex and the primary vertex  $\vec{r}$  is measured in the plane transverse to the beam direction. The most probable transverse b-hadron decay length in the laboratory frame is calculated as

$$L_{xy} = \frac{\hat{u}^T S^{-1} \vec{r}}{\hat{u}^T S^{-1} \hat{u}}, \quad (5.4)$$

where  $\hat{u}$  is the unit vector in the direction of the  $J/\psi$  meson  $p_T$  and  $S$  is the sum of the primary and secondary vertex covariance matrices. From this quantity (which is the projected decay length of the the  $J/\psi$  on transverse plane), the pseudo-proper decay length  $\ell_{J/\psi} = L_{xy} m_{J/\psi}/p_T$  is computed as an estimate of the b-hadron decay length. The pseudo-proper decay length is measured with a resolution of  $\sim 35 \mu\text{m}$ . To measure the fraction of non-prompt  $J/\psi$  (the so called *b-fraction*), the invariant-mass

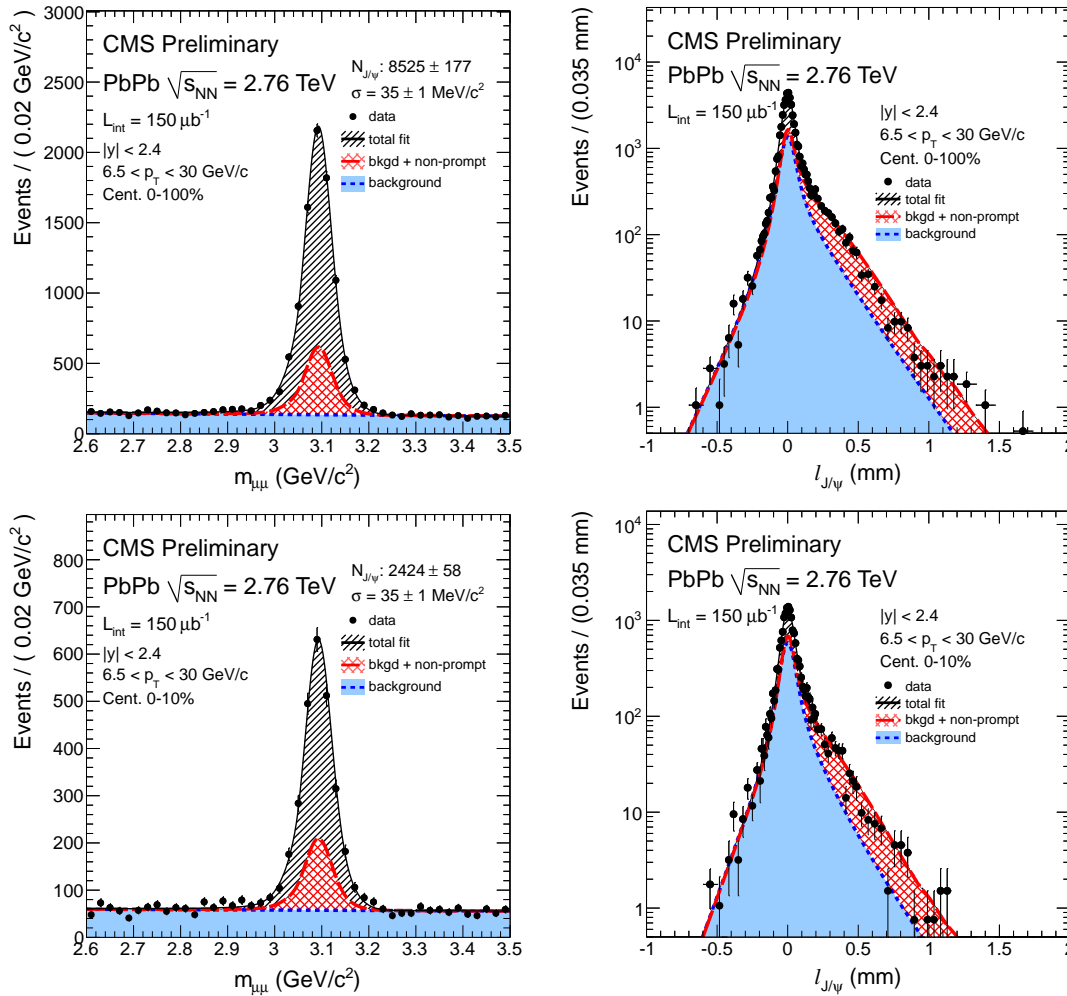


Fig. 64. Invariant-mass spectra (left) and pseudo-proper decay length distribution (right) of  $\mu^+\mu^-$  pairs integrated over centrality (top) and 0–10% most central collisions (bottom). The spectra are integrated over the rapidity range  $0 < |y| < 2.4$  and the  $p_T$  range  $6.5 < p_T < 30$  GeV/c. The projections of the two-dimensional fit onto the respective axes are overlaid as solid black lines. The dashed red lines show the fitted contribution of non-prompt J/ψ. The fitted background contributions are shown as dotted blue lines.

spectrum of  $\mu^+\mu^-$  pairs and their  $\ell_{J/\psi}$  distribution are fitted in a two-dimensional, extended unbinned maximum likelihood fit, in bins of  $p_T$ , rapidity and centrality. In this fit, the fraction of non-prompt  $J/\psi$  is a free fit parameter. The 2D fit is a simultaneous way to take correlated probability between dimuon mass and pseudo-proper decay length into account properly. For example, an event lying on the side-band region will not have high probability to be a prompt or non-prompt  $J/\psi$ . This probability calculation cannot be performed on each event without considering dimuon mass and pseudo-proper decay length at the same time.

The fitting procedure is similar to the one used in the pp analysis at  $\sqrt{s} = 7$  TeV [104] and 2010 PbPb analysis at  $\sqrt{s} = 2.76$  TeV [97]. The invariant-mass spectrum is fitted with an exponential for the background and the sum of a Crystal Ball and a Gaussian function, with common mean, for the signal. The differences compared to the 2010 PbPb analysis are two: using independent widths for the two signal functions in the mass fits, and in the parametrization of the resolution function to describe  $\ell_{J/\psi}$ . The resolution function is now comprised of the sum of two Gaussians which depend on the per-event uncertainty of the measured  $\ell_{J/\psi}$ , determined from the covariance matrices of the primary and secondary vertex fits. One Gaussian function describes the core of the resolution, while the second Gaussian function parametrizes the effect of the uncertainty in the primary vertex assignments. More details about the separation of  $J/\psi$  mesons coming from b-hadron decays and the fitting procedure can be found in [105, 45].

Fig. 64 shows examples of fit projections onto the mass (left) and  $\ell_{J/\psi}$  axes (right), for dimuons with  $6.5 < p_T < 30$  GeV/ $c$  in two ranges of event centrality, 0-100% (top) and 0-10% (bottom), integrated over rapidity,  $|y| < 2.4$ . In the region  $0.5 < \ell_{J/\psi} < 1$  mm, the data are not well described by the fit. It has been found that this difference between the data and the fit is localized in the negative rapidity

region of the detector, while the shape of the data in the positive rapidity region is well described by the fit. The measured b-fractions are  $f_b = 0.235 \pm 0.008$  for  $y < 0$  and  $f_b = 0.234 \pm 0.009$  for  $y > 0$  and agree within their statistical uncertainties. Such an agreement has been verified in all bins under consideration.

#### 5.4. Efficiency corrections

The methods used to correct the raw yields for algorithm and detector inefficiencies are described below. Section 5.4.1 describes how the MC samples are used and errors propagated properly for the efficiencies. This method relies in counting the dimuons in the peak after reconstruction and comparing to what was generated. We cross check efficiencies measured from MC comparing the single muon efficiency obtained with the tag and probe method on MC and data.

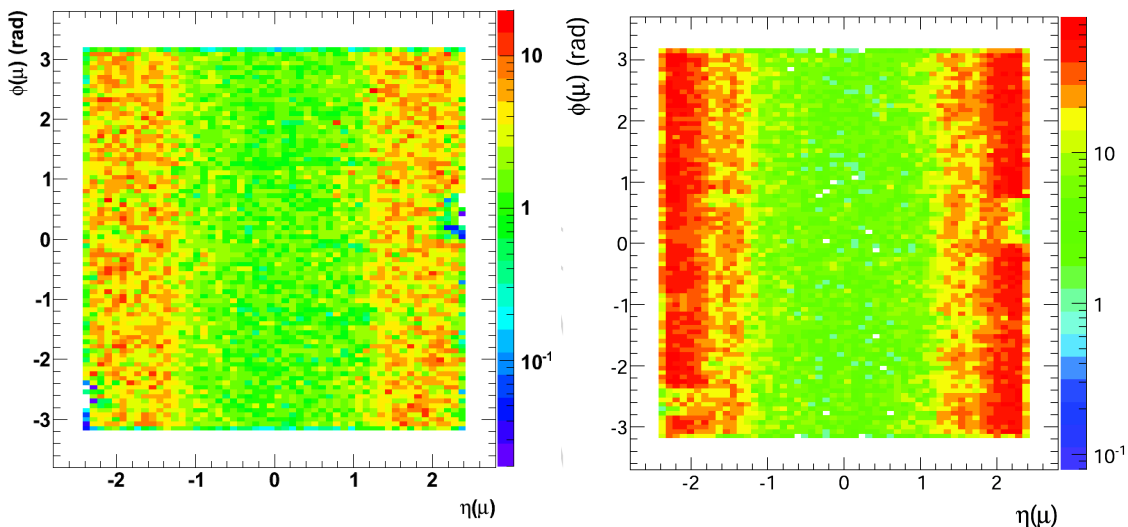


Fig. 65. Single muons  $\eta$  vs  $\Phi$  distributions in MC (left) and data (right) illustrating the presence of dead tracker areas in both MC and data ( $\eta > 2$  and  $\Phi \in [0, 1]$ ,  $\eta < -2$  and  $\Phi \in [-3, -2]$ ).

### 5.4.1. MC samples

Dimuons generated with PYTHIA 6.424 [106] distributions are embedded in PbPb minimum bias collisions, and reconstructed with the heavy ion reconstruction in CMSSW \_4\_4\_2\_patch4 using the global tag STARHI44\_V7::All. This tag accounts for dead areas as seen in Fig. 65 which represent  $\eta$  as a function of  $\Phi$  for the good global muons, where the dead tracker areas are observed in the same positions ( $\eta > 2$  and  $\Phi \in [0, 1]$ , as well as  $\eta < -2$  and  $\Phi \in [-3, -2]$ ) in both MC (left) and data (right).

The Monte-Carlo samples were produced centrally. In order to optimize the generation, a dimuon filter was applied and the embedding was made in bins of dimuon  $p_T$  of 3 GeV from 0 to 30 GeV/c, with 100k events per bin for the first 4 bins and 50k per bin for the rest. To produce the final efficiency numbers, or any distribution using all the  $p_T$  bins, the results are weighted according to the filter efficiency and the number of event per bins to retrieve a continuous dimuon  $p_T$  distributions.

Centrality weights were also applied event by event to retrieve a centrality distribution following a  $N_{coll}$  scaling. For this we used the  $N_{coll}$  table from our Glauber calculation. The weights are used as in section 4.1 of [105], event by event  $\omega_i = \omega_{filter} \times N_{coll}$ .

#### Method

The method consists of estimating the reconstruction efficiency making the ratio of the number of signal events that is reconstructed and passes the quality cuts, and the number of signal events that was generated:  $\varepsilon = \frac{N_{reco}}{N_{gen}}$ , where  $N_{gen}$  is the number of events that fall within our acceptance conditions (see Section 5.2) for each of the muons and  $N_{reco}$  is the number of dimuons that are reconstructed, match the trigger, pass the quality cuts presented in Chapter 4, and fall within the acceptance. The

number of signal events is estimated by counting the number of reconstructed dimuons in mass range  $[2.95 - 3.25]$   $\text{GeV}/c^2$ . An illustration of such a mass distribution is given in Fig. 66 for prompt  $J/\psi$  in a centrality-integrated bin. This can be justified as we embedded one signal event in each underlying HYDJET event and mass cut is wide enough to accommodate all signal dimuons in all bins used in analysis. The reconstructed numbers include all efficiency corrections: trigger, identification (cuts) and tracking.

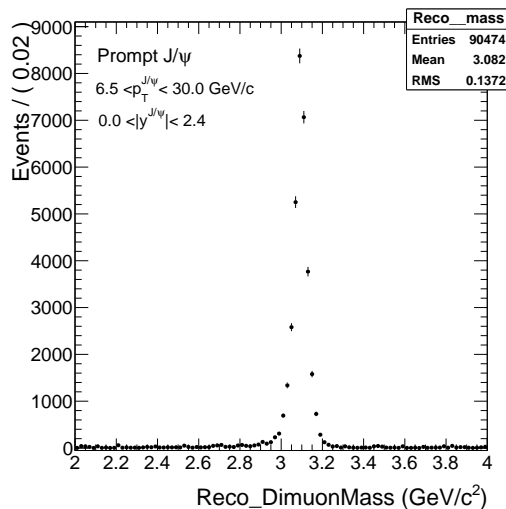


Fig. 66. Illustration of the reconstructed mass for the prompt  $J/\psi$  in a centrality-integrated bin used for the efficiency calculation with the peak counting method.

### Efficiency results

The prompt and non-prompt  $J/\psi$  efficiency with the peak counting method in fine bins is illustrated on Fig. 67 as a function of  $p_T$ ,  $y$  and centrality. The efficiency varies very little as a function of centrality, up to  $p_T=10$   $\text{GeV}/c$  at most between peripheral and central collisions, and stabilizes above 30% and 35% for the non-prompt and prompt  $J/\psi$  respectively. The non prompt  $J/\psi$  efficiencies are lower than the prompt efficiency because of the heavy ion reconstruction algorithm. In contrast to pp, the

PbPb tracking algorithm consists of only one iteration and requires a pixel triplet seed to point within 2 mm to the reconstructed primary vertex. This requirement leads to a lower efficiency to reconstruct non-prompt  $J/\psi$ . All efficiencies, in all kinematic bins used, for both prompt and non-prompt  $J/\psi$  are tabulated and included in Appendix of Ref. [105].

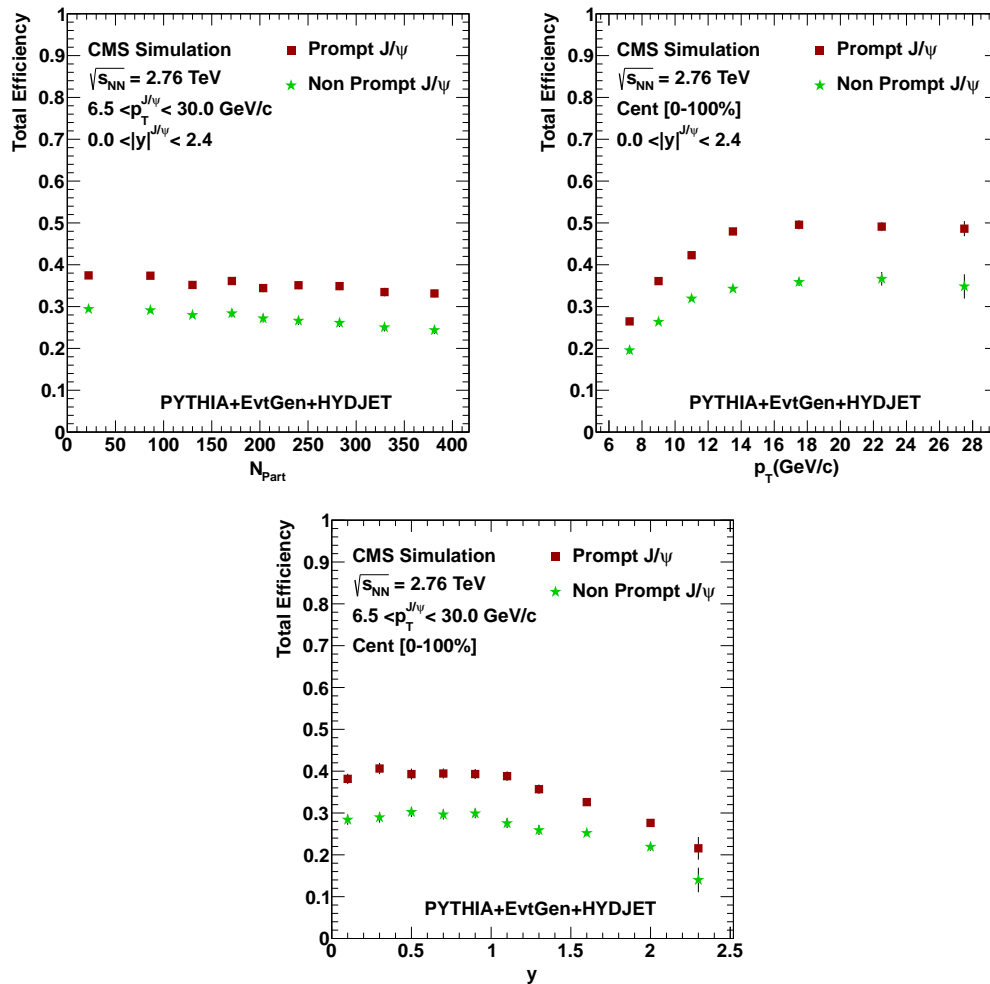


Fig. 67. Efficiency corrections as a function of event centrality (left),  $p_T$  (right) and rapidity (bottom) for prompt and non-prompt  $J/\psi$ .

### 5.5. Systematic uncertainties

The total systematic uncertainty on the  $R_{AA}$  is estimated by summing in quadrature the different contributions. The ranges of the variations are summarized in Table X. The yield extraction uncertainties increase from mid- to forward-rapidity, and for PbPb also from central to peripheral bins. The uncertainties associated with muon reconstruction have a smooth increase from peripheral to central bins, mapping the centrality dependence of efficiency in PbPb, which is smaller in central events compared to peripheral events. The  $T_{AA}$  uncertainties increase from central to peripheral bins.

Table X. Systematic uncertainties on the prompt and non-prompt  $J/\psi$   $R_{AA}$  measured in PbPb collisions.

	prompt $J/\psi$ (%)	non-prompt $J/\psi$ (%)
PbPb yield extraction	0.2–1.7	0.6–4.5
pp yield extraction	0.3–1.6	1.7–8.4
$T\&P^{recoValidation} \times (1 - \epsilon_{PbPb}/\epsilon_{pp})$	1–9	1–10
$T\&P^{triggerCorrection}$	10	10
$T_{AA}$	4.1–18	4.3–15
Total	10.8–23	11.1–22.7

In all the results shown in Figs. 68–69, statistical uncertainties will be represented by error bars and systematic uncertainties by boxes on the points. Boxes plotted at  $R_{AA}=1$  indicate the scale of the global uncertainties.

For results plotted as a function of  $p_T$  or rapidity: a) the statistical and systematic uncertainties include, added in quadrature, the statistical and systematic

uncertainties from both PbPb and pp samples; b) the systematic uncertainty on  $T_{AA}$ , as well as the pp luminosity uncertainty, enter as a global uncertainty; they are added in quadrature and plotted as a gray box as a scale uncertainty at  $R_{AA}=1$ . As a function of centrality: a) the statistical and systematic uncertainties from pp are added in quadrature together with the pp luminosity uncertainty, and plotted as a colored box, as a scale uncertainty, at  $R_{AA}=1$ ; b) the uncertainty on  $T_{AA}$  varies point-to-point and is included in the systematic uncertainties.

## 5.6. Results

### 5.6.1. Prompt $J/\psi$

In Fig. 68 the  $R_{AA}$  of high  $p_T$  prompt  $J/\psi$  as function of centrality,  $p_T$  and rapidity is shown, integrating in each case over the other two variables. No  $p_T$  dependence is observed while the rapidity dependence is very weak, consistent with being at the same level of suppression. A slow decrease of the suppression *vs.* the event centrality is observed, with  $R_{AA}$  being still suppressed in the most peripheral bin in which the measurement was performed (60–100%). The centrality-integrated  $R_{AA}$  value measured for  $6.5 < p_T < 30$  GeV/ $c$  and  $|y| < 2.4$  is  $0.34 \pm 0.02$  (stat.)  $\pm 0.04$  (syst.).

### 5.6.2. Non-prompt $J/\psi$

In 69 the  $R_{AA}$  of high- $p_T$  non-prompt  $J/\psi$  as function of centrality,  $p_T$  and rapidity are shown, integrating in each case over the other two variables. A hint of an increase of the suppression with increasing  $p_T$  and rapidity can be noted. A slow increase of the suppression is observed with increasing centrality of the collision. The centrality-integrated  $R_{AA}$  value measured for  $6.5 < p_T < 30$  GeV/ $c$  and  $|y| < 2.4$  is  $0.45 \pm 0.05$  (stat.)  $\pm 0.06$  (syst.). More details of this study can be found in the CMS public

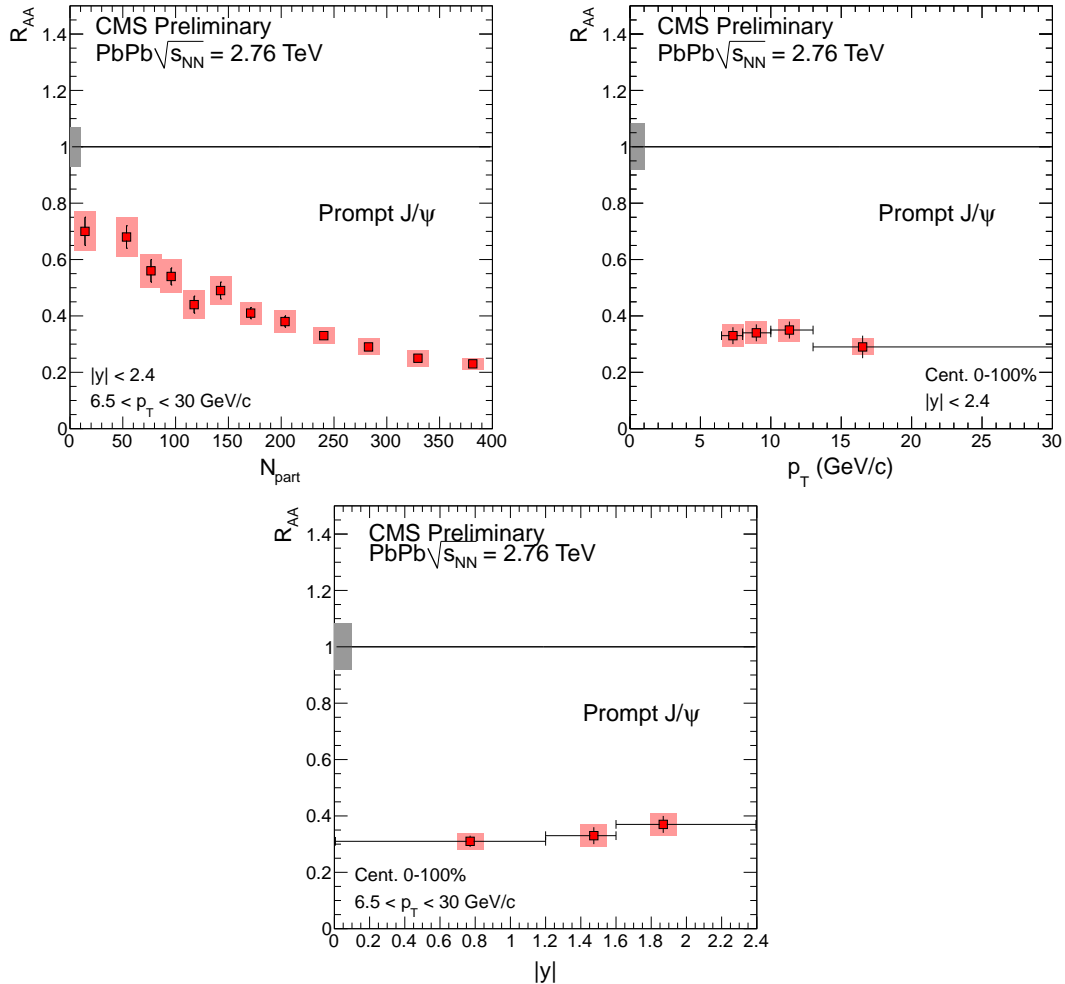


Fig. 68. The nuclear modification factor as function of centrality (*left*),  $p_T$  (*right*) and rapidity (*bottom*) for the prompt  $J/\psi$ . The gray boxes plotted at  $R_{AA} = 1$  indicate the scale of the global uncertainties: (left) the uncertainty of 6% on the measured integrated luminosity of the pp data sample, together with the statistical and systematic uncertainty on the pp data set; (right and bottom) the pp luminosity and the  $T_{AA}$  uncertainties. The bin boundaries are indicated by small horizontal lines where meaningful.

note, Ref. [45, 107].

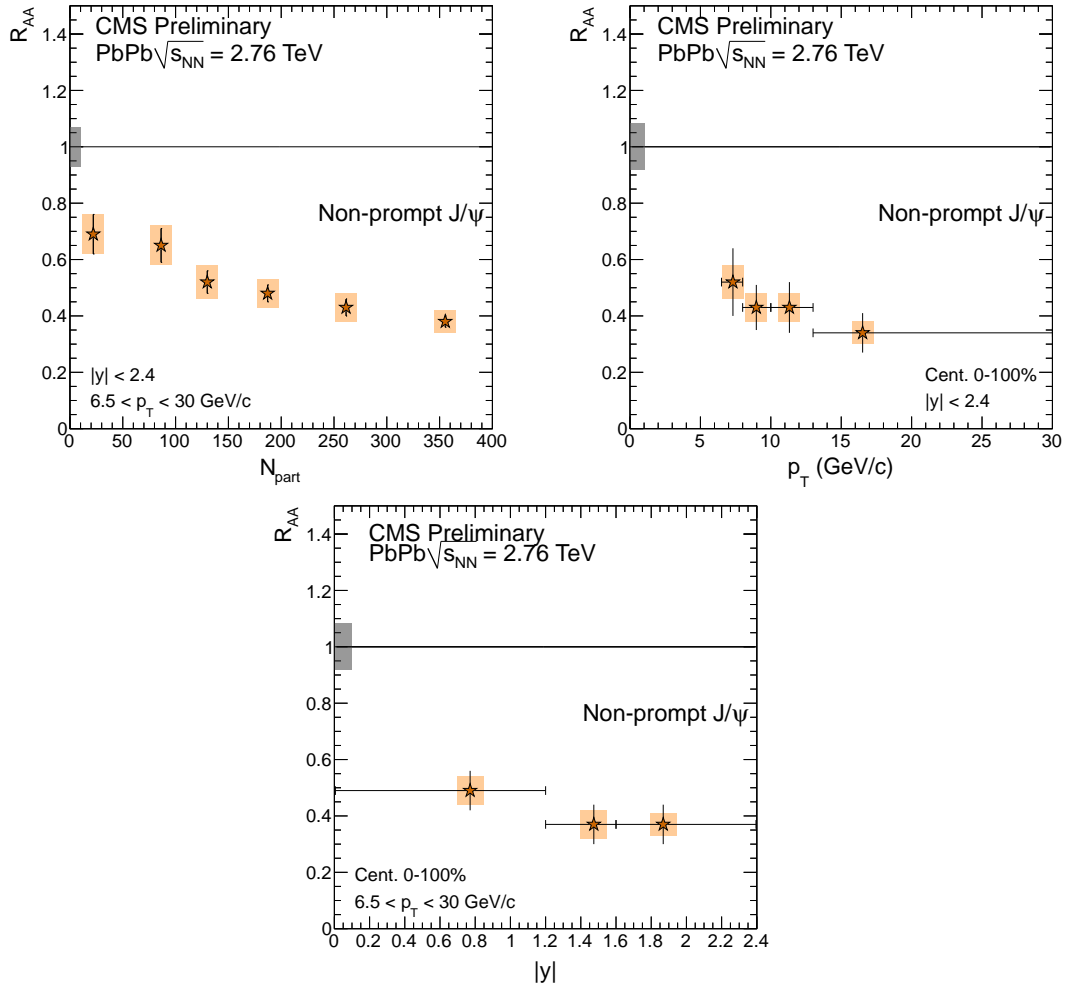


Fig. 69. The nuclear modification factor as function of centrality (*left*),  $p_T$  (*right*) and rapidity (*bottom*) for the non-prompt  $J/\psi$ . The gray boxes plotted at  $R_{AA}=1$  indicate the scale of the global uncertainties: (left) the uncertainty of 6% on the measured integrated luminosity of the pp data sample, together with the statistical and systematic uncertainty on the pp data set; (right and bottom) the pp luminosity and the  $T_{AA}$  uncertainties. The bin boundaries are indicated by small horizontal lines where meaningful.

Fig 70 (Left) shows the nuclear modification factor ( $R_{AA}$ ) of  $J/\psi$  in PbPb collisions at  $\sqrt{s_{NN}} = 2.76$  TeV as a function of number of participants (centrality) measured by CMS [97, 107], comparing with the STAR results [108] at RHIC. It tells

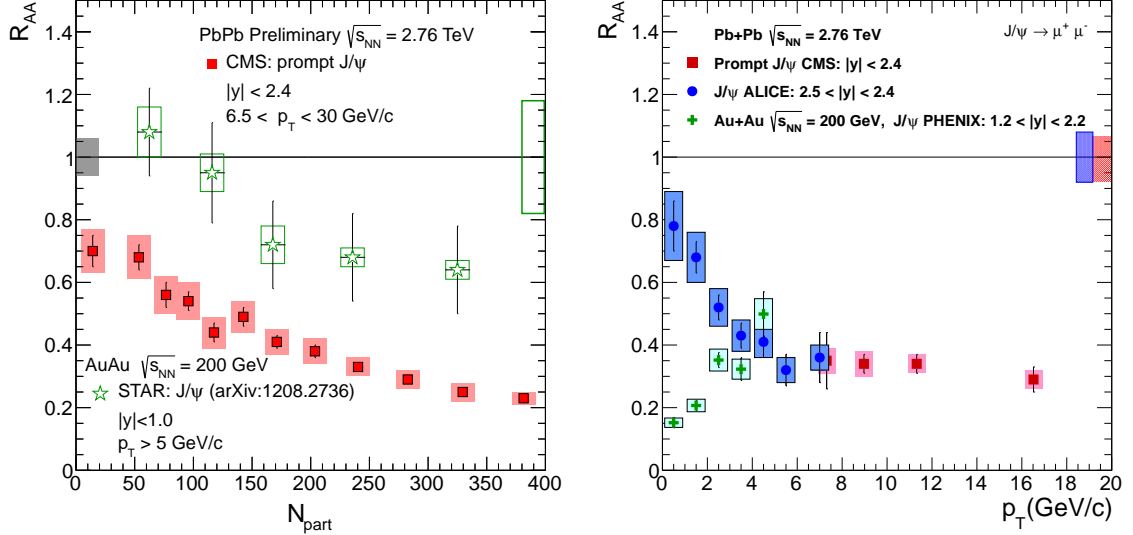


Fig. 70. (Left) The nuclear modification factor ( $R_{AA}$ ) of  $J/\psi$  in PbPb collisions at  $\sqrt{s_{NN}} = 2.76$  TeV as a function of number of participants measured by CMS experiment [97, 107]. RHIC measurements are shown for comparison [108]. (Right) Nuclear modification factor ( $R_{AA}$ ) of  $J/\psi$  as a function of  $p_T$  measured by CMS [97, 107], ALICE [109] and PHENIX [86] experiments.

the suppression of (high  $p_T$ )  $J/\psi$  has increased with collision energy. The ALICE results on  $J/\psi$  correspond to a low  $p_T$  range which have little or no centrality dependence except for the most peripheral collisions [89]. Fig 70 (Right) shows  $R_{AA}$  of  $J/\psi$  in PbPb collisions at  $\sqrt{s_{NN}} = 2.76$  TeV as a function of  $p_T$  measured by CMS, ALICE and PHENIX experiments. The  $R_{AA}$  is found to be nearly independent of  $p_T$  (above 6.5 GeV/c) showing that  $J/\psi$  remains suppressed even at very high  $p_T$  upto 16 GeV/c [97, 107]. The ALICE  $J/\psi$  data [109] shows that  $R_{AA}$  increases with decreasing  $p_T$  below 4 GeV/c. On comparing with the PHENIX forward rapidity

measurement [86], it can be said that  $J/\psi$  with low  $p_T$  are enhanced at LHC in comparison to RHIC. These observations suggest regeneration of  $J/\psi$  at low  $p_T$  by recombination of independently produced charm pairs.

In summary, the prompt  $J/\psi$ , integrated over the rapidity range  $|y| < 2.4$  and high- $p_T$ ,  $6.5 < p_T < 30$  GeV/ $c$ , has been measured in 12 centrality bins, starting with the 0-5% bin (most central), up to 60–100% bin (most peripheral). The  $R_{AA}$  shows a steady and smooth decrease of suppression with the  $R_{AA}$  remaining  $< 1$  in the most peripheral bin. Integrated over rapidity and centrality, there is no evidence of suppression dependence with  $p_T$ , confirming the 2010 results published in two bins [97]. There is no significant rapidity dependence of the high- $p_T$  prompt  $J/\psi$   $R_{AA}$  when integrating over centrality and  $p_T$ . The low- $p_T$  prompt  $J/\psi$  are consistent with the suppression of the high- $p_T$  prompt  $J/\psi$  over all centrality bins.

For non-prompt  $J/\psi$ , the centrality dependence shows a slow decrease of the  $R_{AA}$  with decreasing centrality. For high- $p_T$  non-prompt  $J/\psi$  there is an indication of less suppression in the mid-rapidity region compared to forward region, while the  $p_T$  dependence results show hints of less suppression at low  $p_T$ . However, in both cases, within the present uncertainties, all measured values are compatible with being the same. These measurements represent the first unambiguous and detailed look at the b-quark energy loss dependence on centrality,  $p_T$  and rapidity.

# CHAPTER 6

Measurement of the  $\psi(2S)$  meson in PbPb collisions at  $\sqrt{s_{\text{NN}}} = 2.76$  TeV

## 6.1. Introduction

The  $\psi(2S)$  meson yield in PbPb collisions is of particular interest when compared to the  $J/\psi$  meson. As the  $\psi(2S)$  meson is less bound than the  $J/\psi$ , it is expected to melt already at lower temperatures. This “sequential melting” [110] should manifest itself in a smaller nuclear modification factor ( $R_{AA}$ ) of  $\psi(2S)$  mesons compared to that of the  $J/\psi$ . Since the NA50 experiment at the SPS [111],  $\psi(2S)$  mesons have not been measured anymore in heavy-ion collisions. For a review of charmonium suppression at lower collision energies see *e.g.* Ref. [87].

Due to the large number ( $\mathcal{O}(100)$ ) of charm quarks and antiquarks produced in PbPb collisions at  $\sqrt{s_{NN}} = 2.76$  TeV [112], charmonia may be produced at the hadronization stage of the PbPb collisions from initially uncorrelated charm and anticharm quarks produced in the initial inelastic collisions [64]. Such models typically predict less production of  $\psi(2S)$  than  $J/\psi$  [113, 112]. Due to the thermal nature, recombination effects would be contributing mostly at low charmonium  $p_T$ . Furthermore, cold nuclear matter effects may affect charmonia in pPb and PbPb collisions [114, 112, 115]. In pPb collisions at  $\sqrt{s_{NN}} = 5.02$  TeV, a suppression of  $J/\psi$  has been measured at forward rapidity by ALICE and LHCb [116, 117]. First measurements at RHIC suggest an even stronger suppression of  $\psi(2S)$  than of  $J/\psi$  at low  $p_T$  in central dAu collisions at  $\sqrt{s_{NN}} = 200$  GeV [118].

In this analysis non-prompt  $J/\psi$  and  $\psi(2S)$  are removed with a cut on the pseudo-proper decay length. The results are presented in the form of a double ratio:  $\chi_{\psi(2S)} = (N_{\psi(2S)}/N_{J/\psi})_{PbPb}/(N_{\psi(2S)}/N_{J/\psi})_{pp}$  which compares the ratio of prompt  $\psi(2S)$  over prompt  $J/\psi$  yields ( $R_{\psi} \equiv N_{\psi(2S)}/N_{J/\psi}$ ) in PbPb and pp collisions. The analysis is based on data samples collected in 2011 and 2013, the PbPb (pp) sample corresponds to an integrated luminosity of  $150 \mu\text{b}^{-1}$  ( $5.4 \text{ pb}^{-1}$ ). In the PbPb sample an iterative

track reconstruction (RegIt-Regional Iterative Tracking) is employed to find more tracks in the silicon tracker that can be matched to the standalone muons. The double ratio has the advantage that efficiency and acceptance corrections cancel under the assumption of unmodified polarizations, leading to reduced uncertainties. However, since yields are uncorrected for acceptance and efficiency, any deviation from unity will reflect a yield modification of only the quarkonia that are reconstructed in the CMS detector. The double ratio can also be written as the ratio of  $\psi(2S)$  and  $J/\psi$  nuclear modification factors:  $R_{AA}(\psi(2S))/R_{AA}(J/\psi)$ . Hence, a prompt  $\psi(2S)$   $R_{AA}$  is derived, based on a previously published prompt  $J/\psi$   $R_{AA}$  [97].

## 6.2. Signal extraction

The analysis is performed in two  $(p_T, y)$  kinematical ranges:

- At forward rapidity ( $1.6 < |y| < 2.4$ ),  $J/\psi$  and  $\psi(2S)$  can be reconstructed down to  $p_T = 3 \text{ GeV}/c$ .
- At midrapidity,  $|y| < 1.6$ , only  $J/\psi$  and  $\psi(2S)$  of  $p_T > 6.5 \text{ GeV}/c$  are reconstructed, as imposed by the single-muon acceptance.

For both regions, an explicit upper limit of  $p_T = 30 \text{ GeV}/c$  is imposed. Furthermore, the PbPb sample is binned in collision centrality. The centrality of heavy-ion collisions, *i.e.* the geometrical overlap of the incoming nuclei, is related to the energy released in the collisions. The centrality classes used in this analysis are 40–100%, 20–40%, and 0–20%, ordered from the lowest to the highest HF energy deposit. The corresponding  $\langle N_{\text{part}} \rangle$  values are 32.8, 158.7, and 308.4.

The same single muon acceptance criteria as in Ref. [97] have been applied. Additional minimal muon selection criteria are applied as reported in the same reference.

Only opposite-sign muon pairs are considered that have a  $\chi^2$  probability larger than 1% to originate from a common vertex.

$J/\psi$  and  $\psi(2S)$  mesons coming from b-hadron decays are identified by the measurement of a secondary  $\mu^+\mu^-$ -vertex displaced from the primary collision vertex. From the displacement  $L_{xy}$ , the pseudo-proper decay length  $\ell_{J/\psi} = L_{xy} m_{J/\psi}/p_T$  is computed as an estimate of the b-hadron decay length. The pseudo-proper decay length is measured with a resolution of  $\approx 35 \mu\text{m}$ , decreasing with rapidity. Non-prompt charmonia are removed with a cut on  $\ell_{J/\psi}$ . The cut is tuned on Monte Carlo (MC) simulations, such that 90% of the prompt  $J/\psi$  are kept. This typically rejects 80% of the non-prompt  $J/\psi$ . It has been checked that the same cut applied on the  $\psi(2S)$  yields the same prompt efficiency (within 0.1%) and non-prompt rejection (within 2%), when using the  $\psi(2S)$  mass in the calculation of the pseudo-proper decay length. Due to the different primary vertex resolution in pp and PbPb, the cut is tuned separately for the two collision systems.

The distributions of the prompt  $J/\psi$  efficiencies as a function the pseudo-proper decay length cut are shown in Figs. 71–72. The cut values used in the analysis are summarised in Table XI: As the efficiency of prompt  $J/\psi$  and  $\psi(2S)$  is chosen to be

Table XI. Cuts on the pseudo-proper decay length  $\ell_{J/\psi}$  to reject non-prompt  $J/\psi$  and  $\psi(2S)$ .

$ y $	$p_T$ [GeV/c]	pp	PbPb
0–1.6	6.5–30	$\ell_{J/\psi} < 0.04 \text{ mm}$	$\ell_{J/\psi} < 0.04 \text{ mm}$
1.6–2.4	3–30	$\ell_{J/\psi} < 0.09 \text{ mm}$	$\ell_{J/\psi} < 0.08 \text{ mm}$

always 90%, the efficiency cancels in the double ratio. The remaining non-prompt contamination contributes to the systematic uncertainty.

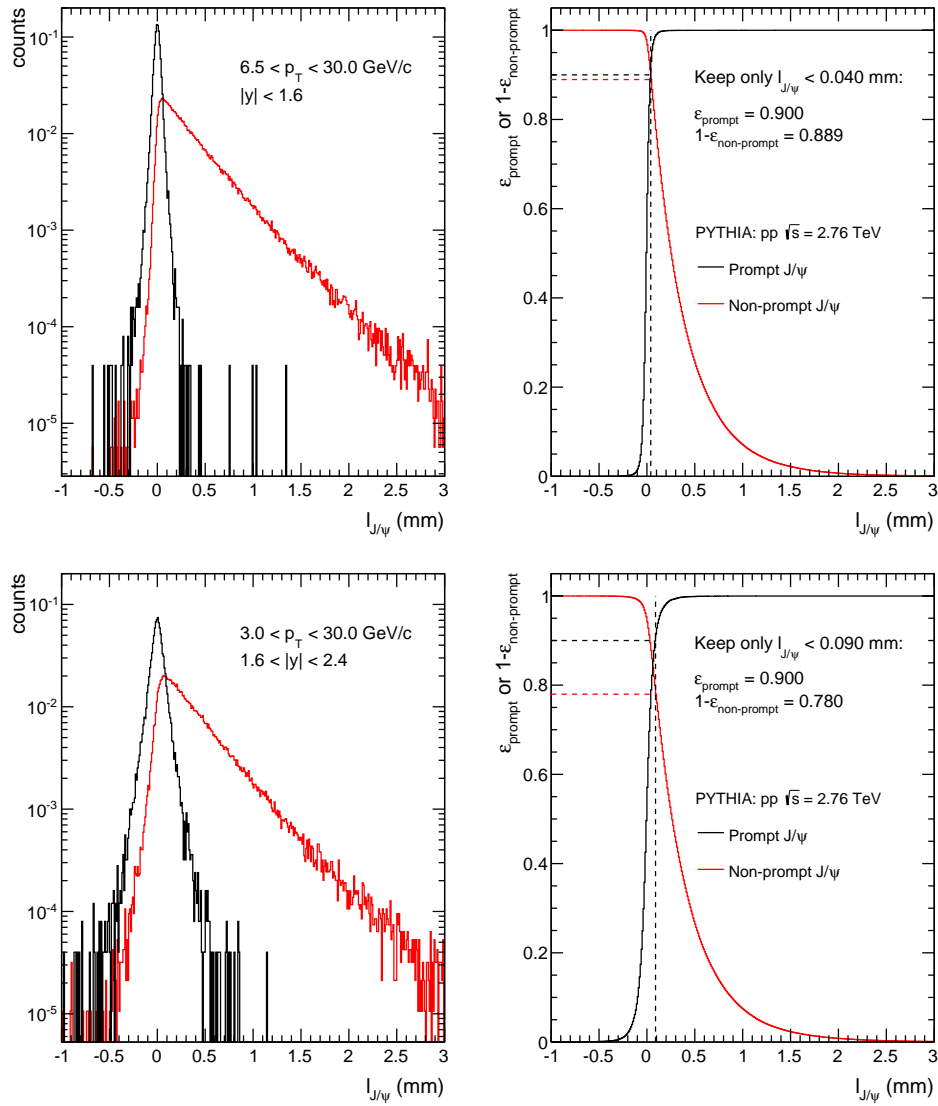


Fig. 71. Pseudo-proper decay length distributions of prompt and non-prompt  $J/\psi$  (left sub-panels) in pp MC simulations. The right sub-panels shows the prompt efficiencies and non-prompt rejection efficiencies as a function of  $l_{J/\psi}$ . Each row is for different kinematic region, which is indicated in the figure.

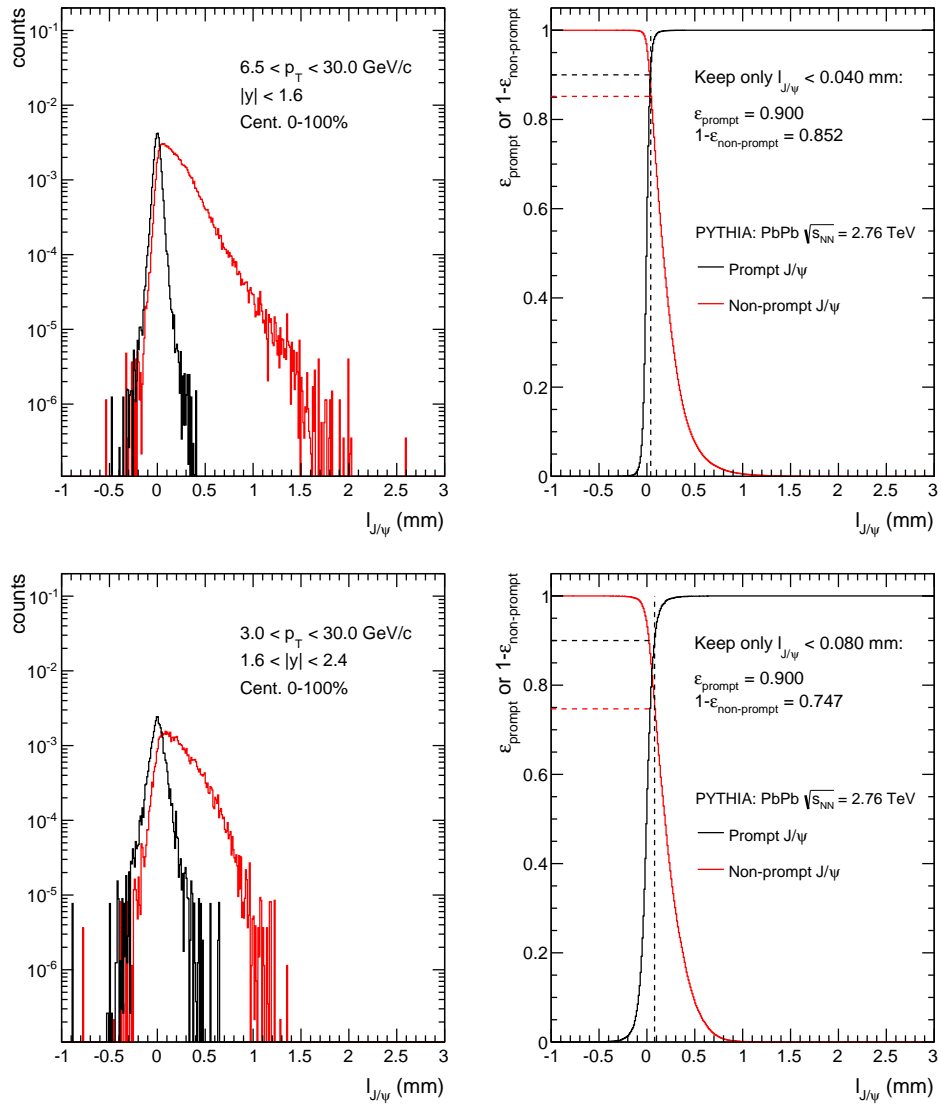


Fig. 72. Prompt and non-prompt pseudo-proper decay length distributions of  $J/\psi$  (left sub-panels) in PbPb MC simulations. The right sub-panels show the prompt efficiency and non-prompt rejection efficiency as a function of  $l_{J/\psi}$ . Each panel is for different kinematic region, which is indicated in the figure.

The  $J/\psi$  signal is well described by the sum of a Gaussian and a Crystal Ball (CB) function [97, 119], with common mean  $m_0$  and independent widths  $\sigma_{\text{Gauss}}$  and  $\sigma_{\text{CB}}$ . The parameter  $\alpha$  defines the transition between the Gaussian core and the power-law function. The same lineshape is used for the  $\psi(2S)$ . The CB parameters  $\alpha$  and  $n$  are common between the  $J/\psi$  and  $\psi(2S)$  functions and fixed to values found in fits to MC simulations. The two width parameters of the Gaussian and CB functions for the  $\psi(2S)$  shape are set to be equal to the  $J/\psi$  parameters multiplied by the world average mass ratio of  $\psi(2S)$  and  $J/\psi$  ( $m_{\psi(2S)}/m_{J/\psi} = 1.1902$ ) [120]. The  $\psi(2S)$  and  $J/\psi$  mean mass ratio is also fixed to the world average. The following parameters are left free in the fit of pp data:  $m_0$ ,  $\sigma_{\text{CB}}$ ,  $\sigma_{\text{Gauss}}$ , and the  $J/\psi$  and  $\psi(2S)$  yields. In the PbPb data fit, the ratio of  $\sigma_{\text{Gauss}}/\sigma_{\text{CB}}$  is fixed to the value found MC simulations.

The background is described by a Chebychev polynomial of order  $N$ . The order  $N$  is determined by performing a log-likelihood ratio (LLR) test separately for each analysis bin. This test compares the resulting minimised negative log-likelihood (NLL) of a fit with order  $N$  to the NLL with orders  $N + 1$  and  $N + 2$  (the second one is necessary to account for the change between odd and even parity as the order is increased). In particular, 2 times the differences between the NLL values for the fits with polynomials of orders  $N$  and  $M > N$  follow a  $\chi^2$  distribution with  $M - N$  degrees of freedom. The variables

$$\begin{aligned}\chi_{N \rightarrow N+1}^2 &:= 2(NLL_N - NLL_{N+1}) \\ \chi_{N \rightarrow N+2}^2 &:= 2(NLL_N - NLL_{N+2})\end{aligned}\tag{6.1}$$

can thus be used to decide whether or not the increase of order allows for the function fit the data *significantly* better, where significantly better is defined to be the case as

long as

$$\begin{aligned}
 p(\chi^2 \geq \chi_{N \rightarrow N+1}^2) &< 0.05 \\
 p(\chi^2 \geq \chi_{N \rightarrow N+2}^2) &< 0.05.
 \end{aligned}
 \tag{6.2}$$

A summary of the best fits is given in Table XII. All analysis bins use polynomials of order  $0 \leq N \leq 3$ . The results of LLR test are confirmed by the Akaike information criterion (AIC) test which is defined as

$$\text{AIC} = 2(k + \text{NLL})
 \tag{6.3}$$

where  $k$  is the number of free parameters in the polynomials of order  $N$ . An example of LLR result for pp and PbPb (0-100%) is given in Table XIII.

Table XII. Order of Chebychev polynomials used as background shapes in the fitting of pp and PbPb data as determined by a LLR test.

$ y $	$p_T$ [GeV/ $c$ ]	Order $N$			
		pp	PbPb (0–20%)	(20–40%)	(40–100%)
0–1.6	6.5–30	3	1	1	0
1.6–2.4	3–30	1	3	2	1

In Figs. 73 and Figs. 74 the invariant-mass spectra of  $\mu^+\mu^-$  pairs in pp and the centrality binned PbPb data (0-20%, 20-40% and 40-100%) at  $\sqrt{s_{\text{NN}}} = 2.76$  TeV at midrapidity ( $|y| < 1.6$  and  $6.5 < p_T < 30 \text{ GeV}/c$ ) and at forward rapidity ( $1.6 < |y| < 2.4$  and  $3 < p_T < 30 \text{ GeV}/c$ ) respectively are shown. The result of a simultaneous fit to all four samples is overlaid. The data are well described by the signal and background shapes in all bins. No significant  $\psi(2S)$  signal is observed in peripheral collisions at midrapidity. While the fits are performed on the unbinned data, a binned pull distribution is shown in the bottom sub-panels of each figure. The

Table XIII. Negative loglikelihoods for fits with Chebychev polynomials of orders 0–5 of pp and PbPb data (0-100%) in  $|y| < 1.6$  and  $6.5 < p_T < 30 \text{ GeV}/c$ . In addition the p-values of the LLR-test for the null-hypothesis are listed. If the p-value is less than 5%, the null-hypothesis is rejected and the higher order polynomial is preferred. Tests of which the null-hypothesis cannot be rejected for two consecutive orders are highlighted in bold, together with the corresponding order.

System	$N$	NLL	$p(H_0: N = 1)$	$p(H_0: N = 2)$	$p(H_0: N = 3)$
PP	0	-155967.86			
	1	-155993.31			
	2	-155993.41	65.4%		
	<b>3</b>	-155999.36	0.2%	0.1%	
	4	-155999.43	0.7%	0.2%	<b>71.2%</b>
	5	-156000.90	0.4%	0.2%	<b>21.4%</b>
PbPb (0–100%)	0	-122178.89			
	<b>1</b>	-122231.11			
	2	-122231.37	<b>47.1%</b>		
	3	-122232.24	<b>32.2%</b>	18.6%	
	4	-122232.26	51.1%	40.9%	84.3%
	5	-122232.30	66.4%	60.0%	94.0%

pulls for a given parameters  $p$  are defined as:

$$pull = \frac{P_{fit} - P_{model}}{\sigma(p_{fit})} \quad (6.4)$$

The  $\chi^2$  is calculated to provide further information about the fit quality. The  $\chi^2$  probability is usually quite good, indicating good agreement between the data and the fitted shape.

Once the best background shape is defined, the pp and PbPb data are fitted simultaneously, with the PDF parameterized such that the three double ratios for the centrality bins 0–20%, 20–40%, and 40–100% appear directly as free parameters, replacing the PbPb single ratios as fit parameters. All three PbPb centrality bins and the pp sample are fitted together. The PbPb single ratios can then be defined as:

$$\begin{aligned} R_\psi(0-20\%) &= \chi_\psi(0-20\%) \times R_\psi(pp) \\ R_\psi(20-40\%) &= \chi_\psi(20-40\%) \times R_\psi(pp) \\ R_\psi(40-100\%) &= \chi_\psi(40-100\%) \times R_\psi(pp). \end{aligned} \quad (6.5)$$

And the  $\psi(2S)$  yields are:

$$\begin{aligned} N_{\psi(2S)}(0-20\%) &= \chi_\psi(0-20\%) \times R_\psi(pp) \times N_{J/\psi}(0-20\%) \\ N_{\psi(2S)}(20-40\%) &= \chi_\psi(20-40\%) \times R_\psi(pp) \times N_{J/\psi}(20-40\%) \\ N_{\psi(2S)}(40-100\%) &= \chi_\psi(40-100\%) \times R_\psi(pp) \times N_{J/\psi}(40-100\%). \end{aligned} \quad (6.6)$$

This definition has the advantage that the fit result can be used easily to calculate upper limits and confidence intervals using the RooStats package [121]. In this simultaneous fit, the background shapes of the four samples are independent. The signal shape parameters in pp are independent from the ones in PbPb. The signal shape parameters are, however, common to the three PbPb centrality bins. It has been

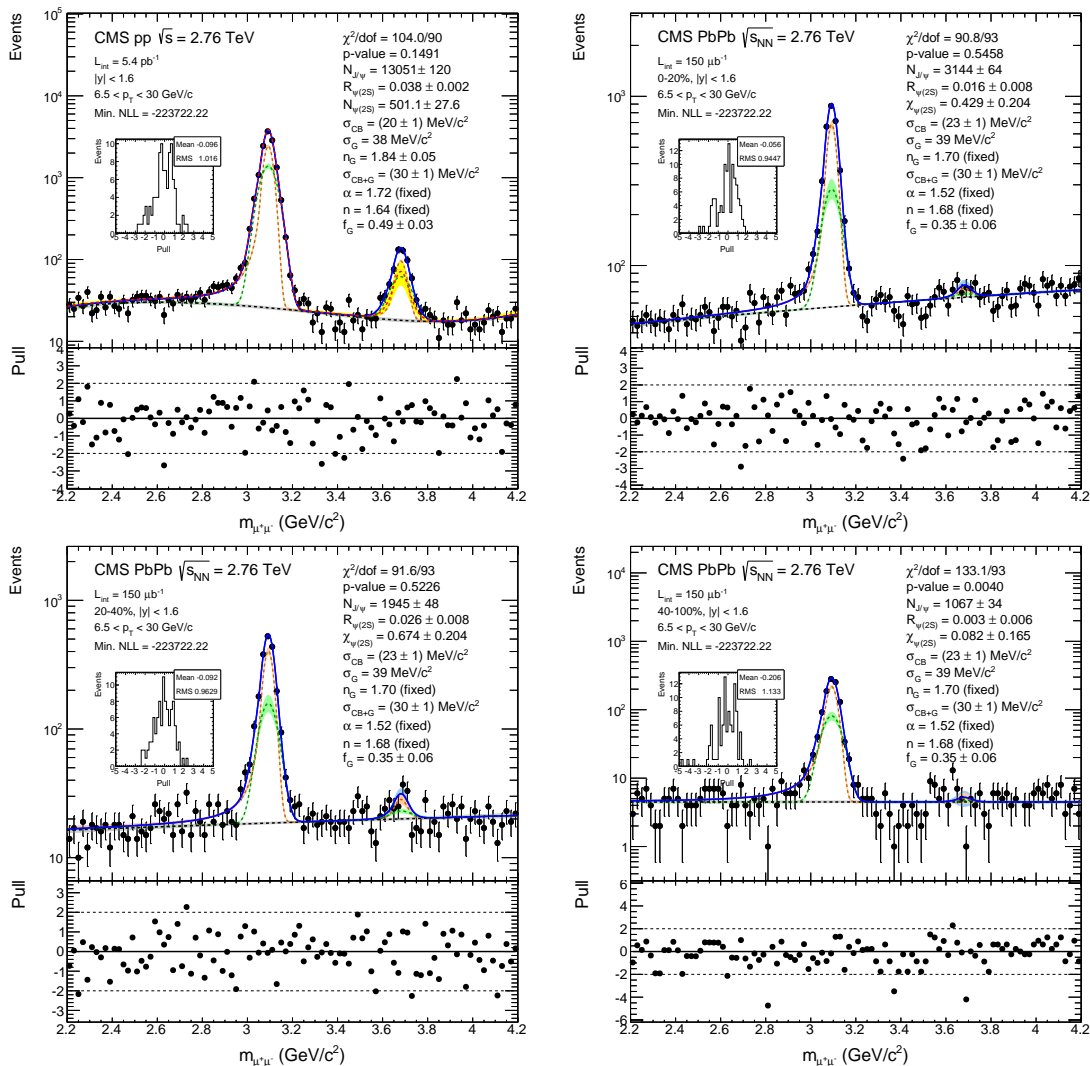


Fig. 73. Invariant-mass spectrum of  $\mu^+\mu^-$  pairs in pp and PbPb data (0-20%, 20-40% and 40-100%). The  $p_T$  and rapidity bins are  $6.5 < p_T < 30 \text{ GeV}/c$  and  $|y| < 1.6$ . The fit to the data with the functions discussed in the text is shown as the black line. The black dashed line represents the background. The orange and green dashed lines are the CB and Gaussian contributions on top of the background, respectively. The shaded bands represent  $\pm 1\sigma$  uncertainty bands due to the statistical uncertainty of the data. The pp data are also overlaid with a shape (red dashed line), in which  $R_{\psi}$  has been set to the value found in each centrality bin. The bottom sub-panels show the pull distributions between data and fit. The small inserts in the upper sub-panel show the pull projections.

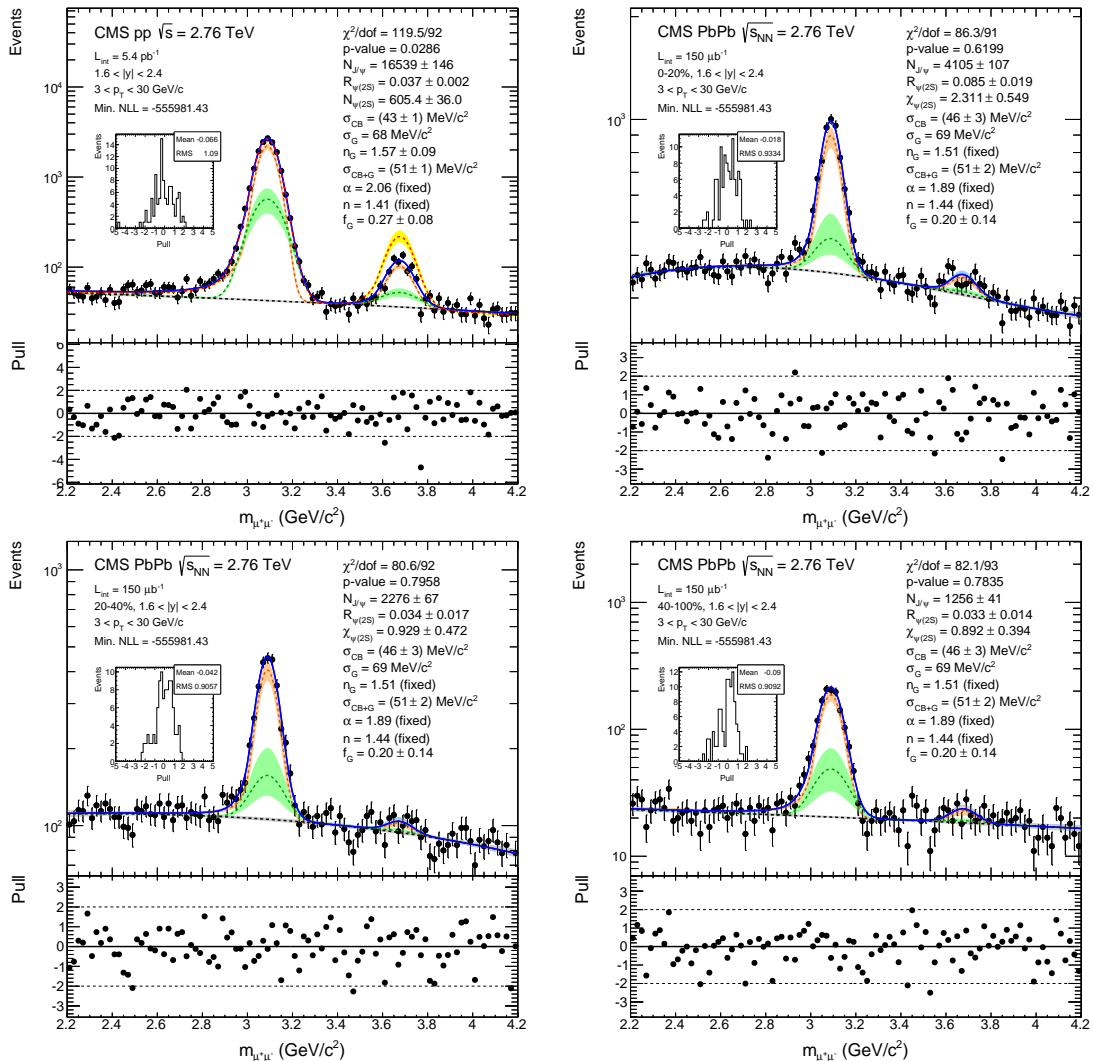


Fig. 74. Invariant-mass spectrum of  $\mu^+\mu^-$  pairs in pp and PbPb data (0-20%, 20-40% and 40-100%). The  $p_T$  and rapidity bins are  $3 < p_T < 30 \text{ GeV}/c$  and  $1.6 < |y| < 2.4$ . The fit to the data with the functions discussed in the text is shown as the black line. The black dashed line represents the background. The orange and green dashed lines are the CB and Gaussian contributions on top of the background, respectively. The shaded bands represent  $\pm 1\sigma$  uncertainty bands due to the statistical uncertainty of the data. The pp data are also overlaid with a shape (red dashed line), in which  $R_b$  has been set to the value found in each centrality bin. The bottom sub-panels show the pull distributions between data and fit. The small inserts in the upper sub-panel show the pull projections.

checked that the signal shapes do not vary significantly as a function of centrality.

### 6.3. Systematic checks and uncertainties

#### 6.3.1. Signal extraction

To evaluate the systematic uncertainty on the signal shape, the sum of two Crystall Ball functions is used. As for the default shape, the means are shared. The second Crystall Ball function uses the same tail parameters  $\alpha$  and  $n$  as the first Crystall Ball function. In the simultaneous fit to pp data and the three PbPb centrality bins the previously fixed parameters  $\alpha(\text{pp})$ ,  $n(\text{pp})$ ,  $\alpha(\text{PbPb})$ ,  $n(\text{PbPb})$ , and  $n_{\text{G}}(\text{PbPb})$  are left free. The difference to the nominal fit, typically 1% at midrapidity and 3% at forward rapidity, is assigned as systematic uncertainty. The background shape uncertainty is determined by an alternate background model, an exponential function with a Chebychev polynomial of order  $X$  as exponent ( $X = 1$ : exponential function,  $X = 2$ : Gaussian function). It was checked with a Toy MC simulation that this kind of background model does not introduce a strong bias on the  $R_{\psi}$  when the actual background has the shape of the nominal background model and vice versa. A LLR test is performed to decide which order fits the data best. The best fits have orders in the range  $1 \leq X \leq 3$  and are summarised in Table XIV. Note that for  $X = 0$  the shape is just a constant. In the case that the nominal fit also finds that the best fit is a constant ( $N = 0$ ), an alternative background shape with order  $X = 1$  is used. The difference to the nominal fit is then assigned as systematic uncertainty, typically 3%. Furthermore the results were cross checked by integrating the data above a background fit, which showed good agreement with the nominal fit.

In addition, an uncertainty was assigned to the sensitivity of the result to the fitted invariant-mass region. For this the data were fit over the invariant-mass interval

Table XIV. Exponential background shapes used as alternatives in the fitting of pp and PbPb data as determined by a LLR test.

$ y $	$p_T$ [GeV/ $c$ ]	Order $X$				
		pp	PbPb (0–100%)	(0–20%)	(20–40%)	(40–100%)
0–1.6	6.5–30	3	1	1	1	1
1.6–2.4	3–30	3	2	3	2	1

1.8–5GeV/ $c^2$ . The result was then used to generate toy experiments that were fitted over the full mass range and over the nominal mass range of 2.2–4.2GeV/ $c^2$ . The difference in the average double ratio for these two mass regions observed in the toy experiments is taken as systematic uncertainty. The differences to the nominal fits are summarised in Table XV. The total systematic uncertainty is the quadratic sum of the signal and background differences and the variation observed from the change of the fitted invariant-mass region.

## 6.4. Efficiency and Acceptance

### 6.4.1. Efficiency studies

Any difference in efficiency and acceptance between PbPb and pp that affects the  $\psi(2S)$  in the same way as the  $J/\psi$  will cancel in the  $R_\psi$  ratio. The only effects that would not cancel in the double ratio are higher order effects that affect  $J/\psi$  and  $\psi(2S)$  differently and, at the same time, do that differently in PbPb and pp. The same trigger logic was employed during the pp and PbPb data taking periods. However, the offline reconstruction algorithm are not the same for the two samples, which can lead to imperfect cancellations of efficiencies. To study the impact of such effects

Table XV. Absolute and relative systematic uncertainty on the data fits. Absolute uncertainties are multiplied by  $10^{-3}$ . The pp column is only to illustrate the size of the variations on  $R_\psi(\text{pp})$ . These variations are already included in the variations of the double ratios shown in the other columns and do not enter as additional term in the systematic uncertainties.

$ y $	$p_T$ [GeV/ $c$ ]	Type	pp	0–100%	0–20%	20–40%	40–100%
0–1.6	6.5–30	Signal	-0.28	40	34	44	47
		Background	-0.22	3.4	15	12	-45
		Fit range	0.27	31	34	34	38
		Total	0.45	51	51	56	75
		Total (rel.)	1%	11%	12%	8%	92%
1.6–2.4	3–30	Signal	0.61	-24	-54	13	6.3
		Background	0.86	-32	-75	28	-2.8
		Fit range	0.04	217	300	260	89
		Total	1.1	220	314	262	89
		Total (rel.)	3%	13%	14%	28%	10%

in the double ratio, efficiencies and acceptances have been calculated from MC simulations of  $\psi(2S)$  and  $J/\psi$  in PbPb and pp. Prompt  $J/\psi$  and  $\psi(2S)$  are produced using PYTHIA 6.424, with non-relativistic quantum chromodynamics matrix elements tuned by comparison with CDF data [122]. The  $J/\psi$  and  $\psi(2S)$  decays are simulated using the EVTGEN package. Prompt  $J/\psi$  and  $\psi(2S)$  are simulated assuming unpolarized production. Final-state bremsstrahlung is implemented using PHOTOS. Underlying heavy-ion events are produced with the HYDJET 1.8 event generator. The detector response is simulated with GEANT4. The signal events are embedded

at the level of detector hits and with matching vertices. The embedded events are then processed through the trigger emulation and the full event reconstruction chain.

Figure 75 shows the comparison between the reconstruction efficiencies of  $J/\psi$  and  $\psi(2S)$  in various kinematic bins. The  $\psi(2S)$  efficiency is always larger than that of  $J/\psi$ , as the average  $p_T$  of muons from  $\psi(2S)$  decays is higher than for muons from  $J/\psi$  due to the mass difference. The efficiency, for either  $J/\psi$  or  $\psi(2S)$  in PbPb, is shown to increase as a function of the event centrality. Table XVI shows the recon-

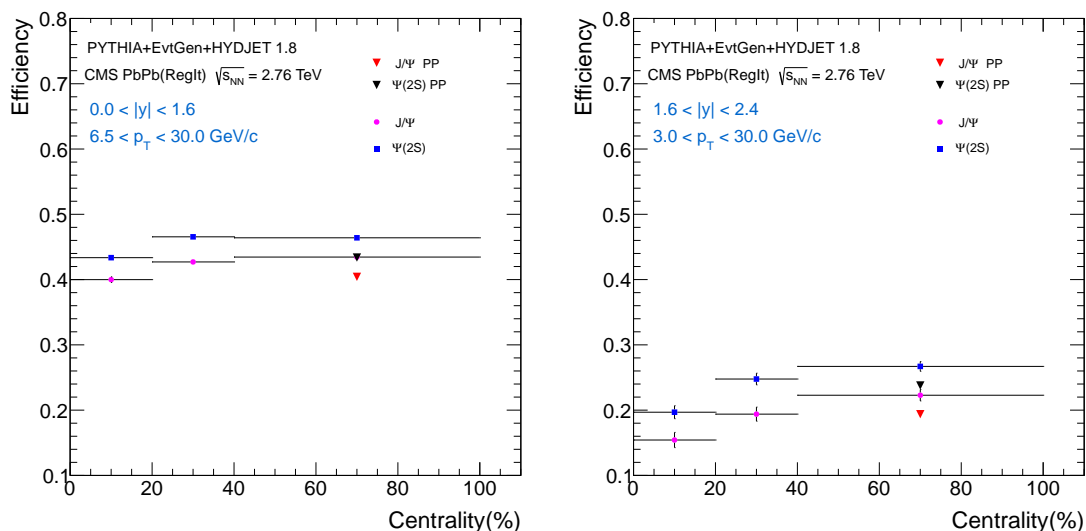


Fig. 75. Reconstruction efficiency as a function of centrality for simulated  $J/\psi$  and  $\psi(2S)$  from RegIt PbPb and pp. The blue square denotes the efficiency of  $\psi(2S)$  and the magenta circle that of  $J/\psi$ .

struction efficiencies of  $\psi(2S)$  and  $J/\psi$  in various kinematic range with centrality bins (0–20%, 20–40%, 40–100% and 0–100%). Similarly the reconstruction efficiency for pp is calculated using simulated events and shown in the same table. These efficiencies include the pseudo-proper decay length cut.

For each analysis bin the double ratio of the efficiencies is calculated as

$$DR_{\varepsilon} = \frac{\varepsilon_{\psi(2S)}(\text{PbPb})/\varepsilon_{J/\psi}(\text{PbPb})}{\varepsilon_{\psi(2S)}(\text{pp})/\varepsilon_{J/\psi}(\text{pp})} \quad (6.7)$$

and listed in the table as well. The efficiency values in the numerator and the denominator are obtained from simulation. This double ratio is the relevant quantity that would need to be applied as correction to the measured (data) double ratio of  $\psi(2S)$  and  $J/\psi$ , if the efficiencies did not cancel. However, the double ratio of efficiencies is found to be compatible with unity in all analysis bins, within the MC statistical uncertainty. Therefore, the statistical uncertainty on the centrality integrated efficiency double ratio is assigned as a systematic uncertainty on the assumption of cancelling efficiency corrections in the double ratio analysis. The statistical uncertainty is 1% (3%) at midrapidity (forward rapidity). The same  $p_T$  and rapidity

Table XVI. Reconstruction efficiency for  $J/\psi$  and  $\psi(2S)$  using bin counting method with RegIt PbPb and pp MC.

$ y $	$p_T[\text{GeV}/c]$	Cent.	$\varepsilon(J/\psi)$	$\varepsilon(\psi(2S))$	$\text{DR}_\varepsilon$
		0–20%	$40.0 \pm 0.4$	$43.4 \pm 0.4$	$1.01 \pm 0.02$
		20–40%	$42.7 \pm 0.4$	$46.6 \pm 0.4$	$1.02 \pm 0.02$
$ y  < 1.6$	$6.5 < p_T < 30$	40–100%	$43.5 \pm 0.3$	$46.4 \pm 0.3$	$1.00 \pm 0.01$
		0–100%	$41.0 \pm 0.3$	$44.5 \pm 0.3$	$1.01 \pm 0.01$
		pp	$40.4 \pm 0.3$	$43.4 \pm 0.3$	
		0–20%	$15.4 \pm 1.2$	$19.7 \pm 1.0$	$1.04 \pm 0.09$
		20–40%	$19.4 \pm 1.1$	$24.8 \pm 0.9$	$1.04 \pm 0.06$
$1.6 <  y  < 2.4$	$3 < p_T < 30$	40–100%	$22.3 \pm 0.9$	$26.7 \pm 0.7$	$0.98 \pm 0.04$
		0–100%	$17.1 \pm 0.8$	$21.6 \pm 0.7$	$1.04 \pm 0.05$
		pp	$19.4 \pm 0.1$	$23.8 \pm 0.2$	

distributions have been used in the simulation of pp and PbPb collisions. Based on existing measurements of the nuclear modification factors ( $R_{AA}$ ) as a function of  $p_T$

and rapidity [97, 45], variations in the  $p_T$  and rapidity distributions of  $\pm 30\%$  are considered following Ref [97]. A double ratio of efficiencies is calculated where the same variations are used for the  $\psi(2S)$  and  $J/\psi$  efficiencies, but opposite variations are used for the PbPb and pp efficiencies. Hence, the following variations are considered:

$$\frac{\varepsilon_{\psi(2S)}^+(\text{PbPb})/\varepsilon_{J/\psi}^+(\text{PbPb})}{\varepsilon_{\psi(2S)}^-(\text{pp})/\varepsilon_{J/\psi}^-(\text{pp})} \quad \text{and} \quad \frac{\varepsilon_{\psi(2S)}^-(\text{PbPb})/\varepsilon_{J/\psi}^-(\text{PbPb})}{\varepsilon_{\psi(2S)}^+(\text{pp})/\varepsilon_{J/\psi}^+(\text{pp})} \quad (6.8)$$

where efficiencies with linearly increasing (decreasing) weights are denoted with  $\varepsilon^+$  ( $\varepsilon^-$ ). Variations between  $\psi(2S)$  and  $J/\psi$  that change from pp to PbPb would be due to physics effects that the double ratio is supposed to measure. Hence they are not considered a systematic uncertainty. The larger of the two observed variations as a function of  $p_T$  is added in quadrature with the largest variation as a function of rapidity and assigned as systematic uncertainty on the kinematic distributions. This never exceeds 1%.

#### 6.4.2. Acceptance studies

The simulated MC sample are used to compute the acceptance. The dimuon acceptance is defined as the fraction of dimuon signals passing the single muon acceptance in a given  $(p_T, y)$  kinematic bin.

$$\alpha = \frac{N_{\text{Gen}(\psi(2S)/J/\psi)}^{\text{detectable}}(p_T, y)}{N_{\text{Gen}(\psi(2S)/J/\psi)}(p_T, y)} \quad (6.9)$$

where  $N_{\text{Gen}(\psi(2S)/J/\psi)}^{\text{detectable}}$  is the number generated events passing the single muon acceptance in the given  $(p_T, y)$  bin and within a mass interval  $M [2.0, 4.0]\text{GeV}/c^2$  for  $\psi(2S)$  and  $J/\psi$  and  $N_{\text{Gen}(\psi(2S)/J/\psi)}$  represents all dimuons generated within the given  $(p_T, y)$  bin.

The acceptance calculated for  $\psi(2S)$  and  $J/\psi$  is given in Table XVII. The acceptance values of  $\psi(2S)$  are larger than that of  $J/\psi$  as expected, since the  $\psi(2S)$  has

heavier mass and more number of  $\psi(2S)$  can pass the acceptance requirement. As

Table XVII. Acceptance of  $\psi(2S)$  and  $J/\psi$ .

$ y $	$p_T[\text{GeV}/c]$	$J/\psi$	$\psi(2S)$
$0.0 <  y  < 1.6$	$6.5 < p_T < 30$	$25.87 \pm 0.95$	$28.37 \pm 0.45$
$1.6 <  y  < 2.4$	$3.0 < p_T < 30$	$12.6 \pm 0.59$	$15.54 \pm 0.53$

the acceptance for  $J/\psi$  and  $\psi(2S)$  is independent of the collision system, it cancels in the double ratio.

Prompt  $J/\psi$  and  $\psi(2S)$  are simulated unpolarized. Measurements at the LHC [123, 124, 125] show indeed no strong polarizations. However, given current uncertainties, polarizations between  $\lambda_\vartheta = \pm 0.2$  in the helicity frame might still be possible in extreme cases. Opposite polarizations for  $\psi(2S)$  ( $\lambda_\vartheta = \pm 0.2$ ) and  $J/\psi$  ( $\lambda_\vartheta = \mp 0.2$ ) that change from pp to PbPb cause variations in the double ratio of efficiencies of  $\approx 1\%$ . Similar variations are observed, if one assumes opposite polarizations of  $\psi(2S)$  and  $J/\psi$  in pp collisions, but zero polarization in PbPb collisions. Such polarization scenarios would cause acceptance variations of  $\approx 20\%$ . Following previous double ratio analyses [98, 99, 126], these polarization effects are not considered as systematic uncertainties.

### 6.4.3. b-Hadron contamination

The measured  $J/\psi$  and  $\psi(2S)$  yields may still include a non-prompt contribution from b-hadron decays of up to 5%, after cutting on the  $\ell_{J/\psi}$ . This value is determined by the product of the b-hadron rejection inefficiency ( $\approx 20\%$ ) and the b-fraction. The b-fraction has been measured for  $J/\psi$  and  $\psi(2S)$  in pp collisions and is roughly

equal [104]. Given its  $p_T$  dependence, at midrapidity and high- $p_T$ , a b-fraction of 25% was used, while at forward rapidity and low- $p_T$  a value of 20% was taken. Measurements of the b-fraction of  $J/\psi$  in PbPb [97, 45] show little variation with respect to pp, as the non-prompt  $J/\psi$  are almost as suppressed as prompt  $J/\psi$ . Due to lack of better knowledge, the remaining b-hadron contamination are assumed to be independent for all four yields entering the double ratio. Hence the systematic uncertainty on the double ratio is  $\sqrt{4}$  times the estimated b-hadron contamination.

The total systematic uncertainty of 10–13% results from adding in quadrature the uncertainties on the fitting, the efficiency cancellation, shape uncertainty, and remaining b contamination.

#### 6.4.4. Summary of systematic uncertainties

All systematic uncertainties and the total are listed in Table XVIII. For comparison, also the statistical uncertainty on the double ratio is shown.

### 6.5. Confidence intervals and Limits

No significant  $\psi(2S)$  yield is found in the 40–100% PbPb centrality bin at midrapidity  $|y| < 1.6$  and high  $p_T$   $6.5 < p_T < 30$  GeV/ $c$ . Hence, a 95% confidence limit (CL) is set on the double ratio in this bin, using the Feldman-Cousins method. The systematic uncertainties are included as nuisance parameters  $\xi_i$  on the double ratio:

$$\left. \frac{(N_{\psi(2S)}/N_{J/\psi})_{PbPb}}{(N_{\psi(2S)}/N_{J/\psi})_{pp}} \right|_{\text{measured}} = \left. \frac{(N_{\psi(2S)}/N_{J/\psi})_{PbPb}}{(N_{\psi(2S)}/N_{J/\psi})_{pp}} \right|_{\text{true}} \cdot \xi_{\text{signal}} \cdot \xi_{\epsilon} \cdot \xi_b \quad (6.10)$$

These nuisance parameters are fixed to unity in the fit, but act as Gaussian constrains in the CL calculation. The width of these Gaussian constrains is set to the systematic uncertainties evaluated for each of the terms: signal extraction, efficiency cancellation,

Table XVIII. Summary of relative systematic uncertainties. For comparison, the statistical uncertainty on the double ratio is shown as well.

$ y $	$p_T$ [GeV/ $c$ ]	Type	0–100%	0–20%	20–40%	40–100%
0–1.6	6.5–30	Fit	11%	12%	8%	92%
		Efficiency	1%	1%	1%	1%
		b contamination	10%	10%	10%	10%
		Systematic	15%	15%	13%	92%
		Statistical	28%	47%	30%	200%
1.6–2.4	3–30	Fit	13%	14%	28%	10%
		Efficiency	5%	5%	5%	5%
		b contamination	8%	8%	8%	8%
		Systematic	16%	16%	30%	14%
		Statistical	20%	23%	50%	44%

and b-hadron contamination. The CL calculation is performed with the RooStats macro “StandardHypoTestInvDemo.C”, which is part of the ROOT tutorial [121]. The background only hypothesis is a double ratio of unity.

Confidence intervals have been determined for all bins, for example, see Fig. 76 for the peripheral bin 40-100% in mid rapidity. The results are summarised in Table XIX. than unity.

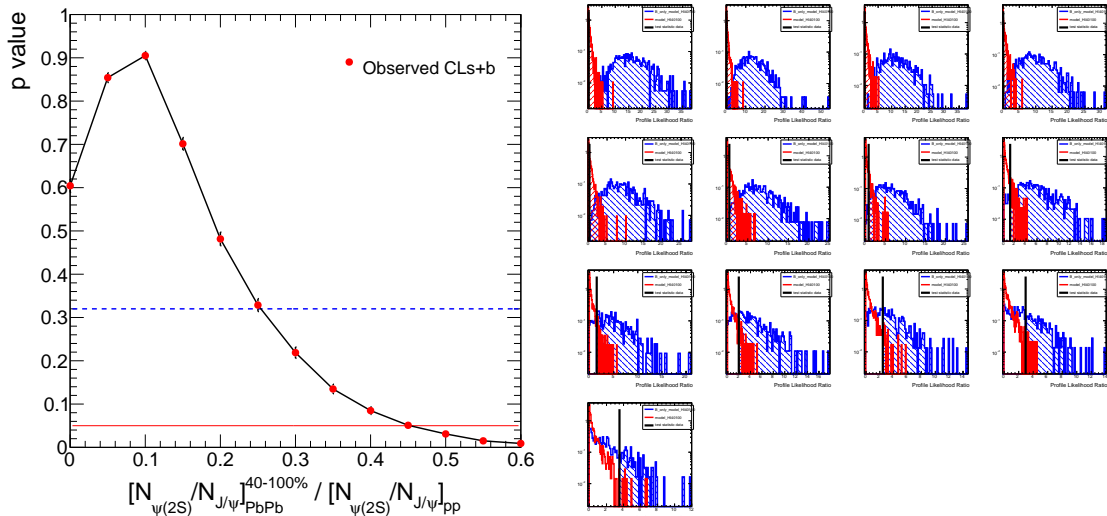


Fig. 76. Scan with Feldman-Cousins method for 95% confidence intervals using 100 Toy MC experiments at each scanned point for centrality bin 40–100% at  $|y| < 1.6$  and  $6.5 < p_T < 30 \text{ GeV}/c$ . The left column shows the result of the FC scan: the red and dashed blue line indicate confidence levels of 95% and 68% ( $1\sigma$ ). The right panel displays the Toy MC distributions for the signal+background and background only hypothesis.

## 6.6. Results

### 6.6.1. Results with old data

The first observation of the  $\psi(2S)$  meson in heavy-ion collisions at the LHC has been presented in a study reported in [128] with pp data sample ( $231 \text{ nb}^{-1}$ ) and PbPb data ( $150 \mu\text{b}^{-1}$ ) at  $\sqrt{s_{NN}} = 2.76 \text{ TeV}$ , collected in the year 2010 and 2011 respectively. The results of the double ratio measurement are shown in 77 as a function of centrality, for the lower  $p_T$  (left) and higher  $p_T$  (right) selections. Since the uncertainties on  $R_{\psi(2S)}(\text{pp})$  are common to all centralities, they are not displayed on each point, but rather shown as a grey area, adding the statistical and systematic uncertainties in quadrature. The error bars and boxes stand for the statistical and

Table XIX. 95% confidence intervals using the Feldman-Cousins method

$ y $	$p_T$ [GeV/ $c$ ]	Cent.	Lower limit	Upper limit
		0–20%	0.031	0.864
0–1.6	6.5–30	20–40%	0.291	1.100
		40–100%	–	0.452
		0–20%	1.257	3.446
1.6–2.4	3–30	20–40%	0.0002	1.906
		40–100%	0.149	1.753

systematic uncertainties due to  $R_{\psi(2S)}(\text{PbPb})$ . Because of large uncertainty from the lower statistics pp data, shown in Fig. 77, we could not reach a conclusion on the observed pattern of the double ratio.

These observations are made for inclusive  $J/\psi$  and  $\psi(2S)$ , not taking into account the non-prompt contribution from b-hadron decays.

### 6.6.2. Results with new data

The results of the double ratio measurement with higher statistics pp data ( $5.4 \text{ pb}^{-1}$ ) are shown in the left panel of Fig. 78 as a function of centrality, for the midrapidity (blue squares) and forward rapidity (red circles) selections. Since the statistical and systematic uncertainties from the pp data of  $\approx 6\%$  are common to all centralities, their quadratic sum is shown as box around unity. The error bars and boxes stand for the statistical and systematic uncertainty from the PbPb data on the double ratio. The right panel of Fig. 78 shows the centrality integrated results. The data values are given in Table XX.

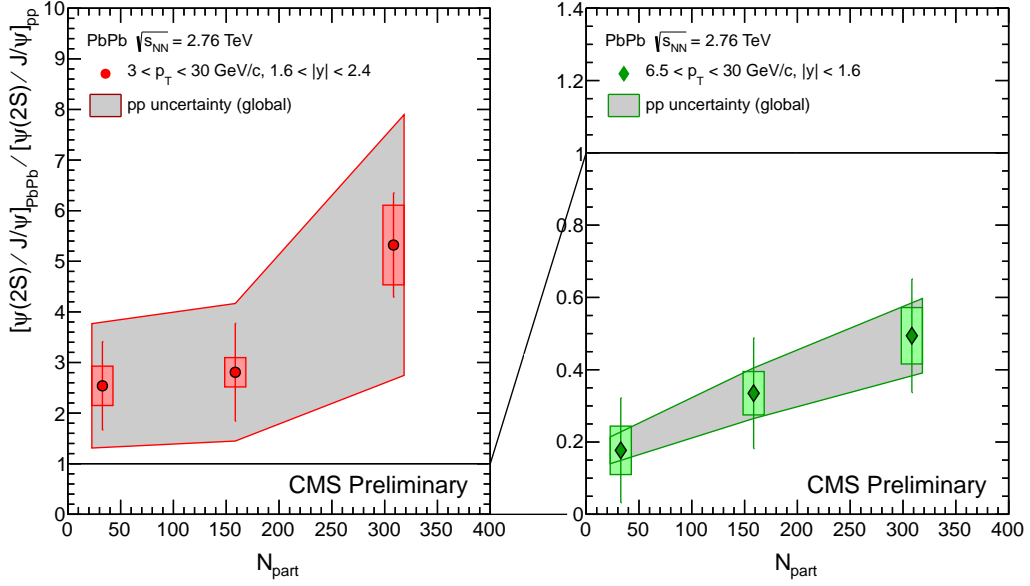


Fig. 77. Measured yield double ratio  $(N_{\psi(2S)}/N_{J/\psi})_{PbPb} / (N_{\psi(2S)}/N_{J/\psi})_{pp}$  as a function of centrality with PbPb data ( $150 \mu b^{-1}$ ) and pp data ( $231 \text{ nb}^{-1}$ ). The  $p_T$  and rapidity bins are  $6.5 < p_T < 30 \text{ GeV}/c$  and  $|y| < 1.6$  (left), and  $3.0 < p_T < 30 \text{ GeV}/c$  and  $1.6 < |y| < 2.4$  (right). The error bars and boxes stand for the PbPb statistical and systematic uncertainties, respectively. The shaded band is the uncertainty on the pp measurement, common to all double-ratio points.

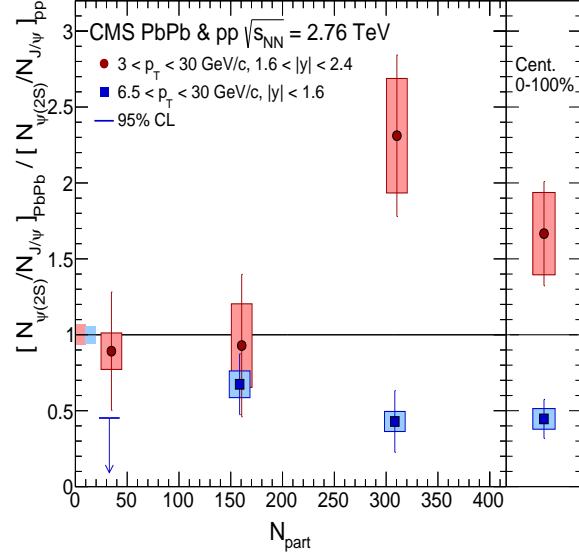


Fig. 78. Double ratio as a function of centrality (left panel): Blue squares show the result integrated over the range  $6.5 < p_T < 30 \text{ GeV}/c$  and  $|y| < 1.6$ . This is compared to the result in  $3 < p_T < 30 \text{ GeV}/c$  and  $1.6 < |y| < 2.4$  (red circles). The latter points are shifted by  $\Delta N_{\text{part}} = 2$  for better visibility. The right panel displays the centrality integrated results. Statistical (systematic) uncertainties are shown as bars (boxes). In the left panel, boxes at one indicate the global uncertainties from the pp data.

For  $p_T > 6.5 \text{ GeV}/c$  and  $|y| < 1.6$  the double ratio is less than unity in all three centrality bins. Within uncertainties, no centrality dependence is observed. For the 40-100% centrality bin, no significant  $\psi(2S)$  signal has been measured. Therefore an upper limit of 0.46 at a confidence level of 95% is set on the double ratio, using the Feldman-Cousins method. The centrality integrated double ratio is  $0.45 \pm 0.13$  (stat.)  $\pm 0.06$  (syst.). The uncorrected average  $p_T$  of  $J/\psi$  in this kinematic region is  $\langle p_T \rangle \approx 10.4 \text{ GeV}/c$ . It is the same in pp and PbPb collisions and does not depend on centrality.

At lower  $p_T$  ( $3 < p_T < 30 \text{ GeV}/c$ ) in the forward rapidity range, the data show an

increase of the double ratio with centrality, beyond the (large) uncertainties. In the most central collisions the double ratio is  $2.31 \pm 0.55$  (stat.)  $\pm 0.27$  (syst.)  $\pm 0.13$  (pp), which indicates that there are more  $\psi(2S)$  compared to  $J/\psi$  than in pp collisions. The significance of this double ratio being larger than unity is  $2.2\sigma$ . In peripheral events, the double ratio is consistent with unity, suggesting that  $\psi(2S)$  are as suppressed as  $J/\psi$ . The centrality integrated double ratio is  $1.67 \pm 0.34$  (stat.)  $\pm 0.16$  (syst.). The uncorrected average  $p_T$  of  $J/\psi$  in this kinematic region is  $\langle p_T \rangle \approx 6.4$  GeV/ $c$ . It is the same in pp and PbPb collisions and does not depend on centrality.

Table XX. Raw ratios of  $\psi(2S)$  over  $J/\psi$  yields ( $R_\psi$ ) for pp and PbPb collisions and their double ratio ( $R_\psi(\text{PbPb})/R_\psi(\text{pp})$ ). Listed uncertainties are statistical first, systematic second, and global scale third.

$ y $	$p_T$ [GeV/ $c$ ]	Cent.	$R_\psi$	$R_\psi(\text{PbPb})/R_\psi(\text{pp})$
0.0–1.6	6.5–30	0–100%	$0.017 \pm 0.005 \pm 0.003$	$0.45 \pm 0.13 \pm 0.07$
		0–20%	$0.016 \pm 0.008 \pm 0.003$	$0.43 \pm 0.20 \pm 0.07 \pm 0.02$
		20–40%	$0.026 \pm 0.008 \pm 0.003$	$0.67 \pm 0.20 \pm 0.09 \pm 0.04$
		40–100%	$0.003 \pm 0.006 \pm 0.003$	$0.08 \pm 0.16 \pm 0.08 \pm 0.01$
		pp	$0.038 \pm 0.002 \pm 0.001$	
1.6–2.4	3–30	0–100%	$0.061 \pm 0.013 \pm 0.010$	$1.67 \pm 0.34 \pm 0.27$
		0–20%	$0.085 \pm 0.019 \pm 0.014$	$2.31 \pm 0.53 \pm 0.38 \pm 0.15$
		20–40%	$0.034 \pm 0.017 \pm 0.010$	$0.93 \pm 0.47 \pm 0.28 \pm 0.06$
		40–100%	$0.033 \pm 0.014 \pm 0.004$	$0.89 \pm 0.39 \pm 0.12 \pm 0.06$
		pp	$0.037 \pm 0.002 \pm 0.001$	

From the centrality integrated double ratios nuclear modification factors of prompt

$\psi(2S)$  can be derived by multiplication with the published prompt  $J/\psi$   $R_{AA}$  [97]. For  $6.5 < p_T < 30$  GeV/ $c$  and  $|y| < 1.6$  one obtains:  $R_{AA}(\psi(2S)) = 0.13 \pm 0.04$  (stat.)  $\pm 0.02$  (syst.)  $\pm 0.01$  (pp), and for  $3 < p_T < 30$  GeV/ $c$  and  $1.6 < |y| < 2.4$ :  $R_{AA}(\psi(2S)) = 0.67 \pm 0.16$  (stat.)  $\pm 0.07$  (syst.)  $\pm 0.07$  (pp). This reveals at forward rapidity that, while  $\psi(2S)$  may be slightly enhanced relative to  $J/\psi$  in PbPb, they are still suppressed relative to pp collisions.

The  $\psi(2S)$   $R_{AA}$  shows a suppression with respect to pp in both kinematic regions investigated. This suppression depends on  $p_T$  and rapidity: at higher  $p_T$  and midrapidity,  $\psi(2S)$  are more suppressed than  $J/\psi$  as expected in a sequential melting scenario and matching the pattern CMS already observed for bottomonia [99]. In contrast, at lower  $p_T$  and forward rapidity, the centrality integrated double ratio is larger than the midrapidity result and even hints towards an enhancement of the  $\psi(2S)$  to  $J/\psi$  ratio in PbPb in comparison to pp. These results are opposite to the expected behaviour in the sequential melting scenario as well as to regeneration models, to the extent that they are still applicable at this relatively high  $p_T$  ( $p_T > 3$  GeV/ $c$ ). Also cold nuclear matter effects have so far been only seen to suppress the excited state stronger than the ground state. Hence, additional rapidity and  $p_T$  dependent mechanisms need to be considered to explain these results. But the double ratio measurement with ALICE exhibits a scenario different to that observed in CMS [127].

In summary, at higher  $p_T$  and midrapidity,  $\psi(2S)$  are more suppressed than  $J/\psi$ . However, at lower  $p_T$  and forward rapidity, the data are consistent with unity in peripheral collisions while for the 0–20% most central collisions they suggest an enhancement of the  $\psi(2S)$  to  $J/\psi$  ratio in PbPb in comparison to pp. This observation is opposite to the expected behaviour in the sequential melting scenario as well as to regeneration models.

More details of the study are given in the CMS Analysis note, Ref. [128, 129, 130].  
This study will be submitted to PRL soon.

# CHAPTER 7

**Suppression of quarkonia states in finite  
size quark gluon plasma in PbPb  
collisions at Large Hadron Collider**

## Suppression of bottomonia

### 7.1. Introduction

The melting temperature of the quarkonia states depends on their binding energy. The ground states,  $J/\psi$  and  $\Upsilon(1S)$  are expected to dissolve at significantly higher temperatures than the more loosely bound excited states. The difference in binding energies among different quarkonia indicate that they melt in a hot QGP at different temperatures and the quarkonium spectrum can serve as plasma thermometer [131, 132]. The  $\Upsilon(2S)$  and  $\Upsilon(3S)$  have smaller binding energies as compared to ground state  $\Upsilon(1S)$  and hence are expected to dissolve at a lower temperature. With the 2011 PbPb run the CMS published results on sequential suppression of  $\Upsilon(nS)$  states as a function of centrality [99] with enlarged statistics over their first measurement [98] where a suppression of the excited  $\Upsilon$  states with respect to the ground state have been observed in PbPb collisions compared to pp collisions at  $\sqrt{s_{NN}} = 2.76$  TeV.

The quarkonia yields in heavy ion collisions are also modified due to non-QGP effects such as shadowing, an effect due to change of the parton distribution functions inside the nucleus, and dissociation due to nuclear or comover interactions [114]. Due to higher mass, the nuclear suppression is expected to be less for bottomonia over charmonia. If large number of heavy quarks are produced in initial heavy ion collisions at LHC energy this could even lead to enhancement of quarkonia via statistical recombination [112, 133]. The effect of regeneration is expected to be less significant for bottomonia as compared to charmonia since bottom quarks are much smaller in number as compared to charm quarks. In addition, due to higher bottom mass the bound state properties obtained from potential models are more reliable. Thus recent years witness a shift in the interest to bottomonia. The ratios of the yields of

excited states to the ground states is considered even more robust QGP probe as the cold nuclear matter effects if any cancel out and can be neglected in the ratios. The calculation of ratios of  $\Upsilon$  states was also made in few works e.g. [134, 135] in past which showed that the  $p_T$  dependence of such ratio would show large variations and this would be a direct probe of the QGP.

In this study, we calculate the bottomonia suppression due to color screening in an expanding QGP using the model by Chu and Matsui [136], which takes into account the finite QGP lifetime and spatial extent. We start by describing the properties of quarkonia obtained from potential models and then give a brief description of the model which is extended to get the survival probabilities of  $\Upsilon$  states as a function of centrality of the collisions. Finally we compare the model calculations with the experimental data recently measured by the CMS experiment.

## 7.2. Properties of the $\Upsilon$ states from potential models

Interaction between the heavy quark and its antiquark inside the quarkonium at zero temperature can be described by Cornell potential [54, 55, 62]. The solution of the Schrodinger equation for such potential gives mass, bound state radius and the formation time  $\tau_F$ , the time needed to form a bound state after the production of heavy quark pairs. All parameters obtained with zero temperature potential using the parameter values given in [62, 137] are summarized in first three rows of Table I, which describe well the experimentally observed quarkonia spectroscopy.

The potential model can be extended to finite temperature with the main assumption that medium effects can be accounted for as a temperature-dependent potential. Instead of just looking at the individual bound states (at  $T = 0$  where quarkonium is well defined), one could rather obtain a unified treatment of bound states, threshold

and continuum by determining the spectral function. Using a class of screened potentials based on lattice calculations of the static quark-antiquark free energy, spectral functions at finite temperature are calculated in a work [138, 139] and it was found that all quarkonium states, except the 1S bottomonium, dissolve in the deconfined phase at temperatures smaller than  $1.5T_C$ . An upper limit on binding energy and the thermal width of different quarkonia states are then estimated using spectral functions in the quark-gluon plasma. Corresponding upper bounds on their dissociation temperatures  $T_D$  [139] are given in second last row of Table I. We used slightly lower values of  $T_D$  given in the last row to obtain a good match with measured  $R_{AA}$ .

### 7.3. Quarkonia suppression in finite size QGP

The bottomonia survival probabilities due to color screening in an expanding QGP are estimated using a dynamical model which takes into account the finite lifetime and spatial extent of the system [136]. The competition between the resonance formation time  $\tau_F$  and the plasma characteristics such as temperature, lifetime and spatial extent decide the  $p_T$  dependence of the survival probabilities of  $\Upsilon$  states. We describe the essential steps used to develop the model which is then extended to get the survival probabilities as a function of centrality of the collision.

The model assumes that quark gluon plasma is formed at some initial entropy density  $s_0$  corresponding to initial temperature  $T_0$  at time  $\tau_0$  which undergoes an isentropic expansion by Bjorken's hydrodynamics [19]. The plasma cools to an entropy density  $s_D$  corresponding to the dissociation temperature  $T_D$  in time  $\tau_D$  which is given by

$$\tau_D = \tau_0 \left( \frac{s_0}{s_D} \right) = \tau_0 \left( \frac{T_0}{T_D} \right)^3, \quad (7.1)$$

As long as  $\tau_D/\tau_F > 1$ , quarkonium formation will be suppressed.

Bottomonium properties	$\Upsilon(1S)$	$\chi_b(1P)$	$\Upsilon(2S)$	$\Upsilon(3S)$	$\chi_b(2P)$	$J/\psi$	$\psi(2S)$	$\chi_c(1P)$
Mass [GeV/ $c^2$ ]	9.46	9.99	10.02	10.36	10.26	3.0969	3.686	3.51
Radius [fm]	0.28	0.44	0.56	0.78	0.68	0.45	0.88	0.70
$\tau_F$ [fm] [62]	0.76	2.60	1.9	2.4		0.89	1.5	2.0
$T_D$ [GeV] upper limit [139]	$2 T_C$	$1.3 T_C$	$1.2 T_C$	$1 T_C$		$1.2 T_C$	$1.0 T_C$	$1.0 T_C$
$T_D$ [GeV] used in the present work	$1.8 T_C$	$1.15 T_C$	$1.1 T_C$	$1.0 T_C$		$1.1 T_C$	$1.0 T_C$	$1.0 T_C$

Table XXI. Quarkonia properties from non-relativistic potential theory [62, 139].

In the finite system produced in heavy ion collision, the suppression and entropy depend on the size of the system. The initial entropy density is assumed to be dependent on radius  $R$  (decided by the centrality of the collision) of the QGP [136] as

$$s_0(r) = s_0 \left( 1 - \left( \frac{r}{R} \right)^2 \right)^{1/4}, \quad (7.2)$$

Using Eq. (7.1) and Eq. (7.2) one can obtain the  $r$  dependence of  $\tau_D$  as

$$\tau_D(r) = \tau_D(0) \left( 1 - \left( \frac{r}{R} \right)^2 \right)^{1/4}. \quad (7.3)$$

where  $\tau_D(0)$  is the value of  $\tau_D$  for resonances produced in the center of the system.

Let a  $Q\bar{Q}$  pair is created at the position  $\mathbf{r}$  in the transverse plane with a transverse momentum  $\mathbf{p}_T$  and transverse energy  $E_T = \sqrt{M^2 + p_T^2}$ . The  $\Upsilon$  formation time is  $\tau_F \gamma$  which on equating with the screening duration  $\tau_D(r)$  given in Eq (7.3) one obtains the critical radius  $r_D$ , which is the boundary of the suppression region as

$$r_D = R \left( 1 - \left( \frac{\gamma \tau_F}{\tau_D(0)} \right)^4 \right)^{1/2}. \quad (7.4)$$

where  $\gamma = E_T/M$  is the Lorentz factor associated with the transverse motion of the pair. A bottom-quark pair can escape the screening region  $r_D$  and form  $\Upsilon$  if the position at which it is created satisfies

$$\left| \mathbf{r} + \frac{\tau_F \mathbf{p}_T}{M} \right| > r_D, \quad (7.5)$$

where the screening region  $r < r_D$  is shrinking because of the cooling of the system. Defining  $\phi$  to be the angle between  $\mathbf{p}_T$  and  $\mathbf{r}$ , the Eq. (7.5) leads to a range of  $\phi$  for which the bottom-quark pair can escape:

$$\cos \phi \geq z \quad \text{where} \quad z = \frac{r_D^2 - r^2 - (\tau_F p_T / M)^2}{2r (\tau_F p_T / M)},$$

With this we can then calculate probability for the pair created at  $\mathbf{r}$  with transverse momentum  $\mathbf{p}_T$  to survive as

$$\begin{aligned}\phi(r, p_T) &= 1 & z \leq -1 \\ &= \left( \frac{\cos^{-1} z}{\pi} \right) & |z| < 1 \\ &= 0 & z \geq 1,\end{aligned}$$

If the probability  $\rho(r)$  of a quark pair to be created at  $r$  which is symmetric in transverse plane is parameterized as

$$\rho(r) = \left( 1 - \left( \frac{r}{R} \right)^2 \right)^{1/2}, \quad (7.6)$$

the survival probability of quarkonia becomes

$$S(p_T, R) = \frac{\int_0^R dr r \rho(r) \phi(r, p_T)}{\int_0^R dr r \rho(r)}. \quad (7.7)$$

The survival probability as a function of centrality can be obtained by integrating over  $p_T$  as follows

$$S(N_{\text{part}}) = \int S(p_T, R(N_{\text{part}})) Y(p_T) dp_T. \quad (7.8)$$

Here  $Y(p_T)$  is  $p_T$  distribution (normalized to one) obtained from Pythia. The size  $R = R(N_{\text{part}})$  as a function of centrality is obtained in terms of the radius of the Pb nucleus given by  $R_0 = r_0 A^{1/3}$  ( $r_0 = 1.2$  fm) and the total number of participants  $N_{\text{part}0} = 2A$  in head-on collisions as

$$R(N_{\text{part}}) = R_0 \sqrt{\frac{N_{\text{part}}}{N_{\text{part}0}}}. \quad (7.9)$$

We assumed initial temperature  $T_0$  is the temperature in 0-5% central collisions and

calculated it for a given initial time  $\tau_0$  by

$$T_0^3 \tau_0 = \frac{3.6}{4a_q \pi R_{0-5\%}^2} \left( \frac{dN}{d\eta} \right)_{0-5\%}, \quad (7.10)$$

Here  $(dN/d\eta)_{0-5\%} = 1.5 \times 1600$  obtained from the charge particle multiplicity measured in PbPb collisions at 2.76 TeV [140] and  $a_q = 37\pi^2/90$  is the degrees of freedom we take in quark gluon phase. Using Eq. (7.9) we can obtain the transverse size of the system for 0-5% centrality as  $R_{0-5\%} = 0.92R_0$ . For  $\tau_0 = 0.1$  fm/c, we obtain  $T_0$  as 0.65 GeV using Eq. (7.10). The critical temperature is taken as  $T_C = 0.170$  GeV [4]. The initial temperature as a function of centrality is calculated by

$$T(N_{\text{part}})^3 = T_0^3 \left( \frac{dN/d\eta}{N_{\text{part}}/2} \right) / \left( \frac{dN/d\eta}{N_{\text{part}}/2} \right)_{0-5\%}. \quad (7.11)$$

where  $(dN/d\eta)$  is the multiplicity as a function of number of participants measured by ALICE experiment [140]. Both ALICE and CMS [23] measurements on multiplicity agree well with each other. Equation (7.11) giving the variation of initial temperature as a function of centrality differs from the approach taken in the work of Ref. [141] where it is taken to vary as a third root of number of participants. The nuclear modification factor,  $R_{\text{AA}}$  is obtained from survival probability taking into account the feed-down corrections as follows,

$$\begin{aligned} R_{\text{AA}}(3S) &= S(3S) \\ R_{\text{AA}}(2S) &= f_1 S(2S) + f_2 S(3S) \\ R_{\text{AA}}(1S) &= g_1 S(1S) + g_2 S(\chi_b(1P)) + g_3 S(2S) + g_4 S(3S) \end{aligned} \quad (7.12)$$

The factors  $f$ 's and  $g$ 's are obtained from CDF measurement [142]. The values of  $g_1$ ,  $g_2$ ,  $g_3$  and  $g_4$  are 0.509, 0.27, 0.107 and 0.113 respectively. Here it is assumed that the survival probabilities of  $\Upsilon(3S)$  and  $\chi_b(2P)$  are same and  $g_4$  is their combined fraction.

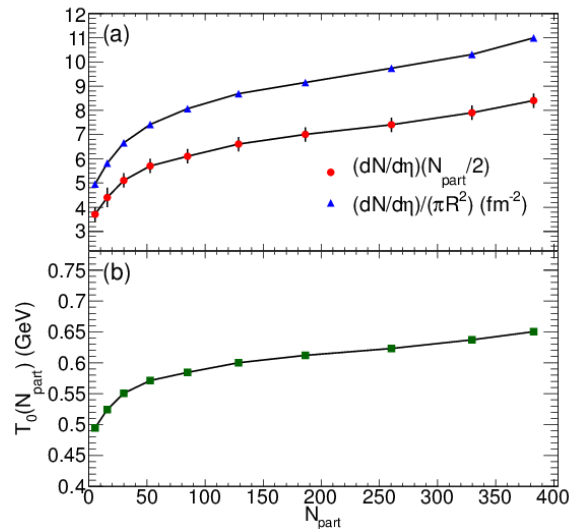


Fig. 79. a) Measured  $(dN/d\eta)/(N_{\text{part}}/2)$  [140] as a function of  $N_{\text{part}}$  along with the function  $(dN/d\eta)/(\pi R^2)$ . (b) The initial temperature obtained from measured multiplicity using Eq. (7.11)

The values of  $f_1$  and  $f_2$  are taken as 0.50 guided by the work from Ref. [143].

#### 7.4. Results and discussions

Figure 79 (a) shows measured  $(dN/d\eta)/(N_{\text{part}}/2)$  [140] as a function of  $N_{\text{part}}$ . The function  $(dN/d\eta)/(\pi R^2)$  gives the multiplicity divided by transverse area obtained using Eq.(7.9). Figure 79 (b) gives the initial temperature obtained from measured multiplicity using Eq. (7.11). Except in peripheral collisions, the initial temperature has weak dependence on centrality of collisions. Figure 80 demonstrates working of the model. It shows the screening radius  $r_D$  (in fm) as a function of  $p_T$  for  $R = 6.8$  fm (corresponding to head-on collisions) and  $R = 3.7$  fm (corresponding to minimum bias collisions) for (a)  $\Upsilon(1S)$  and (b)  $\Upsilon(2S)$ . The straight lines  $|\mathbf{r} + \frac{\tau_F \mathbf{p}_T}{M}|$  mark the distance a bottom quark pair (created at  $r = 0$ ) will travel before forming a bound

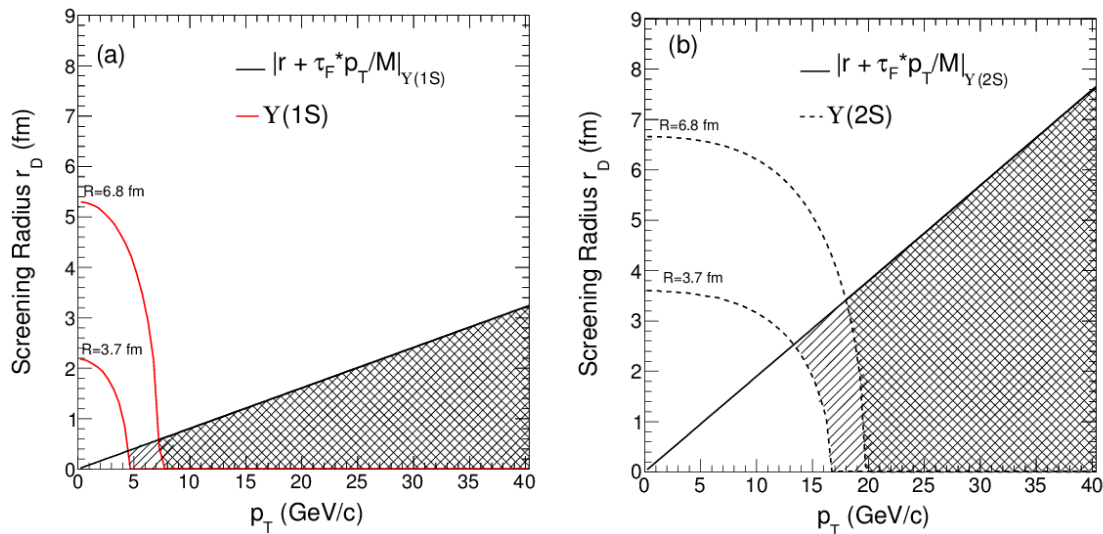


Fig. 80. The screening radius  $r_D$  (in fm) as a function of  $p_T$  for  $R = 6.8$  fm (corresponding to head-on collisions) and  $R = 3.7$  fm (corresponding to minimum bias collisions) for (a)  $\Upsilon(1S)$  and (b)  $\Upsilon(2S)$ . The straight lines  $| \mathbf{r} + \frac{\tau_F \mathbf{p}_T}{M} |$  mark the distance a bottom quark pair (created at  $r = 0$ ) will travel before forming a bound state. The mesh region in both the figures marks the escape region for bottom quark pair in case of head-on collisions and total shaded (mesh+lines) region marks the escape region in case of minimum bias collisions.

state. The mesh region in both the figures marks the escape region for bottom quark pair in case of head-on collisions and total shaded (mesh+lines) region marks the escape region in case of minimum bias collisions. If  $r$  is non-zero, the region where a bottomonium can escape screening, enlarges.

Figure 81 (a) shows the survival probability as a function of  $p_T$  for  $\Upsilon(1S)$ ,  $\Upsilon(2S)$ ,  $\Upsilon(3S)$  and  $\chi_b(1P)$  for  $R = 3.7$  fm (corresponding to average  $N_{\text{part}} = 114$  for minimum bias collisions). The survival probability  $S(p_T)$  has a unique  $p_T$  dependence decided by the  $T_D$  and  $\tau_F$  of each  $\Upsilon$  state. In general, the survival probabilities of resonance states increase with increasing  $p_T$  and become unity at different  $p_T$  for different states

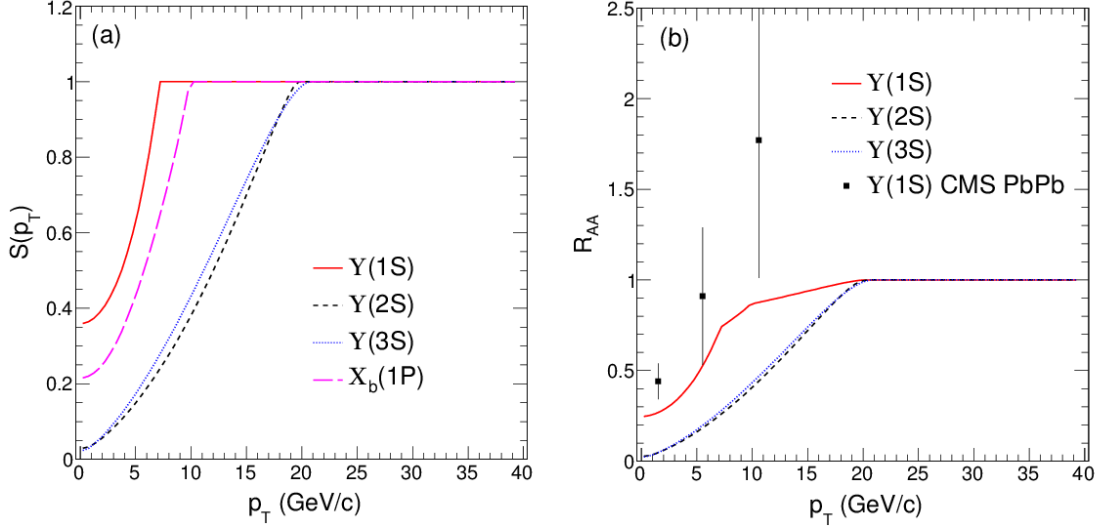


Fig. 81. (a) The survival probability as a function of  $p_T$  for  $\Upsilon(1S)$ ,  $\Upsilon(2S)$ ,  $\Upsilon(3S)$  and  $\chi_b(1P)$  for  $R = 3.7$  fm (corresponding to average  $N_{\text{part}} = 114$  for minimum bias collisions). (b) The nuclear modification factor for  $\Upsilon(1S)$ ,  $\Upsilon(2S)$  and  $\Upsilon(3S)$  which is obtained from survival probabilities including feed down corrections. The solid squares are  $\Upsilon(1S)$   $R_{AA}$  measured in the minimum bias PbPb collisions at  $\sqrt{s_{NN}} = 2.76$  TeV by CMS experiment [97].

corresponding to complete survival. Since  $\Upsilon(1S)$  is expected to dissolve at a higher temperature it has more probability to survive the plasma region even at lower  $p_T$  as compared to the cases of other bottomonia states. The model gives very similar survival probabilities for  $\Upsilon(2S)$  and  $\Upsilon(3S)$ . This is due to the fact that  $\Upsilon(3S)$  has large formation time even though its dissociation temperature is smaller in comparison to  $\Upsilon(2S)$ . Figure 81 (b) shows the nuclear modification factor for  $\Upsilon(1S)$ ,  $\Upsilon(2S)$  and  $\Upsilon(3S)$  which is obtained from survival probabilities including feed down corrections. The solid squares are  $\Upsilon(1S)$   $R_{AA}$  measured in the minimum bias PbPb collisions at  $\sqrt{s_{NN}} = 2.76$  TeV by CMS experiment [97]. The model reproduces the trend of the  $p_T$  dependence of low statistics measurements of  $R_{AA}$  from 2010 PbPb collisions by

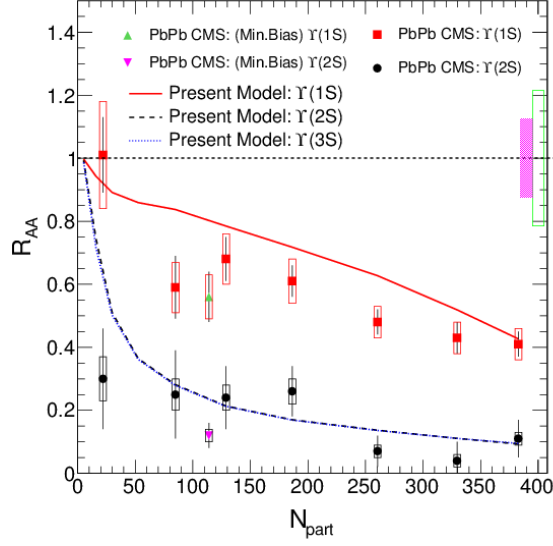


Fig. 82. The nuclear modification factor,  $R_{AA}$  as a function of  $N_{\text{part}}$  for  $\Upsilon(1S)$ ,  $\Upsilon(2S)$  and  $\Upsilon(3S)$ . The solid squares and circles are measured  $R_{AA}$  by CMS experiment in PbPb collisions at  $\sqrt{s_{NN}} = 2.76$  TeV [99] for  $\Upsilon(1S)$  and  $\Upsilon(2S)$  respectively and solid triangles are the minimum bias data points. The boxes at unity are the common systematic uncertainties in pp luminosity measurement and the pp yield. The lines (solid for  $\Upsilon(1S)$ , dashed for  $\Upsilon(2S)$  and dotted for  $\Upsilon(3S)$ ) represent the present model calculations.

CMS.

Figure 82 shows the nuclear modification factor,  $R_{AA}$  as a function of  $N_{\text{part}}$  for  $\Upsilon(1S)$ ,  $\Upsilon(2S)$  and  $\Upsilon(3S)$ . The solid squares and circles are measured  $R_{AA}$  by CMS experiment in PbPb collisions at  $\sqrt{s_{NN}} = 2.76$  TeV [99] for  $\Upsilon(1S)$  and  $\Upsilon(2S)$  respectively and solid triangles are the minimum bias data points. The lines (solid for  $\Upsilon(1S)$ , dashed for  $\Upsilon(2S)$  and dotted for  $\Upsilon(3S)$ ) represent the present model calculations. The common systematic uncertainties in pp luminosity measurement and the pp yield are represented by the boxes at unity. The model correctly reproduces the measured nuclear modification factors of both  $\Upsilon(1S)$  and  $\Upsilon(2S)$  for all centralities

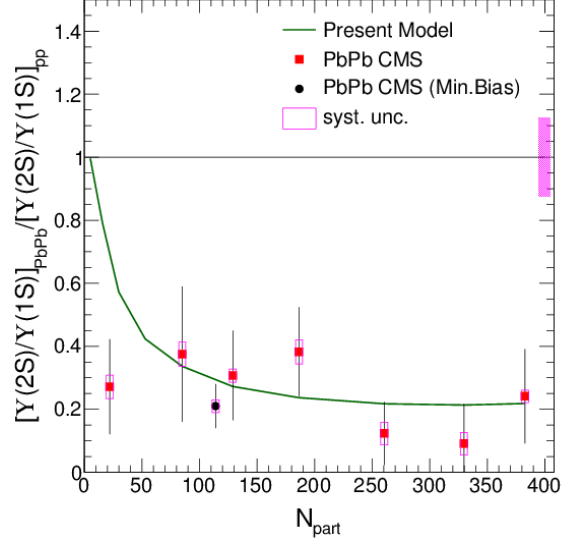


Fig. 83. Double ratio,  $[\Upsilon(2S)/\Upsilon(1S)]_{PbPb}/[\Upsilon(2S)/\Upsilon(1S)]_{pp}$  as a function of  $N_{part}$  measured by CMS experiment [99] along with the present calculation (solid line). The box at unity is the common systematic uncertainty in the pp yield.

using the parameters given in the Table I. The survival probabilities for  $\Upsilon(2S)$  and  $\Upsilon(3S)$  are very similar.

We also calculated the ratio of  $R_{AA}$  of  $\Upsilon(2S)$  to that of  $\Upsilon(1S)$  which is equivalent to the so called double ratio  $[\Upsilon(2S)/\Upsilon(1S)]_{PbPb}/[\Upsilon(2S)/\Upsilon(1S)]_{pp}$ . The double ratio has the advantage that the effects such as initial-state nuclear effects and regeneration which we ignore in our calculations are supposedly canceled out. Figure 83 shows the double ratio measured by CMS experiment [99] along with the present calculation. The calculations reproduce the measured double ratio even for the most peripheral data point.

The most important parameters in above study are formation time and dissociation temperatures of bottomonia states. There are reliable calculations of formation time obtained from zero temperature potential models which reproduce the bottomo-

nia spectroscopy very well. Upper limits are available for dissociation temperatures which are obtained from potential models at finite temperature. We used slightly lower values of the dissociation temperature to get a good description of the measured nuclear modification factors of  $\Upsilon(1S)$  and  $\Upsilon(2S)$ . The dynamics of the system is affected by the initial conditions which in the present calculations are fixed using measured charged particle multiplicity at LHC. There can be suppression due to initial nuclear effects which we assume to be much smaller than that due to colour screening and hence are ignored in the present work. The calculations of shadowing in PbPb show that it will effect the bottomonia yields by approximately 20 % for most central collisions [144]. Thus, the dissociation temperatures obtained by us are still considered to be the upper limits. Conversely there are other views which say that  $\Upsilon$  ground state is not much affected by the color screening up to the temperatures of  $\sim 3 - 4T_C$  and regeneration of the states are not negligible at the LHC [145]. The bottom quark mass is 10 times higher than the temperature we are considering for the system and hence the regeneration effect can be safely ignored in calculating nuclear modification for bottomonia. The uncertainties in the measurements of feed-down fractions would introduce uncertainties in the calculated nuclear modification factor. Finally we mention that the uncertainties arising from the effects other than colour screening are small and supposedly will have little or no effect on the double ratio. The study is published in Ref. [146].

### Suppression of charmonia

Using the same model and parameters used ( $\tau_0$ ,  $T_0$ , etc), we calculate the charmonia suppression due to the color screening. The properties of charmonia and dissociation temperatures  $T_D$  used for the model calculations are given in Table 7.2. The  $R_{AA}$  is obtained from survival probability taking into account the feed-down

corrections as follows,

$$\begin{aligned}
 R_{AA}(\chi_b(1P)) &= S(\chi_b(1P)) \\
 R_{AA}(\psi(2S)) &= S(\psi(2S)) \\
 R_{AA}(J/\psi) &= g_1 S(J/\psi) + g_2 S(\chi_c(1P)) + g_3 S(\psi(2S)) \quad (7.13)
 \end{aligned}$$

The factors  $g$ 's are obtained from PHENIX measurement [147]. The values of  $g_1$ ,  $g_2$  and  $g_3$  are 0.58, 0.32 and 0.096 respectively.

Figure 84 shows the survival probability as a function of  $p_T$  for  $J/\psi$ ,  $\psi(2S)$ , and  $\chi_c(1P)$  for  $R = 3.7$  fm (corresponding to average  $N_{\text{part}} = 114$  for minimum bias collisions). Like in bottomonia, the  $S(p_T)$  shows a unique  $p_T$  dependence decided by the  $T_D$  and  $\tau_F$  of each state and the survival probabilities of resonance states increase with increasing  $p_T$ . Compared to excited states of charmonia,  $J/\psi$  is expected to

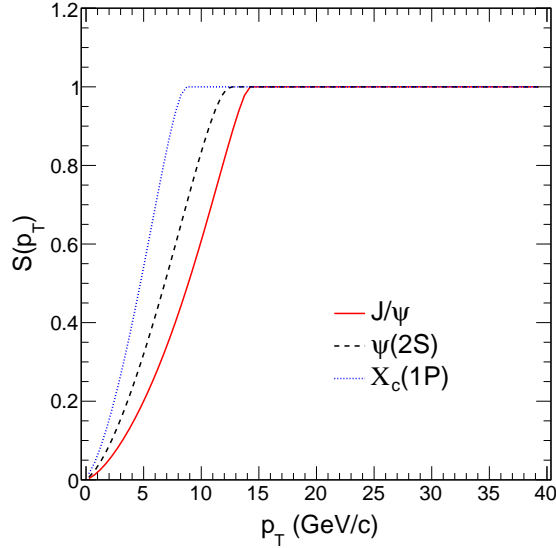


Fig. 84. The survival probability as a function of  $p_T$  for  $J/\psi$ ,  $\psi(2S)$ , and  $\chi_c(1P)$  for  $R = 3.7$  fm (corresponding to average  $N_{\text{part}} = 114$  for minimum bias collisions).

dissolve at a higher temperature due to color screening, because of its smaller radius or higher binding energy. But larger formation time of  $\chi_c(1P)$  and  $\psi(2S)$  benefit them to get survived faster than  $J/\psi$ . Figure 85 shows the nuclear modification factor,  $R_{AA}$

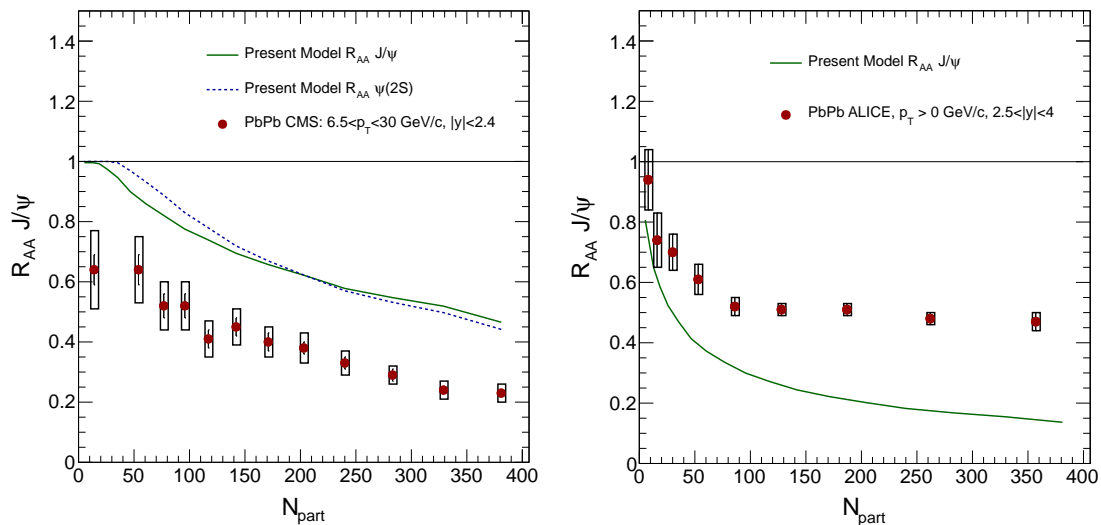


Fig. 85. (Left) The nuclear modification factor,  $R_{AA}$  as a function of  $N_{part}$  for  $J/\psi$ . The solid circles are measured  $R_{AA}$  by CMS experiment in PbPb collisions at  $\sqrt{s_{NN}} = 2.76$  TeV with  $p_T > 6.5$  and  $|y| < 2.4$  [45] for  $J/\psi$ . (b)  $R_{AA}$  measured by ALICE with  $p_T > 0$  and  $2.5 < |y| < 4.0$  [109].

as a function of  $N_{part}$  for  $J/\psi$ . The solid circles are measured  $R_{AA}$  by CMS (Left) and ALICE (Right) experiment in PbPb collisions at  $\sqrt{s_{NN}} = 2.76$  TeV [99]. The solid line represents the present model calculation for  $J/\psi$   $R_{AA}$  and for comparison, model calculation for  $\psi(2S)$   $R_{AA}$ , represented by dashed line, is given in the figure. In the case of high- $p_T$  (lower- $p_T$ )  $J/\psi$ , the model shows lesser (higher) suppression than observed with CMS (ALICE) data points [45, 109], indicating that other nuclear effects, in addition to the color screening, must have played in the modification of charmonium yields.

Figures 86 show double ratio,  $(\psi(2S)/J/\psi)_{PbPb}/(\psi(2S)/J/\psi)_{pp}$  as a function of

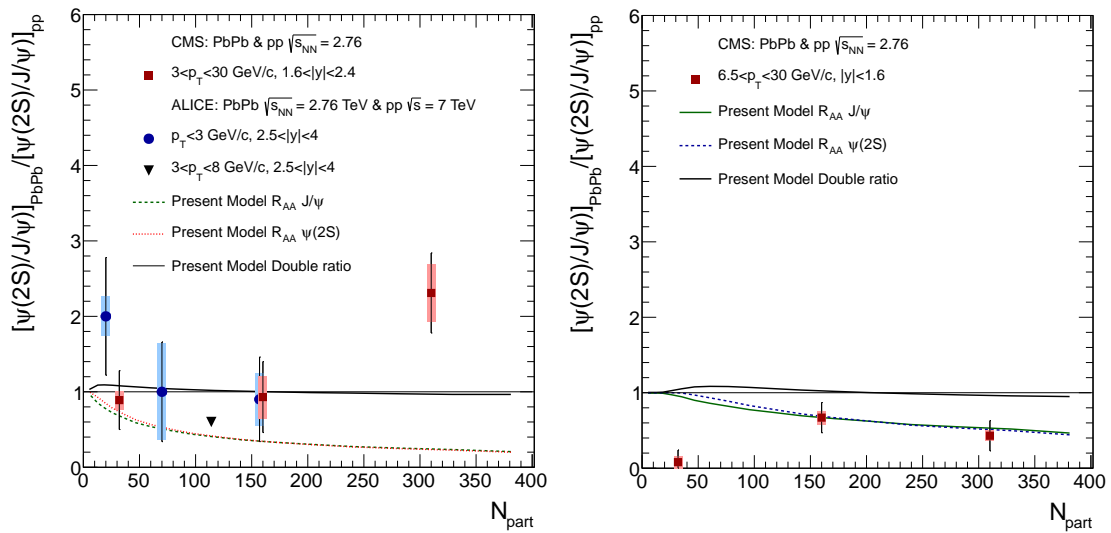


Fig. 86. Double ratio,  $(\psi(2S)/J/\psi)_{\text{PbPb}}/(\psi(2S)/J/\psi)_{\text{pp}}$  as a function of  $N_{\text{part}}$  measured by CMS experiment along with the present calculations for double ratio,  $J/\psi R_{\text{AA}}$  and  $\psi(2S) R_{\text{AA}}$  (solid line, dashed line and dotted line respectively). The  $p_{\text{T}}$  and rapidity bins are (Left)  $3 < p_{\text{T}} < 30$ ,  $1.6 < |y| < 2.4$  and (Right)  $6.5 < p_{\text{T}} < 30$ ,  $|y| < 1.6$ . Also the double ratio measured with ALICE is given for comparison [127].

$N_{\text{part}}$  measured by CMS experiment along with present model calculations for double ratio,  $J/\psi$   $R_{AA}$  and  $\psi(2S)$   $R_{AA}$  (solid line, dashed line and dotted line respectively). The  $p_T$  and rapidity bins are (Left)  $3 < p_T < 30$ ,  $1.6 < |y| < 2.4$  and (Right)  $6.5 < p_T < 30$ ,  $|y| < 1.6$ . Also the double ratio points measured by ALICE are given for comparison [127]. Model calculation lines show that the double ratio is close to unity. It means that effect of color screening cannot explain the data in both cases. The observed difference in the two kinematic bins is that  $\psi(2S)$  is more suppressed than  $J/\psi$  in high- $p_T$  and  $\psi(2S)$  is less suppressed than  $J/\psi$  in low- $p_T$ . This phenomenon requires models with new insights which incorporate different nuclear mechanism of charmonium suppression and regeneration in QGP.

In summary, we calculated the survival probabilities of quarkonium states and obtain the nuclear modification factors due to colour screening in an expanding quark gluon plasma of finite lifetime and size produced during PbPb collisions  $\sqrt{s_{NN}} = 2.76$  TeV. The formation time and dissociation temperatures of quarkonium states obtained from potential models are used as input parameters in the model. We used slightly lower values of the dissociation temperatures to get a good description of the measured nuclear modification factors of  $\Upsilon(1S)$  and  $\Upsilon(2S)$ . The model reproduces the centrality dependence of measured nuclear modification factors of  $\Upsilon(1S)$  and  $\Upsilon(2S)$  and the double ratio very well at  $\sqrt{s_{NN}} = 2.76$  TeV. The model calculation performed for charmonia indicate that the model with sole effect of color screening is not enough to explain the trend exhibited by the data.

# CHAPTER 8

## Conclusion

The CMS experiment with its muon detection capabilities has enabled several measurements on quarkonia (both charmonia as well as bottomonia) via dimuon channel. The excellent mass resolution in dimuon channel allows precise measurement of the quarkonium states and their relative yields in pp and PbPb systems. We did the first measurements of the prompt and non-prompt  $J/\psi$ , as well as of  $\psi(2S)$  mesons via their decay into  $\mu^+\mu^-$  pairs in PbPb and pp collisions at  $\sqrt{s_{NN}} = 2.76$  TeV. The measurements presented in this thesis are based on data recorded with the CMS detector from the LHC PbPb run at the end of years 2010 and 2011, and from the pp run during March 2011 and January 2013 at  $\sqrt{s} = 2.76$  TeV. To obtain good quality muons, an explicit study was carried out by tuning and optimising the cut variables (number of valid tracker hits,  $\chi^2/ndof$  of both the inner track and the global fit, etc) which are applied in all muon physics analysis. Differential cross sections and nuclear modification factors for prompt  $J/\psi$  and non-prompt  $J/\psi$  are measured in multiple bins of rapidity,  $p_T$  and centrality of the collision.

In the measurements of  $J/\psi$  in different kinematic ranges, the prompt  $J/\psi$  integrated over the rapidity range  $|y| < 2.4$  and high- $p_T$  has been measured in 12 centrality bins, starting with the 0-5% bin (most central), up to 60–100% bin (most peripheral). The results are corrected for efficiency loss and the limitations of the detector acceptance. We give the results of these measurements and compare them with the other experiments at LHC and RHIC. The  $R_{AA}$  of these high  $p_T$  prompt  $J/\psi$  decreases with increasing centrality showing moderate suppression even in the most peripheral collisions. On comparing with the STAR results [108] at RHIC, it follows that the suppression of (high  $p_T$ )  $J/\psi$  has increased with collision energy. The ALICE results on  $J/\psi$  correspond to a low  $p_T$  range which have little or no centrality dependence except for the most peripheral collisions [89].

$R_{AA}$  of  $J/\psi$ , shown in Fig. 87, measured in A+A collisions as a function of  $p_T$

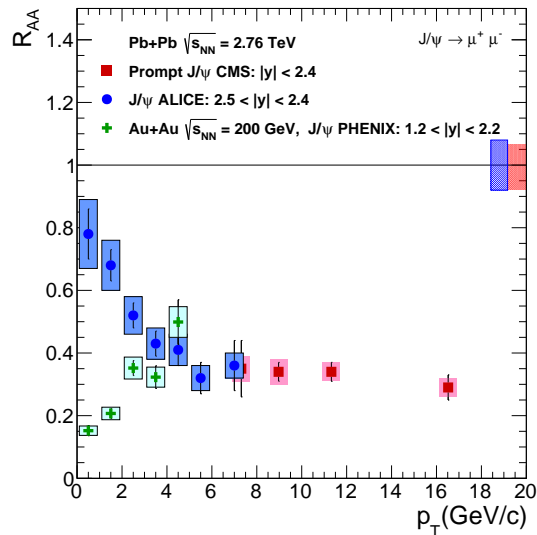


Fig. 87. Nuclear modification factor ( $R_{AA}$ ) of  $J/\psi$  as a function of  $p_T$  measured by CMS [97, 107], ALICE [109] and PHENIX [86] experiments.

at CMS, ALICE and PHENIX experiments, is found to be nearly independent of  $p_T$  (above  $6.5 \text{ GeV}/c$ ) showing that  $J/\psi$  remains suppressed even at very high  $p_T$  upto  $16 \text{ GeV}/c$  [97, 107]. The ALICE  $J/\psi$  data [109] shows that  $R_{AA}$  increases with decreasing  $p_T$  below  $4 \text{ GeV}/c$ . On comparing with the PHENIX forward rapidity measurement [86], it can be said that low  $p_T$   $J/\psi$  at LHC are enhanced in comparison to RHIC. These observations suggest regeneration of  $J/\psi$  at low  $p_T$  by recombination of independently produced charm pairs. Another hint of regeneration is given by CMS measurement of ratios of charmonia in PbPb and pp collisions.

The excellent vertexing capability of CMS detector enables measurement of B mesons via its decay to  $J/\psi$ . The centrality dependence of non-prompt  $J/\psi$  shows a slow decrease of the  $R_{AA}$  with decreasing centrality. We have seen that the  $R_{AA}$  versus  $p_T$  for pions, charged hadrons, D meson and non-prompt  $J/\psi$  from B meson shows that heavier particles (D, B) are less suppressed especially in low  $p_T$  range ( $<$

6 GeV/c ) indicating mass dependence of the in-medium energy loss. Together with this result, the observation of different suppression for charm and beauty hadrons in central collisions manifest the expected hierarchy of suppression,  $R_{AA}^\pi < R_{AA}^D < R_{AA}^B$ .

In charmonia double ratio, the first observation of the  $\psi(2S)$  meson in heavy-ion collisions at the LHC has been presented [128]. The double ratio of measured yields,  $(N_{\psi(2S)}/N_{J/\psi})_{\text{PbPb}}/(N_{\psi(2S)}/N_{J/\psi})_{\text{pp}}$ , is computed in three PbPb event centrality ranges and two kinematical bins: one at midrapidity,  $|y| < 1.6$ , covering the transverse momentum range  $6.5 < p_T < 30$  GeV/c, and the other at forward rapidity,  $1.6 < |y| < 2.4$ , extending to lower  $p_T$ , 3–30 GeV/c. Most of the non-prompt J/ $\psi$  and  $\psi(2S)$  mesons, coming from b-hadron decays, are subtracted through a cut on the pseudo-proper decay length,  $\ell_\psi$ . The  $\ell_\psi$  cut value is tuned from MC simulation studies, separately for the pp and PbPb collision systems, such that 90% of the prompt J/ $\psi$  and  $\psi(2S)$  are kept, typically rejecting 80% of the non-prompt ones. A substantial study is performed to obtain the best shapes of signal and background. The background is described by Chebychev polynomials, of order  $0 \leq N \leq 3$  independently determined for each analysis bin, with LLR and AIC tests.

The CMS measurements show two interesting observations: 1)  $\psi(2S)$  production is suppressed in PbPb collisions with respect to pp collisions, in both kinematic regions investigated; 2) in comparison to J/ $\psi$  production and in the most central PbPb collisions,  $\psi(2S)$  production is suppressed in the mid-rapidity bin, as expected in the sequential melting scenario and matching the corresponding bottomonia pattern [99], while it is enhanced in the forward rapidity bin, as shown in Fig. 88, giving a hint of regeneration that more  $\psi(2S)$  are produced compared to J/ $\psi$  in PbPb than in pp collisions. But the recombination models typically predict less production of  $\psi(2S)$  than J/ $\psi$  [113, 112]. Thus this puzzling observation insist further progress in theoretical interpretations.

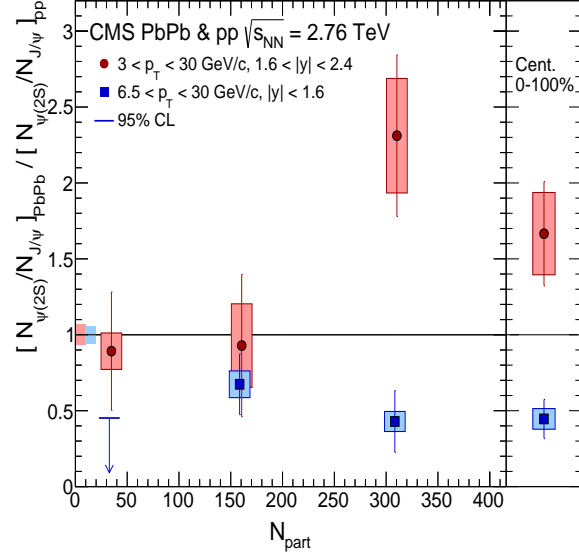


Fig. 88. Double ratio as a function of centrality (left panel): Blue squares show the result integrated over the range  $6.5 < p_T < 30 \text{ GeV}/c$  and  $|y| < 1.6$ . This is compared to the result in  $3 < p_T < 30 \text{ GeV}/c$  and  $1.6 < |y| < 2.4$  (red circles). The right panel displays the centrality integrated results. Statistical (systematic) uncertainties are shown as bars (boxes). In the left panel, boxes at one are the global uncertainties from the pp data.

In phenomenology study, we calculated the survival probabilities of quarkonium ( $\Upsilon$  and  $\psi$ ) states and obtain the nuclear modification factors due to colour screening in an expanding quark gluon plasma of finite lifetime and size produced during PbPb collisions  $\sqrt{s_{NN}} = 2.76 \text{ TeV}$ . The formation time and dissociation temperatures of quarkonium states obtained from potential models are used as input parameters in the model. We used slightly lower values of the dissociation temperatures to get a good description of the measured nuclear modification factors of  $\Upsilon(1S)$  and  $\Upsilon(2S)$ . The model reproduces the centrality dependence of measured nuclear modification factors of  $\Upsilon(1S)$  and  $\Upsilon(2S)$  (see Fig. 89) and the double ratio very well at  $\sqrt{s_{NN}} = 2.76 \text{ TeV}$ . The model calculation performed for charmonia shows that the double ratio is close to

one in all centrality region. It means that sole effect of color screening cannot explain the data in the analysed kinematic bins. This phenomenon requires models with new insights which incorporate different nuclear mechanism of charmonium suppression and regeneration in QGP.

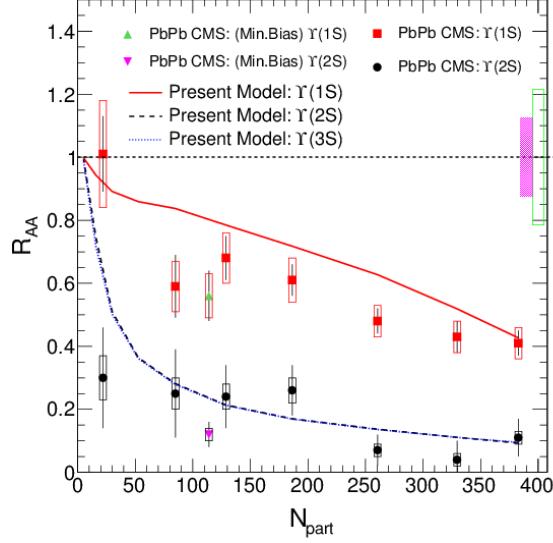


Fig. 89. The nuclear modification factor,  $R_{AA}$  as a function of  $N_{\text{part}}$  for  $\Upsilon(1S)$ ,  $\Upsilon(2S)$  and  $\Upsilon(3S)$ . The solid squares and circles are measured  $R_{AA}$  by CMS experiment in PbPb collisions at  $\sqrt{s_{NN}} = 2.76$  TeV [99] for  $\Upsilon(1S)$  and  $\Upsilon(2S)$  respectively and solid triangles are the minimum bias data points. The lines (solid for  $\Upsilon(1S)$ , dashed for  $\Upsilon(2S)$  and dotted for  $\Upsilon(3S)$ ) represent the present model calculations.

## REFERENCES

- [1] M. Gell-Mann, Phys. Lett. **8**, 214 (1964).
- [2] Georges Aad *et al.* [ATLAS Collaboration], Phys. Lett. B **716**, 1 (2012), arXiv:1207.7214.
- [3] S. Chatrchyan *et al.* [CMS Collaboration], Phys. Lett. B **716**, 30 (2012), arXiv:1207.7235.
- [4] CMS Collaboration, CMS-SMP-12-028, Submitted to Eur. Phys. J. C, arXiv:1410.6765 (2014).
- [5] ATLAS Collaboration, ATLAS-CONF-2013-041 (2013).
- [6] H. D. Politzer, Phys. Rev. Lett. **30**, 1346 (1973).
- [7] D. J. Gross and F. Wilczek, Phys. Rev. Lett. **30**, 1343 (1973).
- [8] P. A. R. Ade *et al.* [Planck Collaboration], arXiv:1303.5062 (2013).
- [9] Y. Kim and D. Yi, “Holography at Work for Nuclear and Hadron Physics”, Adv. High Energy Phys. **2011**, 259025 (2011), arXiv:1107.0155.
- [10] J. Adams *et al.* [STAR Collaboration], Nucl. Phys. A **757**, 102 (2005).
- [11] Rajeev S. Bhalerao, “Relativistic heavy-ion collisions”, arXiv:1404.3294 (2014).
- [12] K. Rajagopal and F. Wilczek, in M. Shifman (ed.): At the frontier of particle physics, Vol. **3**, 2061-2151 (2000), arXiv:hep-ph/0011333.
- [13] M. G. Alford, A. Schmitt, K. Rajagopal, and T. Schaefer, Rev. Mod. Phys. **80**, 1455 (2008).

- [14] S. Borsanyi *et al.*, J. High Energy Phys. **1011**, 077 (2010).
- [15] E. Iancu, “QCD in heavy ion collisions”, arXiv:1205.0579, (2012).
- [16] Yury Gorbunov, Ph.D. Thesis,  
<http://www.star.bnl.gov/~gorbunov/main/node5.html>.
- [17] R. Rapp and H. van Hees, in *The Physics of Quarks: New Research (Horizons in World Physics)*, edited by N. L. Watson and T. M. Grant, (Nova Science Publishers, New York, 2009), p. 87-138; arXiv:0803.0901.
- [18] B. Mueller, J. Schukraft and B. Wyslouch, arXiv:1202.3233, (2012).
- [19] J. Bjorken, Phys. Rev. D **27**, 140 (1983).
- [20] Krajczar K *et al.* [CMS Collaboration], J. Phys. G **38**, 124041 (2011), CMS-PAS-HIN-11-003.
- [21] B. B. Back *et al.* [PHOBOS Collaboration], Nucl. Phys. A **757**, 28 (2005).
- [22] I. Arsene *et al.* [BRAHMS Collaboration], Nucl. Phys. A **757**, 1 (2005).
- [23] S. Chatrchyan *et al.* [CMS Collaboration], J. High Energy Phys. **1108**, 141 (2011).
- [24] K. Aamodt *et al.* [ALICE Collaboration], Phys. Rev. Lett. **106**, 032301 (2011).
- [25] K. Reygers [ALICE Collaboration], “A Quick Tour of Ultra-Relativistic Heavy-Ion Physics at the LHC”, (2012), arXiv:1208.1626.
- [26] Ranbir Singh *et al.*, “Review Article on Heavy-Ion Collisions at LHC”, Adv. High Energy Phys. **2013**, 76147 (2013), arXiv:1107.0155.

- [27] W. Martin, [ALICE Collaboration], Nucl. Phys. A **904**, 573 (2013), arXiv:1210.5958.
- [28] ALICE Collaboration, “Elliptic flow of identified hadrons in PbPb collisions at  $\sqrt{s_{\text{NN}}} = 2.76$  TeV”, arXiv:1405.4632 (2014).
- [29] P. Huovinen, P. F. Kolb, U. W. Heinz, P. V. Ruuskanen and S. A. Voloshin, Phys. Lett. B **503**, 58 (2001).
- [30] CMS Public Note, “Long-range two-particle correlations with  $K_S^0$  and  $\Lambda/\bar{\Lambda}$  in pPb and PbPb collisions”, CMS PAS HIN-14-002 (2014).
- [31] A. Adare, *et al.*, [PHENIX Collaboration], “Deviation from quark-number scaling of the anisotropy parameter  $v_2$  of pions, kaons, and protons in Au+Au collisions at 200 GeV”, Phys. Rev. C **85**, 064914 (2012), arXiv:1203.2644.
- [32] S. Chatrchyan, [CMS Collaboration] *et al.*, Phys. Lett. B **710**, 256 (2012).
- [33] S. Chatrchyan *et al.* [CMS Collaboration], Eur. Phys. J. C **72**, 1945 (2012), arXiv:1202.2554.
- [34] K. Aamodt *et al.* [ALICE Collaboration], Phys. Lett. B **696**, 30 (2011).
- [35] X. N. Wang and M. Gyulassy, Phys. Rev. Lett. **68**, 1480 (1992).
- [36] A. Adare *et al.* [PHENIX Collaboration], arXiv:1208.2254, (2002).
- [37] M. J. Tannenbaum, “Highlights from BNL-RHIC”, arXiv:1302.1833, (2013).
- [38] K. Adcox *et al.* [PHENIX Collaboration], Phys. Rev. Lett. **88**, 022301 (2002).
- [39] G. Aad, [ATLAS Collaboration] *et al.*, Phys. Rev. Lett. **105**, 252303 (2010), arXiv:1011.6182.

- [40] S. Chatrchyan *et al.* [CMS Collaboration], Phys. Rev. C **84**, 024906 (2011), arXiv:1102.1957.
- [41] S. Chatrchyan *et al.* [CMS Collaboration], Phys. Lett. B **712**, 176 (2012).
- [42] B. Abelev *et al.* [ALICE Collaboration], arXiv:1401.1250, (2014).
- [43] B. Abelev *et al.* [ALICE Collaboration], J. High Energy Phys. **1209**, 112 (2011).
- [44] E. L. Kryshen [ALICE Collaboration], “Overview of ALICE results”, arXiv:1310.5819, (2013).
- [45] CMS Public Note, “Prompt and non-prompt  $J\psi$   $R_{AA}$  with  $150 \mu\text{b}^{-1}$  integrated PbPb luminosity at  $\sqrt{s_{NN}} = 2.76 \text{ TeV}$ ”, CMS PAS HIN-12-014 (2012).
- [46] B. Abelev *et al.* [ALICE Collaboration], Phys. Lett. B **720**, 52 (2013).
- [47] M. Cacciari, M. Greco, and P. Nason, J. High Energy Phys. **05**, 007 (1998).
- [48] B. Abelev *et al.* [ALICE Collaboration], Phys. Rev. Lett. **109**, 112301 (2012).
- [49] S. LaPointe *et al.* [ALICE Collaboration], arxiv:1401.6858 (2014).
- [50] Magdalena Djordjevic and Marko Djordjevic, “LHC jet suppression of light and heavy flavor observables”, arXiv:1307.4098, (2013).
- [51] R. Rapp and H. van Hees, in *Quark-Gluon Plasma 4*, edited by R. Hwa and X.N. Wang, (World Scientific Singapore, 2010), p. 111-206; arXiv:0903.1096 [hep-ph].
- [52] J. J. Aubert, U. Becker, P. J. Biggs, J. Burger, M. Chen, G. Everhart, P. Goldhagen, J. Leong, T. McCarriston, T. G. Rhoades, M. Rohde, S. C. C. Ting, S. L. Wu and Y. Y. Lee, Phys. Rev. Lett. **33**, 1404 (1974).

- [53] J. Paterson, M. Perl, B. Richter, and P. Rapidis, Phys. Rev. Lett. **33**, 1406 (1974).
- [54] E. Eichten, K. Gottfried, T. Kinoshita, K. D. Lane and T. M. Yan, Phys. Rev. D **17**, 3090 (1978) [Erratum-ibid. D **21**, 313 (1980)].
- [55] E. Eichten, K. Gottfried, T. Kinoshita, K. D. Lane and T. M. Yan, Phys. Rev. D **21**, 203 (1980).
- [56] S. Jacobs, M. G. Olsson and C. I. Suchyta, Phys. Rev. D **33**, 3338 (1986) [Erratum-ibid. D **34**, 3536 (1986)] [Phys. Rev. D **34**, 3536 (1986)].
- [57] H. Satz, Nucl. Phys. A **783**, 249 (2007), arXiv:0609197[hep-ph].
- [58] K. Nakamura [Particle Data Group], J. Phys. G **37**, 075021 (2010).
- [59] L. Antoniazzi, M. Arenton, Z. Cao, T. Chen, S. Conetti *et al.* [E705 Collaboration], Phys. Rev. D **46**, 4828 (1992).
- [60] I. Abt, A. Abyzov, M. Adams, H. Albrecht, V. Amaral *et al.* [HERA-B Collaboration], Phys. Lett. B **561**, 61 (2003).
- [61] F. Karsch and R. Petronzio, Z. Phys. C **37**, 627 (1988).
- [62] F. Karsch, M. T. Mehr and H. Satz, Z. Phys. C **37**, 617 (1988).
- [63] T. Matsui and H. Satz, Phys. Lett. B **178**, 416 (1986).
- [64] A. Andronic, P. Braun-Munzinger, K. Redlich and J. Stachel, Nucl. Phys. A **789**, 334 (2007).
- [65] L. Grandchamp and R. Rapp, Phys. Lett. B **523**, 60 (2001).
- [66] H. Fritzsch, Phys. Lett. B **67**, 217 (1977).

- [67] F. Halzen, Phys. Lett. B **69**, 105 (1977).
- [68] J. F. Amundson, O. J. P. Eboli, E. M. Gregores, and F. Halzen, Phys. Lett. B **372**, 127 (1996), arXiv:9512248[hep-ph].
- [69] G. T. Bodwin, E. Braaten, and G. P. Lepage, Phys. Rev. D **51**, 1125 (1995).
- [70] F. Abe *et al.* [CDF Collaboration] Phys. Rev. Lett. **69**, 3704 (1992).
- [71] J. Campbell, *et al.*, Phys. Rev. Lett. **98**, 252002 (2007).
- [72] Y.Q. Ma, *et al.*, Phys. Rev. D **83**, 111503 (2011).
- [73] G. Aad, [ATLAS Collaboration] *et al.*, Nucl. Phys. B **850**, 387 (2011), arXiv:1104.3038.
- [74] Y.Q. Ma, K. Wang and K.T. Chao, Phys. Rev. Lett. **106**, 042002 (2011), [arXiv:1009.3655].
- [75] S. Chatrchyan *et al.* [CMS Collaboration], J. High Energy Phys. **1202**, 011 (2012), arXiv:1111.1557.
- [76] R. Aaij *et al.* [LHCb Collaboration] “Production of  $J/\psi$  and  $\Upsilon$  mesons in  $pp$  collisions at  $\sqrt{s} = 8 \text{ TeV}$ ” CERN-PH-EP-2013-071, arXiv:1304.6977 [hep-ex].
- [77] K. J. Eskola, H. Paukkunen and C. A. Salgado, J. High Energy Phys. **0904**, 065 (2009).
- [78] L. Kluberg and H. Satz, “Color Deconfinement and Charmonium Production in Nuclear Collisions”, arXiv:0901.3831 (2009).
- [79] M. L. Miller, K. Reygers, S. J. Sanders and P. Steinberg, Ann. Rev. Nucl. Part. Sci. **57**, 205 (2007).

- [80] S. J. Brodsky and A. H. Mueller, Phys. Lett. B **206**, 685 (1988). N. Armesto and A. Capella, Phys. Lett. B **430**, 23 (1998).
- [81] D. Kharzeev and H. Satz, Phys. Lett. B **334** (1994).
- [82] M. E. Peskin, Nucl. Phys. B **156**, 365 (1979); G. Bhanot and M. E. Peskin, Nucl. Phys. B **156**, 391 (1979).
- [83] S. Gupta and H. Satz, Phys. Lett. B **283**, 439 (1992).
- [84] S. Digal, P. Petreczky and H. Satz, Phys. Rev. D **64**, 094015 (2001).
- [85] H. Satz, “Opening Talk at the *5th Berkeley School on Collective Dynamics in High Energy Collisions*, LBNL Berkeley/California, May 14 - 18, 2012 ”, Int. J. Mod. Phys. E **21**, 1230006 (2012), arXiv:1207.0341v1 (2012).
- [86] A. Adare *et al.* [PHENIX Collaboration], Phys. Rev. C **84**, 054912 (2011).
- [87] N Brambilla, S Eidelman, B K Heltsley, R Vogt, G T Bodwin, E Eichten, A D Frawley and A B Meyer *et al.* Eur. Phys. J. C **71**, 1534 (2011), arXiv:1010.5827.
- [88] A Andronic, P Braun-Munzinger, K Redlich, J Stachel, Phys. Lett. B **571**, 36 (2003).
- [89] B. Abelev *et al.* [ALICE Collaboration], Phys. Rev. Lett. **109**, 072301 (2012).
- [90] M. L. Miller et al., “Glauber modeling in high energy nuclear collisions”, Ann. Rev. Nucl. Part. Sci. **57**, 205 (2007).
- [91] B. Alver et al., “The PHOBOS Glauber Monte Carlo”, (2008) arXiv:0805.4411v1..

- [92] Z.W. Lin, C.M. Ko, B.A. Li, B. Zhang, and S. Pal, A multi-phase transport model for relativistic heavy ion collisions, *Phys. Rev. C* **72**, 064901 (2005).
- [93] H. De Vries, C. W. De Jager, and C. De Vries, “Nuclear charge and magnetization density distribution parameters from elastic electron scattering”, *Atom. Data Nucl. Data Tabl.* **36**, 495 (1987).
- [94] G.L. Bayatyan *et al.*, CERN-LHCC-2005-023, CMS-TDR-007 (2005).
- [95] CMS Analysis Note, ”Centrality determination for Heavy-Ion Data 2010”, CMS-AN-HIN-10-412 (2010).
- [96] CMS Analysis Note, ”Measurement of the azimuthal anisotropy of prompt and non-prompt  $J/\psi$  in PbPb collisions at  $\sqrt{s_{NN}} = 2.76$  TeV”, CMS-AN-HIN-11-496 (2011).
- [97] S. Chatrchyan *et al.* [CMS Collaboration], *J. High Energy Phys.* **1205**, 63 (2012).
- [98] S. Chatrchyan *et al.* [CMS Collaboration], *Phys. Rev. Lett.* **107**, 052302 (2011).
- [99] S. Chatrchyan *et al.* [CMS Collaboration], *Phys. Rev. Lett.* **109**, 222301 (2012).
- [100] CMS Analysis Note, ”Quarkonium production in PbPb collisions”, CMS-AN-HIN-11-062 (2011).
- [101] D. d’Enterria *et al.* [CMS Collaboration], *J. Phys. G* **34**, 2307 (2007), doi:10.1088/0954-3899/34/11/008.
- [102] C. Roland [CMS Collaboration], *Nucl. Instrum. Meth. A* **566**, 123 (2006), doi:10.1016/j.nima.2006.05.023.
- [103] B. Alessandro [ALICE Collaboration], *J. Phys. G* **32**, 1295 (2006), doi:10.1088/0954-3899/32/10/001.

- [104] S. Chatrchyan *et al.* [CMS Collaboration], “  $J\psi$  and  $\psi(2S)$  production in pp collisions at  $\sqrt{s} = 7$  TeV”, J. High Energy Phys. **02**, 011 (2012), arXiv:1111.1557.
- [105] CMS Analysis Note, ”J/ $\psi$  results from CMS in PbPb collisions, with  $150 \mu\text{b}^{-1}$  data at  $\sqrt{s_{NN}} = 2.76$  TeV”, CMS-AN-HIN-12-246 (2012).
- [106] T. Sjostrand, S. Mrenna and P.Z. Skands, *PYTHIA 6.4 Physics and Manual*, J. High Energy Phys. **05**, 026 (2006), [hep-ph/0603175].
- [107] C. Miranov [CMS Collaboration] Nucl. Phys. A **904**, 194 (2013), Report No. CMS-HIN-12-014
- [108] Z Tang (STAR Collaboration) J. Phys. G **38** 124107 (2011), arXiv: 1107.0532.
- [109] B. Abelev *et al.* [ALICE Collaboration], CERN-PH-EP-2013-203 (2013), arXiv:1311.0214.
- [110] S. Digal, P. Petreczky and H. Satz, Phys. Rev. D **64**, 094015 (2001), doi:10.1103/PhysRevD.64.094015, arXiv:hep-ph/0106017.
- [111] B. Alessandro *et al.* [NA50], Eur. Phys. J. C **49**, 559 (2007), arXiv:0612013.
- [112] X. Zhao and R. Rapp, Nucl. Phys. A **859**, 114 (2011).
- [113] A Andronic, P Braun-Munzinger, K Redlich, J Stachel, J. Phys. G **38**, 124081 (2011).
- [114] R. Vogt, Phys. Rev. C **81**, 044903 (2010).
- [115] F. Arleo, Nucl. Phys. A **910**, 223 (2013).
- [116] B. Abelev *et al.* [ALICE Collaboration], J. High Energy Phys. **02**, 73 (2014), arXiv:1308.6726.

- [117] R. Aaij *et al.* [LHCb Collaboration], J. High Energy Phys. **02**, 72 (2014), arXiv:1308.6729.
- [118] A. Adare, *et al.*, [PHENIX Collaboration], Phys. Rev. Lett. **111**, 202301 (2013).
- [119] M. J. Oreglia, “A Study of the Reactions  $\psi' \rightarrow \gamma\gamma\psi$ ” Ph.D. Thesis, Appendix D, (1980).
- [120] J. Beringer, [Particle Data Group], “Review of Particle Physics (RPP)“, Phys. Rev. D **86**, 010001 (2012).
- [121] L. Moneta, *et al.*, ”13<sup>th</sup> International Workshop on Advanced Computing and Analysis Techniques in Physics Research (ACAT2010)“, p:057, (2010), arXiv:1009.1003.
- [122] D. Acosta *et al.* [CDF Collaboration], Phys. Rev. D **71**, 032001 (2005), doi:10.1103/PhysRevD.71.032001, arXiv:hep-ex/0412071.
- [123] B. Abelev *et al.* [ALICE Collaboration], Phys. Rev. Lett. **108**, 082001 (2011).
- [124] S. Chatrchyan *et al.* [CMS Collaboration], Phys. Lett. B **727**, 381 (2013), arXiv:1307.6070.
- [125] R. Aaij *et al.* [LHCb Collaboration], Eur. Phys. J. C **73**, 2631 (2013), arXiv:1307.6379.
- [126] S. Chatrchyan *et al.* [CMS Collaboration], J. High Energy Phys. **04**, 103 (2014), arXiv:1312.6300.
- [127] R. Arnaldi, [ALICE Collaboration], “J/ $\psi$  and  $\psi(2S)$  production in Pb-Pb collisions with the ALICE Muon Spectrometer at the LHC”, Nucl. Phys. A **904**, 595 (2013), arXiv:1211.257.

- [128] CMS Public Note, “Measurement of the  $\psi(2S)$  meson in PbPb collisions at  $\sqrt{s_{NN}} = 2.76$  TeV”, CMS PAS HIN-12-007 (2012).
- [129] CMS Analysis Note, “Measurement of prompt  $\psi(2S)$  to  $J/\psi$  yield ratios in PbPb and pp collisions at  $\sqrt{s_{NN}} = 2.76$  TeV”, CMS-AN-HIN-12-118 (2012).
- [130] CMS Heavy-Ion Public Results,  
<https://twiki.cern.ch/twiki/bin/view/CMSPublic/PhysicsResultsHIN12007>.
- [131] H. Satz, Int. J. Mod. Phys. E **21**, 1230006 (2012).
- [132] A. Mocsy, P. Petreczky and M. Strickland, Int. J. Mod. Phys. A **28**, 1340012 (2013).
- [133] X. Zhao and R. Rapp, Phys. Rev. C **82**, 064905 (2010).
- [134] J. P. Blaizot and J. Y. Ollitrault, Phys. Lett. B **199**, 499 (1987).
- [135] J. F. Gunion and R. Vogt, Nucl. Phys. B **492**, 301 (1997).
- [136] M. C. Chu and T. Matsui, Phys. Rev. D **37**, 1851 (1988).
- [137] H. Satz, J. Phys. G **32**, R25 (2006)
- [138] A. Mocsy and P. Petreczky, Phys. Rev. D **77**, 014501 (2008).
- [139] A. Mocsy and P. Petreczky, Phys. Rev. Lett. **99**, 211602 (2007).
- [140] K. Aamodt *et al.* [ALICE Collaboration], Phys. Rev. Lett. **106**, 032301 (2011).
- [141] M. Strickland, Phys. Rev. Lett. **107**, 132301 (2011).
- [142] T. Affolder *et al.* [CDF Collaboration], Phys. Rev. Lett. **84**, 2094 (2000).
- [143] M. Strickland and D. Bazow, Nucl. Phys. A **879**, 25 (2012).

- [144] M. Bedjidian *et al.*, arXiv:0311048 [hep-ph].
- [145] A. Emerick, X. Zhao and R. Rapp, arXiv:1111.6537.
- [146] Abdulla Abdulsalam and Prashant Shukla, Int. J. Mod. Phys. A **28**, 1350105 (2013), arXiv:1210.7584.
- [147] A. Adare *et al.* [PHENIX Collaboration], Phys. Rev. D **85**, 092004 (2012).
- [148] M Djordjevic and M Gyulassy, Nucl. Phys. A **733** 265 (2004).
- [149] C. W. De Jager, H. De Vries and C. De Vries, Atom. Data Nucl. Data Tabl. **14**, 479 (1974).

## APPENDIX A

## GLAUBER MODEL

In this section I give a brief review of the Glauber model and introduce two important quantities linking A+A collisions with elementary nucleon-nucleon (N+N) collisions: 1) the number of binary collisions,  $N_{\text{coll}}$ , 2) the number of participants or wounded nucleons,  $N_{\text{part}}$ , which are nucleons from the projectile or the target which suffer at least one inelastic collision. In the Glauber model the collision between two nuclei, A and B, consisting of  $A$  and  $B$  nucleons, respectively, is considered as a superposition of (binary) collisions of the individual incoming nucleons. The geometry of the Glauber model is schematically sketched in Fig. 90.

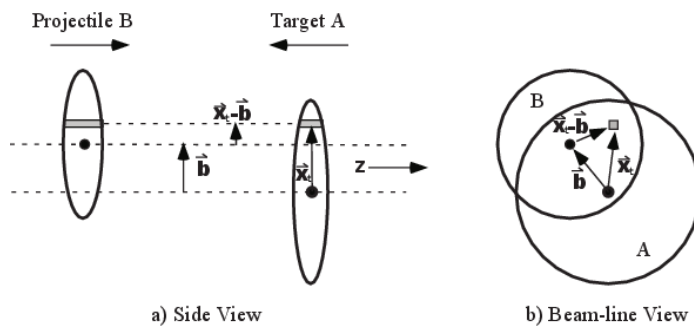


Fig. 90. Schematic representation of the geometry of Glauber model. Left panel: transverse view. Right panel: longitudinal view.

The inputs of the Glauber model are 1) nuclear charge densities, usually taken as a Wood-Saxon density profile,

$$\rho(r) = \frac{\rho_0}{1 + \exp\left(\frac{r-R}{a}\right)}, \quad (\text{A.1})$$

where  $\rho_0=0.17 \text{ fm}^{-3}$  is the nucleon density in the center of the nucleus,  $R$  is the nuclear radius and  $a$  is the thickness of the nuclear skin. For  $^{197}\text{Au}$ ,  $R=6.38 \text{ fm}$ ,  $a=0.535 \text{ fm}$ .

For  $^{208}\text{Pb}$ ,  $R=6.62$  fm,  $a=0.549$  fm [149]; 2) Inelastic nucleon-nucleon cross section,  $\sigma_{inel}^{NN}$ , which can be obtained from experimental measurements, *e.g.* ,  $\sigma_{inel}^{NN}=30(42)$  mb at SPS (RHIC) [58].

The nuclear thickness function,

$$T_A(\vec{x}_t) = \int dz \hat{\rho}_A(\vec{x}_t, z) , \quad (\text{A.2})$$

can be interpreted as the probability of finding a nucleon within a unit transverse area at  $\vec{x}_t$  of nucleus A. The  $\hat{\rho}_A$  is the nuclear density in Eq. (A.1) normalized to 1, namely,

$$\int \hat{\rho}_A d^2x_t dz = \frac{1}{A} \int \rho_A d^2x_t dz = 1 . \quad (\text{A.3})$$

Therefore  $T_A(\vec{x}_t)T_B(\vec{x}_t - \vec{b})$  is the joint probability of finding a pair of nucleons from nuclei A and B, respectively, within the common unit transverse area at  $\vec{x}_t$ . Their corresponding number of collisions is given by  $T_A(\vec{x}_t)T_B(\vec{x}_t - \vec{b})\sigma_{inel}^{NN} d^2x_t$ . Integrating over the transverse plane we obtain the total number of collisions contributed by this pair,

$$N_{\text{coll}}^{pair}(b) = \sigma_{inel}^{NN} T_{AB}(b) = \sigma_{inel}^{NN} \int T_A(\vec{x}_t)T_B(\vec{x}_t - \vec{b}) d^2x_t , \quad (\text{A.4})$$

where  $T_{AB}(b)$  is called the nuclear overlap function. Since from the two nuclei A and B a total number of  $AB$  such pairs can be found and each of them contributes an equal number of collisions, we obtain the following expression for the total number of binary collisions

$$N_{\text{coll}}(b) = AB T_{AB}(b) \sigma_{inel}^{NN} . \quad (\text{A.5})$$

The centrality of heavy-ion collisions is often expressed in terms of the number wounded nucleons (participants),  $N_{\text{part}}$ . In the Glauber model,  $N_{\text{part}}$  can be estimated as follows: The probability for a given nucleon from nucleus A to be located at transverse position  $\vec{x}_t$  is  $T_A(\vec{x}_t)$ , and the probability for this nucleon to collide with a

nucleon from nucleus B (located at  $(\vec{x}_t - \vec{b})$ ) is  $T_A(\vec{x}_t) T_B(\vec{x}_t - \vec{b}) \sigma_{\text{inel}}^{\text{NN}}$ . The probability of not colliding is thus  $T_A(\vec{x}_t) (1 - T_B(\vec{x}_t - \vec{b}) \sigma_{\text{inel}}^{\text{NN}})$ . The probability of not colliding with any of the  $B$  nucleons from nucleus B is thus  $T_A(\vec{x}_t) [1 - T_B(\vec{x}_t - \vec{b}) \sigma_{\text{inel}}^{\text{NN}}]^B$ . Therefore the probability for the nucleon at  $\vec{x}_t$  suffering at least one collision is  $T_A(\vec{x}_t) (1 - [1 - T_B(\vec{x}_t - \vec{b}) \sigma_{\text{inel}}^{\text{NN}}]^B)$ . Integrating over the transverse plane we obtain the probability for a given nucleon in nucleus A suffering at least one collision,

$$P_{wo}^A(b) = \int T_A(\vec{x}_t) \left\{ 1 - \left[ 1 - T_B(\vec{x}_t - \vec{b}) \sigma_{\text{inel}}^{\text{NN}} \right]^B \right\} d^2x_t . \quad (\text{A.6})$$

Since there are  $A(B)$  nucleons in nucleus A(B) we obtain the total number of wounded nucleons (participants) in A+B collisions at impact parameter  $b$  as

$$\begin{aligned} N_{\text{part}}(b) &= A P_{wo}^A(b) + B P_{wo}^B(b) \\ &= A \int T_A(\vec{x}_t) \left\{ 1 - \left[ 1 - T_B(\vec{x}_t - \vec{b}) \sigma_{\text{inel}}^{\text{NN}} \right]^B \right\} d^2x_t \\ &\quad + B \int T_B(\vec{x}_t - \vec{b}) \left\{ 1 - \left[ 1 - T_A(\vec{x}_t) \sigma_{\text{inel}}^{\text{NN}} \right]^A \right\} d^2x_t . \end{aligned} \quad (\text{A.7})$$

## APPENDIX B

## CENTRALITY TABLE

Table XXII.  $N_{\text{coll}}$ ,  $N_{\text{part}}$ , impact parameter  $b$ , and  $T_{\text{AA}}$  values in bins of centrality.

Bin	(%)	$\langle N_{\text{part}} \rangle$		$\langle N_{\text{coll}} \rangle$		$\langle b \rangle$ (fm)		$\langle T_{\text{AA}} \rangle$ (mb $^{-1}$ )	
		Mean	RMS	Mean	RMS	Mean	RMS	Mean	RMS
0	0.0–2.5	393.6220	12.4851	1747.8600	127.7500	1.8757	0.7881	27.3103	1.9961
1	2.5–5.0	368.9650	16.7561	1567.5300	151.0910	3.0190	0.7265	24.4927	2.3608
2	5.0–7.5	342.3290	17.5397	1388.3900	147.2190	3.9168	0.6113	21.6936	2.3003
3	7.5–10.0	316.4950	18.8501	1231.7700	147.4540	4.6335	0.6089	19.2464	2.3040
4	10.0–12.5	293.4980	19.7212	1098.2000	144.9600	5.2311	0.5995	17.1594	2.2650
5	12.5–15.0	271.9830	20.7154	980.4390	143.4860	5.7602	0.5882	15.3194	2.2420
6	15.0–17.5	249.6560	19.0765	861.6090	128.8810	6.3029	0.5402	13.4626	2.0138
7	17.5–20.0	230.5340	16.8995	766.0420	113.3450	6.7538	0.4874	11.9694	1.7710
8	20.0–22.5	212.2800	15.6885	676.5150	103.8770	7.1864	0.4661	10.5705	1.6231
9	22.5–25.0	194.5040	15.2686	593.4730	97.2514	7.6138	0.4674	9.2730	1.5196
10	25.0–27.5	178.5470	13.6373	521.9120	85.8589	8.0007	0.4422	8.1549	1.3415
11	27.5–30.0	163.2570	13.5508	456.5420	81.5744	8.3702	0.4509	7.1335	1.2746
12	30.0–32.5	149.0520	12.4969	398.5460	72.8881	8.7295	0.4450	6.2273	1.1389
13	32.5–35.0	135.9200	11.2145	346.6470	64.4269	9.0649	0.4329	5.4164	1.0067
14	35.0–37.5	123.2830	10.7961	299.3050	58.2632	9.3992	0.4351	4.6766	0.9104
15	37.5–40.0	111.6790	9.6757	258.3440	52.0660	9.7179	0.4299	4.0366	0.8135
16	40.0–42.5	100.7920	9.5055	221.2160	47.0498	10.0290	0.4447	3.4565	0.7352
17	42.5–45.0	90.7132	8.7438	188.6770	41.3714	10.3253	0.4460	2.9481	0.6464
18	45.0–47.5	80.9352	8.1942	158.9860	36.8075	10.6339	0.4544	2.4842	0.5751
19	47.5–50.0	72.6085	7.4698	134.7000	31.3360	10.9062	0.4603	2.1047	0.4896
20	50.0–52.5	64.1535	7.3698	112.5470	28.1519	11.1920	0.4774	1.7585	0.4399

Bin	(%)	$\langle N_{\text{part}} \rangle$		$\langle N_{\text{coll}} \rangle$		$\langle b \rangle$ (fm)		$\langle T_{\text{AA}} \rangle$ (mb $^{-1}$ )	
		Mean	RMS	Mean	RMS	Mean	RMS	Mean	RMS
21	52.5–55.0	56.6117	6.5275	93.4537	23.8043	11.4650	0.4859	1.4602	0.3719
22	55.0–57.5	49.9501	6.3155	77.9314	20.9925	11.7230	0.4972	1.2177	0.3280
23	57.5–60.0	43.3918	5.8555	63.5031	17.6548	11.9969	0.5121	0.9922	0.2759
24	60.0–62.5	37.8395	5.2455	52.0469	14.4684	12.2456	0.5231	0.8132	0.2261
25	62.5–65.0	32.7056	5.0172	42.3542	12.4243	12.4983	0.5445	0.6618	0.1941
26	65.0–67.5	27.8665	4.5192	33.9204	10.2231	12.7662	0.5663	0.5300	0.1597
27	67.5–70.0	23.7921	4.1070	27.3163	8.5081	13.0055	0.5916	0.4268	0.1329
28	70.0–72.5	20.2031	3.7775	21.8028	6.9508	13.2400	0.6168	0.3407	0.1086
29	72.5–75.0	16.8503	3.4842	17.2037	5.7991	13.4958	0.6604	0.2688	0.0906
30	75.0–77.5	14.0489	3.2613	13.5881	4.8713	13.7467	0.7054	0.2123	0.0761
31	77.5–80.0	11.6080	2.9527	10.6538	3.9753	13.9898	0.7503	0.1665	0.0621
32	80.0–82.5	9.5582	2.6466	8.3555	3.3047	14.2324	0.7994	0.1306	0.0516
33	82.5–85.0	7.7203	2.3779	6.4089	2.7151	14.4911	0.8507	0.1001	0.0424
34	85.0–87.5	6.4487	2.0858	5.1334	2.2187	14.6929	0.9028	0.0802	0.0347
35	87.5–90.0	4.9690	1.7596	3.7322	1.7441	14.9968	0.9741	0.0583	0.0273
36	90.0–92.5	4.2267	1.6512	3.0663	1.5859	15.1817	1.0270	0.0479	0.0248
37	92.5–95.0	3.5079	1.2218	2.4193	1.1475	15.3836	1.0493	0.0378	0.0179
38	95.0–97.5	3.1751	1.0571	2.1190	0.9863	15.4915	1.0664	0.0331	0.0154
39	97.5–100.0	2.7904	0.6539	1.7695	0.6083	15.6048	1.0792	0.0276	0.0095

APPENDIX C

TRIGGER RATE

Table XXIII. Active L1 Trigger Summary

Bit	Name	Rate Hz
1	L1_BscMinBiasOR_BptxAND	10.97
4	L1_BscMinBiasThreshold1_BptxAND	2.43
30	L1_ZdcScintTightVertex_BptxAND	3.08
32	L1_SingleMu3_BptxAND	17.19
34	L1_SingleJet30U_BptxAND	57.53
39	L1_ZdcCaloPlus_BptxAND	1.58
40	L1_ZdcCaloMinus_BptxAND	1.60
42	L1_ZdcCaloPlus_ZdcCaloMinus_BptxAND	10.83
85	L1_BptxXOR_BscMinBiasOR	7.54
87	L1_SingleEG5_BptxAND	51.15
88	L1_SingleJet20U_NotBptxOR	11.44
89	L1_SingleJet50U_BptxAND	46.49
93	L1_HcalHfMmOrPpOrPm_BptxAND	3.07
94	L1_HcalHfCoincidencePm_BptxAND	2.39
99	L1_DoubleMuOpen_BptxAND	6.41
110	L1_DoubleEG5_BptxAND	40.81
121	L1_BptxPlusANDMinus	4.85
123	L1_BptxXOR	4.85
126	L1_HcalHfCoincPmORBscMinBiasThresh1_BptxAND	62.67

Table XXIV. HLT path names with their accepted fraction and rate at 200 Hz

HLT Path	Accept Fraction	Rate@200Hz
HLT_HIJet35U	0.019698	3.939567
HLT_HIJet50U	0.002740	0.548016
HLT_HIJet75U	0.000747	0.149303
HLT_HIPhoton15_Cleaned	0.004367	0.873384
HLT_HIPhoton20_Cleaned	0.002641	0.528167
HLT_HIPhoton30_Cleaned	0.000643	0.128590
HLT_HIL1DoubleMuOpen	0.051699	10.339707
HLT_HIL1SingleMu3	0.132986	26.597114
HLT_HIL1SingleMu5	0.055636	11.127261
HLT_HIL1SingleMu7	0.031461	6.292263
HLT_HIL2DoubleMu0	0.026429	5.285766
HLT_HIL2DoubleMu3	0.003297	0.659346
HLT_HIL2Mu3	0.029856	5.971151
HLT_HIL2Mu5Tight	0.008233	1.646680
HLT_HIL2Mu20	0.001855	0.371098